THE GEOCHEMISTRY OF METALLIFEROUS BLACK SHALES:

UNDERSTANDING PRIMARY ENRICHMENTS, METAMORPHIC PROCESSES, AND THE ROLE OF METAL-RICH BLACK SHALES IN ARCHIVING EARTH EVOLUTION

Sean C. Johnson

(BSc. Hon., University of St Andrews)

CODES, ARC Centre of Excellence in Ore Deposits

School of Physical Sciences (Earth Sciences)

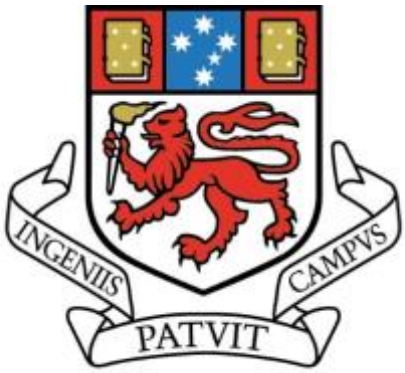

UNIVERSITY OF TASMANIA

Submitted in fulfilment of the requirements for the degree of

Doctor of Philosophy

University of Tasmania

November 2016

Declaration

This thesis does not contain any material that has been accepted for a degree or diploma by the University or any other institution, except where it has been duly acknowledged in the thesis. To the best of the author's knowledge it also contains no previously published material written by another person, except where it is acknowledged in the text of the thesis.

Sean C. Johnson

Supervisors: Professor Ross Large and Associate Professor Sebastien Meffre

Authority of Access

The content of the thesis may be made available for loan and limited copying and communication in accordance with the Copyright Act 1968.

Abstract

Black shales offer an important context to study the evolution of the oceans and atmosphere. As an archive of past climatic, evolutionary and geodynamic events in Earth history they offer the opportunity to further understand the nature of such events. Various redox sensitive and bio-essential trace metals can become enriched in black shales as a function of the nature of the environment in which they were deposited. Of particular interest are shales with high metal enrichment, as they may represent an important geochemical flux. In addition to archiving paleo-ocean and climatic conditions, metal-rich black shales offer important economic targets for hydrocarbon and mineral exploration. Previous work has shown that many important trace metals in black shales are hosted by diagenetic pyrite. Furthermore, metal-rich pyrite has been argued as a potential source for orogenic gold deposits where the metamorphic breakdown of pyrite to pyrrhotite releases gold and other trace metals.

This thesis presents a series of studies on aspects of black shale enrichment and mineralogy and offers greater insight as to the evolution of our oceans and atmosphere and how this may relate to secular metal enrichments. Each adopts a multi-proxy, geochemical approach, augmenting pyrite trace element chemistry with isotopic, and whole-rock geochemical or mineralogical data. In addition to addressing the nature of the depositional environment of black shales, mechanisms of ore genesis via the metamorphism of metal-rich shale sequences are also presented and evaluated. Four main aspects of the geochemistry of black shales are investigated in this thesis: 1) primary metal enrichment as a result of the changing nature of the water column during climatic perturbation, 2) the application of pyrite trace element chemistry along with other geochemical techniques to understand, and differentiate, primary metal enrichments and metamorphic overprint, 3) mechanisms by which pyrite may convert to pyrrhotite in black shale and what implications this may have for metal mobility, and 4) understanding of metal enrichments in black shale through geological time in the context of geodynamic and geochemical evolution.

The understanding of primary metal enrichments in black shales is critical in order to interpret the nature of the depositional environment. Chapters 2, 3 and 4 offer reviews of metal enrichment in sediments through time, as well as whole rock and pyrite trace element chemistry, as a means to record the chemical nature of the water column at the time of deposition. This is then applied in Chapter 5 to a metalliferous black shale section in NW Estonia of Cambrian to Ordovician age. This work contains a new detailed sedimentological study of the section to establish a depositional context. This is augmented by a high-resolution multi-proxy data and isotope geochemistry suggests that the section archives a major carbon isotope excursion (the Steptoean Positive Isotope Excursion; SPICE), not previously reported in these rocks, and allows the section to be placed in a global context. The high phosphorous content of the biograinstones deposited prior to the carbon isotope excursion suggests that phosphogenesis may have led to increased bio-productivity, affecting the carbon cycle. The high pyrite content and the geochemistry of this mineral in the lower portion of the black shale, which sits above the isotope excursion, suggests that the SPICE event may have led to the onset of low-oxygen conditions across the Baltica shallow shelf, and the deposition of metal-rich black shales.

In Chapter 6, the geodynamic and biochemical processes associated with metal enrichments in the formation metal-rich shales are reviewed and discussed together with a geochemical and mineralogical study of the Talvivaara deposit in Finland. As the world's largest black-shale poly-metallic deposit it offers a context to evaluate the economic aspects of black shale enrichment. The Paleoproterozoic age of this deposit and the fact that there are no known analogues that match its size, suggests that there may have been unique environmental factors that played a role in its metal enrichment. Much like the Estonian example, Talvivaara was deposited in the immediate wake of a large, global carbon isotope excursion. The excursion (the Lomagundi- Jatuli event, ~2.1 Ga) is the largest carbon isotope excursion preserved in the rock record and is followed by the first, and largest, mass burial of organic carbon in Earth history. This suggests that there may be analogous processes operating, but on different scales, in order to facilitate such enrichments. The deposit has been metamorphosed to amphibolite facies with only some primary pyrite, zircon and bituminous organic matter preserved. In-situ δ^{34}S-isotopic values of the sulfide phases and LA-ICP-MS analyses of iron sulfide phases, shows that the earliest pyrite

(interpreted to be of syn-sedimentary to early-diagenetic in origin) is trace metal rich. The $\delta^{34}S$ values in these pyrites suggest bacterial sulfate reduction from an open sulfate reservoir. The earliest pyrite is the most metal-rich, suggesting that the original depositional environment facilitated high metal concentrations. The shale package was then metamorphosed releasing trace elements and sulfur that then went on to form their own phases.

Chapter 7 presents new data and insights as to the nature of metamorphic reduction of pyrite to pyrrhotite in black shales. Often this transformation is only considered as proceeding at greenschist facies metamorphism (~300°C, and above). An experimental study, focusing on the magnetic character of pyrite, suggests that the transformation begins at ~177°C. The lower temperature proposed is supported by LA-ICP-MS studies of pyrite and pyrrhotite in Estonian oil shale and diagenetic to catagenetic sulfide concretions in sub-greenschist facies black shales from NW Russia. A model is presented suggesting that the degradation of organic matter during catagenesis is sufficient in producing enough reducing potential to facilitate the initial stages of the transformation to pyrrhotite.

Chapter 8 presents a synthesis of the geochemistry of metal-rich black shales. Some of the most metal-rich black shales worldwide are classified and compared to 'normal' black shales from throughout Earth history. In doing so, a new model is presented which suggests that during the Phanerozoic, plate collisional events led to increased detrital material into basins, leading to increased bio-productivity and atmospheric O_2. With increasing O_2 in the atmosphere, the processes of weathering and erosion became more vigorous leading to further influx of detritus and blooms of bio-productivity promoting the development of water column anoxia. Eventually, the cycle breaks when uptake by organisms exceeds input from the continents, leading to the return of 'normal' black shales and increasing carbon release to the atmosphere. This process is likely to have been the dominant process during the Phanerozoic, where supercontinent cycles are more dynamic and cover greater surface area. However, the Proterozoic also has some of the largest metalliferous, and organic-rich, sediments in the rock record and do not directly correlate to periods of supercontinent amalgamation. Instead, a discussion is presented that addresses the influence of widespread glaciations as a process to effectively erode, whilst simultaneously release oxygen, leading to increased oxidative weather and bio-productivity in their aftermath.

Acknowledgements

Over the course of my 3 and a bit years down in Tassie and CODES I have encountered many people, without whom my time here would have been considerably less enjoyable. Firstly, I would like to thank my supervisors for their help and support during my time at CODES. I would say that I am lucky to have the best arrangement of skills and support from Ross Large, who always thought about things both in terms of big and small pictures and Sebastien Meffre, who instilled into me the standards and rigor when collecting and analysing my data that ensured it was of the highest standard. In addition, despite his huge workload, he really stepped up in the final when Ross was, unfortunately, out of action. I thank him very much for this. Finally, Peter McGoldrick who, despite his retirement, has always made himself available and taken a keen interest in my work (when he's not doing some casual retirement DIY around the house, that is!). Critically, they have all allowed me the freedom to explore new avenues and ideas- this is something for which I am truly grateful. Especially the case when a variety of issues facilitated a change in focus of my project. They were always encouraging and helpful in generating new ideas and looking over grant proposals.

There have been many students who have come and gone over my time here, all of whom I remember fondly and wish the best in their future path. Many of whom have become like family to me: Dan and Selina, who picked me up from the airport on day one and took me out for a jet-lagged beer, and ensured I got settled. Jeff, for helping me to get settled in my first few weeks. Mark and Vic who I view as my fun and mischievous brother and sister. There is never a dull moment with those two around. Thanks to Chris, and his kids, Elly and Riley, who made me feel like part of the family from my first day in Hobart. Marley, Glo, Ross, Peter and Katie always welcomed me into their home so at no point did I ever feel as though I was on the other side of the world, away from family and friends. Thanks to Anita and Nathan for many sunny afternoon BBQs and late night chats debating whether or not to quit geology and open a café instead. These are two of the nicest people who, along with their kids, always bring a smile to my face. My office mates Nathan, Jacob, and 'the other Nathan', who made the office a relaxed and fun place to be and for putting up with me in my final few weeks. CODES has been a very

interesting place to work and I've enjoyed spending time with my fellow students whom I shall avoid listing in case of embarrassing omissions! Rose, Deb, Izzy, and 'Auntie' Jane in the office have been so gracious with their time, especially when I have silly questions about paperwork. I always leave with a smile on my face after chats with them. The lab staff; Sarah, Paul, Sasha, Elena, Ivan, Katie, Karsten, Sandrin, Chris, Christine, and Jay. Their dedication is the backbone of what makes UTas successful, and critically they are always there to ensure we all get the best out of our samples. I am truly grateful to Leonid, who trusted and believed in me to give me a job in the labs and extra responsibility not usually afforded to a PhD student. It gave me a deeper knowledge and appreciation of the day-to-day workings of our labs behind the scenes. In addition to that, I will always be indebted for the generous financial support of the SEG, SGA, NERC and the Mining Institute of Scotland for fieldwork and analytical costs, without which I would have been unable to complete all of the work for this thesis. Thanks to Adrian Boyce at SUERC for organising access and giving me free reign on the laser sulfur line. I think if it were not for Adrian and his enthusiasm for geology and ore deposits many years ago I would have ended up on a very different path.

My thanks to Alex, Sam and Claire, Martin and Dorren, Esi, David, Bianca, Brain and Cass, Roisin, Indrani, Laura, Georgina and Ben, for many great times, coffees and strolls at the market, lazy weekends, long hikes, and helping me to feel at home. I will particularly miss my daily coffee and weekend beer with Ben, discussing everything from partitioning of trace elements and metamorphic reactions to debating whether we'd rather have a foot for a hand or vice versa. I know that his brilliance will continue when he moves to Canada. Thanks to Kat and Ebba at Nant for helping to 'fuel the engines of research'. Many fun chats with Jodi and Margy helped to refresh my mind and were a welcome escape from work. Thanks to Isi for always bringing a smile to my face. From post-lab whisky in my office after I accidently made a 1st year cry, to Sunday brunches, naps on the balcony, and everything in between, thanks to Jess for always being there.

Finally, I would like to thank my parents for their support and encouragement over the years. This is dedicated to them.

Table of Contents

List of Tables

List of Figures

Chapter 1

Introduction

1.1. Preamble

Black shale deposition is ubiquitous throughout earth history and has been the focus of intense study in order to understand everything from oil formation, paleontological and palynological studies, mineral deposits, and critically, their ability to archive changes in Earth's environment and ocean-atmosphere evolution. This thesis aims to investigate the cross-over between these final two topics, to understand whether the nature of metal enrichment in black shales may also provide a greater understanding of paleo-environmental conditions during deposition through critical periods in Earth's history.

Black shales are dark-coloured, usually thinly-laminated, mudstones containing appreciable organic carbon (> 0.5%), iron sulfides, and silt to clay-sized detrital particles. They are most often accumulated under anoxic bottom waters in marine basins or continental margins (Arthur and Sageman, 1994). Compared to other shales or average crustal-derived sedimentary rocks, black shales are commonly highly enriched in many redox sensitive and/or sulfide-forming elements, including: Cr, Mo, V, U, Cu, Zn, Se, Ni, Co, Pb, Sb, Re, Cd, Ag, Au, and P. In some cases they can also be enriched in platinum group elements (PGE), Li, Hg and the rare earth elements (REE). In some examples, the grades of these metals are sufficient enough for mining (e.g. Talvivaara, Finland; Kontinen et al., 2013; Alum Shale, Sweden; Leventhal, 1991; and the Cambrian Ni-Mo-rich shales in Southern China; Xu et al., 2013). The processes of their enrichment can be varied, ranging from exhalation; interaction with hydrothermal fluids, late stage fluid infill or primary enrichments during deposition (e.g. Vine and Tourtelot, 1970; Coveney et al., 1991; Lehmann et al., 2007; Jiang et al., 2008; Large et al., 2015). Trace metals such as Mo, Cu, Ni and Zn also play an integral role in many biological processes and are absorbed by organisms such as nitrogen-fixing bacteria and algae (Anbar, 2004). Consequently some of the primary elemental enrichments in black shales can be linked to variations in primary productivity,

and ultimately, the state of the atmosphere/ocean during this time. It is this concept that will be the primary focus of this study.

The uptake of these metals by syn-genetic and diagenetic sulfides from sea water and pore fluids may lead to enhanced metal concentrations within the shale and has recently been proposed as a way of tracking the first order changes in ocean chemistry and nutrient supply through time (Large et al., 2014; 2015; Long et al., 2015). Understanding the applicability of this technique, either in unison with traditional whole-rock and isotope geochemical approaches or solely, may provide further avenues to understanding both metal enrichment in black shales and how these may archive changes in ocean chemistry through time.

1.2. Research rationale

Black shales are common components of the sedimentary record since the Late Archean (Condie et al., 2001) and their ability to archive geological and geochemical evolution has been the focus of many studies over the decades (See reviews by Meyer and Kump, 2008; Lyons et al., 2009; Jenkins, 2010). Critically, some shales are extraordinarily metal-rich compared to others. A variety of reasons have been proposed for their enrichments 1) trace element up-take from seawater by shallow water organisms; 2) direct absorption onto organic matter and detritus; 3) incorporation of Ni, Co, Mo, Zn, As, Se, Cu, Pb, and Sb into sedimentary pyrite during sedimentation and early diagenesis; and 4) metals sourced from hydrothermal vents and upwelling zones (i.e. Huerta-Diaz and Morse, 1992; Mao, et al., 2002; Piper and Perkins, 2004; Tribovillard et al., 2006; Lehmann et al., 2007; Large et al., 2011). This thesis aims to explore aspects of these processes but to also address the notion that while all black shales are common throughout geological time, it requires the marriage of tectonics, bio-productivity and changes in the atmosphere/ocean system at certain points in Earth history in order to produce metal enrichments. Recently, the application of marine pyrite geochemistry (Large et al., 2014) has led to a new tool that can be utilized in understanding the nature of the depositional environments of these shales. Throughout this thesis, pyrite chemistry will be used in unison with other geochemical tools in order to validate and unravel the environment of deposition, and what this may mean for ore formation

processes and/or periods of geochemical and geodynamic changes. The secular distribution of metal-rich black shales and their occurrence coeval with period of perturbation and environmental change suggest that more than just hydrothermal activity and reduced, organic-rich sediments are required. This thesis aims to test the following hypotheses with regard to metal-rich black shales: 1) the Cambro-Ordovician black shales of Estonia were influenced by changes in bio-productivity and seawater chemistry following a large, carbon isotope excursion. 2) the metal enrichments at Talvivaara are the result of massive geochemical and biochemical changes in the wake of the Great Oxidation Event. 3) the organic matter in black shale may influence the rate and processes by which minerals may be affected during metamorphism, and 4) the secular distribution of metal-rich black shales is a function of the evolution of the ocean/atmosphere/ biosphere system and that period in which all of these processes were acting in unison can effectively pre-condition the basins for metal-enrichment.

1.3. Structure of thesis and objectives of each chapter

Chapters 2, 3 and 4 present reviews of current knowledge of sedimentary metal enrichments, secular distributions of black shales, geochemical proxies to understand the nature of the depositional environment and pyrite trace element chemistry. Chapter 2 introduces, and reviews, the accumulation of metals in sediments and the processes that may govern it. It offers a review of the major types of sediment-hosted metal deposits and their occurrence through Earth history. The timing and mechanisms of metal enrichment are reviewed and discussed, as are the biogeochemical factors that may ultimately control much of the metal enrichments.

Chapter 3 builds upon aspects discussed towards the end of Chapter 2, namely, the biological and redox state of seawater on the fate of trace metals. This chapter offers a review of trace metal behavior in seawater as a function of varying redox states. It also discusses the fate of metals in terms of their ultimate partitioning into mineral phases or organic complexes.

Chapters 5, 6, 7 and 8 are formatted as manuscripts, versions of which will be prepared for submission, and revised for publication. These chapters aim to address various aspects of black shale formation and geochemistry and, in doing so, provide an original contribution to geological knowledge.

Chapter 5 discusses a metalliferous black shale section in NW Estonia of Cambrian to Ordovician age. This chapter aims to address primary metal enrichments in black shale, the development of anoxic to euxinic conditions during sedimentary deposition, and the response of pyrite and whole-rock trace element chemistry to these changes. The work contains a new detailed sedimentological study of the Cambrian to Ordovician section in Estonia to establish a depositional context. A high-resolution multi-proxy approach is used to understand redox in the depositional environment. This work suggests that the section preserves a major carbon isotope excursion (SPICE event), not previously reported in these rocks, allowing the section to be placed in a global context and showing that the SPICE excursion is synchronous with the onset of anoxic conditions across the shallow Baltic shelf. To complement the isotopic work, whole-rock and in-situ pyrite trace element chemistry was conducted to understand the link between the carbon excursion and pyrite chemistry.

Chapter 6 addresses whether primary enrichments mechanisms in shales can be recognized after the effects of metamorphism. In order to address this, a geochemical and mineralogical study of the Talvivaara deposit in Finland was conducted. As the world's largest black-shale polymetallic deposit, it also offers a context to evaluate the economic aspects of black shale enrichment. The Paleoproterozoic age of this deposit and the fact that there are no know analogues that match its tonnage suggest that this locality also offers the potential to study extreme enrichments in the context of potential geodynamic drivers. Furthermore, since the deposit has undergone metamorphism, it provides a context to understands these effects on metal-rich black shales.

Chapter 7 presents new data and insights as to the nature of metamorphic reduction of pyrite to pyrrhotite. Often this reaction is considered as occurring at temperatures above greenschist facies. The experimental heat study of pyrite, augmented by real-world examples, suggests that the conversion may occur at substantially lower temperatures. A new conceptual framework is developed that relates the concurrent breakdown of organic matter and mineral-scale transfer at low temperatures. This mechanism may aid our understanding of the formation of orogenic gold deposits and further exploration for such deposits.

Chapter 8 aims to synthesize the formation of metal-rich black shale through time in the context of potential drivers for such enrichments. This chapter compiles data from a variety of metal-rich black shales and evaluates them based on comparisons to 'typical' black shale (e.g. SDO-1; Hyuck, 1989). A new definition of 'highly- metalliferous black shales' is defined for the most metal-rich examples and their whole-rock and pyrite trace element enrichments are presented and discussed, culminating in a new model for these enrichments. In this model, it is argued that black shale enrichments represent peaks geodynamic drivers, atmospheric oxygen and bio-productivity, which, in unison, create the conditions for maximum metal concentration during black shale deposition.

Chapter 9 presents the main conclusions and the contribution to knowledge that these entail. Future work and questions arising are discussed along with potential means to address them.

1.4. Statement of authorship

This thesis comprises an introduction and conclusion, three review chapters, and four chapters that present original work. I was the author for all of these chapters and received comments and edits during their completion. Prof. Ross Large, Ben Cave and A. Prof. Sebastien Meffre (CODES, University of Tasmania) provided comments and edits for the review chapters (Chapters 2, 3 and 4). Chapters, 5, 6, 7, and 8 are formatted as manuscripts, versions of which will soon be submitted and reviewed for publication. For these chapters (5, 6, 7 and 8) I was the author, collected all samples, conducted all fieldwork, and designed the experiments. I performed all sample preparation and analysis myself except for a large portion of the LA-ICP-MS reference dataset of marine pyrite, used in Chapter 8 (from Large et al., 2015), to which I contributed 15% of the LA-CP-MS data and conducted all TOC% and S% for the samples in that dataset (n= >250). Additional whole-rock data and comments on the samples for the compilation in Chapter 8 were provided by Dr. Jeff Steadman (CODES, University of Tasmania), Prof. Ray Coveney (University of Missouri-Kansas City) and Karen Kelley (U.S Geological Survey). In Chapter 7, the magnetic experiments were conducted with Tim Raub (University of St Andrews and California Institute of Technology), who also assisted with the data processing (contribution- 8%) but I provided the samples and designed the experiment. Prof. Ross

Large, Dr Sebastien Meffre and Dr Peter McGoldrick (CODES, University of Tasmania) assisted in the interpretation and provided comments for all of these chapters. While additional comments on the depositional environment for some of the black shales listed in Chapter 8 were provided by Dr. Patrick Sack (Yukon Geological Survey), Dr. John Slack (U.S Geological Survey) and Dr. Daniel Gregory (University of California, Riverside). Fieldwork, and the selection of appropriate sites for sample collection in Chapter 5, was conducted with the assistance of Ylo Sostra (Tallinn University of Technology; contribution – 2%). Access to Talvivaara was facilitated in collaboration with Asko Kontinen (Geological Survey of Finland, 8%) who also provided assistance with updating the stratigraphic profile, cross sections through the deposit and unraveling the local deposit geology. In addition, access to archive core after the mine closed was provided by Peter Sorgen-Ward (Geological Survey of Finland, 2%).

1.5. References

Anbar, A.D., 2004. Molybdenum stable isotopes: observations, interpretations and directions. Reviews in Mineralogy and Geochemistry, 55, p.429-454.

Arthur, M.A. and Sageman, B.B., 1994. Marine shales: depositional mechanisms and environments of ancient deposits. Annual Review of Earth and Planetary Sciences, 22, p.499-551.

Condie, K.C., Des Marais, D.J., Abbott, D. 2001. Precambrian superplumes and supercontinents: a record in black shales, carbon isotopes, and paleoclimates? Precambrian Research, 106, p. 239-260.

Coveney, R.M., Watney, W.L. and Maples, C.G., 1991. Contrasting depositional models for Pennsylvanian black shale discerned from molybdenum abundances. Geology, 19, 2, p.147-150.

Huerta-Diaz, M. A., and Morse, J. W., 1992, Pyritization of trace metals in anoxic marine sediments: Geochimica et Cosmochimica Acta, v. 56, no. 7, p. 2681-2702.

Huyck, H.L.O., 1989. When is a metalliferous black shale not a black shale?: U.S. Geological Survey Circular 1058, p. 42–56.

Jenkyns, H.C., 2010. Geochemistry of oceanic anoxic events. Geochemistry, Geophysics, Geosystems, 11(3).

Jiang, S.Y., Yang, J.H., Ling, H.F., Chen, Y.Q., Feng, H.Z., Zhao, K.D. and Ni, P., 2007. Extreme enrichment of polymetallic Ni–Mo–PGE–Au in Lower Cambrian black shales of South China: an Os isotope and PGE geochemical investigation. Palaeogeography, Palaeoclimatology, Palaeoecology, 254, 1, p. 217-228.

Kontinen, A.T., Sorojen-Ward, P., Huhma, H., Lahtinen, H., 2013. Lithostratigraphy, sedimentary environment and origin of the Talvivaara black schist hosted Ni-Zn-Cu-Co deposit. Geological Survey of Finland, Report 198.

Large, R.R., Bull, S.W. and Maslennikov, V.V., 2011. A carbonaceous sedimentary source-rock model for Carlin-type and orogenic gold deposits. Economic Geology, 106, p. 331-358.

Large, R.R., Halpin, J.A., Danyushevsky, L.V., Maslennikov, V.V., Bull, S.W., Long, J.A., Gregory, D.D., Lounejeva, E., Lyons, T.W., Sack, P.J. and McGoldrick, P.J., 2014. Trace element content of sedimentary pyrite as a new proxy for deep-time ocean–atmosphere evolution. Earth and Planetary Science Letters, 389, p. 209-220.

Large, R.R., Halpin, J.A., Lounejeva, E., Danyushevsky, L.V., Maslennikov, V.V., Gregory, D., Sack, P.J., Haines, P.W., Long, J.A., Makoundi, C. and Stepanov, A.S., 2015. Cycles of nutrient trace elements in the Phanerozoic ocean. Gondwana Research, 28, p. 1282-1293.

Lehmann, B., Nagler, T.F., Holland, H.D., Willie, M., Mao, J., Pan, J., Dongsheng, M., Dulski, P., 2007. Highly metalliferous carbonaceous shale and Early Cambrian seawater. Geology, 35, p. 403-406.

Leventhal, J.S., 1991. Comparison of organic geochemistry and metal enrichment in two black shales: Cambrian Alum Shale of Sweden and Devonian Chattanooga Shale of United States. Mineralium Deposita, 26, p. 104-112.

Long, J.A., Large, R.R., Lee, M.S., Benton, M.J., Danyushevsky, L.V., Chiappe, L.M., Halpin, J.A., Cantrill, D. and Lottermoser, B., 2015. Severe selenium depletion in the Phanerozoic oceans as a factor in three global mass extinction events. Gondwana Research.

Lyons, T.W., Anbar, A.D., Severmann, S., Scott, C. and Gill, B.C., 2009. Tracking euxinia in the ancient ocean: a multiproxy perspective and Proterozoic case study. Annual Review of Earth and Planetary Sciences, 37, p. 507-534.

Mao, J., Lehmann, B., Du, A., Zhang, G., Ma, D., Wang, Y., Zeng, M., and Kerrich, R., 2002, Re-Os dating of polymetallic Ni-Mo-PGE-Au mineralization in Lower Cambrian black shales of South China and its geologic significance: Economic Geology, v. 97, no. 5, p. 1051-1061.

Meyer, K.M. and Kump, L.R., 2008. Oceanic euxinia in Earth history: causes and consequences. Annual Reviews in Earth Planetary Science, 36, p. 251-288.

Piper, D.Z., Perkins, R.B., 2004. A modern vs. Permian black shale— the hydrography, primary productivity, and water-column chemistry of deposition. Chemical Geology, 206, p. 177–197.

Tribovillard, N., Algeo, T.J., Lyons, T. and Riboulleau, A., 2006. Trace metals as paleoredox and paleoproductivity proxies: an update. Chemical geology, 232, p. 12-32.

Vine, J.D. and Tourtelot, E.B., 1970. Geochemistry of black shale deposits—a summary report. Economic Geology, 65, 3, p. 253-272.

Xu, L., Lehmann, B. and Mao, J., 2013. Seawater contribution to polymetallic Ni–Mo–PGE–Au mineralization in Early Cambrian black shales of South China: Evidence from Mo isotope, PGE, trace element, and REE geochemistry. Ore Geology Reviews, 52, p. 66-84.

Chapter 2

Metal enrichments in sediments and their temporal distribution

2.1. Introduction to metal enrichment processes and black shale formation

Deposits located in sedimentary basins account for a large majority of the world's base and precious metal resources and offer a range of characteristics in terms of their commodity type, age and global location (Fig. 2.1). The metal enrichment in these basins can be varied, ranging from exhalation; interaction with hydrothermal fluids, late stage fluid infill or primary enrichments during deposition. Black shales or mudstones are common sedimentary rocks in marine basins, continental shelves and epicontinental seas (Arthur and Sageman, 1994). They are dark-coloured (grey to black), fine-grained, laminated sedimentary rocks that generally are argillaceous and contain organic carbon (ranging from 0.5 to as much as >50 wt. %; Huyck, 1989). They are commonly enriched in a range of redox sensitive trace elements including; Mo, Ni, Co, Zn, As, Cu, Cr, Pb, Sb, Se, U and V. Metal enrichment can be attributed to a combination of processes: 1) trace element up-take from seawater by organisms; 2) direct absorption onto organic matter and detritus; 3) incorporation of Ni, Co, Mo, Zn, As, Se, Cu, Pb and Sb into sedimentary pyrite during sedimentation and early diagenesis (Huerta-Diaz and Morse, 1992; Piper and Merando, 1994; Mao, et al., 2002; Tribovillard et al., 2006; Large et al., 2011; Gregory et al., 2014); and 4) metals sourced from hydrothermal vents and upwelling zones. Trace metals such as Mo, Cu, Ni and Zn also play an integral role in many biological processes and are concentrated in organisms such as nitrogen-fixing bacteria and algae (Anbar, 2004). Redox sensitive metals (i.e. Mo, Zn, Cu, U) have high rates of transfer to the sediment due to uptake by organic matter or authigenic minerals, or both (Morford and Emerson, 1999), therefore, the redox state of the overlying seawater can exert a strong influence on metal concentrations in sediments. Metal enrichment requires conditions conducive to the accumulation of a large amount of organic matter (such as low oxygen in bottom and pore waters) and slow accumulation rates so as to not dilute the concentration of trace metals (Algeo, 2004; Perkins et al., 2008). Black shales due to their large extents and in many cases significant metal endowments can

represent important economic mineral targets. In the case of Phanerozoic metasedimentary-hosted orogenic Au deposits, these shales can act as an important metal source rock (Large et al., 2007; Pitcairn et al., 2010; Goldfarb and Graves, 2015). Furthermore, due to conditions required in order to develop metal-rich black shales, they offer the potential to help to elucidate the state of the water column under which they were deposited.

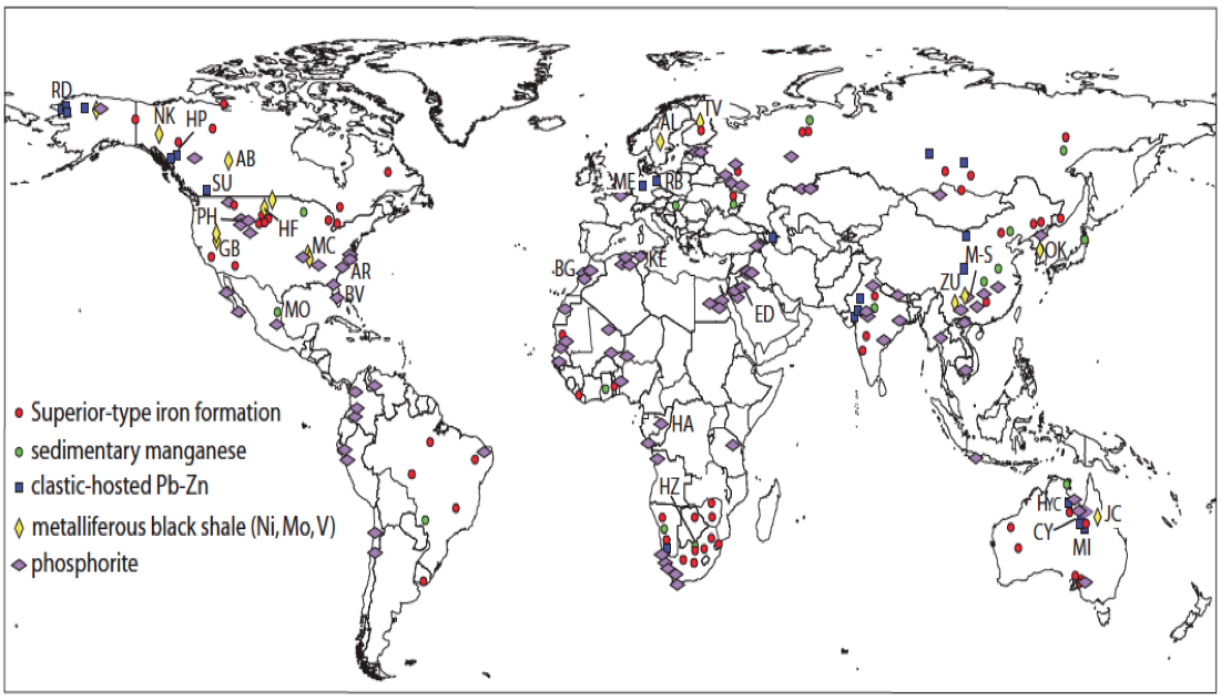

Figure 2.1. Distribution and nature of various sediment-hosted deposits (Scott et al., 2014). (AB = Alberta Shale, Canada; AL = Alum Shale, Sweden; AR = Aurora, North Carolina; BG = Benguérir, Morocco; BV = Bone Valley, Florida; CY = Century, Australia; ED = Eshidiya, Jordan; GB = Gibellini and Bisoni-McKay, United States; HA = Hinda, Congo (Brazzaville); HF = Heath Formation, United States; HP = Howards Pass, Canada; HYC = HYC, Australia; HZ = Hotazel, South Africa; JC = Julia Creek, Australia; KE = Kef Eschfair, Tunisia; ME = Meggen, Germany; NK = Nick, Yukon, Canada; MC = Mid-Continent, United States; MI = Mt. Isa, Australia; MO = Molango, Mexico; M-S = Maluping-Shabatu, China; PH = Phosphoria Formation, Idaho and Wyoming, United States; RB = Rammelsberg, Germany; RD = Red Dog, United States; SU = Sullivan, Canada; TV = Talvivaara, Finland; ZU = Zunyi, southern China.)

2.2. Prominent periods of black shale deposition in Earth History

Black shales are ubiquitous in the geological record, from small graphite occurrences in ~3.7 Ga metasediments in Greenland (Ohmoto et al., 2014) through to present day. There are prominent maxima in black shale abundance in Earth history, occurring in the Late Archean (2.7–2.5 Ga) and Paleoproterozoic (2.0–1.7 Ga). There are also less prominent peaks in the late Neoproterozoic (800–600 Ma) and during the Phanerozoic (Fig. 2.2; Condie et al., 2001). Peaks in black shale deposition can be linked to various geodynamic or geochemical processes. For instance, Condie (2001) proposed that black shale occurrences in the Archean and Paleoproterozoic may be a by-product of mantle super-plume events and supercontinent formation at ~2.7 ('Kenorland') and ~2.0 Ga ('Columbia'/'Nuna'). Super-plume events may have expelled large amounts of CO_2 rich volcanic gases into the atmosphere–ocean system and led to an increase in depositional rates of carbon. In addition, the sudden influx of CO_2 can lead to fluctuations of global temperature, changing weathering patterns and processes.

This may be a valid hypothesis for Archean black shale formation when biological activity was relatively limited. However, in the Proterozoic and Phanerozoic increased black shale deposition may reflect a combination of hydrothermal fluid influx into the ocean (introducing nutrients and trace elements); increased erosion, delivering nutrients and trace metals to the oceans; periods of anoxia ('Ocean Anoxic Event's- OAE's); and disrupted ocean currents, such as during glaciation, when ocean circulation is altered; or during periods of continental amalgamation, affecting and changing ocean circulation patterns (Tribovillard et al., 2006; Scott et al., 2014). Ocean anoxic events are prevalent during the Phanerozoic as punctuated periods of high carbon burial that led to drawdown of atmospheric carbon dioxide (often producing pronounced carbon isotope excursions), lowering of bottom-water oxygen concentrations and, in some cases, significant biological extinction or turnover. Most ocean anoxic events are accompanied by high productivity and export of carbon from surface waters to the sediments that are then preserved as black shales. However, the factors that triggered some of these events in the Phanerozoic remain uncertain.

Peaks in black shale abundance at ~2.1 Ga and 800–600 Ma correlate with peaks in ^{13}C in marine carbonates, (Lomagundi-Jatuli excursion, the largest positive isotope excursion ever recorded ~2.1Ga;

Martin et al., 2013), an increase in atmospheric oxygen (following the Great Oxidation Event- G.O.E.), large-scale glaciations (800-600Ma 'Snowball Earth') and high chemical alteration index values in shales (Condie et al., 2001; Melezhik et al., 2004; Melezhik et al., 2013). Peaks in black shale abundance also occur during times of supercontinent formation at 2.1–1.9 Ga (Columbia/Nuna: Evans et al., 2011) and again at 800–600 Ma (Rodinia: Bradley et al., 2005; Evans et al., 2009), which would have led to many partially closed marine basins, disruption of ocean currents (maybe even spatial heterogeneity within the ocean system) and increased hydrothermal influx from vents at ocean ridges or basin margins. All of the aforementioned processes, either singularly or in unison, can contribute to widespread anoxia in marine basins. It is evident that black shales are deposited during turbulent periods of earth history and, therefore, may provide a suitable context upon which to focus research to develop our understanding of these periods.

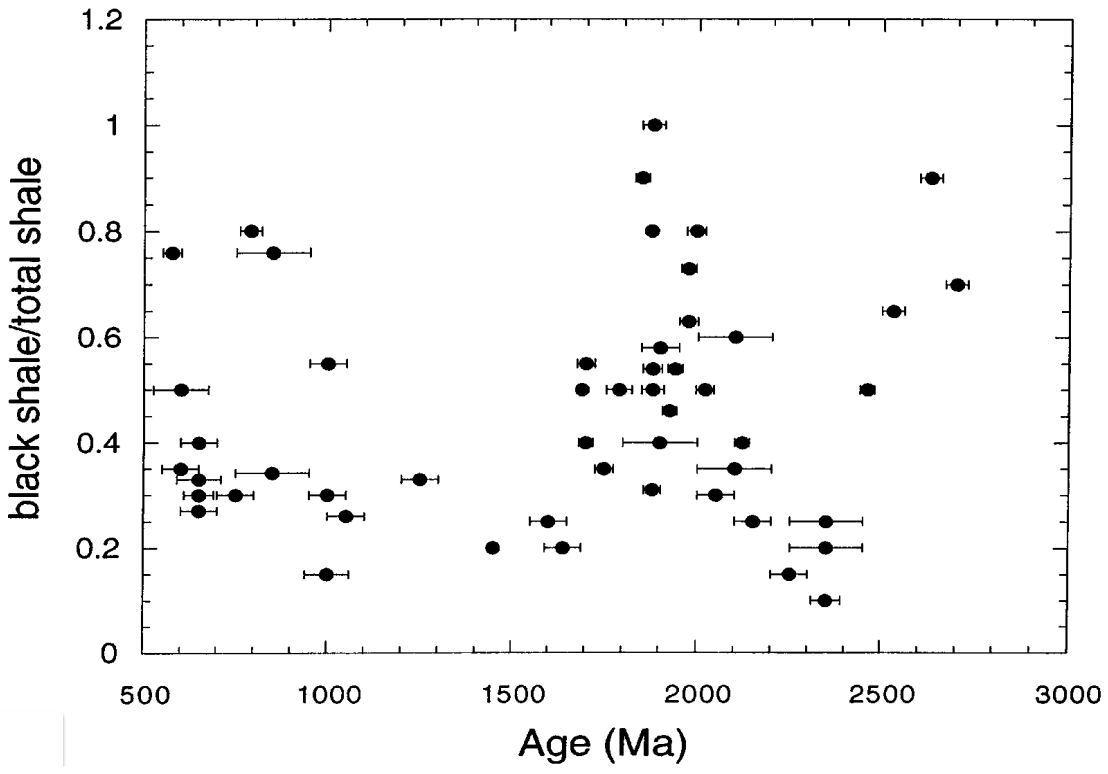

Figure 2.2. Distribution of black shale deposition through Earth History (Condie, 2001).

2.3. Metalliferous black shales

Black shales are common constituents of sedimentary basins and can often be enriched in metals compared to average crust. However certain black shales can contain a wide variety of metal enrichments, some of which can reach economic concentrations of Co, Ni, Zn, Cu, Mo, U, V and/or REE, Y and PGE (e.g., Mao et al., 2002; Coveney, 2003). Hyuck (1989) proposed a designation of 'metalliferous black shale' as being a shale that is enriched in metals by a factor of 2x (except for beryllium, cobalt, molybdenum, and uranium, for which 1x is sufficient) relative to the U.S. Geological Survey Standard SDO-1. Approximately 25% of global black shale examples can fit this description and some are currently being exploited.

Thin sulfide layers in Lower Cambrian shales of South China have been actively mined for decades and contain grades of over 4 wt % Mo and up to 4 wt % Ni, 2 wt % Zn, along with appreciable Pt, Pd and Ir concentrations (Coveney and Nansheng, 1991). Similar stratiform mineralized zones occur in black shales of Middle to Late Devonian age at the Nick horizon in the Yukon as well as other metal-rich horizons in the Selwyn Basin of North Western America (e.g. Magnall et al., 2015). The most economically significant metalliferous black shale (in terms of tonnage) is the Talvivaara Zn-Ni-Cu deposit in Finland that was mined from 2008 to 2013.

High-grade and high-tonnage black shales like those listed above are rare and can be argued to reflect unusual origins compared to 'typical' Phanerozoic black shale occurrences. For example, metals in the deposits in South China are proposed as being derived predominantly from seawater (Lehmann et al., 2007; Xu et al., 2013), but syn-depositional hydrothermal processes may have also provided some metal input (Pi et al., 2013, and references therein). In contrast, the Talvivaara deposit contains a thick but disseminated metal-rich precursor black shale, developed in an anoxic, metal-rich basin before being subjected to metamorphic mobilization (this study; Loukola-Ruskeeniemi and Lahtinen, 2013).

Metalliferous black shales are numerous in the Phanerozoic. At present metal prices the majority are sub-economic. However, recent exploration has continued searching for significant deposits in metalliferous black shales (e.g., Cretaceous shale units in the Alberta, Canada (Sabag, 2008); the Cambrian to Ordovician Alum Shale in Sweden (e.g., Leventhal, 1991; Dyni, 2005; Aura Energy Ltd.,

2014) and the Cretaceous Julia Creek deposit of Queensland, Australia (Lewis et al., 2010). Economic potential of metalliferous black shales is often limited by the thickness of the shales, e.g., the Mecca Quarry Shale (United States of America) contains up to 10,000 ppm V (Coveney and Martin, 1983). However, it is only a few tens of centimeters thick, and consequently is not economic.

It is becoming clear that metalliferous black shale deposition can be broadly constrained to certain time periods in Earth history, namely, the Paleproterozoic, the Cambrian, Devonian, Permian and Cretaceous. This begs the question as to whether there is a temporal evolution of metal-rich black shales and whether wider geodynamic processes may influence their evolution?

2.3.1. Metal sources in metalliferous black shales

Debate on whether metals enriched in metalliferous black shales are sourced directly from the seawater or hydrothermally derived, has been ensuing for many years (e.g., Coveney and Glascock, 1989; Lehmann et al., 2007). Metalliferous black shales with high concentrations of Mo, V, Zn, and other trace metals are common in the Phanerozoic. Modern analogues are known in euxinic basins (e.g., the Black Sea, Lyons et al., 2003), strengthen the suggestion that the source of many metals in most black shales are likely derived from seawater (i.e. Lehmann et al., 2007; Fig. 2.3.). Black shales with high metal concentrations derived from the interaction of hydrothermal solutions (such as those near present-day hydrothermal vent systems, i.e., the TAG Hydrothermal Field; Rona et al., 1993; Petersen et al., 2000) can exhibit elemental zonations and enrichments of Cr, Co, Mn Sb, and Ba, as well as base metals such as Ni, Zn Cu and Pb, and silica and/or Fe-oxide phases. Concurrent enrichments of these metals with U, Mo and V would require a very unique fluid history and composition if they were entirely derived form hydrothermal fluids. Therefore contributions of seawater and primary organic matter would still be required to account for enrichments of Mo, V and U. Furthermore, pyrites derived from hydrothermal solutions should hold much higher $\delta^{34}S$ values (i.e. Herzig, and Hannington, 1995; Elderfield and Schultz, 1996; Large, 2000; Slack et al., 2007; Saez et al., 2011).

Biogenic sulfide (H_2S_{aq}) is produced in most modern carbonaceous, low-oxygen sediments, and pyrite is a common phase in black shales. However, not all pyritic black shales are the same, and the processes

of sulfide formation and the amount of H_2S_{aq} generated can exert influence on their formation of (Scott and Lyons, 2012). Where organic carbon deposition rates are low, bottom waters are more oxidizing and bacterial sulfate reduction is restricted to pore waters in the sediment below the sediment-water interface (Scott and Lyons, 2012). In that environment, H_2S_{aq} concentrations can be low and trace metal enrichments tend to be small (Scott and Lyons, 2012). In contrast, where organic carbon sedimentation rates are high, bottom waters can become more reducing and sulfate reduction takes place closer to the sediment-water interface. In zones within highly reduced settings, microbial sulfate reduction leads to H_2S_{aq} build up and the establishment of euxinic conditions in the water column itself. It is under these conditions that the highest concentrations of trace metals can form (Scott et al., 2008; Sahoo et al., 2012; Scott and Lyons, 2012; Scott et al., 2013).

Euxinic conditions are more common in the Neoarchean (Reinhard et al., 2009; Scott et al., 2010) and the Proterozoic (Poulton et al., 2004; Scott et al., 2008; Planavsky et al., 2012; Scott et al., 2014) than in other periods of Earth history. However, trace metal contents (V, Cr, Zn, Mo, U) are generally lower than those of typical Phanerozoic black shales. This depletion of metals in Precambrian euxinic black shales, relative to the Phanerozoic, can be attributed to many factors including lower weathering flux into the oceans and a higher biological turnover in sulfidic environments (Scott et al., 2008; Sahoo et al., 2012; Partin et al., 2013; Reinhard et al., 2013).

Anbar and Knoll (2002) proposed that redox-sensitive trace metals would be low in late Paleoproterozoic and Mesoproterozoic oceans, and also within the expansion of sulfidic environments in the wake of the Great Oxidation Event (GOE; Canfield, 1998). Anbar and Knoll (2002) further suggested that the bio-limitation of critical trace metals (i.e. Mo and V) might have been responsible for the delay in the diversification of eukaryotes.

The transition from generally metal-poor Precambrian black shales to metal-rich Phanerozoic black shales appears to correlate with widespread oxygenation of the deep oceans at the end of the Neoproterozoic, expansion of the seawater sulfate reservoir, and the first appearance of metazoans (Scott et al., 2008; Sahoo et al., 2012). Therefore, the distribution of metalliferous black shale appears to a function of the evolution of biogeochemical cycles and the dynamics of Earth's redox state.

The Phanerozoic record includes many examples of black shales that have trace metal hyper-enrichments (>1,000 ppm V, Zn, and Mo; Scott et al., 2014). These hyper-enrichments, relative to typical black shale, are enigmatic as they are not present prior to 635 Ma, with the exception of Talvivaara, and do not occur in modern environments. It has been suggested by some workers that such extreme metal enrichments require a hydrothermal component (e.g., Coveney and Glascock, 1989; Emsbo, 2009). However, hydrothermal fluids in oceanic settings tend not to be enriched in V, Mo, or Cr relative to seawater (Douville et al., 2002). Furthermore, because hyper-enriched black shales are found almost exclusively in the Phanerozoic, it is plausible that these trace metal enrichments may record first order variations in major biogeochemical cycles and therefore, do not require a hydrothermal component.

The ultimate trigger that produced these hyper-enrichments remains debatable. However, the enrichments of Zn in modern sediments (Skei, 1988), and work on the reduction of V^{4+} to V^{3+} (Wanty and Goldhaber, 1992), propose that high concentrations of dissolved H_2S_{aq} are required to facilitate enrichments of these elements in black shales. Possible processes relating the association of trace metal enrichment and hyper-sulfidic conditions are discussed in later sections of this thesis (within Chapters 3, 5, 6 and 8). This relationship may provide a new and useful tool in understanding paleo-redox conditions as well as in the study and exploration of various sediment-hosted ore deposits.

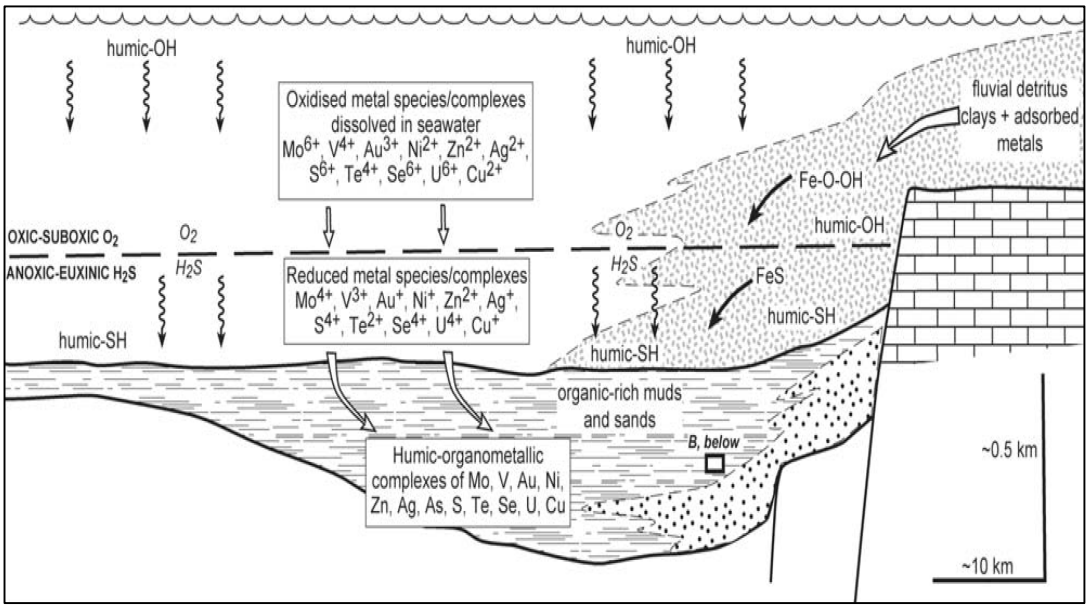

Figure 2.3. Metal input and uptake in black shales (Large et al., 2009).

2.4. Sedimentary metal enrichments and sediment hosted ore deposits

2.4.1. Sediment-Hosted Iron Deposits

Sediment-hosted iron deposits (e.g. Bekker et al., 2010, 2014) encompass both iron formations and ironstones. Iron formations contain ≥30 wt % Fe and are the principal source of iron ore. Ironstones are characterized by lower iron contents (>15 wt % Fe; McGregor et al., 2010) and are of lesser economic importance.

Sediment-hosted iron formations are commonly found in Precambrian terranes, with the largest deposits located in Australia, Brazil, India and South Africa. Major ironstone deposits, are mainly of Phanerozoic age and are found in Kazakhstan, Australia, Algeria, and the United States of America (Scott et al., 2014).

Iron formations that occur in sedimentary successions are classed as "Superior-type", while others that are hosted by volcanic rocks are classed as "Algoma-type" (Gross, 1980). Superior-type formations are found along ancient margins in sedimentary sequences containing sandstone, shale and carbonate. Two distinct textures are apparent in Archean and Paleoproterozoic iron formations that are indicative of their depositional depth. The first are Banded Iron Formations (BIFs) that display alternating layers of iron-rich minerals and chert or quartz. These are interpreted to have formed in relatively deep waters (Gross, 1980). Granular iron formations (GIFs) are dominated by iron-rich granules that formed from sedimentary reworking in shallow waters above wave base (Pufahl and Fralick, 2004; Bekker et al., 2010). "Rapitan-type" iron formations are found exclusively in Late Neoproterozoic successions (750–560 Ma) and are often interbedded with glacial deposits, suggesting a link between global glaciation during this time and iron oxide deposition in their wake.

Main periods of iron deposition were during the Neoarchean, Paleoproterozoic and Neoproterozoic (Bekker et al., 2010, 2014). Each of these is coeval with major oxygenation events. The nature of iron formations have also appeared changed over time. BIFs dominate the Archean until ~2.4 Ga, after which GIF dominated for the remainder of the Paleoproterozoic, while Rapitan-type (consisting of laminated and nodular hematite, magnetite and jasper) denotes late-Neoproterozoic iron formations (Gross, 1994).

Other models argue mantle plumes and hydrothermal venting were likely a major source of dissolved iron (Bekker et al., 2010; Taylor and Konhauser, 2011; Bekker et al., 2014). This can explain the decoupling of ages for iron formations and the GOE. Iron, in its reduced state (Ferrous, Fe^{2+}), can readily be transported in anoxic and sulfate-poor oceans, allowing for deposition of iron formations far from the source of iron. Early models (Cloud, 1973) suggested widespread anoxia in the deep oceans and locally oxygenated surface oceans, suggesting a link between the mass deposition of iron and the emergence of cyanobacteria. In this model, Fe-oxyhydroxides are precipitated in upwelling regions where two water masses mixed.

Iron-oxidizing bacteria are argued to contribute to the precipitation of Fe-oxides under redox stratified oceans (Konhauser, 1989; Bekker et al., 2014). These chemoautotrophic bacteria (organisms that fixate carbon chemically rather than via light) fix CO_2 using Fe^{2+} rather than H_2O.

The oxidation of Fe with free oxygen is still considered to be the origin of Paleoproterozoic iron formations. However, negative Ce anomalies in iron formations that would record oxic water column conditions are lacking in samples older than 2.4 Ga (Planavsky et al., 2010). Since most Archean iron formations formed in the absence of free oxygen, anoxygenic photosynthetic oxidation of Fe^{2+} has been considered as a dominant process that governs iron formations prior to the GOE (Konhauser, 1998; Bekker et al., 2014).

Modelling suggests that both Fe oxidizers can oxidize Fe^{2+} at rates fast enough to account for the deposition of iron formation (Konhauser et al., 2002). Despite cyanobacteria being extant by 2.7 Ga, it is believed to have had little influence on iron formation deposition prior to the GOE, when anoxygenic ferrophototrophs (Fe-utilizing photosynthetic bacteria) were likely driving Fe mineralization in sediments (Bekker et al., 2010, 2014). Following the GOE, cyanobacteria began to wildly perforate, leading to greater influence over the deposition and accumulation of iron.

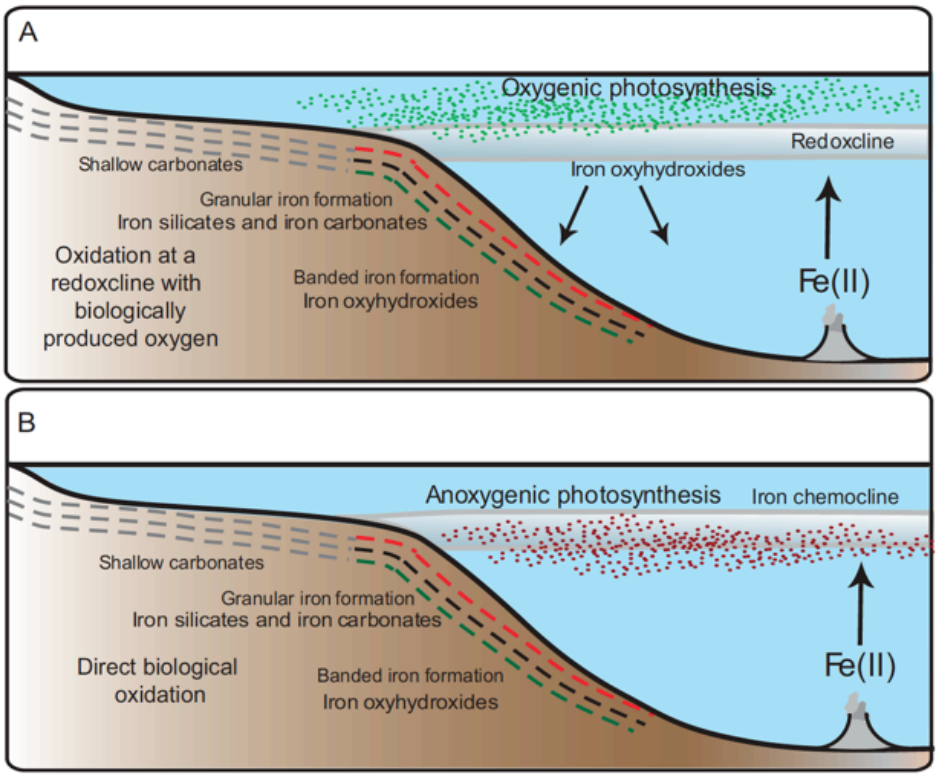

Figure 2.4. Schematic depiction of iron transport and deposition (Scott et al., 2014).

2.4.2. Sediment-hosted Pb-Zn Deposits

Sediment-hosted Pb-Zn deposits account for 39 and 65% of the world's Zn and Pb resources, respectively (Goodfellow and Peter, 2010). These deposit types can be hosted by shale, sandstone, siltstone and carbonate within clastic sequences (Fig. 2.5.), however, the largest deposits are usually hosted within carbonaceous and sulfidic black shale (e.g., Red Dog: Dumoulin et al., 2004; Howards Pass: Goodfellow, 2004; Century, HYC: Large et al., 2005).

The main Pb and Zn ore minerals are galena and sphalerite, and most are preferentially enriched in Zn. Pyrite is often the primary Fe-sulfide mineral present but can be variable concentrations (Goodfellow and Peter, 2010). Sediment-hosted Pb-Zn deposits occur globally but the largest are found in North America, Australia, Asia and Europe. The largest Phanerozoic examples are in the Irish midlands (Navan, Lisheen), northern Alaska (Red Dog district) British Columbia, and in the Yukon, Canada (e.g., Sullivan; Howards Pass and other Selwyn Basin deposits), while Proterozoic examples are found in northern Australia (HYC, Century, Mt. Isa).

Sediment-hosted Pb-Zn deposits form in a range of depositional settings (Leach et al., 2010) that include; passive margins (e.g., Red Dog, Slack et al., 2014), continental rifts (e.g., Sullivan; Emsbo et al., 2009), continental rift-sag sequences (i.e. McArthur Basin deposits; McGoldrick et al., 2010) and carbonate platforms (e.g., Navan; Blakeman et al., 2002). A modern-day analogy could be that of the Red Sea where active hydrothermal venting and fluid circulation are actively depositing metals in the depocentres were clastic material is also accumulating (e.g., Bischoff, 1969).

Tectonics appears to be the most important influence in forming basin architecture, the clastic rocks from which metals may be leached, and the pathways along which metal-rich fluids brines can ingress along faults. For example, the high number of Pb-Zn occurrences aged between ~550 and 300 Ma is considered to be a function of the final assembly of Gondwana and Pangea (Leach et al., 2010) and the paleo-distribution of these deposits corresponds to locations of ancient passive-margin environments (Bradley, 2008; Leach et al., 2010).

Ore fluids are thought to be metal-rich basinal brines with temperatures and salinities of 100 to 200°C and ~20 wt % NaCl, respectively (Cooke et al., 2002; Leach et al., 2005). Low-temperature (≤100°C) Pb-Zn deposits source the majority of sulfide ($H_2S^-_{aq}$) from the microbial reduction of sulfate, coupled to oxidation of organic matter (e.g. Navan, Fallick et al., 2001). Therefore, in addition to tectonic factors (Leach et al., 2010), a component of high primary productivity in surface waters, fast accumulation of organic matter and development of oxygen-poor conditions all play a role. While some pyritic host-rocks were deposited under anoxic, H_2S-bearing bottom waters (e.g., Howards Pass: Slack et al., 2012), many others formed under oxic to suboxic bottom waters (e.g., Red Dog: Dumoulin et al., 2014; Navan, Fallick et al., 2001; Blakeman et al., 2002) with sulfate reduction being restricted to the pore fluids. Since one of the most important biogeochemical processes in the genesis of sediment-hosted Pb-Zn deposits is microbial reduction of sulfate to sulfide. It has been suggested that sulfate supply was insufficient to form Pb-Zn deposits prior to ~ 1.8 Ga (Lyons et al., 2006; Goodfellow and Lydon, 2007; Leach et al., 2010). This suggests that while Zn is an important nutrient element in biological cycles, it was likely tectonic and hydrothermal processes, rather than sulfate supply and atmospheric oxygenation, were the primary control on the formation of Proterozoic sediment-hosted Zn-Pb deposits.

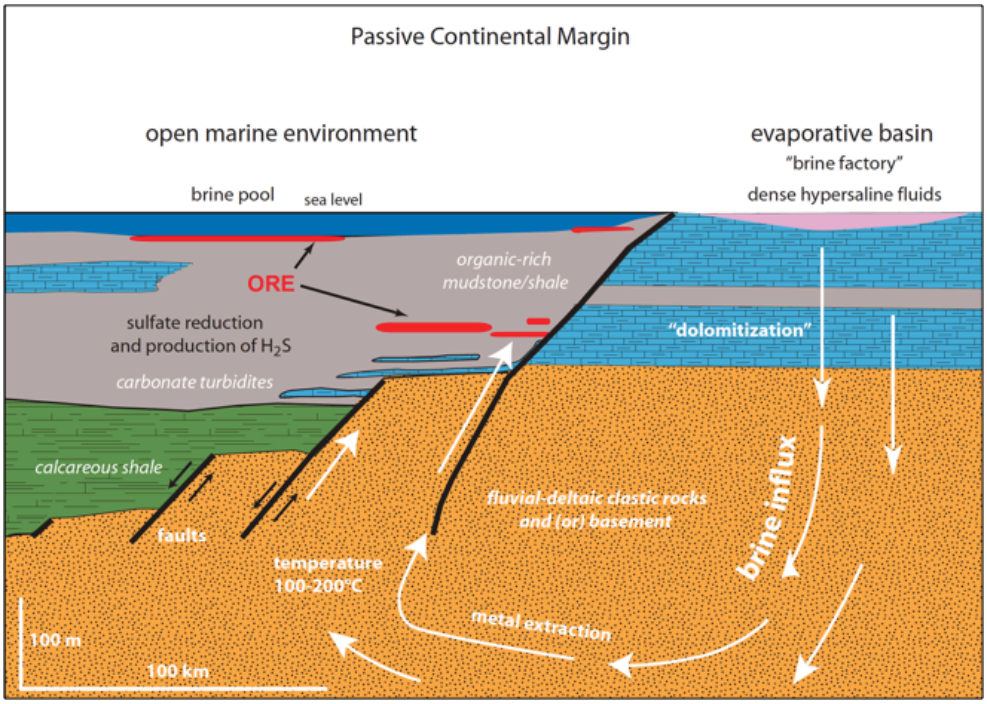

Figure 2.5. Example of brine influx model proposed for the Red Dog Deposit (Leach et al., 2004).

2.4.3. Phosphorite Deposits

Phosphorites (≥ 18 wt % P_2O_5) are critical resources of P for fertilizer. Phosphorites occur in modern and ancient sedimentary sequences, principally those that formed in shallow waters on continental shelves at zones of deep-water upwelling at tropical latitudes (Filippelli, 2008; Pufahl, 2010; Piper and Perkins, 2014).

Major phosphorite deposits occur in Phanerozoic strata in the Congo, the southern USA, as well as the Phosphoria Formation in Idaho and Wyoming, and the Georgina Basin, Australia (Pufahl, 2010; Scott et al., 2014). Some of the largest deposits are found in Northern Africa, for example Kef Eschfair in Tunisia; Benguérir in Morocco; Eshidiya in Jordan, which constitute some of the world's major resources (Scott et al., 2014).

Ancient marine phosphorites are often found associated with black shale, minor chert and limestone (Pufahl, 2010). Phosphorites can form as laminated sediments, coated grains, ooids, nodules and as P-rich crusts. The main constituent is carbonate fluorapatite, along with minor quartz, calcite or dolomite and variable amounts of organic matter (Pufahl, 2010; Piper and Perkins, 2014).

The main periods of phosphorite formation are: Paleoproterozoic, Neoproterozoic - Cambrian, Permian,

and Eocene to Miocene (Pufahl and Hiatt, 2012). Explanations for the temporal distribution in Earth History suggest that periods of warmer climate and greater weathering rates led to more P transport to the oceans, together with high biological productivity and burial of organic carbon (Filippilli, 2011).

Many modern and ancient phosphogenic sediments are associated with upwelling zones, usually along basin margins (Baturin, 1988; Pufahl, 2010), where elevated primary productivity results in burial of large volumes of organic carbon without the development of sulfidic bottom waters. While upwelling of phosphorous is an apt mechanism, recent research has focused on a sulfide-oxidizing bacteria and its influence in concentrating and retaining P in sediments (Schulz et al., 1999; Schulz and Schulz, 2005; Crosby and Bailey, 2012; Bailey et al., 2013). This process has also been used to explain the formation of Paleoproterozoic phosphorites in the Kola region of NW Russia (Lepland et al., 2013, Melezhik et al., 2013).

These sulfide-oxidizing bacteria concentrate at the chemocline in the surface sediments where they can incorporate $H_2S^-_{aq}$ and NO^{-3}. Sulfide oxidizers hydrolyze polyphosphate and release phosphate back into pore waters as a function of the dynamic redox front produced mixing of nitrate and sulfidic waters (Schulz and Schulz, 2005; Brock and Schulz-Vogt, 2011). Release of phosphate to pore waters promotes saturation and precipitation of apatite, or apatite group minerals (Jarvis et al. 1994). Such conditions would require increased rates of bio-productivity but also a mechanism, such as upwelling, in order for bottom water renewal to enhance organic carbon contents with developing sulfidic conditions (Jarvis et al. 1994; Pufahl, 2010).

2.4.4. Sedimentary manganese deposits

Shale-hosted manganese deposits are documented in Neoarchean, Early Paleoproterozoic, Late Mesoproterozoic, Late Neoproterozoic and Oligocene sedimentary sequences (Maynard, 2010). Many Precambrian Mn-deposits are broadly coeval with periods of oxygenation as well as some iron formations suggesting a link between redox and geochemical transitions and the deposition of shale-hosted Mn deposits.

The source of Mn in large deposits is likely seawater, although Mn is considered to be ultimately

derived from submarine-hydrothermal fluids (e.g., Maynard, 2003).

The largest sedimentary Mn deposit is in the 2.3 to 2.2 Ga Hotazel Formation, South Africa, which accounts for > 50% of the world's reserves (Laznicka, 1992). The Hotazel Formation is unique from other Mn deposits due to its size and because it occurs as interbeds within banded iron formations. It is also of interest due to its temporal relationship with the GOE. Other, smaller, Mn deposits occur in Fe-poor, carbonate-rich sediments during the Middle to Late Paleoproterozoic (~ 1.8 Ga) and late-Neoproterozoic (~ 800–600 Ma; Maynard, 2003).

In the example of the Hotazel Formation, the inferred enrichment process suggests precipitation of Mn oxides within oxygenated surface waters, followed by deposition of the Mn oxides into the sediment itself (Laznicka, 1992). Within the sediments, Mn oxides likely were reduced during organic carbon remineralization and then reprecipitated (Laznicka, 1992; Maynard, 2003). This mechanism is similar to that described for the formation of shale-hosted Mn deposits (e.g., Maynard, 2003), however, significant amounts of organic carbon or pyrite are not preserved in the Hotazel Formation. This suggests that that if organic carbon was present, it was remineralized without accompanying sulfate reduction.

The Hotazel Formation (2.3 to 2.2 Ga) is roughly synchronous with potentially global-scale glaciations, the loss of the mass-independent fractionation of sulfur (Bekker et al., 2004, 2010), as well as the initial expansion of the seawater sulfate reservoir (Scott et al., 2014).

Manganese ores hosted within black shales are commonly found but require certain depositional and biogeochemical environments (Force and Cannon, 1988; Okita and Shanks, 1992; Maynard, 2003). These settings require high primary productivity, so much so that the deepest parts of the basin or margin becomes euxinic (Maynard, 2003). Euxinic bottom waters strongly sequester Fe^{2+} (via Fe sulfide precipitation in the water), but not for Mn^{2+}. Therefore, where large sulfidic basins form, manganese becomes concentrated below the chemocline (e.g., Black Sea; Lyons and Severmann, 2006; Lyons et al., 2003). Above the chemocline, Mn oxides will precipitate via microbial mediation and settle to the sediment-water interface along basin margins and begin to accumulate as a "bathtub ring" around the euxinic basin (Force and Cannon, 1988; Okita and Shanks, 1992; Maynard, 2003).

2.5. Metal enrichments in sediments- an archive of the chemical and biological cycles in Earth evolution.

2.5.1. Biochemistry of metal accumulation in sediments

A wide range of biological processes can exert influence on the formation of ore deposits. Tomkins (2013) proposed that the evolution of Earth's biogeochemical cycles may be used to account for the secular distribution of Au deposits. While others have made the suggestion that the distribution of ore deposits or metal-rich sediments can provide contexts in which to study the evolution of biogeochemical cycles (e.g., Lyons et al., 2006, Large et al., 2015, Maynard, 2010). Therefore, there is great potential to better integrate the study of ore deposits and their links to geobiology, biogeochemistry and Earth system evolution.

The biogeochemical cycling of the major elements (C, S, Mn, and Fe) can influence the biological and geochemical processes in basins and sediments, playing critical roles in facilitating metal enrichments in sediments. Increases in atmospheric oxygen can result from vast, and sustained, organic carbon burial (e.g. Berner, 2009). In the oceans, >90% of organic carbon is oxidized aerobically in the water column and when buried, upper parts of the sediments can become extremely reducing (e.g., Canfield et al., 1993; Thamdrup et al., 1994). Within these sediments, various microbial communities use a range of oxidants present to facilitate the degradation of organic carbon, a thermodynamically favored reaction (e.g. Froelich et al., 1979; Canfield et al., 1993; Jorgensen et al., 2004). The most significant of these oxidants are O_2, NO_3^-, Mn oxides, Fe oxides, and sulfate. These are used in order as depth increases and sediments become more reducing (Scott and Lyons, 2012). The order in which oxidants are utilized is considered to be a function of the free-energy gain associated with each coupled redox reaction (Froelich et al., 1979), where the oxidant providing the greatest free energy gain is utilized first until it (or the organic carbon) is exhausted.

2.5.1.1. Manganese

Mn-reducing bacteria facilitate a coupled reduction of Mn oxides with oxidation of organic matter, leading to a release of Mn^{2+} and HCO_3^- to pore waters (Nealson et al., 1991; Thamdrup et al., 2000):

$$CH_3COO^- + 4MnO_2 + 3H_2O \rightarrow 2HCO_3^- + 4Mn^{2+} + 7OH^-$$

It is uncommon for Mn^{2+} to form sulfides, rather it diffuses upward into oxygenated pore waters. This process of recycling Mn in oxygenated water in the upper sediment results in enrichments in Mn oxide particles, especially where sustained Mn recycling can sufficiently drive the pore waters to Mn carbonate saturation (Calvert and Pedersen, 1996),

2.5.1.2. Iron

Iron-reducing bacteria couple the oxidation of organic matter to the reduction of dissolved and particulate ferric iron (Konhauser, 1998; Canfield, 2005):

$$CH_3COO^- + 8FeOOH + 3H_2O \rightarrow 2HCO_3^- + 8Fe^{2+} + 15OH^-$$

Unlike manganese, Fe^{2+} will readily react with H_2S, forming an FeS precursor initially and then FeS_2 upon further burial (Rickard, 2012). In sediments with appreciable organic carbon content and where ferric iron is reduced, some of the residual Fe^{2+} will diffuse upward (Jorgenson et al., 2004). Many strains of Fe-oxidizing bacteria are present in the marine environment (Canfield, 2005; Bekker et al., 2010). Abiotic Fe oxidation can proceed at far greater rates than abiotic Mn oxidation, under low oxygen conditions (Canfield, 2005). This process can also be catalyzed by the presence of anoxygenic phototrophs (Widdel et al., 1993):

$$4Fe^{2+} + CO_2 + 4H^+ + \text{UV light} \rightarrow CH_2O + 4Fe^{3+} + H_2O.$$

This is rare in modern marine settings since anoxic and Fe-rich waters in the photic zone are uncommon (Canfield et al., 2006) however such conditions and compositions of seawater were widespread during the Archean where this biological pathway was likely more profound and potentially important in the formation of Archean iron deposits (Konhauser, 1998; Bekker et al., 2010, 2014).

2.5.1.3. Sulfur

Microbial sulfate reduction is common in all sediments where organic carbon is present and accounts for most (55%) of the organic carbon oxidized in marine sediments (Canfield et al., 2006):

$$CH_3COO^- + SO_4^{2-} \rightarrow 2HCO_3^- + HS^-$$

Sulfate reduction can take place in anoxic bottom waters or oxygen-minimum zones, leading to the production of H_2S_{aq} in the water column (euxinia). This is restricted to only a few localities in modern settings but is likely a common component to many Proterozoic ocean basins (Canfield et al., 1998)

The accumulation of H_2S_{aq} is dependent upon many variables including reoxidation, sulfate reduction rates and the precipitation of metal sulfides (e.g., pyrite; Jorgenson and Nelson, 2004). Limited amounts (5–20%) of the dissolved sulfide produced in shelf sediments become permanently fixed as Fe sulfides, with the remainder being re-oxidized to sulfate (Jorgensen and Nelson, 2004). Dissolved sulfide can be oxidized abiotically by Fe oxides, Mn oxides, NO_3^-, or O_2 (Canfield, 2005).

2.5.2. Trends in metal enrichment, atmospheric oxygenation and biological cycles

The occurrence of many sediment-hosted ore deposits appear to be closely linked to secular trends in major biogeochemical cycles (Figs. 2.6. and 2.7.), including the oxygenation of Earth's surface and the evolving seawater chemistry and its contained contents (i.e. Fe, Mn, S and trace metals). The critical step in this process was the evolution of oxygenic photosynthesis:

$$CO_2 + H_2O + \text{UV light} \rightarrow CH_2O + O_2$$

Anoxygenic forms of photosynthesis can also operate and are likely to have done so since the Early Archean, but they are considered minimal in terms of overall contribution to primary productivity (Canfield et al., 2006). Recent work proposes that locally oxygenated shallow waters were present as far back as 3.0 Ga, however, the commonly accepted age for the emergence of oxygenic cyanobacteria is

~2.7 Ga (Crowe et al., 2013; Planavsky et al., 2014). By ~ 2.3 Ga, widespread oxygenation of surface environments had been achieved (Bekker et al., 2004; Bekker and Holland, 2012).

The oxygenation of Earth's surface has often been described as a two-step, unidirectional process. The first occurred between 2.4 and 2.3 Ga (the Great Oxidation Event or GOE; Holland, Bekker et al., 2004), when atmospheric oxygen first exceeded 0.001% of present atmospheric levels (PAL; Pavlov and Kasting, 2002), as reflected in the demise of the mass-independent fractionation of sulfur isotopes that requires UV photochemical pathways (Farquhar et al., 2000). The second was in the late Neoproterozoic (ca. 800–635 Ma), after a period of global glaciation and coincident with the appearance of metazoan life (Sahoo et al., 2012; Partin et al., 2013). In between the two oxygenation events, the Earth is believed to have gone through a protracted state of intermediate redox, during which oxygen was present in the atmosphere and surface oceans but was absent from the deep ocean (Canfield, 2005; Scott et al., 2014). The established idea of broadly euxinic (anoxic and sulfidic) Proterozoic oceans (Canfield, 1998) has been challenged, with recent models infer suboxic (Slack et al., 2007, 2009) or ferruginous (anoxic and Fe bearing; Poulton and Canfield, 2011; Planavsky et al., 2011) conditions dominating the deep ocean with euxinia restricted to areas of high primary productivity along continental margins.

The idea of a two-step oxygenation process has also been debated. Recent work (Bekker and Holland, 2012; Planavsky et al., 2012; Partin et al., 2013; Scott et al., 2014) suggests that a dramatic rise and fall in Earth's oxidation state occurred during and after the Lomagundi carbon isotope excursion at ~2.2 to 2.055 Ga (Karhu and Holland, 1996; Martin et al., 2013, Melezhik et al., 2013). This is the largest and longest carbon isotope excursion in the geological record. Most important in terms of metal enrichments is evidence that suggests expansion and contraction of the marine sulfate reservoir between 2.4 and 2.0 Ga (Schroder et al., 2008; Planavsky et al., 2012; Scott et al., 2014).

Various other geochemical proxies suggest decline in the oxidation state of seawater during this time such as a narrowing of the sulfur isotope values of pyrite and carbonate-associated sulfate (Planavsky et al., 2012; Scott et al., 2014), concentrations of redox-sensitive elements in black shales and Fe formations (Scott et al., 2008; Konhauser et al., 2012; Partin et al., 2013; Reinhard et al., 2013), Cr

isotopes (Frei et al., 2009), and the return of minor occurrences of Superior-type iron formations at ~1.9 Ga (Bekker et al., 2010). The exact magnitude and duration of the oxygen increase between 2.3 and 2.0 Ga, and the subsequent fall in the marine oxidation state are still debated. However, recent studies by Bekker and Holland (2012) and Luo et al. (2016) argue that the oxygen rise was large and rapid, on the order of <10 m.y.

The input of sulfate to the oceans and the size of the reservoir is ultimately facilitated by oxidative weathering of the crust. In turn, the size of the sulfate reservoir increases as a result of progressive oxygenation of the atmosphere (Canfield, 2005, Anbar, 2008). Prior to the GOE, the presence of small mass-dependent fractionation of sulfur in sedimentary pyrite supports the suggestion of low seawater sulfate concentrations (≤200 μM; Farquhar et al., 2000). The preservation of large mass-independent fractionations of sulfur in Archean sedimentary rocks is also consistent with limited oxidative weathering (Canfield, 2005; Farquhar et al., 2000). In the wake of the GOE, mass-dependent sulfur isotope fractionations increase greatly (Farquhar et al., 2000) at the same time as mass-independent fractionations disappear (Bekker et al., 2004).

During the long intermediate redox state of the Mesoproterozoic, the size of the seawater sulfate reservoir was likely less that that of the Phanerozoic, but still sufficient enough to promote the formation of large Zn and Pb sulfide deposits. Seawater sulfate reached higher concentrations following the late Neoproterozoic glaciations and the oxygenation of the deep oceans, and has likely remained at these levels (Canfield, 2005).

Oxidative weathering of continental crust also delivers trace metals of economic interest (e.g., Mo, V, Zn) to the ocean, and their concentrations may reflect changes in the oxygenation of the atmosphere and ocean, as well as the delivery of sulfate (Scott et al., 2014; Large et al., 2015; Fig. 2.6.). Since these redox-sensitive metals are a product of oxidative weathering and are most efficiently removed from seawater and concentrated in sulfidic environments (Scott et al., 2014), their secular trends in enrichments within euxinic black shales have been used to interpret the redox state of the oceans through time (Scott et al., 2008; Anbar, 2008; Sahoo et al., 2012; Reinhard et al., 2013; Scott et al., 2013). In addition, these metals and others (i.e. Ni, Cu, Se, Co, Cd) due to their micronutrient behavior

have been used as proxies for biological evolution (e.g., Anbar and Knoll, 2002; Large et al., 2015). Prior to the GOE, black shale-hosted enrichments of these metals are mostly absent (Scott et al., 2008; Sahoo et al., 2012). However, many Mo and V occurrences during the Proterozoic and Phanerozoic have been documented and appear to follow trends in atmospheric oxygen and the sulfate concentration in seawater (Scott et al., 2008).

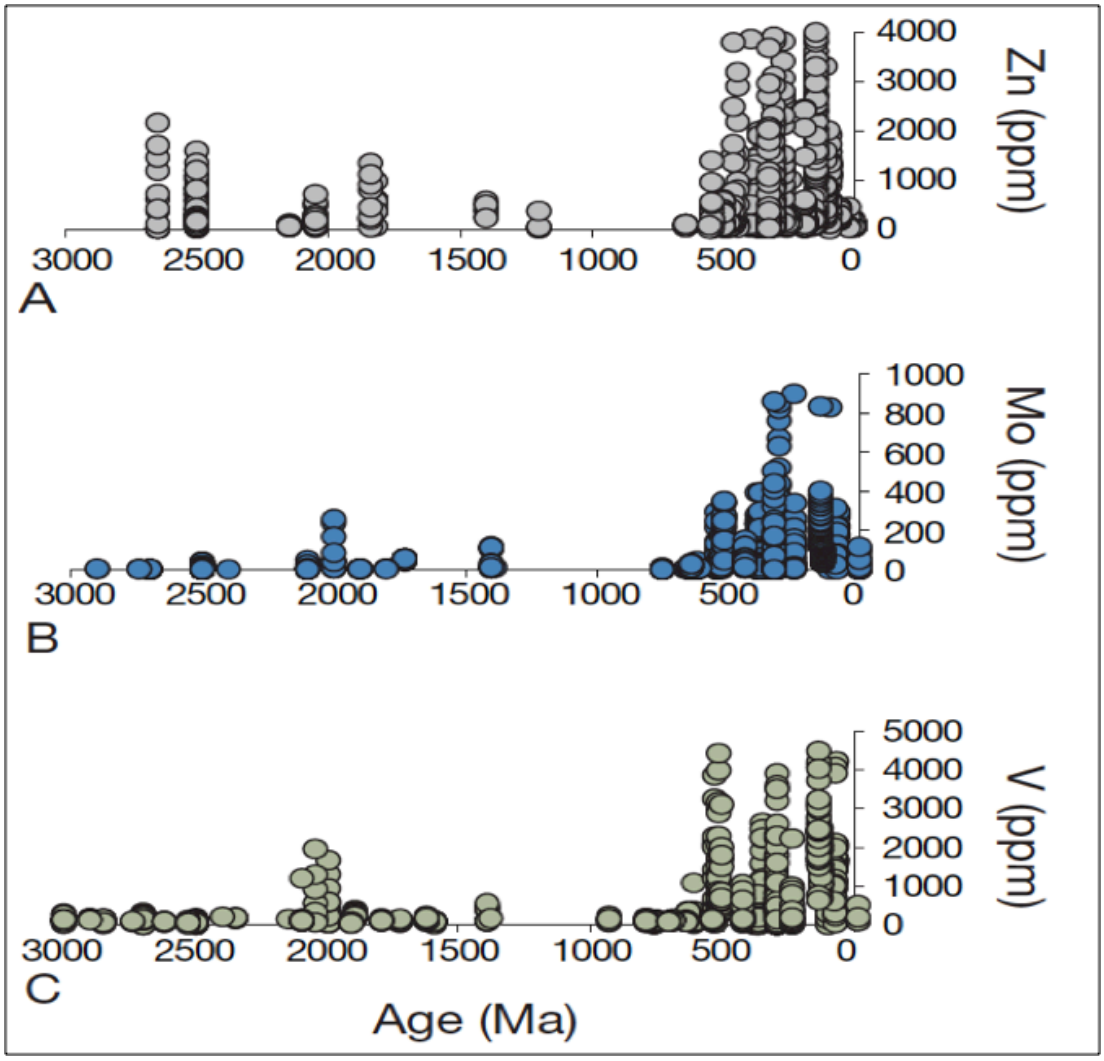

Figure 2.6. Nutrient trace elements zinc, molybdenum and vanadium values in black shales through Earth History (Sahoo et al., 2012; Scott et al., 2014).

In conclusion, it is clear that the distribution of the majority of metal enrichments in sediments appear to be synchronous with changes in Earth's biological and geochemical cycles (Fig. 2.7.). The final metal enrichments in black shales represent a complex interplay between a variety of tectonic, redox and biological processes. The behavior of trace elements in in seawater and, ultimately, in black shales is reviewed in the following chapter (Chapter 3) and discussed throughout this thesis. However, it is clear that the metal concentration in black shales can be related to changes of the biogeochemistry at the time of deposition. Thereby, signifying the intimate relationship between sedimentary ore deposits and Earth's evolution and establishing the context for this study.

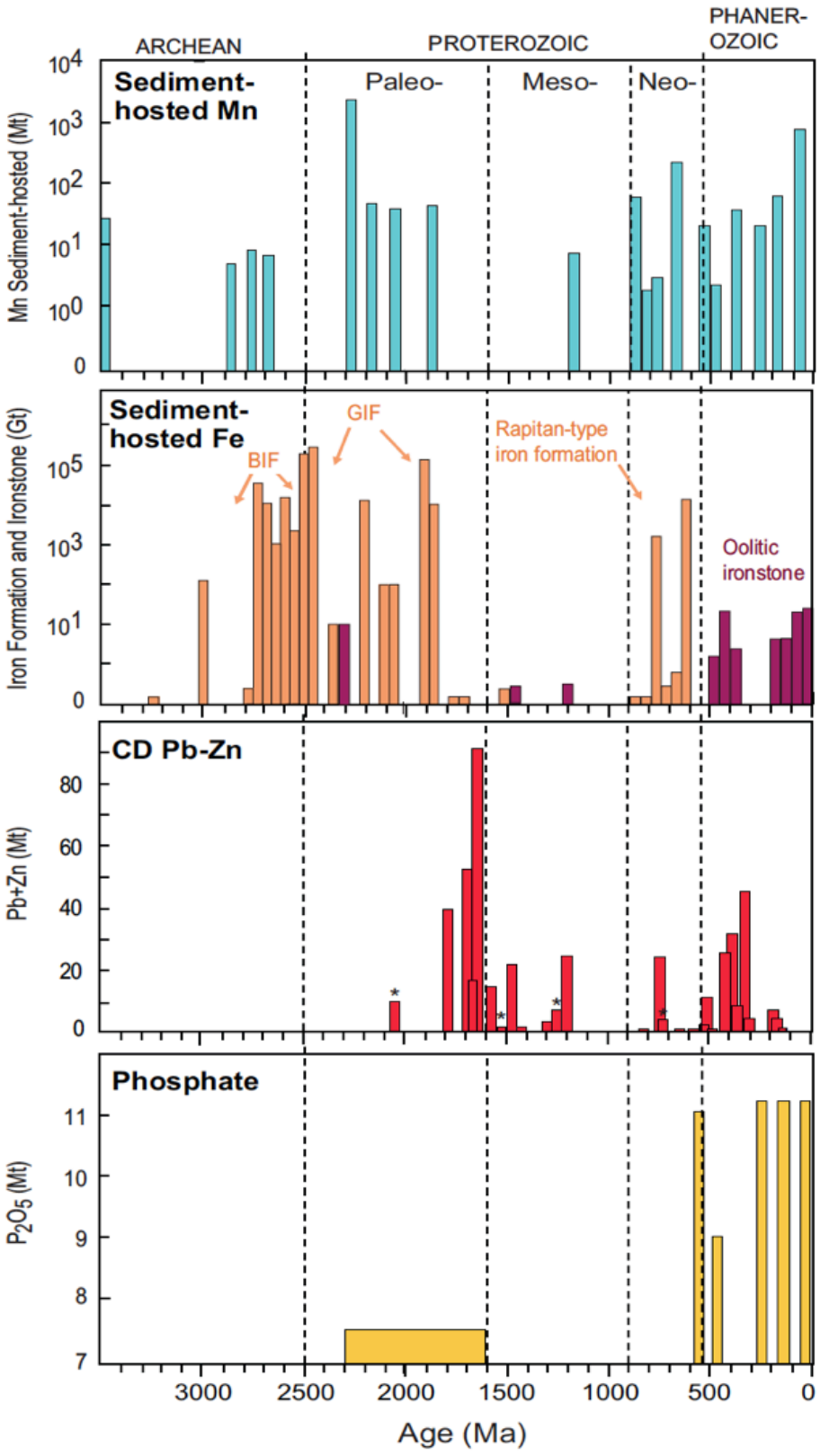

Figure 2.7. Distribution of various sediment-hosted enrichments through Earth history (Scott et al., 2014).

2.6. References

Algeo, T.J., and Maynard, J.B., 2004. Trace-element behavior and redox facies in core shales of Upper Pennsylvanian Kansas-type cyclothems. Chemical Geology, 206, p. 289-318.

Anbar, A.D., and Knoll, A., 2002. Proterozoic ocean chemistry and evolution: A bioinorganic bridge? Science, 297, p. 1137–1142.

Anbar, A.D., Duan, Y., Lyons, T.W., Arnold, G.L., Kendall, B., Creaser, R.A., Kaufman, A.J., Gordon, G.W., Scott, C., Garvin, J., and Buick, R., 2007. A whiff of oxygen before the Great Oxidation Event? Science, 317, p. 1903–1906.

Arthur, M.A. and Sageman, B.B., 1994. Marine shales: depositional mechanisms and environments of ancient deposits. Annual Review of Earth and Planetary Sciences, 22, p. 499-551.

Bailey, J.V., Corsetti, F.A., Greene, S.E., Crosby, C.H., Liu, P., and Orphan, V.J., 2013. Filamentous sulfur bacteria preserved in modern and ancient phosphatic sediments: Implications for the role of oxygen and bacteria in phosphogenesis. Geobiology, 11, p. 397 405.

Baturin, G.N., 1988. Disseminated phosphorous in oceanic sediments—a review: Marine Geology, 84, p. 95–104.

Bekker, A., and Holland, H.D., 2012. Oxygen overshoot and recovery during the early Paleoproterozoic. Earth and Planetary Science Letters, 317– 318, p. 295–304.

Bekker, A., Holland, H.D., Wang, P.L., Rumble, D., Stein, H.J., Hannah, J.L., Coetzee, L.L., and Beukes, N.J., 2004. Dating the rise of atmospheric oxygen. Nature, 427, p. 117–120.

Bekker, A., Karhu, J.A., and Kaufman, A.J., 2006. Carbon isotope record for the onset of the Lomagundi carbon isotope excursion in the Great Lakes area, North America. Precambrian Research, 148, p. 145–180.

Bekker, A., Slack, J.F., Planavsky, N., Krapež, B., Hofmann, A., Konhauser, K.O., and Rouxel, O.J., 2010. Iron formation: The sedimentary product of a complex interplay among mantle, tectonic, oceanic, and biospheric processes. Economic Geology, 105, p. 467–508.

Bekker, A., Planavsky, N.J., Krapež, B., Rasmussen, B., Hofmann, A., Slack, J.F., Rouxel, O.J., and Konhauser, K.O., 2014. Iron formations: Their origins and implications for ancient seawater chemistry. Treatise on Geochemistry, 2nd ed., 9, p. 561–628

Bischoff, J.L., 1969. Red Sea geothermal brine deposits: their mineralogy, chemistry, and genesis. In Hot brines and recent heavy metal deposits in the Red Sea (pp. 368-401). Springer Berlin Heidelberg.

Blakeman R.J., Ashton J.H., Boyce A.J., Fallick A.E., and Russell M.J., 2002. Timing of interplay between hydrothermal and surface fluids in the Navan Zn + Pb orebody, Ireland: evidence from metal distribution trends, mineral textures and 34S analyses. Economic Geology, 97, p. 73-91

Bradley, D.C., 2008. Passive margins through Earth history: Earth-Science Reviews, 91, p. 1–36.

Calvert, S.E., and Pedersen, T.F., 1996. Sedimentary geochemistry of manganese: Implications for the environment of formation of manganiferous black shales. Economic Geology, 91, p. 36-47

Canfield, D.E., Jorgensen, B.B., Fossing, H., Flud, R., Gundersen, J., Ramsing, N.B., Thamdrup, B., Jansen, J.W., Nielsen, L.P., and Hall, P.O.J., 1993. Pathways of organic carbon oxidation in three continental margin sediments: Marine Geology, 113, p. 27–40.

Canfield, D.E., 1998. A new model for Proterozoic ocean chemistry. Nature, 396, p. 450–453.

Canfield, D.E, 2005. The early history of atmospheric oxygen. Homage to Robert M. Garrels: Annual Review of Earth and Planetary Sciences, 33, p. 1–36.

Canfield, D.E., Poulton, S.W., Knoll, A.H., Narbonne, G.M., Ross, G., Goldberg, T., and Strauss, H., 2008, Ferruginous conditions dominated later Neoproterozoic deep-water chemistry. Science, 15, p. 949–952.

Canfield, D.E., and Thamdrup, B., 2009. Toward a consistent classification scheme for geochemical environments, or, why we wish the term "suboxic" would go away. Geobiology, 7, p. 385–392.

Cloud, P., 1973. Paleoecological significance of banded iron-formation. Economic Geology, 68, p. 1135–1143.

Cooke, D.R., Bull, S.W., Large, R.R., and McGoldrick, P.J., 2000. The importance of oxidized brines for the formation of Australian Proterozoic stratiform sediment-hosted Pb-Zn (Sedex) deposits. Economic Geology, 95, p. 1–18.

Condie, K.C., Des Marais, D.J., Abbott, D. 2001. Precambrian superplumes and supercontinents: a record in black shales, carbon isotopes, and paleoclimates? Precambrian Research, 106, 239-260.

Coveney, R.M., Jr., 2003. Metalliferous Paleozoic black shales and associated strata, in Lentz, D.R., ed., Inorganic geochemistry of sediments and sedimentary rocks: Evolutionary considerations to mineral deposit-forming environments: Geological Association of Canada, GeoText 4, 135–144.

Coveney, R.M., Jr., Leventhal, J.S., Glascock, M.D., and Hatch, J.R., 1987. Origins of metals and organic matter in Mecca Quarry shale and stratigraphically equivalent beds across the Midwest. Economic Geology, 82, 915-933.

Coveney, R.M., and Glascock, M.D., 1989. Review of the origins of metal rich Pennsylvanian black shales, central U.S.A., with an inferred role for basinal brines. Applied Geochemistry, 4, 347–367.

Coveney, R.M., Jr., and Martin, S.P., 1983. Molybdenum and other heavy metals of the Mecca Quarry and Logan Quarry shales. Economic Geology, 78, 132-149.

Crosby, C.H., and Bailey, J.V., 2012. The role of microbes in the formation of modern and ancient phosphatic mineral deposits: Frontiers in Microbiology, 3, 241.

Crowe, S.A., D.ssing, L.N., Beukes, N.J., Bau, M., Kruger, S.J., Frei, R., and Canfield, D.E., 2013. Atmospheric oxygenation three billion years ago. Nature, 501, p. 535–538.

Douville, E., Charlou, J.L., Oelkers, E.H., Bienvenu, P., Colon, C.J., Donval, J.P., Fouquet, Y., Prieur, D. and Appriou, P., 2002. The rainbow vent fluids (36 14'N, MAR): the influence of ultramafic rocks and phase separation on trace metal content in Mid-Atlantic Ridge hydrothermal fluids. Chemical Geology, 184, p. 37-48.

Dumoulin, J.A., Harris, A.G., Blome, C.D., and Young, L.E., 2004. Depositional settings, correlation, and age of Carboniferous rocks in the western Brooks Range, Alaska: Economic Geology, 99, p. 1355–1384.

Dyni, J.R., 2005, Geology and resources of some world oil-shale deposits: U.S. Geological Survey Scientific Investigations Report 2005-5294, 49 p.

Elderfield, H. and Schultz, A., 1996. Mid-ocean ridge hydrothermal fluxes and the chemical composition of the ocean. Annual Review of Earth and Planetary Sciences, 24, p.191-224.

Emsbo, 2009. Geologic Criteria for the Assessment of Sedimentary Exhalative (Sedex) Zn-Pb-Ag Deposits. U.S. Geological Survey Scientific Investigations Report 2009-1209, 25 p.

Fallick, A.E., Ashton, J.H., Boyce, A.J., Ellam, R.M., and Russell, M.J., 2001. Bacteria were responsible for the magnitude of the world-class hydrothermal base-metal sulfide orebody at Navan, Ireland. Economic Geology, 96, 885–890.

Fan, D. L., Ye, J., Yin, L.-M., and Zhang, R.-F., 1999. Microbial processes in the formation of the Sinian Gaoyan manganese carbonate ore, Sichuan Province, China. Ore Geology Reviews, 15, 79–93.

Farquhar, J., Bao, H., and Thiemens, M., 2000. Atmospheric influence of Earth's earliest sulfur cycle. Science, 289, 756–758.

Farquhar, J., Zerkle, A.L., and Bekker, A., 2011. Geological constraints on the origin of oxygenic photosynthesis. Photosynthesis Research, 107, 11–36.

Filippelli, G.M., 2008. The global phosphorus cycle: Past, present, and future. Elements, 4, 89–95.

Filippelli, G.M., 2011. Phosphate rock formation and marine phosphorous geochemistry: The deep time perspective. Chemosphere, 84, 759–766.

Filippelli, G.M., and Delaney, M.L., 1992. Similar phosphorus fluxes in ancient phosphorite deposits and a modern phosphogenic environment. Geology, 20, 709–712.

Force, E.R., and Cannon, W.F., 1988. Depositional model for shallow-marine manganese deposits around black shale basins. Economic Geology, 83, p. 93–117.

Frei, R., Gaucher, C., Poulton, S.W., and Canfield, D.E., 2009. Fluctuations in Precambrian atmospheric oxygenation recorded by chromium isotopes. Nature, 461, p. 250–254.

Froelich, P.N., Klinkhammer, G.P., Bender, M.L., Luedtke, N.A., Heath, G.R., Cullen, D., and Dauphin, P., 1979. Early oxidation of organic matter in pelagic sediments of the eastern equatorial Atlantic: Suboxic diagenesis. Geochimica et Cosmochimica Acta, 43, p. 1075 1090.

Goldhammer, T., Brüchert, V., Ferdelman, T.G., and Zabel, M., 2010. Microbial sequestration of phosphorus in anoxic upwelling sediments. Nature Geoscience, 3, p. 557–561.

Goodfellow, W.D. and Lydon, J.W., 2007. Sedimentary-exhalative (SEDEX) deposits: Geological Association of Canada, Mineral Deposits Division, Special Publication 5, p. 163–183.

Gross, G.A., 1996. Algoma-type iron-formation. Geology of Canadian Mineral deposits types. Eds Eckstrand, O.R., Sinclair, W.D. and Thorpe, R.I., Geological survey of Canada. Geology of Canada, 8, 66-73.

Herzig, P.M. and Hannington, M.D., 1995. Polymetallic massive sulfides at the modern seafloor a review. Ore Geology Reviews, 10(2), p.95-115.

Huyck, H.L.O., 1989. When is a metalliferous black shale not a black shale?: U.S. Geological Survey Circular 1058, p. 42–56.

Karhu, J.A. and Holland, H.D., 1996. Carbon isotopes and the rise of atmospheric oxygen. Geology, 24, p. 867–870.

Konhauser, K.O., 1998. Diversity of bacterial iron mineralization. Earth-Science Reviews, 43, p. 91–121.

Konhauser, K.O., Hamade, T., Raiswell, R., Morris, R.C., Ferris, F.G., Southam, G., Canfield, D.E., 2002. Could bacteria have formed the Precambrian banded iron formations? Geology, 30, p. 1079–1082.

Konhauser, K.O., Lalonde, S.V., Planavsky, N.J., Pecoits, E., Lyons, T.W., Mojzsis, S.J., Rouxel, O. J., Barley, M.E., Rosiere, C., Fralick, P.W., Kump, L.R., and Bekker, A., 2012. Aerobic bacterial pyrite oxidation and acid rock drainage during the Great Oxidation Event. Nature, 478, p. 369–373.

Large, R.R., Bull, S.W., Cooke, D.R., and McGoldrick, P.J., 1998, A genetic model for the HYC deposit, Australia: Based on regional sedimentology, geochemistry, and sulfide-sediment relationships. Economic Geology, 93, 1345–1368.

Large, R.R., Bull, S.W., McGoldrick, P.J., Walters, S., Derrick, G.M., and Carr, G.R., 2005, Stratiform and strata-bound Zn-Pb-Ag deposits in Proterozoic sedimentary basins, northern Australia. Economic Geology 100th Anniversary Volume, p. 931–963.

Large, R.R., Danyushevsky, L., Hollit, C., Maslennikov, V., Meffre, S., Gilbert, S., Bull, S., Scott, R., Emsbo, P., Thomas, H., Singh, B., and Foster, J., 2009. Gold and trace element zonation in pyrite using a laser imaging technique: Implications for the timing of gold in orogenic and Carlin-style sediment-hosted deposits. Economic Geology, 104, p. 635–668.

Large, R.R., Bull, S.W., and Maslennikov, V.V., 2011, A carbonaceous sedimentary source-rock model for Carlin-type and orogenic gold deposits. Economic Geology, 106, p. 331–358.

Large, R.R., Halpin, J.A., Danyushevsky, L.V., Maslennikov, V.V., Bull, S.W., Long, J.A., Gregory, D.D., Lounejeva, E., Lyons, T.W., Sack, P.J. and McGoldrick, P.J., 2014. Trace element content of sedimentary pyrite as a new proxy for deep-time ocean–atmosphere evolution. Earth and Planetary Science Letters, 389, p. 209-220.

Large, R.R., Halpin, J.A., Lounejeva, E., Danyushevsky, L.V., Maslennikov, V.V., Gregory, D., Sack, P.J., Haines, P.W., Long, J.A., Makoundi, C. and Stepanov, A.S., 2015. Cycles of nutrient trace elements in the Phanerozoic ocean. Gondwana Research, 28, p.1282-1293.

Laznicka, P., 1992, Manganese deposits in the global lithogenetic system: Quantitative approach. Ore Geology Reviews, 7, 279–356.

Leach, D.L., Marsh, E., Emsbo, P., Rombach, C., Kelley, K.D., Reynolds, J., and Anthony, M., 2004. Nature of hydrothermal fluids at the shale-hosted Red Dog Zn-Pb-Ag deposits, Brooks Range, Alaska. Economic Geology, 99, 1449–1480.

Leach, D.L., Sangster, D.F., Kelley, K. D., Large, R. R., Garven, G., Allen, C. R., Gutzmer,J., and Walters, S., 2005, Sediment-hosted lead-zinc deposits: A global perspective. Economic Geology 100th Anniversary Volume, p. 561–608.

Leach, D.L., Bradley, D.C., Huston, D., Pisarevsky, S.A., Taylor, R.D., and Gardoll, S.J., 2010. Sediment-hosted lead-zinc deposits in Earth history. Economic Geology, 105, 593–625.

Lehmann, B., Nägler, T.F., Holland, H.D., Wille, M., Mao, J.-W., Pan, J.-Y., Ma, D.-S., Dulski, P., 2007. Highly metalliferous carbonaceous shale and Early Cambrian seawater. Geology, 35, 403–406.

Lepland, A. Joosu, L., Kirsimäe, K., Prave, A.R., Romashkin, A.E., Črne, A.E., Martin, A.P., Fallick, A.E., Somelar, P., Üpraus, K., Mänd, K., Roberts, N.M.W., van Zuilen, M.A., Wirth, R., and Schreiber, A., 2013, Potential influence of sulphur bacteria on Palaeoproterozoic phosphogenesis. Nature Geoscience, 7, 20–24.

Leventhal. J.S., Briggs, P.H., and Bakker, J.W., 1983. Geochemistry of the Chattanooga shale, Dekalb County, central Tennessee. Southeastern Geology, 24, p. 101–116.

Leventhal, J.S., 1991. Comparison of organic geochemistry and metal enrichment in two black shales: Cambrian Alum Shale of Sweden and Devonian Chattanooga Shale of United States. Mineralium Deposita, 26, p.104-112.

Lewis, S.E., Henderson, R.A., Dickens, G.R., Shields, G.A., and Coxhell, S., 2010. The geochemistry of primary and weathered oil shale and coquina across the Julia Creek vanadium deposit (Queensland, Australia): Mineralium Deposita, 45, p. 599–620.

Long, J.A., Large, R.R., Lee, M.S., Benton, M.J., Danyushevsky, L.V., Chiappe, L.M., Halpin, J.A., Cantrill, D. and Lottermoser, B., 2015. Severe selenium depletion in the Phanerozoic oceans as a factor in three global mass extinction events. Gondwana Research, in press.

Lyons, T.W., and Severmann, S., 2006. A critical look at iron paleoredox proxies: New insights from modern euxinic marine basisns: Geochimica et Cosmochimica Acta, 70, p. 5698–5722.

Lyons, T.W., Werne, J.P., Hollander, D.J., and Murray, R.W., 2003. Contrasting sulfur geochemistry and Fe/Al and Mo/Al ratios across the last oxic-toanoxic transition in the Cariaco Basin, Venezuela: Chemical Geology, 195, 131–157.

Lyons, T.W., Gellatly, A.M., McGoldrick, P.J., and Kah, L.C., 2006. Proterozoic sedimentary exhalative (SEDEX) deposits and links to evolving global ocean chemistry: Geological Society of America Memoir 198, p. 169–184.

Magnall, J. M., Gleeson, S. A., Paradis, S., 2015. The Importance of Siliceous Radiolarian-Bearing Mudstones in the Formation of Sediment-Hosted Zn-Pb ± Ba Mineralization in the Selwyn Basin, Yukon, Canada. Economic Geology, 110, p. 2139—2146.

Martin, A.P., Condon, D.J., Prave, A.R., Melezhik, V.A., Lepland, A., Fallick, A.E. 2013. Dating the termination of the Palaeoproterozoic Lomagundi-Jatuli carbon isotopic event in the North Transfennoscandian Greenstone Belt. Precambrian Research, 224, p. 160-168.

Martin, A.P., Condon, D.J., Prave, A.R., Melezhik, V.A., Lepland, A. and Fallick, A.E., 2013. Dating the termination of the Palaeoproterozoic Lomagundi-Jatuli carbon isotopic event in the North Transfennoscandian Greenstone Belt. Precambrian Research, 224, p.160-168.

Melezich, V. A., Prave, A., Fallick, A.E., Kump, L., Struass, H., Lepland, A., Hanski, E., (Eds), 2013. Reading the Archive of Earth's oxygenation. Volume 1.: The Paleoproterozoic of Fennoscandia as Context for the Fennoscandian Arctic Russia Drilling Early Earth Project. Frontiers in Earth Sciences. Springer, Hiedelberg.

Melezhik, V .A., Filippov, M .M., and Romashkin, A.E., 2004. A giant Palaeoproterozoic deposit of shungite in NW Russia: genesis and practical applications: Ore Geology Reviews, 24, p. 135–154,

Maynard, J.B., 2003, Manganiferous sediments, rocks, and ores: Treatise on Geochemistry, 7, p. 289–308.

Maynard, J.B., 2010. The chemistry of manganese ores through time: A signal of increasing diversity of Earth-surface environments: Economic Geology, 105, p. 535–552.

McGoldrick, P.J., 1999. Northern Australian "Sedex" deposits: Microbial oases in Proterozoic seas, in Stanley, C.J., ed., Mineral deposits: Processes to processing: Rotterdam, A.A. Balkema, p. 885–888.

Morford J.L. and Emerson, S., 1999. The geochemistry of redox sensitive trace metals in sediments. Geochimica et Cosmochimica Acta, 63, p. 1735–1750.

Morse, J.W., Luther III, G.W., 1999. Chemical influences on trace metal–sulfide interactions in anoxic sediments. Geochimica et Cosmochimica Acta, 63, p. 3373–3378.

Nelson, M., Kyser, K., and Clark, A., 2007. Carbon isotope evidence for microbial involvement in exotic copper silicate mineralization, Huinquintipa and Mina Sur, northern Chile. Economic Geology, 102, p. 1311–1320.

Ohtomo, Y., Kakegawa, T., Ishida, A., Nagase, T. and Rosing, M.T., 2014. Evidence for biogenic graphite in early Archaean Isua metasedimentary rocks. Nature Geoscience, 7, p.25-28.

Okita, P.M., and Shanks, W.C., III, 1992. Origin of stratiform sediment hosted manganese ore deposits. Examples from Molango, Mexico, and Tao-Jiang, China: Chemical Geology, 99, p. 139–164.

Partin, C.A., Bekker, A., Planavsky, N.J., Scott, C.T., Gill, B.C., Podkovyrov, V., Maslov, A., Lalonde, S.V., Love, G.D., Poulton, S.W., and Lyons, T.W., 2013. Large-scale fluctuations in Precambrian atmospheric and oceanic oxygen levels from the record of U in shales. Earth and Planetary Science Letters, 369, p. 284–293.

Pavlov, A.A., and Kasting, J.F., 2002. Mass-independent fractionation of sulfur isotopes in Archean sediments: Strong evidence for anoxic Archean atmosphere. Astrobiology, 2, p. 27–41.

Petersen, S., Herzig, P.M. and Hannington, M.D., 2000. Third dimension of a presently forming VMS deposit: TAG hydrothermal mound, Mid-Atlantic Ridge, 26 N. Mineralium Deposita, 35, p.233-259.

Piper D.Z., and Perkins R.B., 2014, Geochemistry of a marine phosphate deposit: A signpost to phosphogenesis: Treatise on Geochemistry, 2nd ed., 13, p. 293–312.

Planavsky, N.J., Rouxel, O.J., Bekker, A., Lalonde, S.V., Konhauser, K.O., Reinhard, C.T., and Lyons, T.W., 2010, The evolution of the marine phosphate reservoir. Nature, 467, p. 1088–1090.

Planavsky, N.J., McGoldrich, P., Scott, C.T., Li, Chao, Reinhard, C.T., Kelly, A.E., Chu, X., Bekker, A., Love, G.D., and Lyons, T.W., 2011, Widespread iron-rich conditions in the mid-Proterozoic ocean. Nature, 477, p. 448–451.

Planavsky, N.J., Bekker, A., Hofmann, A., Owens, J.D., and Lyons, T.W., 2012. Sulfur record of rising and falling marine oxygen and sulfate levels during the Lomagundi. Proceedings of the National Academy of Sciences, 109, p. 18,300–18,305.

Planavsky, N.J., Asael, D., Hofmann, A., Reinhard, C.T., Lalonde, S.V., Knudsen, A., Wang, X., Ossa Ossa, F., Pecoits, E., Smith, A.J.B., Buekes, N.J., Bekker, A., Johnson, T.M., Konhauser, K.O., Lyons, T.W., and Rouxel, O.J., 2014. Evidence for oxygenic photosynthesis half a billion years before the Great Oxidation Event. Nature Geoscience, 7, p. 283–286.

Pitcairn I.K., Teagle, D.A.H., Craw, D., Olivo G.R., Kerrich, R., Brewer, T.S., 2006. Sources of metals and fluids in orogenic gold deposits: insights from the Otago and Alpine Schists, New Zealand. Economic Geology, 101, p. 525- 1546.

Pitcairn I.K., Olivo, G.R., Teagle, D.A.H., Craw, D., 2010. Sulfide evolution during prograde metamorphism of the Otago and Alpine Schists, New Zealand. Canadian Mineralogist, 48, p. 1267-1295.

Piper, D.Z., Perkins, R.B., 2004. A modern vs. Permian black shale— the hydrography, primary productivity, and water-column chemistry of deposition. Chemical Geology, 206, p. 177–197.

Poulton, S.W., and Canfield, D.E., 2011. Ferruginous conditions: A dominant feature of the oceans through Earth's history. Elements, 7, p. 107–112.

Poulton, S.W., Fralick, P.W., and Canfield, D.E., 2004. The transition of a sulphidic ocean ~1.84 billion years ago. Nature, 431, p. 173–177.

Pufahl, P.K., 2010. Bioelemental sediments, in James, N.P., and Dalrymple, R.W., eds., Facies models: Geological Association of Canada, 4th ed., p. 477–503.

Pufahl, P.K., and Hiatt, E.E., 2012. Oxygenation of the Earth's atmosphereocean system: A review of physical and chemical sedimentologic responses. Marine and Petroleum Geology, 32, p. 1–20.

Reinhard, C.T., Planavsky, N.J., Robbins, L.J., Partin, C.A., Gill, B.C., Lalonde, S.V., Bekker, A., Konhauser, K.K., and Lyons, T.W., 2013. Proterozoic ocean redox and biogeochemical stasis. Proceedings of the National Academy of Sciences, 110, p. 5357–5362.

Rona, P.A., Hannington, M.D., Raman, C.V., Thompson, G., Tivey, M.K., Humphris, S.E., Lalou, C. and Petersen, S., 1993. Active and Reliet Sea-Floor Hydrothermal Mineralization at the TAG Hydrothermal Field, Mid-Atlantic Ridge. Economic Geology, 88, p. 1989-1989.

Sáez, R., Moreno, C., González, F. and Almodóvar, G.R., 2011. Black shales and massive sulfide deposits: causal or casual relationships? Insights from Rammelsberg, Tharsis, and Draa Sfar. Mineralium Deposita, 46, p.585-614.

Schroder, S., Bekker, A., Buekes, N.J., Strauss, H., and van Niekerk, H.S., 2008. Rise in seawater sulfate concentration associated with the Paleoproterozoic positive carbon isotope excursion: Evidence from sulphate evaporates in the ~2.2-2.1 Gyr shallow-marine Lucknow Formation, South Africa. Terra Nova, 20, p. 108–117.

Schulz, H.N., and Schulz, H.D., 2005. Large sulfur bacteria and the formation of phosphorite. Science, 307, p. 416–418.

Schulz, H.N., Brinkoff, T., Ferdelman, T.G., Hernandez Marin., M., Teske,A., and Jorgensen, B.B., 1999. Dense populations of a giant sulfur bacterium in Namibian shelf sediments. Science, 284, p. 493–495.

Scott, C., and Lyons, T.W., 2012. Contrasting molybdenum cycling and isotopic properties in euxinic versus non-euxinic sediments and sedimentary rocks: Refining the paleoproxies. Chemical Geology, 324, p. 19–27.

Scott, C., Lyons, T.W., Bekker, A., Shen, Y., Poulton, S.W., Chu, X., and Anbar, A.D., 2008. Tracing the stepwise oxygenation of the Proterozoic ocean. Nature, 452, p. 456–459.

Scott, C.T., Bekker, A., Reinhard, C.T., Schnetger, B., Krapež, B., Rumble III, D., and Lyons, T.W., 2010. Late Archean euxinic conditions before the rise of atmospheric oxygen. Geology, 39, p. 119–122.

Scott, C., Planavsky, N.J., Dupont, C.L., Kendall, B., Gill, B.C., Robbins, L.J., Husband, K. F., Arnold, G.L., Wing, B.A., Poulton, S.W., Bekker, A., Anbar, A.D., Konhauser, K.K., and Lyons, T.W., 2013. Bioavailability of zinc in marine systems through time. Nature, 6, p. 125–128.

Scott, C., Wing, B., Bekker, A., Planavsky, N.J., Medvedev, P., Bates, S.M., Yun, M., and Lyons, T.W., 2014. Pyrite multiple-sulfur isotope evidence for rapid expansion and contraction of the early Paleoproterozoic seawater sulfate reservoir. Earth and Planetary Science Letters, 389, p. 94–104.

Scott, C., Kelley, K.D., Slack, J.F., 2014. The geobiology of sediment-hsted ore deposits. Society of Economic Geologists Special Publication, 18, p. 17-35.

Skei, J. M., 1988. Partitioning and enrichment of trace elements in a sediment core from Framvaren, south Norway. Marine Chemistry, 23, p. 269–281.

Slack, J.F., Grenne, T., Bekker, A., Rouxel, O.J., and Lindberg, P.A., 2007. Suboxic deep seawater in the late Paleoproterozoic: Evidence from hematitic chert and iron formation related to seafloor-hydrothermal sulfide deposits, central Arizona, USA: Earth and Planetary Science Letters, 255, p. 243–256.

Slack, J.F., Grenne, T., and Bekker, A., 2009. Seafloor-hydrothermal Si-Fe-Mn exhalites in the Pecos greenstone belt, New Mexico, and the redox state of ca. 1720 Ma deep seawater. Geosphere, 5, p. 302–314.

Thamdrup, B., Fossing, H., and Jorgensen, B.B., 1994. Manganese, iron, and sulfur cycling in a coastal marine sediment, Aarhus Bay, Denmark. Geochimica et Cosmochimica Acta, 23, p. 5115–5129.

Wanty, R.B., and Goldhaber, M.B., 1992. Thermodynamics and kinetics of reactions involving vanadium in natural systems: Accumulation of vanadium in sedimentary rocks. Geochimica et Cosmochimica Acta, p. 1471–1483.

Widdel, F., Schnell, S., Heising, S., Ehrenreich, A., Assmus, B., and Schink, B., 1993. Ferrous iron oxidation by anoxygenic phototrophic bacteria. Nature, 362, p. 834–835.

Xu, L., Lehmann, B., and Mao, J., 2013. Seawater contribution to polymetallic Ni-Mo-PGE-Au mineralization in Early Cambrian black shales of South China: Evidence from Mo isotope, PGE, trace element, and REE geochemistry. Ore Geology Reviews, 52, p. 66–84.

Chapter 3

A review of redox conditions and geochemical proxies for the paleo-ocean environment

3.1. Introduction

The study of redox conditions in the marine realm capture and track the nature and evolution of an environment by comparing the relative distributions of redox processes across depositional and diagenetic conditions, as well as, the biogeochemical processes that may ultimately control them (see detailed review of Tribovillard et al., 2006 and references therein). Understanding redox conditions in the geological past, requires us to first determine whether conditions were predominantly oxidizing or reducing. This synopsis will provide a review of certain elements and elemental ratios traditionally employed in paleo-environmental studies, specifically those trace elements that are enriched in metal-rich black shales, and highlight the considerations that must made when using whole rock geochemical data.

This chapter uses the redox grading system outlined in Tribovillard et al., (2006: Fig. 3.1.). Anoxic conditions (dissolved oxygen is <0.5mg/l) may be further subdivided based on whether they are anoxic and non-sulfidic, or anoxic and sulfidic. In the latter case, such conditions can be termed as euxinic and is characterized by free hydrogen sulfide (H_2S) within the water column (Tribovillard et al., 2006). Euxinic conditions, in modern settings, are usually confined to restricted or semi-enclosed basins such as the modern Black Sea or the Cariaco Basin (Lyons et al, 2003). H_2S is produced as a catabolic byproduct of sulfate reducing bacteria (Canfield, 1998). Suboxic environments (>0.5 to 2mg/l) are generally categorized as those with very low or trace level dissolved oxygen concentrations in the water column. Here H_2S may only be present in pore waters below the sediment water interface (Tribovillard

et al., 2006).

3.1.1. Anoxic (suboxic) vs. euxinic settings

A variety of trace elements (TE) show sensitivities to differing redox conditions. Two divisions can be made based on speciation and redox behavior: Cr, U and V can accumulate under anoxic conditions, where nitrate-reducing bacteria may dominate. Whereas Ni, Co, Cu, Zn, Cd and Mo tend to show enrichment under sulfate-reducing conditions (Tribovillard et al., 2006; Fig. 3.1.). Workers can use the behavior of these two groups of trace elements in order to understand and interpret the redox gradations that governed the depositional environment of the sediments. For example, the occurrence U and V enrichments without significant Mo enrichment, suggests a suboxic/anoxic depositional environment without free H_2S (Lyons et al., 2003; Scott et al., 2008; Lyons et al., 2009). However, sediments that display concurrent enrichments in U, V and Mo can reflect the development of euxinic conditions in the water column or at the sediment–water interface (Algeo and Maynard, 2004; Tribovillard et al., 2006). However, there are some caveats and considerations to be made when using these geochemical proxies in order to make broad-sweep interpretations of regional paleo-environments. For example, the development of periodic euxinia during anoxic events may require high-resolution sampling in order to resolve this. In addition, the trace element variation in shale may be attributed to changing detrital influx or the predominance of a particular mineral phase, therefore using ratios against Al or enrichment factors relative to other shales may help to address these.

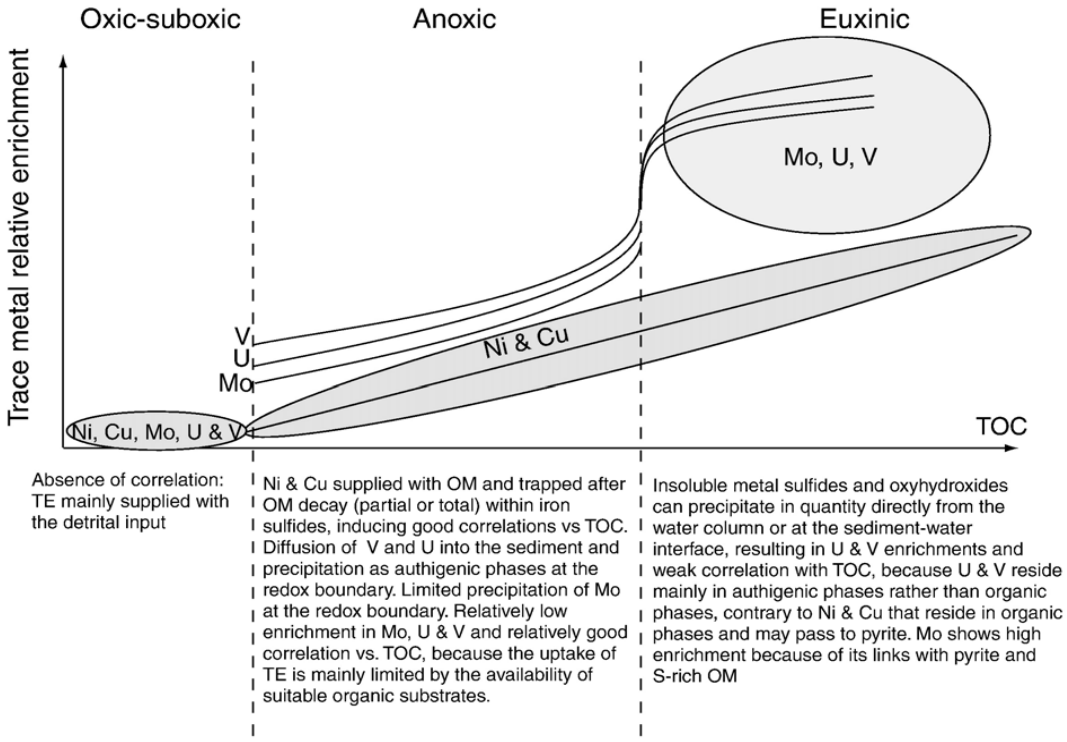

Figure. 3.1. Schematic behavior of Ni, Cu, Mo, U and V as a function of the redox conditions of the depositional environment and correlations to total organic carbon (TOC) (Tribovillard et al., 2006).

3.2. Comments on common trace elements used in paleo-redox and paleo-environmental studies

Within the past decade the amount of studies that have focused on using trace elements in order to decipher past oceanic and atmospheric cycles has increased almost exponentially. Much work has focused on current euxinic basins in order to identify commonalities in geochemical processes (e.g. Lyon et al., 2006, Scott et al., 2008; Scott et al., 2012). These studies have provided an understanding of the conditions that governed black shale deposition and metal enrichments in ancient oceans and basins. The major elements (Fe, S, C, and Mn) that are of interest in black shales and in biochemical and geochemical processes have been discussed in Chapter 2. Here, some of the common trace elements that are of interest in paleoredox studies are discussed.

3.2.1. Phosphorous

As discussed in Chapter 2, the phosphate content of sediments may reach such high quantities that economic phosphorite deposits can be formed (Pufahl, 2010). High P concentrations in phosphorites are usually the result of hydrodynamic working of apatite-rich sediments and can be promoted at zones of upwelling (Pufahl, 2010; Piper and Perkins, 2014). Jarvis et al. (1994) noted that the francolite (apatite; $Ca_5(PO_4)_3(OH,F,Cl)$) group structure is relatively 'open' allowing for a range of potential substitutions to occur at the two Ca sites as well as the PO_4 and F sites. These substitutions can affect major and trace element contents. Some trace metals show notable enrichments in phosphorites, compared to those of average shales, such as Cd (discussed later in this section). Therefore, phosphorous-minerals have the potential to influence the trace element budget and element phase partitioning in sediments. These elements are mainly Ag, Cd, Mo, Se, U, Y and Zn, as well as rare earth, and Br, Cu, Cr, I, Pb and V (Lucas et al., 1990; Jarvis et al., 1994; Nathan et al., 1997). It must be noted however that these trace elements are not necessarily within the apatite structure and may also be related to other minerals (usually sulfide phases) or organic matter (OM) (Jarvis et al., 1994), that are also common in phosphorous-rich sediments.

In many modern marine sediments, Cd appears to mirror PO_4, this has led to the proposal that it may be used to interpret Phanerozoic paleo-productivity (Jarvis et al., 1994; Van Geen et al., 1995). A number of studies have used Cd/Ca ratios in foraminifera for paleo-environmental interpretations (e.g., Rosenthal et al., 1997; Henderson, 2002). Uranium, as U^{4+}, also substitutes for Ca in the structures of many apatites, but U is predominantly complexed with organic matter and is not always in significant quantities in the apatite lattice (Jarvis et al., 1994; Trappe, 1998). Nevertheless, the fact that some of the trace elements popularly used as paleo-redox proxies are enriched in phosphorites underlines the necessity of determining the primary phases of residence of each element if using traditional whole-rock methods exclusively, and the potential pitfalls of drawing inferences regarding the environmental significance of T.E. enrichments without adequately resolving this issue.

3.2.2. Barium

The majority of barium in marine sediments is mainly hosted in detrital plagioclase, mica, and in the form of barite, in such conditions where Ba-sulfate reaches saturation (Bishop, 1988; Rutsch et al., 1995). The major transport mechanism of Ba from land into the ocean is via detrital feldspars and micas where Ba can be substituted into their crystal structure (e.g., Tribovillard et al., 2006). Natural seawater is under-saturated with respect to barite. Therefore, it has been proposed that barite precipitation is promoted during the decay of phytoplankton (Monnin et al., 1999). The emerging links between OM and biogenic barite accumulation, and its refractory nature in sediments without sulfate reduction, has lent credence to the use of barite and biogenic barium as a paleo-productivity proxy (e.g. Dymond et al., 1992; François et al., 1995; McManus et al., 1998; Sanchez-Vidal et al., 2005).

Many studies have focused on probing the link between surface productivity, export of OM into sediments, and the biogenic Ba abundance in the water column (e.g., Dymond et al., 1992), as well as surface sediments (e.g., Paytan et al., 1996, 2003). Others have employed biogenic Ba as a paleo-productivity proxy in older sediments (e.g., Jacot des Combes et al., 1999; Martinez-Ruiz et al., 2000). However, there are caveats to using Ba in the case of sediments that may have undergone much sulfate reduction, as this can result in barite dissolution, and Ba diffusion through pore waters (e.g., Van Os et al., 1991; Reitz et al., 2004).

3.2.3. Nickel

Nickel behaves as a micronutrient in oxic marine conditions, and can be present as soluble Ni^{2+} cations or $NiCl^{+}$ ions. However, it predominantly occurs in the form of soluble Ni carbonate ($NiCO_3$) or tied to organic matter as it is readily adsorbed onto humic and fulvic acids (Calvert and Pedersen, 1993; Whitfield, 2002; Algeo and Maynard, 2004). The formation of Ni-organic complexes can accelerate the scavenging process in the water column, leading to enrichment in the sediments (Piper and Perkins, 2004; Nameroff et al., 2004; Naimo et al., 2005; Tribovillard et al., 2006).

Upon the decay of organic matter, Ni may be released from organometallic complexes into pore waters (Calvert and Pedersen, 1993; Tribovillard et al., 2006). In reducing sediments, Ni is cycled from the

sediment into the overlying waters because sulfides and Mn oxides are absent, while under euxinic conditions, Ni may be readily incorporated into pyrite (Huerta-Diaz and Morse, 1990). Occasionally, the Ni brought to the sediments by OM may also be incorporated into organic complexes and may be preserved under reducing (anoxic/euxinic) conditions (Lewan and Maynard, 1982).

3.2.4. Copper

In oxic marine environments, Cu is dominantly as organometallic complexes and as $CuCl^+$ ions, though, this is less common (Calvert and Pedersen, 1993; Whitfield, 2002; Algeo and Maynard, 2004). Copper acts as a micronutrient but can also be scavenged from solution in deep water (Calvert and Pedersen, 1993; Tribovillard et al., 2006). Copper is incorporated as organometallic complexes, as well as adsorbed onto particulate Fe–Mn-oxyhydroxides, enhancing scavenging rates, and sedimentary enrichment (Nameroff et al., 2004).

Upon OM decay and/or reductive dissolution of Fe–Mn-oxyhydroxides, Cu may be released to pore waters (Tribovillard et al., 2006). Under reducing conditions (especially with H_2S), Cu(II) is reduced to Cu(I) and may be incorporated in pyrite or, less commonly, as its own sulfide phases (e.g. CuS and CuS_2) if the sulfide levels are high enough (Huerta-Diaz and Morse, 1990, 1992; Morse and Luther, 1999).

3.2.5. Zinc

Zinc behaves as a micronutrient and may be present as soluble Zn^{2+} cations or $ZnCl^+$ ions in oxic environments. However, it is mostly present as complexes with humic/fulvic acids or adsorbed onto Fe–Mn-oxyhydroxide particles in the water column (Calvert and Pedersen, 1993; Algeo and Maynard, 2004). Upon OM decay, Zn may be released from organometallic complexes to pore waters (Tribovillard et al., 2006). Under reducing conditions (notably in the bacterial sulfate reduction zone), it may be incorporated in pyrite or it may form its own sulfides, sphalerite (ZnS), in highly euxinic conditions (Huerta-Diaz and Morse, 1992; Tribovillard et al., 2006; Scott et al., 2012).

3.2.6. Cadmium

Differing from Ni, Cu and Zn, that have been discussed previously, Cd is present in only one valence state (Cd (II)) in the water column and sediments, and has a nutrient behavior and, therefore, a relatively short residence time (Boyle, 1981, 1988; Rosenthal et al., 1997; Morford and Emerson, 1999). Cadmium is deposited in sedimentsby way of its association with OM (Piper and Perkins, 2004), with Cd being released into interstitial waters during OM decay, and becoming enriched in sediments, in the form of sulfide or tied to hydroxyapatite where, as previously discussed, it can substitute for Ca (Gobeil et al., 1997; Morford and Emerson, 1999; Morford et al., 2001).

In the presence of H_2S, Cd can form its own separate insoluble sulfide phase (CdS) or is preferentially incorporated into sphalerite that may be forming (either separately or as inclusions within the pyrite), rather than being incorporated directly within the FeS_2 itself (Huerta-Diaz and Morse, 1992). Cadmium can show marked enrichments in reducing sediments (Calvert and Pedersen, 1993; Rosenthal et al., 1995; Russell and Morford, 2001).

3.2.7. Uranium

In seawater, U is present mainly as U(VI) in the form of uranyl ions that can then complex with carbonate ions, forming $UO_2(CO_3)_3^{4-}$, this form tends to dominate the U-speciation in most natural waters (Langmuir, 1978). In oxic or euxinic marine settings, dissolved U(VI) is not reduced to the thermodynamically favored U(IV), nor does it become scavenged by particulates in the water column (Anderson et al., 1989; Tribovillard et al., 2006). The main process of U sequestration in sediments is via the diffusion of $UO_2(CO_3)_3^{4-}$ from seawater to the sediments, followed by the reduction of U(VI) to U(IV), and then via adsorption or precipitation, commonly as distinct uraninite ($U^{(IV)}O_{2(s)}$) (Klinkhammer and Palmer, 1991; Crusius et al., 1996; Zheng et al., 2000; Morford et al., 2001; McManus et al., 2005). Organic-rich shelves, sediments and anoxic basins are sites for authigenic U deposition (Klinkhammer and Palmer, 1991). Authigenic U enrichment is proposed to take place in the sediment and not the water column itself. This is because the reduction of U(VI) to U(IV) is decoupled from the concentration of H_2S and, therefore, is not directly influenced by it (Algeo and Maynard, 2004;

McManus et al., 2005). Zheng et al. (2002), however, argue that Fe and sulfate reduction may have a regulatory effect on U.

Since the enrichment takes place within the sediment, the oxygen penetration depth and the sedimentation rate may play a role, in that slower sedimentation rates allow more time for diffusion of uranyl ions from the water column, leading to greater enrichments in the sediment (Crusius and Thomson, 2000). In reduced sediments, removal of U from the water column to the sediment may be accelerated by the formation of organometallic complexes and/or humic acids (Klinkhammer and Palmer, 1991; Zheng et al., 2002; McManus et al., 2005). Wignall and Maynard (1993) and Algeo and Maynard (2004) also discussed the influence of organic substrates on U uptake by the sediments. U abundance usually shows a good correlation with organic carbon input rate (McManus et al., 2005) and the organic-carbon content (TOC%) in anoxic (non-sulfidic) sediments (Algeo and Maynard, 2004).

3.2.8. Vanadium

In oxygenated waters, vanadium is present as vanadate oxyanions (HVO_4^{2-} and $H_2VO_4^-$) and adsorbed onto Mn- and Fe-oxyhydroxides (Calvert and Piper, 1984) and clays (Breit and Wanty, 1991).

Under reducing conditions, V(V) is reduced to V(IV), and forms vanadyl ions (VO_2^-), vanadium-hydroxyl groups (e.g., $VO(OH)_3^-$) and insoluble hydroxides $VO(OH)_2$. In the marine environment, the V(IV) species can be removed by surface adsorption or by the formation of organometallic ligands, becoming enriched in the sediments (Emerson and Huested, 1991; Morford and Emerson, 1999).

Under more strongly reducing (euxinic) conditions, the presence of H_2S, via bacterial sulfate reduction, leads to the reduced V(III), which can be taken up by geoporphyrins, or precipitated as solid oxide V_2O_3, or as hydroxide $V(OH)_3$ phases (Breit and Wanty, 1991; Wanty and Goldhaber, 1992, Scott et al., 2014). Vanadium does not readily form a solid solution with Fe-sulfides (Algeo and Maynard, 2004) and may be removed from pore waters below the level of Mn–Fe-oxyhydroxides reduction (Hastings et al., 1996; Morford and Emerson, 1999). In the diagenetic environment, V(III) readily substitutes for aluminum sites of clay minerals (Breit and Wanty, 1991) and therefore would be commonly present in the matrix component of black shales (Large et al., 2014).

3.2.9. Cobalt

Cobalt forms the dissolved cation, Co^{2+}, or is complexed with organic matter under oxic conditions (Saito et al., 2002; Whitfield, 2002). In reduced waters, Co forms insoluble CoS, which can be taken up in solid solution by Fe-sulfides (Huerta-Diaz and Morse, 1992). However, very slow reaction kinetics may limit CoS incorporation (Huerta-Diaz and Morse, 1992). Also, the concentration of Co in sediments is strongly reliant on the abundance of clastic material, limiting its use as a reliable redox proxy (Tribovillard et al., 2006).

3.2.10. Molybdenum

Molybdenum is the most abundant transition metal in modern seawater and is a bio-essential element, occurring mainly as the molybdate anion (MoO_4^{2-}; Morford and Emerson, 1999). Along with many other transition metals, Mo becomes authigenically enriched in sulphidic environments, where molybdate is converted to organic thiomolybdates and sequestered in sediment or by inorganic Fe–Mo–S complexes.

Hydrogen sulfide (H_2S) availability is an integral part of transformation of Mo from a conservative element to a reactive species (Erickson and Helz, 2000). Erickson and Helz (2000) state that because each successive sulfidation reaction is roughly an order of magnitude slower than the previous one, (dithio- ↔trithio- and trithio-↔tetra-thiomolybdate) the reaction would not be successful in seasonally or intermittently sulfidic waters (Erickson and Helz, 2000). Moderate- to long-term sulfidic conditions are thereby required, making Mo a popular euxinia proxy (e.g. Lyons and Severmann, 2006).

Once the reaction to create thiomolybdate is complete, Mo can be effectively scavenged, this occurs by combining with metallic particles, sulfur-rich organic matter (Helz et al., 1996; Tribovillard et al., 2004, 2006) and Fe-sulfide (Vorlicek et al., 2004). Work by Helz et al. (1996) suggests the formation of Fe–Mo–S clusters is a likely step, and Bostick et al. (2003) and Chappez et al. (2014) showed that these clusters can be retained on pyrite surfaces.

However, studies have started to scrutinize the use of Mo as a paleo-redox proxy especially in restricted depositional settings such as the modern Black Sea (Algeo, 2004; Algeo and Lyons, 2006). These

studies emphasize the role of the termed “basin reservoir effect”: this is where increasing restriction of a basin results in an overall lowering of deep water Mo concentrations, leading to lower Mo/TOC ratios, due to rates of Mo removal to the sediment faster than rates of Mo replenishment.

Neubert et al. (2008) also studied how H_2S levels control Mo isotope fractionation, defining an action point of switch (APS), where water column concentrations of $H_2S_{(aq)}$ must be higher than 11 μmol/l for thiommolybdate to dominate over molybdate. This is what causes Mo isotope fractionation in the ocean. Based on this data they argue that the Mo isotopic composition in seawater does not simply reflect oxic vs anoxic vs euxinic. Instead they can act in a more stringent manner, marking the point between strongly euxinic environments, where H_2S is above the APS, and those that have lower values as ranging from weakly euxinic, through to oxic.

3.2.11. Chromium

In oxygenated seawater, chromium Cr is mainly present as Cr(VI) in the chromate anion, CrO_4^{2-} and, to a lesser extent as Cr(III) in the hydroxyl ion, $Cr(H_2O)_4(OH)_2^+$ (Calvert and Pedersen, 1993). Under oxic seawater conditions, the chromate anion is soluble, but under anoxic conditions, Cr(IV) is reduced to Cr(III) ($Cr(OH)_2^+$, $Cr(OH)_3$, $(Cr,Fe)(OH)_3$), which can readily complex with humic/fulvic acids or adsorb onto Fe- and Mn-oxyhydroxides (Breit and Wanty, 1991; Algeo and Maynard, 2004).

Chromium has incompatibilities with pyrite, therefore Cr(III) uptake by Fe-sulfides can be limited (Huerta-Diaz and Morse, 1992; Morse and Luther, 1999). In addition, Cr does not form an insoluble sulfide (Morse and Luther, 1999). Therefore, upon OM remineralization by sulfate-reducing bacteria, Cr is not readily trapped within the sediments as a sulfide and may be lost via diffusion to the overlying water column (Huerta-Diaz and Morse, 1992; Tribovillard et al., 2006). In addition, Cr is usually sourced from clastic fractions (e.g., Hild and Brumsack, 1998), making its use as paleo-environmental proxy somewhat limited.

3.3. Selenium- an analogue for Sulfur?

Recent work by Large et al. (2014) has shown Se to be an important element in ocean geochemical cycling and appears to track the relative oxygen content in the atmosphere considerably well, in addition to showing strong links with major biological events throughout Earth history. It also forms an integral part of discussions and ideas in future chapters. Selenium has enjoyed a shift towards the forefront of research in recent years due to its apparent similarities to sulfur and as such, readily, substitutes stoichiometrically into pyrite. Therefore, it is deemed that selenium is deserving of a more comprehensive overview in this section of the chapter.

The biogeochemical cycle of sulfur (S) has been studied extensively and has informed our understanding of many aspects of Earth's evolution, including the emergence of life, major changes in ocean chemistry and the oxygenation of the atmosphere (Berner and Canfield, 1989; Canfield and Teske, 1996; Canfield and Raiswell, 1999; Canfield et al., 2000; Canfield, 2004; Canfield et al., 2007; Large et al, 2014, 2015). More recently, there has been interest in providing complimentary geochemical information using other systems such as Se. Given the multiple oxidation states and multiple isotopes, Se has the potential to be a powerful paleo-environmental proxy (Johnson et al., 2004; Carignan and Wen, 2007; Mitchell et al., 2012).

Selenium exhibits four major oxidation states, similar to sulfur: -II, 0, +IV, and +VI. It also has six stable isotopes: ^{74}Se, ^{76}Se, ^{77}Se, ^{78}Se, ^{80}Se and ^{82}Se. Se-isotopes behave in a similar manner to the sulfur isotope system, but are much less sensitive to temperature dependent fractionation (Carignan and Wen, 2007). Se enrichments, its isotopes and its oxidation states may have future potential implications for use in evaluating petroleum shale formations as well as fluid interactions ore-deposits. This is especially useful in terrains that have seen high thermal histories whereby the use of the less mobile, less temperature sensitive Se-isotope system could preserve information lost by high temperature re-equilibration of other stable isotope systems, (i.e. sulfur, Johnson, 2004) such as in metamorphosed or altered sedimentary basins.

3.3.1. The biogeochemistry and marine cycling of Selenium

Unlike seawater sulfate, modern seawater Se concentrations are very low (<0.08ppb) and can be spatially variable (Cutter and Bruland, 1984). The crustal Se/S ratio is $7.8x10^{-5}$ (mol/mol) (Mitchell et al., 2012) and $2.6x10^{-8}$ in modern seawater (mol/mol). The different abundances of S and Se are also reflected in contrasting ocean residence times of 8.7 million years for SO_4^{2-} and 26,000 years for Se (Cutter and Cutter, 1985).

Sulfur is essential for life, incorporated through the assimilatory pathway of sulfate reduction. In addition, sulfate is a common electron acceptor for microbial respiration (Canfield et al., 1993). Selenium is less abundant but is still an essential micronutrient due to its incorporation into selenocysteine (the 21st amino acid) (Böck et al., 1991). Selenocysteine has been found in eukaryotes, bacteria and archaea (Mitchell et al., 2012) further emphasizing its pivotal link to evolving life through geological time.

Selenium exhibits nutrient behavior, with very low concentrations at the surface due to biological uptake (e.g., Johnson, 2004). Organic selenide may be taken up by marine phytoplankton in the surface ocean (Baines, 2001), and may be the dominant source of Se in the surface waters.

The two main sources of Se to the ocean basins are via particulate matter delivered by rivers, generally as adsorbed Se(IV), and by deposition of organic matter from the overlying water column (Mitchell et al., 2012). The fate of organic Se when it eventually reaches the seafloor is still a focus of further study. However, it is usually considered to concentrate in sulfides, selenides or, less commonly, as elemental Se (Belzile et al., 2000).

Suzuki et al. (1979) described the marine Se cycle (Fig. 3.2.), identifying three factors that control Se in the oceans: 1) exchanges between surface and deep waters, 2) biological assimilation of dissolved inorganic Se (DISe) into particulate organic (POSe) form, and 3) regeneration of dissolved inorganic and dissolved organic Se (DOSe) from POSe and subsequent reoxidation of DOSe. Cutter and Bruland (1984) propose a similar model but expand it to include the uptake of DOSe by phytoplankton and speculate that Se(0) may also be bioavailable, a point confirmed by Charlet et al. (2007).

Both terrestrial plants and phytoplankton can emit Se compounds such as dimethyl selenide (DMSe) and

dimethyl diselenide (DMDSe), these compounds represent the main input of Se to the atmosphere (Amouroux et al., 2001). Dimethyl diselenide (DMSe) is thought to be the main form of volatile selenium that reaches the atmosphere (Carignan and Wen, 2007). This is highly reactive with a short residence time in the atmosphere (<6 hours; Atkinson et al., 1990).

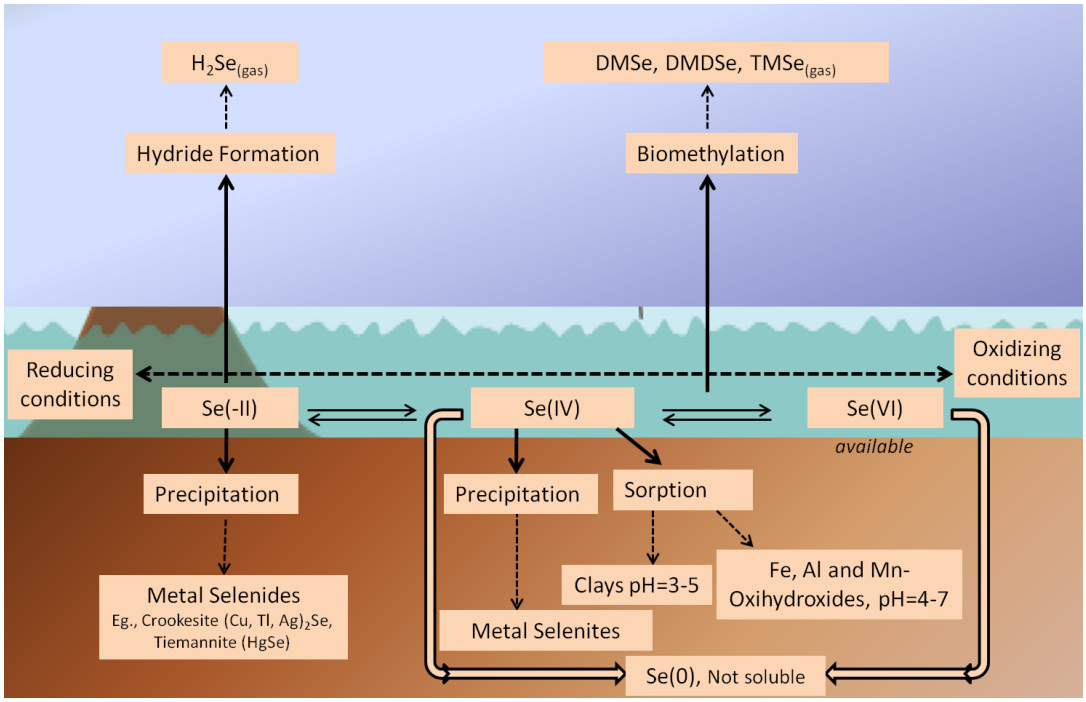

Figure 3.2. Selenium redox cycling and diagenetic distribution in the Earth system (modified after Oduro, unpublished and Mitchell, 2012)

3.4. Interpreting paleo-redox conditions: Some of the common ratios and patterns used

3.4.1. S/C Ratios in Sediments

Sedimentary rocks, in particular marine black shales, can be extraordinarily enriched in pyrite. Such enrichments are often interpreted to be primary or early diagenetic in origin. Many workers have focused on black shales as an archive of euxinia due to the inter-relation between Fe-sulfide formation

and organic matter (Berner and Raiswell 1983). Typical marine shales deposited from oxic waters have S contents (mostly as pyrite, FeS_2) that track organic carbon (C_{org}) content (Berner and Raiswell 1983). This indicates that the processes that lead to the preservation of organic carbon also promoted pyrite preservation. Berner and Raiswell (1983) interpret sediments depleted in S relative to C_{org} as non-marine, and those enriched in S relative to C_{org} as deposited under euxinic conditions where pyrite precipitation in the water column may have decoupled S contents from C_{org} preservation. While a useful guide, this model does not account for the potential variation of organic carbon input through geological time, or the possibility of the small-scale development of euxinia or sulfide enrichments via hydrothermal solutions.

3.4.2. C/P Ratio

In modern anoxic sediments, phosphorus is preferentially regenerated relative to organic carbon (Ingall et al. 1993). As a result, sediments beneath anoxic water columns tend to exhibit higher C/P ratios in the preserved organic matter. As discussed in Chapter 2, exact mechanism is still a matter of investigation but potential drivers include desorption of phosphate from Fe-oxide particles as they encounter reducing conditions, as well as less retention of phosphate by anaerobic bacteria (Ingall et al. 1993).

3.4.3. Proxies for Organic Matter

In addition to their variable behavior in response to different redox conditions, trace elements can be distinguished by their relationships to OM. For example, unlike U and V, Ni and Cu are dominantly delivered to sediments in association with OM (organometallic complexes). These elements are also sulfide forming and are released through OM decay before then become trapped by pyrite, if sulfate-reducing conditions dominate (Huerta-Diaz and Morse, 1992; Nameroff et al., 2002, 2004; Piper and Perkins, 2004; Algeo and Maynard, 2004).

Tribovillard et al. (2005) state that, high contents of Ni and Cu may be an indication of: (1) a high OM flux which brought in a great abundance of these elements to the basin sediments and/ or (2) that reducing conditions were met, allowing Ni and Cu fixation in the sedimentary package. Therefore, Ni

and Cu concentrations may be a marker of a relatively high OM flux, and, to compliment this, U, V and Mo can decipher the paleo-redox conditions. In addition, Ni and Cu can be retained within sediments, usually in the form of solid solution or inclusions in sulfides, whereas OM may be remineralized by bacterial activity or even later remobilized or recrystallized by hydrothermal or metamorphic processes. In the case of the latter, Cu and Ni contents may reflect an original OM abundance even if it is lost or thermally altered after deposition.

3.4.4. Trace element–TOC patterns

Many studies of sedimentary rocks (e.g., Tribovillard et al., 2005; Fig. 3.1.), and recent sediments have shown that T.E. concentrations (in particular, U, V, Mo, Ni and Cu) are correlated with TOC. Black shales that show a large range of TOC (<2–30%) are not uncommon in the rock record, and can exhibit positive correlations with Ni and Cu, regardless of redox conditions (suboxic to euxinic). U, Mo and V typically show good positive correlations with TOC but mostly when TOC is below a certain threshold value (~ 1 to 2% in the Cariaco Basin, ~2 to 3% in the Saanich Inlet, and > 10%, up to 40% TOC in Pennsylvanian shales of Kansas; Coveney and Glascock, 1989; Algeo and Maynard, 2004; Tribovillard et al., 2005, 2006). The correlation of U, V, and TOC% begins to disappear above the threshold value, where Mo enrichment accompanies U and V enrichments, suggesting the development of euxinic conditions (Tribovillard et al., 2006; Algeo and Lyons, 2006). Therefore the enrichment of Mo, along with U and V, but with weak correlations with TOC may mark the boundary between anoxia and the development of euxinic conditions.

3.4.5. Degree of Pyritization

Under euxinic conditions, the supply of reactive Fe (i.e. Fe that will react with free sulfide to form pyrite) can limit the amount of pyrite formed. Based on this, Fe in euxinic sediments tend to show a large degree of pyritization (DOP) (Raiswell et al., 1988) defined as the ratio of pyrite Fe to total reactive Fe (digestible in HCl). Raiswell et al. (1988) show that DOP is a better discriminant of sediments deposited under oxic, anoxic, and euxinic bottom-water conditions than S/C ratios. However,

DOP values have been shown to span the range from well oxygenated to highly euxinic in certain environments (Roychoudhury et al., 2003). Therefore, DOP should be high in euxinic environments, but should be used cautiously and with the support of other established redox proxies.

3.4.6. Pyrite Size Distribution

Pyrite formation in the water column of euxinic basins is reflected in the size of pyrite framboids. The size discrimination was used by Wilkin et al. (1996) in a study of various euxinic and non-euxinic basins. Their study showed that framboidal pyrite forming under euxinic deep water conditions had a narrower size distribution and were on average smaller (<10μm) than those formed in reducing sediments under an oxic water column. This proxy has been applied with success to Late Permian sediments by Nielsen & Shen (2004). Since size distributions are not readily affected by diagenesis, this proxy appears to be a useful and robust indicator of euxinic conditions.

3.5. Pyrite, an emerging tool for tracking T.E. concentrations

Inferences regarding paleo-environmental conditions that result from the study of T.E. data are unreliable if single element distributions are used, because T.E. concentrations are influenced by a variety of physical, biological and chemical mechanisms. Factors that can influence T.E. enrichment include the detrital siliciclastic flux, primary productivity rate and OM, which can each vary independently.

One must address of the possibility of T.E. mobility during diagenesis, which can produce elemental distributions that may not reflect the primary (i.e., paleo-environmental) controls. One such way of helping to mitigate the potential uncertainty of T.E. modification as a function of multiple mineral residences is to simply use one robust mineral, such as pyrite (Large et al., 2014). Recent work has argued that the trace element content of pyrite can serve as a useful proxy for first order trends in ocean chemistry (Large et al., 2014, 2015).

Much of this chapter has touched on the potential bias of using whole rock geochemistry, influenced by multiple mineral phases that may influence the overall element budget. The influence of multiple

mineral phases on trace element partitioning (as alluded to in the above section) adds an additional uncertainty. The use of a single mineral in paleo-environmental studies may help to reduce this uncertainty and add strength to the traditional whole-rock method when used in unison.

3.6. References

Algeo, T.J., Maynard, J.B., 2004. Trace-element behavior and redox facies in core shales of Upper Pennsylvanian Kansas-type cyclothems. Chemical Geology, 206, p. 289–318.

Amouroux, D., Liss, P.S., Tessier, E., Hamren-Larsson, M. and Donard, O.F., 2001. Role of oceans as biogenic sources of selenium. Earth and Planetary Science Letters, 189, p. 277-283.

Anbar, A.D., 2004. Molybdenum stable isotopes: observations interpretations and directions. Reviwes in Mineralogy and Geochemistry, 55, p. 429–454.

Anbar, A.D., Knoll, A.H., 2002. Proterozoic ocean chemistry and evolution: a bioinorganic bridge? Science, 297, p. 1137–1142.

Anderson, R.F., Fleisher, M.Q., LeHuray, A.P., 1989. Concentration, oxidation state and particulate flux of uranium in the Black Sea. Geochimica Cosmochimica Acta, 53, p. 2215–2224.

Arnold, G.L., Anbar, A.D., Barling, J., Lyons, T.W., 2004. Molybdenum isotope evidence for widespread anoxia in Mid-Proterozoic oceans. Science, 304, p. 87–90.

Atkinson, R., Aschmann, S.M., Hasegawa, D., Thompson-Eagle, E.T. and Frankenberger Jr, W.T., 1990. Kinetics of the atmospherically important reactions of dimethyl selenide. Environmental Science & Technology, 24, p. 1326-1332.

Belzile, N., Chen, Y.W. and Xu, R., 2000. Early diagenetic behaviour of selenium in freshwater sediments. Applied Geochemistry, 15, p. 1439-1454.

Benitez-Nelson, C.R., 2000. The biogeochemical cycling of phosphorus in marine systems. Earth Science Reviews, 51, p. 109–135.

Berner, R.A. and Raiswell, R., 1983. Burial of organic carbon and pyrite sulfur in sediments over Phanerozoic time: a new theory. Geochimica et Cosmochimica Acta, 47, p. 855-862.

Bishop, J.K.B., 1988. The barite-opal-organic carbon association in oceanic particulate matter. Nature, 332, p. 341–343.

Boyle, E.A., 1981. Cadmium, zinc, copper and barium in foraminifera tests. Earth and Planetary Science Letters, 53, p. 11–35.

Boyle, E.A., 1988. Cadmium: chemical tracer of deep water paleoceanography. Paleoceanography, 3, p. 471–489.

Böck, A., Forchhammer, K., Heider, J., Leinfelder, W., Sawers, G., Veprek, B. and Zinoni, F., 1991. Selenocysteine: the 21st amino acid. Molecular microbiology, 5, p. 515-520.

Brumsack, H.J., 1989. Geochemistry of recent TOC-rich sediments from the Gulf of California and the Black Sea. Geoligische Rundschau. 78, p. 851–882.

Brumsack, H.J., Gieskes, J.M., 1983. Interstitial water trace-element chemistry of laminated sediments of the Gulf of California (Mexico). Marine Chemistry, 14, p. 89–106.

Calvert, S.E., Pedersen, T.F., 1993. Geochemistry of recent oxic and anoxic sediments: implications for the geological record. Marine Geology, 113, p. 67–88.

Calvert, S.E., Pedersen, T.F., 1996. Sedimentary geochemistry of manganese: implications for the environment of formation of manganiferous black shales. Economic Geology, 91, p. 36–47.

Calvert, S.E., Piper, D.Z., 1984. Geochemistry of ferromanganese nodules: multiple diagenetic metal sources in the deep sea. Geochimica Cosmochimica Acta 48, p. 1913–1928.

Canfield, D.E., Jorgensen, B.B., Fossing, H., Flud, R., Gundersen, J., Ramsing, N.B., Thamdrup, B., Jansen, J.W., Nielsen, L.P., and Hall, P.O.J., 1993. Pathways of organic carbon oxidation in three continental margin sediments: Marine Geology, 113, p. 27–40.

Caplan, M.L., Bustin, R.M., 2001. Paleoenvironmental and paleoceanographic control on black, laminated mudrock deposition: example from Devonian–Carboniferous strata, Alberta, Canada. Sedimentary Geology, 145, p. 45–72.

Cardinal, D., Savoye, N., Trull, T.W., André, L., Kopczynska, E.E., Dehairs, F., 2005. Variations of carbon remineralisation in the Southern Ocean illustrated by the Baxs proxy. Deep-Sea Res., Part 1, Oceanography Research Papers, 52, p. 355–370.

Chaillou, G., Anschutz, P., Lavaux, G., Schäfer, J., Blanc, G., 2002. The distribution of Mo, U, and Cd in relation to major redox species in muddy sediments of the Bay of Biscay. Marine Chemistry, 80, p. 41–59.

Chappaz, A., Lyons, T.W., Gregory, D.D., Reinhard, C.T., Gill, B.C., Li, C. and Large, R.R., 2014. Does pyrite act as an important host for molybdenum in modern and ancient euxinic sediments?. Geochimica et Cosmochimica Acta, 126, p. 112-122.

Charlet, L., Scheinost, A.C., Tournassat, C., Greneche, J.M., Géhin, A., Fernández-Martı, A., Coudert, S., Tisserand, D. and Brendle, J., 2007. Electron transfer at the mineral/water interface: Selenium reduction by ferrous iron sorbed on clay. Geochimica Cosmochimica Acta, 71, p. 5731-5749.

Coveney, R.M. and Glascock, M.D., 1989. A review of the origins of metal-rich Pennsylvanian black shales, central USA, with an inferred role for basinal brines. Applied Geochemistry, 4, p. 347-367.

Cowie, G., Calvert, S.E., de Lange, G.J., Keil, R., Hedges, J., 1998. Extents and implications of organic matter alteration at oxidation fronts in turbidites from the Madeira Abyssal Plain. In: Weaver, P. P.E., Schmincke, H.U., Firth, J.V., Duffield,W. (Eds.), Proc. ODP, Sci. Results, vol. 157. Ocean Drilling Program, College Station, TX, pp. 581–590.

Cruse, A.M., Lyons, T.W., 2004. Trace metal records of regional paleoenvironmental variability in Pennsylvanian (Upper Carbonaferous) black shales. Chemical Geology, 206, p. 319–345.

Cutter, G.A, Bruland, K.W., 1984. The marine biogeochemistry of selenium: a re-evaluation. Limnol Oceanograph 29, p. 1179-1192.

Cutter, G.A. and Cutter, L.S., 1995. Behavior of dissolved antimony, arsenic, and selenium in the Atlantic Ocean. Marine Chemistry, 49, p.295-306.

Dymond, J., Suess, E., Lyle, M., 1992. Barium in deep-sea sediments: a geochemical proxy for paleoproductivity. Paleoceanography 7, p. 163–181.

Dymond, J., Collier, R., McManus, J., Honjo, S., Manganini, S., 1997. Can the aluminium and titanium contents of ocean sediments be used to determine the paleoproductivity of the oceans? Paleoceanography, 12, p. 586–593.

Emerson, S.R., Huested, S.S., 1991. Ocean anoxia and the concentration of molybdenum and vanadium in seawater. Marine Chemistry, 34, p. 177–196.

Erickson, B.E., Helz, G.R., 2000. Molybdenum(VI) speciation in sulfidic waters: stability and lability of thiomolybdates. Geochimica Cosmochimica Acta, 64, p. 1149–1158.

Fernex, F., Février, G., Benaïm, J., Arnoux, A., 1992. Copper, lead and zinc trapping in Mediterranean deep-sea sediments: probable coprecipitation with manganese and iron. Chemical Geology, 98, p. 293–308.

Filippelli, G.M., 1997. Controls on P concentrations and accumulation in oceanic sediments. Marine Geology, 139, p. 231–240.

Filippelli, G.M., 2001. Carbon and phosphorus cycling in anoxic sediments of the Saanich Inlet, British Columbia. Marine Geology, 174, p. 307–321.

Föllmi, K.B., 1996. The phosphorus cycle, phosphogenesis and marine phosphate-rich deposits. Earth Science Reviews. 40, p. 55–124.

Froelich, P.N., Klinkhammer, G.P., Bender, M.L., Luedtke, N.A., Heath, G.R., Cullen, D., Dauphin, P., Hammond, D., Hartman, B., Maynard, V., 1979. Early oxidation of organic matter in pemagic sediments of the eastern Equatorial Atlantic: suboxic diagenesis. Geochimica Cosmochimica Acta, 43, p. 1075–1090.

Glenn, C.R., Prévôt-Lucas, L., Lucas, J. (Eds.), 2000. Marine Authigenesis: from Global to Microbial. SEPM Special Publication, 66, 536 pp.

Huerta-Diaz, M.A., Morse, J.W., 1990. A quantitative method for determination of trace metal concentrations in sedimentary pyrite. Marine Chemistry, 29, p. 119–144.

Huerta-Diaz, M.A., Morse, J.W., 1992. Pyritisation of trace metals in anoxic marine sediments. Geochimica Cosmochimica Acta, 56, p. 2681–2702.

Ingall, E., Jahnke, R., 1997. Influence of water-column anoxia on the elemental fractionation of C and P during sediment diagenesis. Marine Geology, 139, p. 219–229.

Ingall, E., Bustin, R.M., Van Cappellen, P., 1993. Influence of water column anoxia on the burial and preservation of carbon and phosphorus in marine shales. Geochimica Cosmochimica Acta, 57, p. 303–316.

Jacot des Combes, H., Caulet, J.-P., Tribovillard, N., 1999. Pelagic productivity changes in the equatorial area of the NW Indian Ocean during the last 400 kyr. Marine Geology, 158, p. 27–55.

Jarvis, I., Burnett, W.C., Nathan, Y., Almbaydin, F.S.M., Attia, A.K. M., Castro, L.N., Flicoteaux, R., Hilmy, M.E., Husain, V., Qutawnnah, A.A., Serjani, A., Zanin, Y.N., 1994. Phosphorite geochemistry: state of the art and environmental concerns. Eclogae Geol. Helv. 87, p. 643–700.

Jeandel, C., Tachikawa, K., Bory, A., Dehairs, F., 2000. Biogenic barium in suspended and trapped material as a tracer of export production in tropical NE Atlantic (EUMELI sites). Marine Chemistry, 71, p. 125–142.

Johnson, T.M. and Bullen, T.D., 2004. Mass-dependent fractionation of selenium and chromium isotopes in low-temperature environments. Reviews in mineralogy and geochemistry, 55, p. 289-317.

Jones, B., Manning, D.A.C., 1994. Comparison of geochemical indices used for the interpretation of paleoredox conditions in ancient mudstones. Chemical Geology, 114, p. 111–129.

Klinkhammer, G.P., Palmer, M.R., 1991. Uranium in the oceans: where it goes and why. Geochimica Cosmochimica Acta, 55, p. 1799–1806.

Kuhn, T., Bostick, B.C., Koschinsky, A., Halbach, P. and Fendorf, S., 2003. Enrichment of Mo in hydrothermal Mn precipitates: possible Mo sources, formation process and phase associations. Chemical geology, 199, p. 29-43.

Lucas, J., El Faleh, E.M., Prévôt, L., 1990. Experimental study of the substitution of Ca by Sr and Ba in synthetic apatites. In: Notholt, A. J.G., Jarvis, I. (Eds.), Phosphorite Research and Development. Geological Society Special Publication, 52, pp. 33–47.

Lyons, T.W., 1997. Sulfur isotopic trends and pathways for iron sulfide formation in upper Holocene sediments of the anoxic Black Sea. Geochimica Cosmochimica Acta, 61, p. 3367–3382.

Lyons, T.W., Werne, J.P., Hollander, D.J., Murray, R.W., 2003. Contrasting sulfur geochemistry and Fe/Al and Mo/Al ratios across the last oxic-to-anoxic transition in the Cariaco Basin, Venezuela. Chemical Geology, 195, p. 131–157.

Lyons, T.W., and Severmann, S., 2006. A critical look at iron paleoredox proxies: New insights from modern euxinic marine basisns: Geochimica et Cosmochimica Acta, 70, p. 5698–5722.

McManus, J., Beulson, W.M., Klinkhammer, G.P., Kilgore, T.E., Hammond, D.E., 1994. Remobilization of barium in continental margin sediments. Geochimica Cosmochimica Acta, 58, p. 4899–4908.

Mitchell, K., Mason, P.R., Van Cappellen, P., Johnson, T.M., Gill, B.C., Owens, J.D., Diaz, J., Ingall, E.D., Reichart, G.J. and Lyons, T.W., 2012. Selenium as paleo-oceanographic proxy: A first assessment. Geochimica Cosmochimica Acta, 89, p. 302-317.

Monnin, C., Jeandel, C., Cattaldo, T., Dehairs, F., 1999. The marine barite saturation state of the world's oceans. Marine Chemistry, 65, p. 253–261.

Morford, J.L., Emerson, S., 1999. The geochemistry of redox sensitive trace metals in sediments. Geochimica Cosmochimica Acta, 63, p. 1735–1750.

Morse, J.W., Luther III, G.W., 1999. Chemical influences on trace metal–sulfide interactions in anoxic sediments. Geochimica Cosmochimica Acta, 63, p. 3373–3378.

Murphy, A.E., Sageman, B.B., Hollander, D.J., 2000. Eutrophication by decoupling of the marine biogeochemical cycles of C, N and P: a mechanism for the Late Devonian mass extinction. Geology 28, p. 427–430.

Nameroff, T.J., Balistrieri, L.S., Murray, J.W., 2002. Suboxic trace metal geochemistry in the eastern tropical North Pacific. Geochimica Cosmochimica Acta, 66, p. 1139–1158.

Nameroff, T.J., Calvert, S.E., Murray, J.W., 2004. Glacial–interglacial variability in the eastern tropical North Pacific oxygen minimum zone recorded by redox-sensitive trace metals. Paleoceanography, 19

Paytan, A., Kastner, M., 1996. Benthic Ba fluxes in the central Equatorial Pacific, implications for the oceanic Ba cycle. Earth Planetary Science Letters, 142, p. 439–450.

Pedersen, T.F., Vogel, J.S., Southon, J.R., 1986. Copper and manganese in hemipelagic sediments: diagenetic contrasts. Geochimica Cosmochimica Acta 50, p. 2019–2031.

Piper, D.Z., Perkins, R.B., 2004. A modern vs. Permian black shale— the hydrography, primary productivity, and water-column chemistry of deposition. Chemical Geology, 206, p. 177–197.

Piper D.Z., and Perkins R.B., 2014, Geochemistry of a marine phosphate deposit: A signpost to phosphogenesis: Treatise on Geochemistry, 2nd ed., 13, p. 293–312.

Raiswell, R., Canfield, D.E., 1998. Sources of iron for pyrite formation in marine sediments. American Journal of Science, 298, p. 219–245.

Rimmer, S.M., 2004. Geochemical paleoredox indicators in Devonian– Mississippian black shales, Central Appalachian Basin (USA). Chemical Geology, 206, p. 373–391.

Roychoudhury, A.N., Kostka, J.E. and Van Cappellen, P., 2003. Pyritization: a palaeoenvironmental and redox proxy reevaluated. Estuarine, Coastal and Shelf Science, 57, p. 1183-1193.

Sanchez-Vidal, A., Collier, R.W., Calafat, A., Fabres, J., Canals, M., 2005. Particulate barium fluxes on the continental margin: a study from the Alboran Sea (western Mediterranean). Marine Chemistry, 93, p. 105–117.

Saito, M.A., Moffett, J.W., Chisholm, S.W., Waterbury, J.B., 2002. Cobalt limitation and uptake in Prochlococcus. Limnol. Oceanogrography, 47, p. 1629–1636.

Scott, C., Lyons, T.W., Bekker, A., Shen, Y.A., Poulton, S.W., Chu, X.L. and Anbar, A.D., 2008. Tracing the stepwise oxygenation of the Proterozoic ocean. Nature, 452, p. 456-459.

Scott, C. and Lyons, T.W., 2012. Contrasting molybdenum cycling and isotopic properties in euxinic versus non-euxinic sediments and sedimentary rocks: refining the paleoproxies. Chemical Geology, 324, p. 19-27.

Tribovillard, N., Algeo, T.J., Lyons, T. and Riboulleau, A., 2006. Trace metals as paleoredox and paleoproductivity proxies: an update. Chemical Geology, 232, p. 12-32.

Tribovillard, N., Ramdani, A., Trentesaux, A., 2005. Controls on organic accumulation in Late Jurassic shales of northwestern Europe as inferred from trace-metal geochemistry. In: Harris, N. (Ed.), The Deposition of Organic-Carbon-Rich Sediments: Models, Mechanisms, and Consequences. SEPM Special Publication, 82, p. 145–164.

Tyson, R.V., Pearson, T.H., 1991. Modern and ancient continental shelf anoxia: an overview. In: Tyson, R.V., Pearson, T.H. (Eds.), Modern and Ancient Continental Shelf Anoxia. Geological Society Special Publication, 58, p. 1–26.

van Beek, P., Reyss, J.-L., Bonte, P., Schmidt, S., 2003. Sr/Ba in barite: a proxy of barite preservation in marine sediments? Marine Geology, 199, p. 205–220.

Van Geen, A., McCorckle, D.C., Klinkhammer, G.P., 1995. Sensitivity of the phosphate–Cd–C isotope relation in the ocean to Cd emoval by suboxic sediments. Paleoceanography 10, p. 159–162.

Van Os, B.J.H., Middelburg, J.J., de Lange, G.J., 1991. Possible diagenetic mobilization of barium in sapropelic sediments from the eastern Mediterranean. Marine Geology, 100, p. 125–136.

Wang, Y., van Cappellen, P., 1996. A multicomponent reactive transport model of early diagenesis: application to redox cycling in coastal marine sediments. Geochimica Cosmochimica Acta 60, p. 2993–3014.

Wanty, R.B., Goldhaber, R., 1992. Thermodynamics and kinetics of reactions involving vanadium in natural systems: accumulation of vanadium in sedimentary rock. Geochimica Cosmochimica Acta 56, p. 171–183.

Wen, H. and Carignan, J., 2007. Reviews on atmospheric selenium: emissions, speciation and fate. Atmospheric environment, 41, p. 7151-7165.

Whitfield, M., 2002. Interactions between phytoplankton and trace metals in the ocean. Advances in Marine Biology, 41, 3–120.

Wignall, P.B., Maynard, J.R., 1993. The sequence stratigraphy of transgressive black shales. In: Katz, B.J., Pratt, L.M. (Eds.), Source Rocks in a Sequence Stratigraphic Framework. AAPG Studies in Geology, 37, p. 35–47.

Wilkin, R.T., Barnes, H.L. and Brantley, S.L., 1996. The size distribution of framboidal pyrite in modern sediments: an indicator of redox conditions. Geochimica et Cosmochimica Acta, 60, p. 3897-3912.

Zheng, Y., Anderson, R.F., van Geen, A., Kuwabara, J., 2000. Authigenic molybdenum formation in marine sediments: a link to pore water sulfide in the Santa Barbara Basin. Geochimica Cosmochimica Acta 64, p. 4165–4178.

Chapter 4

Pyrite growth in black shales and trace element incorporation

Sedimentary pyrite forms within the water column under euxinic (anoxic and sulfidic) bottom water conditions (Lyons, 1997; Lyons et al., 2003) or within the uppermost layers of mud under the sediment-water interface. In the present day, euxinia is limited to a few localities in the ocean, epicontinental seas and continental shelf areas, and most pyrite is formed within the sediments. However, there have been many examples of periods in Earth history when water column euxinia was common. Under such conditions trace elements dissolved in the water can adsorb onto the surface of the growing Fe-sulfides and are subsequently incorporated into the structure of pyrite. Trace elements are also released into the pore waters from degrading OM and Fe (hydro)-oxides that can also be incorporated into pyrite (Tribovillard et al., 2006). This chapter aims to provide a brief synopsis of pyrite formation, T.E. incorporation, and how pyrite may be used as another method to understand the conditions of the seawater at the time of deposition as well as providing a source of metals in ore deposits.

4.1. Pyrite formation in organic rich sediments

Syngenetic and diagenetic pyrite form in an euxinic water column, or most commonly within the upper layers of organic rich muds, at, or in the 10's of centimeters below the sediment water interface, where euxinic conditions develop and the diffusion of reduced iron and H2S in the pore waters in this zone lead to Fe-sulfide formation (Raiswell and Canfield, 1998; Jorgensson et al., 2004). Mechanisms governing the formation of sedimentary pyrite have been the focus of much research (Rickard and Luther, 1997; Schoonen and Barnes, 1991; Schoonen, 2004). Many of the proposed models start with the precipitation of an intermediate Fe-monosulphide phase that is rapidly nucleated. Mackinawite is suggest to be the most common precursor Fe-monosulphide invoked in studies of pyrite growth (Wolthers et al., 2003; Schoonen, 2004). It is proposed that Fe-monosulphides convert to pyrite

according to the following reactions (Rickard and Luther, 1997):

$$FeS_{am} + H_2S \leftrightarrow FeS_{aq}$$

$$FeS_{aq} + H_2S \leftrightarrow [\ FeS\text{-}SH_2\ ]$$

$$[\ FeS\text{-}SH_2\ ] \leftrightarrow [\ FeS_2.H_2\ ]$$

$$[\ FeS_2.H_2\ ] \leftrightarrow FeS_2\,(\text{pyrite}) + H_2$$

Micro-organisms and bacteria can influence the transformation of Fe-monosulphides to pyrite (i.e. Donald and Southam, 1999) and can aid in the formation of diagenetic pyrite by binding Fe^{3+} on to anionic sites on their cell walls. Close proximity of these sites in the cells with one another promotes the formation of a thin FeS film on along the cell wall. This film then reacts to form pyrite along a similar stepped-reaction pathway as outlined above (Schoonen, 2004).

Detrital Fe-(hydro)oxides can also be converted into pyrite in the presence of sulfidic water via reductive dissolution (Dos Santos Afonso and Stumm, 1992; Poulton, 2003), which frees iron to form pyrite as well as releasing any adsorbed trace elements to then become incorporated into pyrite. A similar process can be proposed to occur within sediments with strong biologically-mediated redox fronts that promote H_2S production coupled to the anaerobic oxidation of methane (Jorgensen et al., 2004). In this case, dissolved Fe in pore water and that which is liberated by the conversion of Fe-(hydro)oxides meets with the sulfidation front in the upper layers of sediment and promotes Fe-sulfide formation.

4.2. Trace element incorporation into pyrite

The exact method by which the trace elements are released into diagenetic fluids and incorporated into pyrite is still a matter of debate and is reviewed in detail in Gregory (2014); Gregory et al. (2014); Large et al. (2014) and Huerta-Diaz and Morse (1990). Morse and Arakaki (1993) propose that the pyrite precursor mineral mackinawite ($FeS_{0.9}$) can adsorb several trace elements (e.g., Cd, Co, Cr, Cu, Ni, and Zn). The accumulation of these trace elements into the mackinawite structure is controlled by

the relative solubility of the metal sulfides and mackinawite. Metal sulfides with higher solubility than mackinawite, such as MnS, have similar surface affinities to mackinawite, and therefore relatively low partition coefficients into mackinawite. Metal sulfides with lower solubility, such as ZnS, have higher surface affinities that decrease with increasing metal solubility; therefore, partition coefficients of the trace elements into mackinawite increases with increasing surface affinities (Morse and Arakaki, 1993). This relationship may be used to explain the incorporation of trace elements into pyrite; however, it should be noted that mackinawite is a precursor of pyrite formation only when transient or localized oxidation is possible (Benning et al., 2000) and even under these conditions the reaction pathway is complicated, with greigite acting as an intermediate in the pathway (Benning et al., 2000). Trace elements may be released to solution during the transformation steps.

It has been shown that trace elements tend to be incorporated into pyrite during deposition and diagenesis of anoxic sediments by two possible mechanisms: precipitation or co-precipitation, Prior to their incorporation, trace elements are usually adsorbed at the pyrite surface or the surface of pyrite precursors, and their redox state may be changed (Dellwig et al., 2002; Berner et al., 2013). Berner et al. (2013) also showed that different elements held in pyrite can be grouped as heavy elements (Cu, Ni, Co, Pb, Bi, and Tl), oxyanionic elements (As, Mo, and Sb), elements that occur in submicroscopic Zn-sulfide inclusions (Zn and Cd), and elements that occur as inclusions of silicates or organic matter (Ga and V). In addition to these elements, U, Ba, Sn, and W have also been identified to occur as inclusions of different non-sulfide minerals within pyrite (Thomas et al., 2011). This process is considered to be most active in redistributing trace elements at, or in the first meter below the sediment-water interface where the initial deposition and subsequent break-down of organic matter and detrital phases during burial can release trace elements to forma authigenic phases, such as pyrite and precursor Fe-monosulfides (Sweeney and Kaplan, 1973; Berner, 1984). Furthermore, Large et al. (2014) discussed this notion, presenting evidence from the modern Cariaco basin, suggesting that much of the transfer of trace elements to directly from the seawater or in the first few 10s cm of sediment (Berner, 1984; Raiswell and Canfield, 1998).

As is one of the most common trace elements in pyrite and it's concentration in pyrite has been

suggested to be an important factor for the incorporation of other trace elements as it can enhance their uptake in pyrite (Deditius et al., 2008). It can be incorporated into pyrite in three different ways: substitution for S(–II) (Reich and Becker, 2006), substitution for Fe(II) (Deditius et al., 2008; Qian et al., 2013), and as inclusions of amorphous As-Fe-S domains within in pyrite (Deditius et al., 2008). In more reducing conditions, As in the (–I) oxidation state and substitutes for S(–II), while in more oxidizing conditions As is in the As(III) oxidation state and can substitute for Fe(II) (Deditius et al., 2008). The substitution of As for S is often accompanied by the uptake of elements with similar ionic radius and charge to Fe(II) (e.g., Co(II), Ni(II), Cu(II), Zn(II); Michel et al., 1994; Deditius et al., 2008; Reich et al., 2013). The substitution of As for Fe enhances the uptake of larger cations (e.g., Au(I), Ag (I), Pb (II) (Deditius et al., 2008). This relationship is due to the distortion and vacancies in the lattice caused by As(III) substituting for Fe(II) (charge balance of 2As(III) substitution will leave one vacancy) (Deditius et al., 2008). The relationship between the As content of pyrite and the content of other trace elements has been especially well documented for Au, which is strongly dependent on the amount of As (Reich et al., 2005). Au and other large cations, are believed to be incorporated into pyrite at distortions in the lattice or vacancies (Cook and Chryssoulis, 1990; Fleet and Mumin, 1997).

Though the mechanism of enrichment is still a matter of debate, experiments and observations by Morse and Luther (1999) suggest that elements are taken up by sedimentary pyrite in the following order of concentration: Hg > As = Mo > Cu ≥ Co > Ni >> Mn > Zn > Cr = Pb > Cd. Their observations where based on a kinetic and thermodynamic approach. Both Mo and As, which are accumulated into pyrite with a high degree of trace metal pyritization (DTMP), exist as oxyanions. These must be reduced prior to their accumulation into pyrite and are more dependent on redox reaction pathways and less on substitution reactions, meaning that they may be more likely to co-precipitate than adsorb (Morse and Luther, 1999; Rickard, 2012). Recent studies have also shown that Mo is often more likely to be held within matrix minerals and/ or organic matter (Chappaz et al., 2014), and that the results obtained by Morse and Luther (1999) may not hold true for all systems. The other elements (other than Cr) are more dependent on water exchange reaction kinetics. Nickel and Co both have water exchange reactions that are slower than the formation of mackinawite; thus, they are still available for

incorporation into mackinawite as it forms and as such have relatively high DTMP. Conversely, Pb, Zn, and Cd have faster exchange reactions and may form their own metal sulfide (MeS) phases prior to the formation of mackinawite and therefore have lower DTMPs (Morse and Luther, 1999). Other elements are more complicated. For example, Mn is preferentially incorporated into carbonate phases early in diagenesis and is therefore only incorporated into pyrite at very high degrees of pyritization when dissolved sulfide is present in high quantities (Morse and Luther, 1999).

4.3. Application of pyrite chemistry to understanding seawater chemistry and ore formation

4.3.1. Pyrite as source of metals in sedimentary ore deposits

Pyrite is a common mineral in many sulfide ore deposits where studies have used its chemistry to unravel ore processes and the evolution of ore fluids. In addition, it has been proposed that the trace metal content of diagenetic pyrite may also play a role in the formation of many sediment-hosted gold deposits (Pitcairn et al., 2006; Large et al., 2007; 2009; Pitcairn et al., 2010; Thomas et al., 2011; Large et al., 2011, 2012). These studies propose that under anoxic to euxinic conditions a large number of trace metals are concentrated into organic-rich marine sediments. During diagenesis the metals are released from organic matter and Fe-(hydr-)oxide detritus and become incorporated into diagenetic pyrite. Their models postulate that during metamorphism (above greenschist facies) the pyrite begins to breakdown and form pyrrhotite or recrystallize, with both processes leading to the release of Au, As and other metals. The metals released from the diagenetic pyrite can then carried by metamorphic fluids to favorable structural traps or depositional sites where they become orogenic or Carlin-style gold deposits.

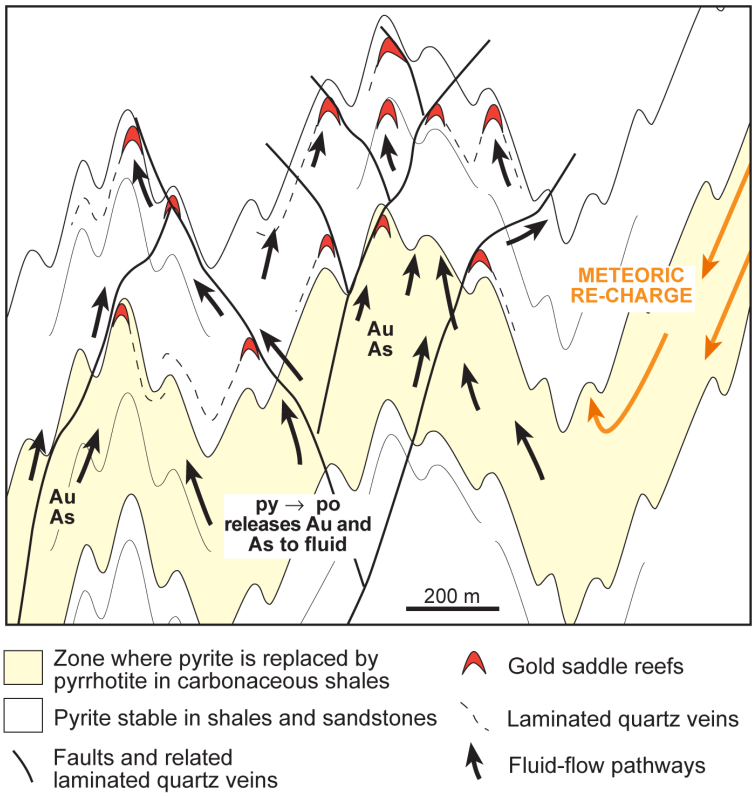

Figure 4.1. Example of pyrite breakdown and release of trace elements as a critical source for orogenic gold deposits (Large et al., 2011).

4.3.2. Pyrite as an archive of paleo-ocean conditions

The previous chapters (Chapter 2 and 3) touched on the variability of trace metals in sediments and potential bias of using whole rock geochemistry. The influence of multiple mineral phases on trace element partitioning (as alluded to in Chapter 3) adds an additional uncertainty to an area of study that is already fraught with such.

Sedimentary accumulations of trace elements may be hosted by various phases, e.g., metal sulfides, in solid solution in pyrite, insoluble oxides and oxyhydroxides, phosphate, sulfate, organometallic complexes and adsorbed onto organic or mineral surfaces. Consequently, the behavior of different trace elements is highly variable during diagenesis, depending on the specific pH and Eh conditions of the burial environment. The use of a single mineral in palaeo-environmental studies helps to reduce this uncertainty.

In the absence of post-depositional replenishment of oxidizing agents, sulfides are stable and the elements engaged in or co-precipitated with sulfides (pyrite) typically are not mobile during diagenesis (Huerta-Diaz and Morse, 1992; Abanda and Hannigan 2006). Many of the elements discussed previously are readily incorporated into syngenetic and diagenetic pyrite under a variety of ocean oxygenation states, from anoxic to euxinic, and even suboxic settings. Trace elements present in the ocean column will be taken up into the pyrite during its growth, allowing us to view a 'snapshot' of ocean geochemistry at that time and sufficiently quantify T.E. abundances with in-situ analysis.

To that extend, Large et al. (2014; 2015) has produced a dataset (n= >5000) of LA-ICP-MS analyses of diagnetic pyrite in black shales throughout Earth history. Their work proposes that the T.E. content of marine pyrite (which can be concentrated by many orders of magnitude compared to whole-rock) may reflect the composition and conditions of the seawater at the time of deposition. Berner et al. (2013) has also used a similar logic to elucidate the differences in depositional conditions in the Toarsian shales of the Posidonia Formation. Large et al., (2014; 2015) has produced a series of time curves of bio-essential trace elements (i.e., Se, Ni, Zn, Mo, Cu, Co) that appear to show a first order correlation with oxygen levels through time (Fig. 4.2.), mass extinctions and other geodynamic process.

Large et al. (2014; 2015) set out a series of criteria for the selection of suitable pyrites for this technique:

1) Only pyrite that has textures indicative of syngenesis or formation during early diagenesis. (i.e. framboids, microcrystalline pyrite in clouds in the shale, microcrystalline pyrite aligned parallel to bedding, small cubic euhedral and bladed crystals, small porous patches and rounded or elongate nodules.).
2) Samples that had undergone metamorphism of greenschist facies and above were not, and
3) Samples that contained late-stage pyrrhotite were also not suitable. The latter two relate to the fact that metamorphism can lead to the destruction or recrystallization of pyrite and the

release of trace metals. These are aspects that will be discussed further in the latter parts of this thesis.

It must be noted however, as attested to by Abanda and Hannigan (2006), that pyrite is extremely robust in diagenetic conditions, but it does tend to only account for <10% of the mineral phases in black shales. A combination of multiple approaches will aid in producing the most reliable results and subsequent interpretations. Therefore the application of high-resolution analysis of pyrite, whole rock, and isotope geochemistry may prove to be a powerful tool in understanding wider depositional environment of black shales.

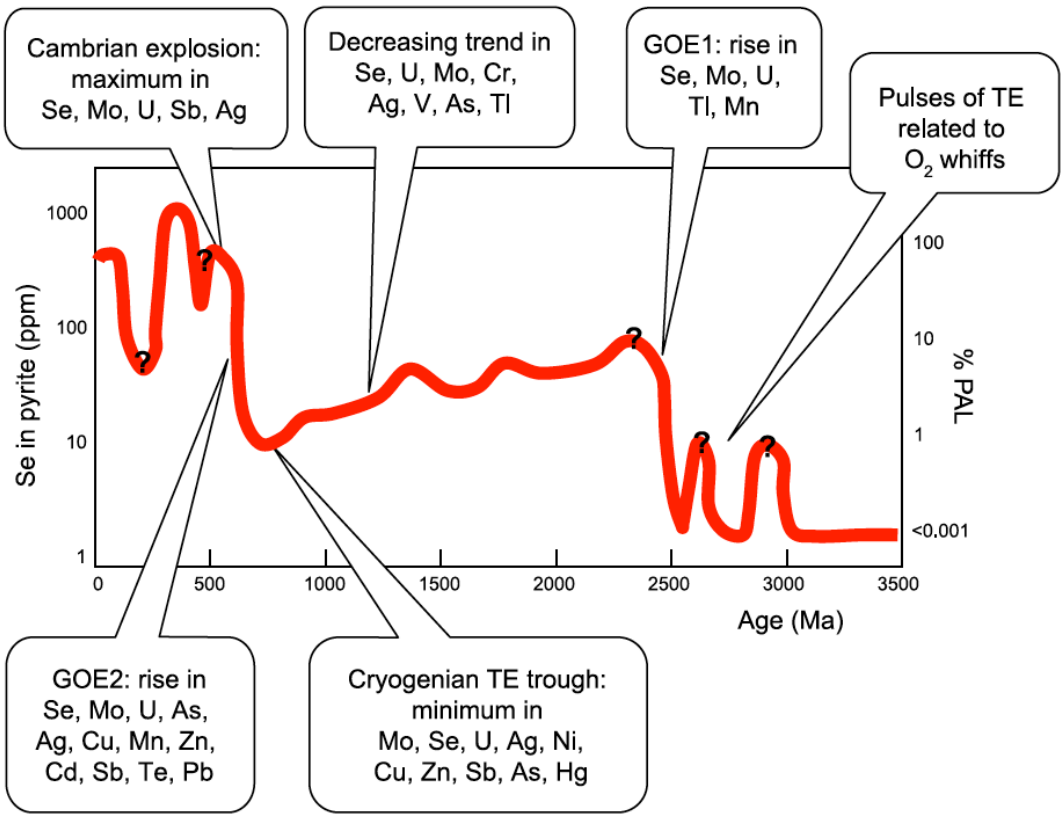

Figure 4.2. Se (ppm) in marine pyrite through time (Large et al., 2014).

4.4. References

Abanda, P.A. and Hannigan, R.E. 2006. Effect of diagenesis on trace element partitioning in shales. Chemical Geology, 230, p. 42-59

Benning, L.G., Wilkin, R.T. and Barnes, H.L., 2000. Reaction pathways in the Fe–S system below 100 C. Chemical Geology, 167, p. 25-51.

Berner, R.A., 1984. Sedimentary pyrite formation: an update. *Geochimica et cosmochimica Acta*, *48*, p.605-615.

Berner, Z.A., Puchelt, H., Noeltner, T. and Kramar, U.T.Z., 2013. Pyrite geochemistry in the Toarcian Posidonia Shale of south-west Germany: Evidence for contrasting trace-element patterns of diagenetic and syngenetic pyrites. Sedimentology, 60, p. 548-573.

Chappaz, A., Lyons, T.W., Gregory, D.D., Reinhard, C.T., Gill, B.C., Li, C. and Large, R.R., 2014. Does pyrite act as an important host for molybdenum in modern and ancient euxinic sediments?. Geochimica et Cosmochimica Acta, 126, p.112-122.

Deditius, A.P., Utsunomiya, S., Renock, D., Ewing, R.C., Ramana, C.V., Becker, U. and Kesler, S.E., 2008. A proposed new type of arsenian pyrite: Composition, nanostructure and geological significance. Geochimica et Cosmochimica Acta, 72, p. 2919-2933.

Deditius, A.P., Utsunomiya, S., Reich, M., Kesler, S.E., Ewing, R.C., Hough, R. and Walshe, J., 2011. Trace metal nanoparticles in pyrite. Ore Geology Reviews, 42, p. 32-46.

Dellwig, O., Böttcher, M.E., Lipinski, M. and Brumsack, H.J., 2002. Trace metals in Holocene coastal

peats and their relation to pyrite formation (NW Germany). Chemical Geology, 182, p.423-442.

Donald, R. and Southam, G. 1999. Low temperature anaerobic bacterial diagenesis of ferrous monosulfide to pyrite. Geochimica et Cosmochimica Acta, 63, p. 2019-2023.

Dos Santos Afonso, M. and Stumm, W., 1992. Reductive dissolution of iron(III) (hydr)oxides by hydrogen sulfide. Langmuir, 8, p. 1671–1675.

Fleet, M.E. and Mumin, A.H., 1997. Gold-bearing arsenian pyrite and marcasite and arsenopyrite from Carlin Trend gold deposits and laboratory synthesis. American Mineralogist, 82, p. 182-193,

Gregory, D., Meffre, S. and Large, R., 2014. Comparison of metal enrichment in pyrite framboids from a metal-enriched and metal-poor estuary. American Mineralogist, 99, p. 633-644.

Huerta-Diaz, M.A. and Morse, J.W., 1990. A Quantitative Method for Determination of Trace Metal Concentrations in Sedimentary Pyrite. Marine Chemistry, 29, p. 119-144.

Jørgensen, B.B., Böttcher, M.E., Lüschen, H., Neretin, L.N. and Volkov, I.I., 2004. Anaerobic methane oxidation and a deep H 2 S sink generate isotopically heavy sulfides in Black Sea sediments. Geochimica et Cosmochimica Acta, 68, p. 2095-2118.

Large, R.R., Maslennikov, V.V., Robert, F., Danyushevsky, L.V., and Chang, Z.S., 2007. Multistage sedimentary and metamorphic origin of pyrite and gold in the giant Sukhoi Log deposit, Lena gold province, Russia. Economic Geology, 102, p. 1233–1267.

Large, R.R., Danyushevsky, L., Hollit, C., Maslennikov, V., Meffre, S., Gilbert, S., Bull, S., Scott, R., Emsbo, P., Thomas, H., Singh, B., and Foster, J., 2009. Gold and trace element zonation in pyrite using

a laser imaging technique: Implications for the timing of gold in orogenic and Carlin-style sediment-hosted deposits. Economic Geology, 104, p. 635–668.

Large, R.R., Bull, S.W., and Maslennikov, V.V., 2011, A carbonaceous sedimentary source-rock model for Carlin-type and orogenic gold deposits. Economic Geology, 106, p. 331–358.

Large, R., Thomas, H., Craw, D., Henne, A. and Henderson, S., 2012. Diagenetic pyrite as a source for metals in orogenic gold deposits, Otago Schist, New Zealand. New Zealand Journal of Geology and Geophysics, 55, p. 137-149.

Large, R.R., Halpin, J.A., Danyushevsky, L.V., Maslennikov, V.V., Bull, S.W., Long, J.A., Gregory, D.D., Lounejeva, E., Lyons, T.W., Sack, P.J. and McGoldrick, P.J., 2014. Trace element content of sedimentary pyrite as a new proxy for deep-time ocean–atmosphere evolution. Earth and Planetary Science Letters, 389, p. 209-220.

Large, R.R., Halpin, J.A., Lounejeva, E., Danyushevsky, L.V., Maslennikov, V.V., Gregory, D., Sack, P.J., Haines, P.W., Long, J.A., Makoundi, C. and Stepanov, A.S., 2015. Cycles of nutrient trace elements in the Phanerozoic ocean. Gondwana Research, 28, p. 1282-1293.

Lyons, T.W., 1997. Sulfur isotopic trends and pathways of iron sulfide formation in upper Holocene sediments of the anoxic Black Sea. *Geochimica et Cosmochimica Acta*, *61*, p. 3367-3382.

Lyons, T.W., Werne, J.P., Hollander, D.J. and Murray, R.W., 2003. Contrasting sulfur geochemistry and Fe/Al and Mo/Al ratios across the last oxic-to-anoxic transition in the Cariaco Basin, Venezuela. Chemical Geology, 195, p. 131-157.

Michel, D., Giuliani, G., Olivo, G.R, and Marini, OJ., 1994. As growth banding and the presence of Au

in pyrites from the Santa Rita gold vein deposit hosted in Proterozoic metasediments Goias State, Brazil. Economic Geology, 89, p. 193-200.

Morse J. W. and Arakaki T., 1993. Adsorption and coprecipitation of divalent metals with mackinawite (FeS). Geochimica et Cosmochimica Acta, 57, p. 3635–3640.

Morse J. W. and Luther, G.W. 1999. Chemical influences on trace metal-sulfide interactions in anoxic sediments. Geochimica et Cosmochimica Acta, 63, p. 3373-3378.

Pitcairn I.K., Teagle, D.A.H., Craw, D., Olivo G.R., Kerrich, R., Brewer, T.S., 2006. Sources of metals and fluids in orogenic gold deposits: insights from the Otago and Alpine Schists, New Zealand. Economic Geology, 101, p. 525- 1546.

Pitcairn I.K., Olivo, G.R., Teagle, D.A.H., Craw, D., 2010. Sulfide evolution during prograde metamorphism of the Otago and Alpine Schists, New Zealand. Canadian Mineralogist, 48, p. 1267-1295.

Poulton, S.W., 2003. Sulfide oxidation and iron dissolution kinetics during the reaction of dissolved sulfide with ferrihydrite, Chemical Geology, 202, p. 79-94.

Qian, G., Brugger, J., Testemale, D., Skinner, W. and Pring, A., 2013. Formation of As (II)-pyrite during experimental replacement of magnetite under hydrothermal conditions. Geochimica et Cosmochimica Acta, 100, p. 1-10.

Raiswell, R., and Plant, J., 1980. The incorporation of trace elements into pyrite during diagenesis of black shales, Yorkshire, England. Economic Geology, 75, p. 684–699.

Raiswell, R. and Canfield, D.E., 1998. Sources of iron for pyrite formation in marine sediments. *American Journal of Science*, *298*, p.219-245.

Reich, M., Deditius, A., Chryssoulis, S., Li, J.W., Ma, C.Q., Parada, M.A., Barra, F. and Mittermayr, F., 2013. Pyrite as a record of hydrothermal fluid evolution in a porphyry copper system: A SIMS/EMPA trace element study. Geochimica et Cosmochimica Acta, 104, p. 42-62.

Reich, M., Becker, U. 2006. First-principles calculations of the thermodynamic mixing properties of arsenic incorporation into pyrite and marcasite. Chemical Geology 225, p. 278-290.

Reich, M., Kesler, S.E., Utsunomiya, S., Palenik, C.S., Chryssoulis, S.L., Ewing, R.C., 2005. Solubility of gold in arsenian pyrite. Geochimica et Cosmochimica Acta, 69, p. 2781–2796.

Rickard D., 1995. Kinetics of FeS precipitation: Part 1. Competing reaction mechanisms. Geochimica et Cosmochimica Acta 59, p. 4367–4379.

Rickard, D. and Luther, G.W. III., 1997, Kinetics of pyrite formation by the H_2S oxidation of iron(II) monosulfide in aqueous solutions between 25°C and 125°C: the mechanism. *Geochimica et Cosmochimica Acta*, 61 p. 135-147.

Rickard, D., 2012, Sulfidic sediments and sedimentary rocks: Developments in Sedimentology, 65, p. 801.

Schoonen, M.A.A., Barnes, H.L., 1991. Reactions forming pyrite and marcasite from solution: II. Via FeS precursors below 100 C. Geochimica et Cosmochimica Acta, 55, p. 1505-1514.

Schoonen, M.A.A., 2004. Mechanisms of sedimentary pyrite formation. Geological Society of America

Special Papers, 379, p. 117-134.

Sweeney, R.E. and Kaplan, I.R., 1973. Pyrite framboid formation; laboratory synthesis and marine sediments. *Economic Geology*, *68*, p.618-634.

Thomas, H.V., Large, R.R., Bull, S.W., Maslennikov, V., Berry, R.F., Fraser, R., Froud, S. and Moye, R., 2011. Pyrite and pyrrhotite textures and composition in sediments, laminated quartz veins, and reefs at Bendigo gold mine, Australia: insights for ore genesis. Economic Geology, 106, p. 1-31.

Wolthers, M., Van der Gaast, S.J. and Rickard, D., 2003. The structure of disordered mackinawite. American Mineralogist, 88, p. 2007-2015.

Chapter 5

Primary metal enrichment in black shale related to changes in the depositional environment, and geochemical cycles

5.1. Foreword

As attested to in the previous chapters, trace element geochemistry of black shales has been effectively utilised in many paleo-redox studies. Here, this method has been augmented by multi-isotope and pyrite trace element geochemistry, culminating in the first high-resolution, multi-proxy dataset for the Phanerozoic. This chapter introduces new sedimentological and geochemical data from a well-preserved shallow-water black shale sequence that was deposited in the wake of the largest carbon isotope excursion in the Phanerozoic. This allows for a combined approach, utilizing pyrite, whole-rock, and isotope geochemistry in order to unravel the nature of the depositional environment during this period of perturbation. This chapter is written in the same format as a paper to facilitate publication of the data and interpretations.

5.2. The sedimentology and geochemistry of the Turisalu Shale, Estonia: Evidence for shallow marine anoxia at the Cambrian- Ordovician boundary

5.2.1. Abstract

The first study of Phanerozoic rocks to adopt coupled high-resolution, whole–rock, isotopic, and in-situ pyrite trace element data has been applied to a shallow-marine black shale/biograinstone sequence at the Cambro-Ordovician boundary. Sedimentological analyses and field relations suggest that the change between Late Cambrian shallow-marine carbonates and Early Ordovician black shale represents an on-lapping surface, corresponding to relative sea-level rise. At this boundary $\delta^{13}C_{carb}$ values of +5‰ are

reported for the Late Cambrian biograinstones, potentially linking this locality to the Steptoean Positive Isotope Excursion (SPICE) event (Saltzman et al., 2000). At this horizon, the phosphorous content also increases. Whole-rock and pyrite trace element data from the overlying black shale sequence suggest that redox sensitive and bio-essential elements (e.g., Ni, Cu, Zn and Mo) are highly enriched compared to average shale (Ni EF*= 11, Zn EF*= 22, Cu EF*= 8, and Mo EF*= 367). This suggests that anoxic waters with punctuated sulfidic intervals may have dominated the depositional environment with in the wake of the carbon isotope excursion and phosphogenesis. Since this isotope event is considered to be global in nature, it is possible that such conditions may have been pervasive across the Baltica continental shelf and, potentially common in other basins at the time.

5.2.2. Introduction

One critical period of black shale deposition in Earth History occurs at the Middle to Late Cambrian, through to the Early Ordovician when the metal-rich Alum Shale of Baltica was deposited. This shale package is synchronous with a major excursion in the carbon isotope record, biological turnover and sea-level rise (Saltzman et al., 1998). Such events have been documented in other localities, suggesting that the dynamics that govern these events were global in nature (Dahl et al., 2014). Integral to our understanding of the dynamics of this period, and its implications for black shale deposition and seawater chemistry during this time, is the need for further detailed, site-specific studies in order to fully understand the interplays between biology, black shale deposition and changing geochemical cycles during this period. The metal enriched, black shales of the Turisalu Formation in Estonia offer such an opportunity. The shale is laterally extensive and provides a future economic resource of metals and, in places, low-grade hydrocarbons (Mens et al., 1996). It has been interpreted to represent the shallow water equivalent to upper horizons of the Cambrian Alum Shale of Sweden (Nielsen and Schovsbo, 2011), thereby, offering the potential to expand our understanding of black shale deposition across Baltica at this time. The vast metal accumulation in the Turisalu and Alum shales and their temporal occurrence with respect to potential geodynamic drivers that may influence sea level variation, and the evolution of marine life, stimulated this research in order to understand the wider context of Cambro-Ordovician shale deposition. This study aimed to address these aspects by first compiling an updated

sedimentological framework in order to understand the depositional and hydrodynamic setting during the shale deposition. Secondly, by conducting isotope geochemical profiles through the section in order to investigate whether the section preserves the same carbon isotopic anomaly that has been documented in other localities during this interval. Finally, by using high-resolution whole-rock and pyrite trace element chemistry in order to elucidate the nature of the seawater and depositional environment during shale deposition, and how this may influence metal enrichment as well as marine life.

5.2.3. Geological setting

Baltica during the Cambrian- Ordovician

At the beginning of Tremadocian (488-479 Ma), the Baltic palaeobasin was situated at the western margin of the continent, facing the Iapetus Ocean to the west and the Tornquist Sea and Gondwana in the south and south-west (Cocks and Torsvik, 2005) (Fig. 5.1.). Within this basin, the Turisalu Formation occurs as a widely distributed, Upper Cambrian to Lower Ordovician black shale belt across Baltoscandian region, extending from western Russia (Andersson et al., 1985), through Estonia and southern Sweden (Fig.5.1.). Nielsen and Schovsbo (2006) considered the Estonian and Russian Tremadocian black shale to be a shallow-water tongue of the Alum Shale of Sweden, a major uranium resource for Europe. In Estonia, the Turisalu shale occurs within a tectonically and hydrothermally undisturbed lower Palaeozoic sedimentary sequence (Fig. 5.2.). Its distribution in Estonia and Russia has been considered one of the best examples of shallow marine near-shore Cambrian and Early Ordovician siliciclastic deposits (Kaljo et al., 1986; Mens and Pirrus, 1997).

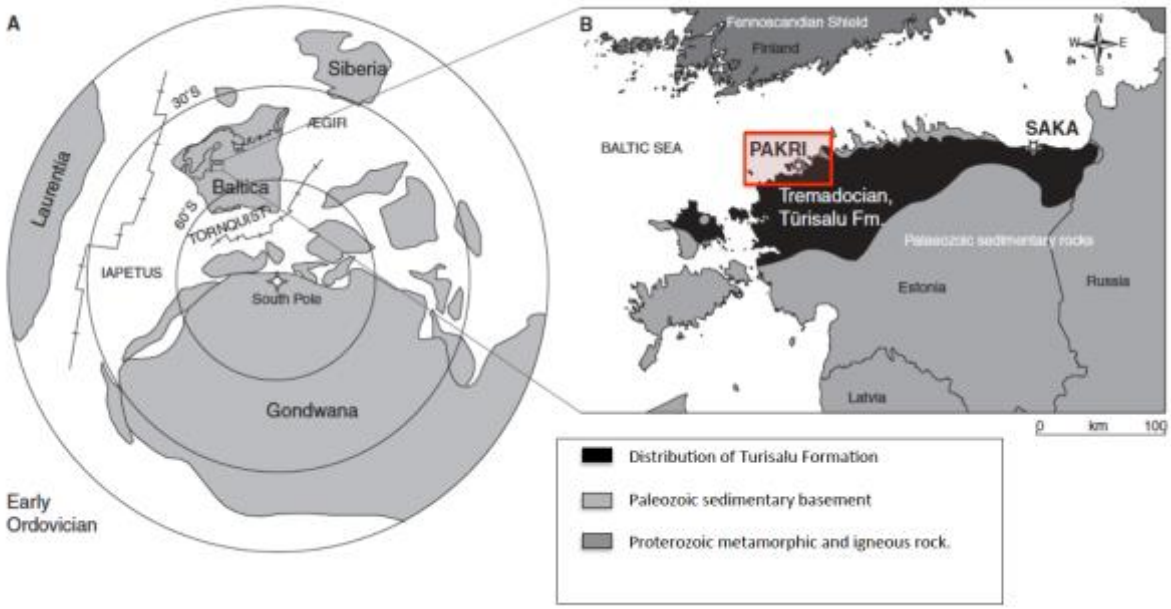

Figure 5.1. Map of paleogeography of Baltica during the Early Ordovician; insert shows the distribution of the Turisalu shale across Estonia and locations visited. Adapted from Nielsen and Schovsbo (2011).

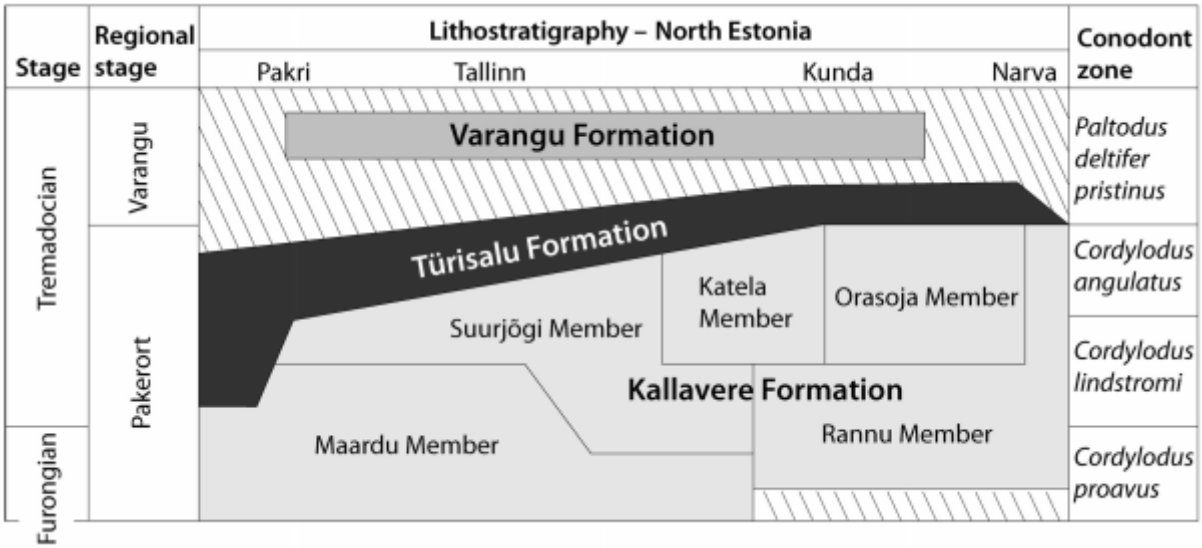

Figure 5.2. Time-space distribution of Upper-Cambrian and Ordovician sediments across Estonia (after Heinsalu et al., 2003; Nielsen, and Schovsbo, 2006).

Carbon isotope excursions and sea level variation during the Cambrian-Ordovician

Worldwide, ^{13}C- isotope excursions recorded during the Paleozoic appear to represent a transition between the large fluctuations observed in the Neoproterozoic and the more stable Mesozoic and Cenozoic periods. A composite $\delta^{13}C$ curve for the Lower Paleozoic exhibits many excursions, some with peaks of 7‰ (Kump et al., 1999; Saltzman et al., 2000, 2005; Sial et al., 2013; Figure 5.3). These are comparable in amplitude to Neoproterozoic values but are shorter in duration (i.e. ~3-5 Myrs). A large, positive $\delta^{13}C$ excursion in Upper Cambrian (Steptoean age) carbonates has been reported from Kazakhstan, Australia, China and North America and is coeval with the start of a global extinction of many trilobite species. The Steptoean Positive Isotope Excursion (SPICE; Saltzman et al., 1998, 2000) represents a large-scale perturbation in the carbon cycle at ~495 Ma (Furongian Epoch) and is believed to have lasted for ~3-4 Myr. Following this is a pronounced negative excursion (SNICE) (Sial et al., 2008). Throughout the Ordovician, multiple carbon isotope excursions are reported, especially from the mid-upper Ordovician. These have been linked to glaciations that altered the CO_2 budget in the atmosphere (Sial et al., 2013). The Late Cambrian- Early Ordovician isotopic shifts are enigmatic as there is no evidence of glaciation and a general lack of consensus as to the cause. Many authors agree that the period of isotopic enrichment corresponds to a major rise in sea level and suggest that tectonic factors may be an exerting influence, however the exact process remains unclear (Saltzman et al., 2000, 2004; Sial et al., 2013, Dahl et al., 2014). In addition, the period of the SPICE event and sea level rise appears to correspond with the mass extinction of a variety of shallow water trilobite species (Saltzman et al., 2000) suggesting that there are complex interplays between potential geodynamic drivers, sea level rise and changes the biological and geochemical cycles. This study addresses the presence of similar carbon isotope anomalies in the Pakri section and to what extent this event may have influenced the depositional environment and metal enrichment of the overlying Turisalu Formation, as well the implications for other similar settings globally.

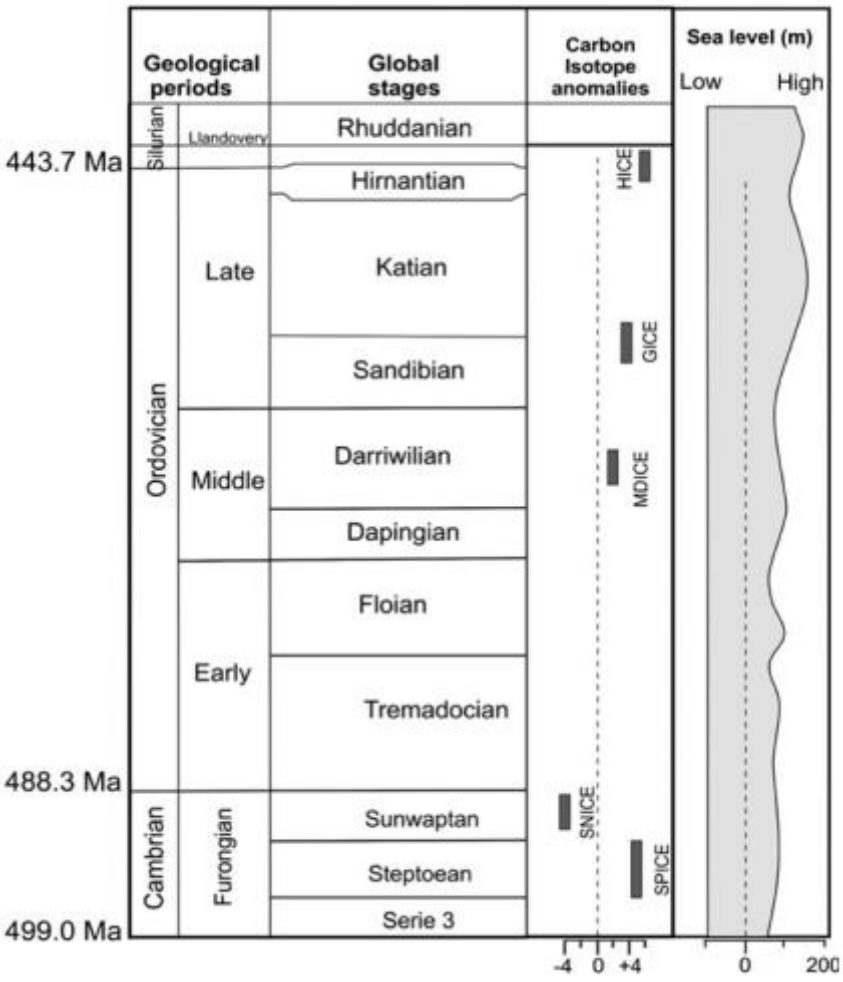

Figure 5.3. Summary of Cambrian and Ordovician carbon isotope excursions and sea level variations. Adapted from Sial et al. (2013).

5.2.4. Description of main rock units and their geological context

A series of localities that contain lower and upper contacts of the Ordovician Turisalu shale were visited and sampled. The focus was in the Pakri Cape region, NW Estonia (59 376 N, 24 036 E) as it exhibited the best exposure and the complete stratigraphy of the Lower Cambrian and through the Ordovician. This area was re-logged in detail and sampled at a high-resolution in order to fully integrate the nature of the depositional environment and to combine the field observations outlined here with the previous work on regional sea-level reconstructions and depositional models (Fig. 5.4 and appendix A1.).

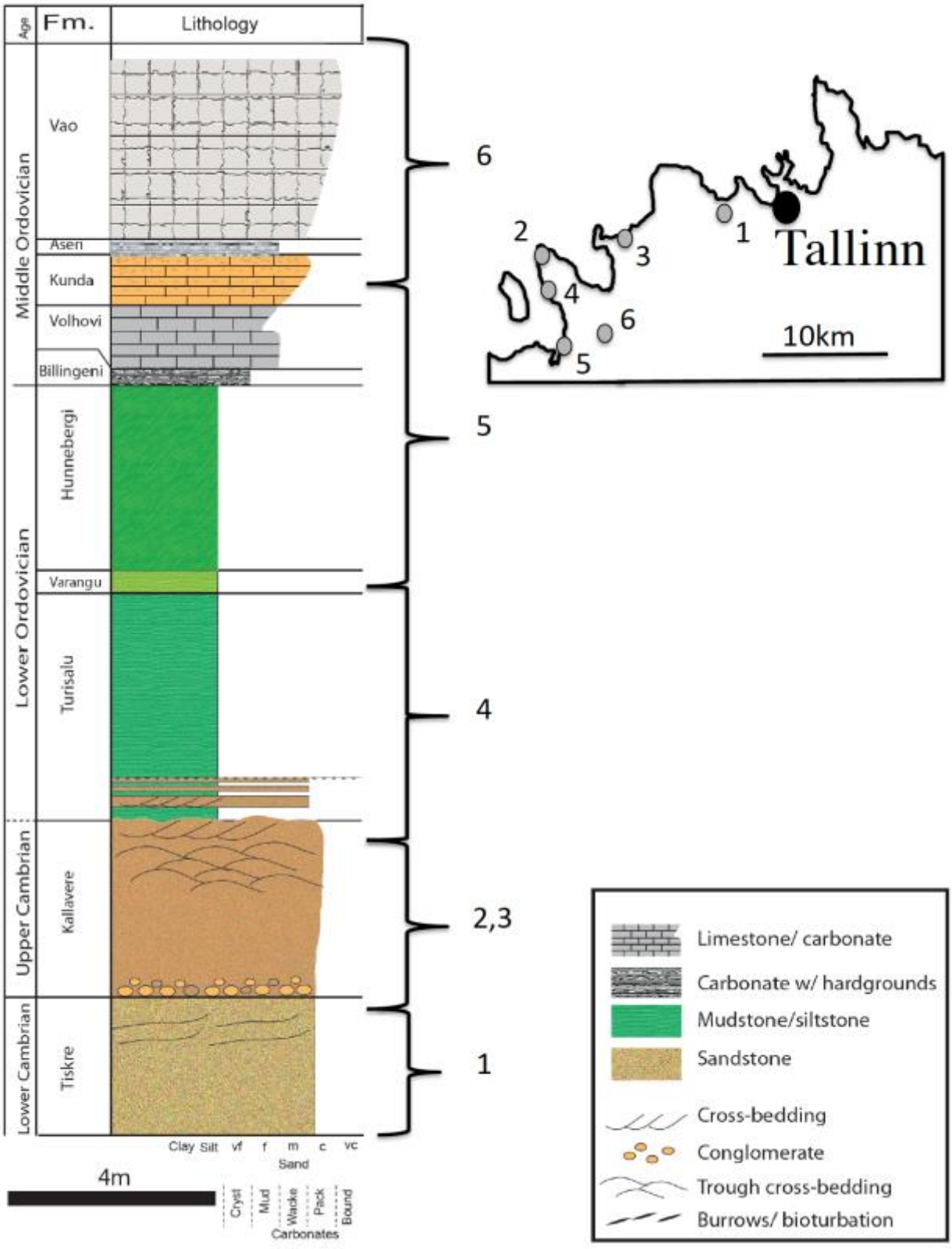

Figure 5.4. Composite stratigraphy from sites across the Pakri Peninsula. The full section is present in the Uuga Cliff at site 4, but only the upper Kallavere to the base of the Hunnenberg was accessible at that locality.

Furongian (upper Cambrian)–Lower Ordovician

Pakerort Stage.

In the Pakri Cape region, the Pakerort Stage is represented by the Kallavere Formation (~ 4 m thick) and the overlying black shale (Turisalu Formation) over a total thickness of ~ 8.05m.

The lower boundary of the Kallavere Formation varies over m-scale across the area. In several localities (i.e. Nemliher and Puura 1996, Fig.5.4. Sites 2 and 3), it is marked by distinct erosional surface featuring m-scale lenses of matrix supported conglomerate, incorporating pebbles of different maturation and sources (Nemliher and Puura 1996) as well as boulders from the underlying Tiskre Formation (Fig. 5.5).

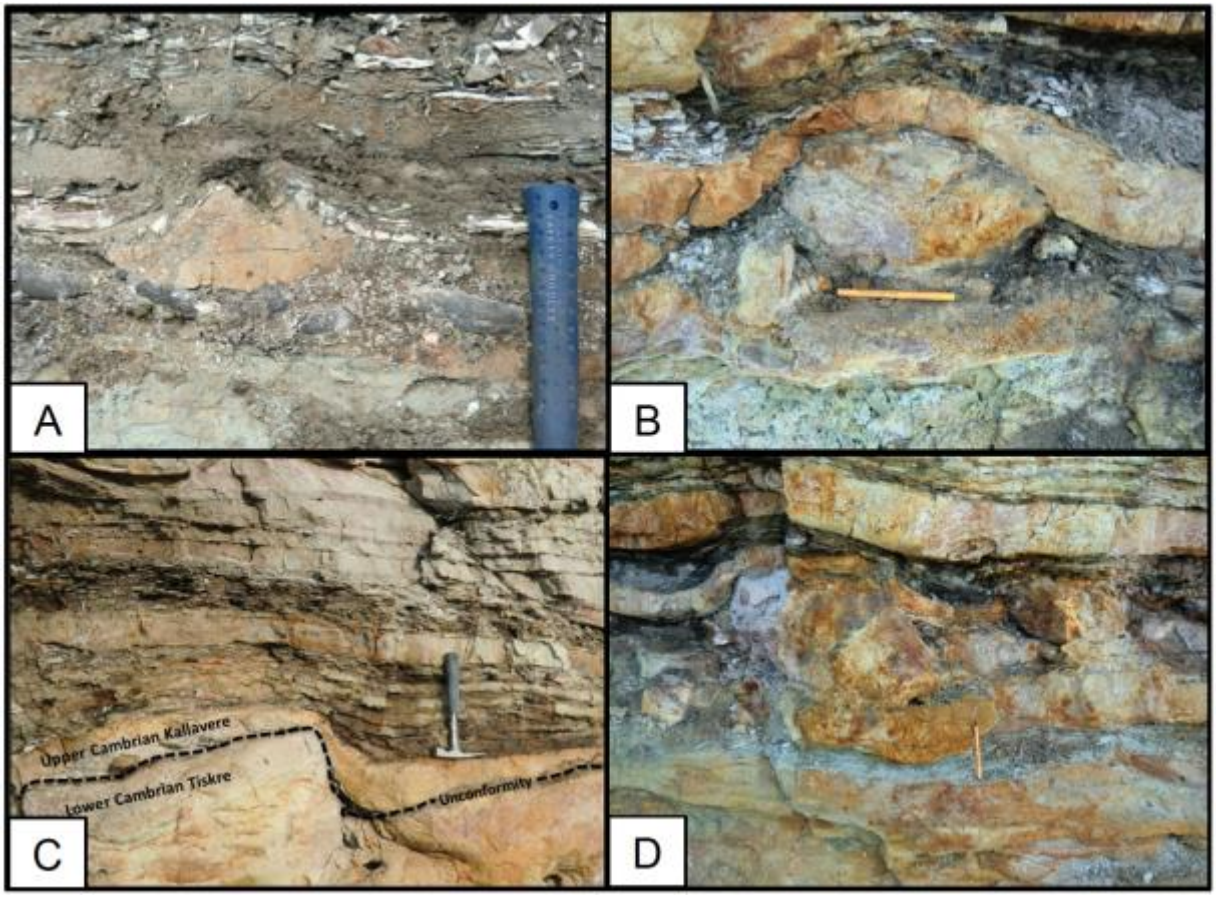

Figure 5.5. Pictures of the Basal Conglomerate at the base of the Kallavere Formation at Pakri. (A) Flattened pyrite-rich sandstone pebbles are found in parts of the conglomerate (B) A boulder of the underlying Tiskre Formation (pencil for scale). (C) The unconformity between the Lower Cambrian Tiskre Formation and the Upper Cambrian Basal Conglomerate. (D) A boulder of underlying Tiskre composition showing the disruption of the overlying sand and shale beds (pencil for scale).

The Upper-Cambrian Kallavere Formation is a mature, phosphatic biograinstone with minor organic carbon content with increasing pyrite content towards the top (Fig. 5.6.). The high phosphate content is a result of the accumulation of apatite shell debris of phosphatic lingula brachiopods, denoting a large-scale skeletal phosphorite accumulation episode during the Late Cambrian (Ilyin and Heinsalu 1990). This phosphogenic event appears in other Late Cambrian units such as in the Georgia Basin in Australia (Southgate and Shergold, 1991), which has been interpreted to be a result of a sea-level transgression that promoted upwelling towards the near shore environment. Lateral variations in shell concentration,

and therefore phosphate content, support the idea that the Kallavere enrichments are also likely a result of coastal upwelling during the early Palaeozoic, creating favourable conditions for lingula brachiopods (Southgate and Shergold, 1991).

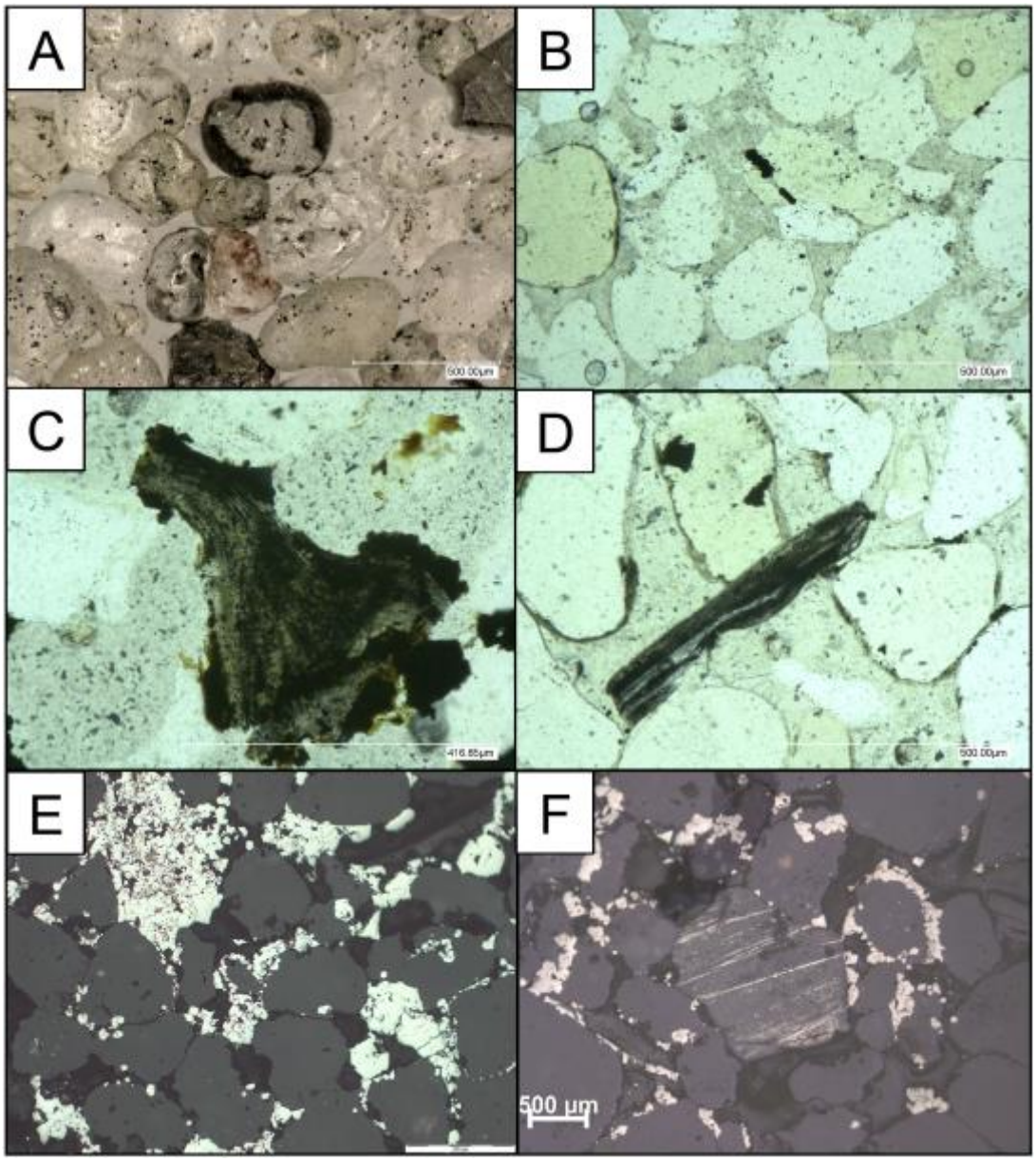

Figure 5.6. Photomicrographs of the phosphatic Kallavere sandstone. (A) Stereo-microscope image of the well-rounded quartz grains and calcite with green-black phosphate dispersed. (B) Transmitted light image of rounded quartz grains, with calcite cement and organic fragments. (C and D) Example of organic fragments and phosphate within the Kallavere. (E and F) Reflected light images of diagenetic pyrite clusters and agglomerates forming interstitial cement.

At Pakri Cape, the top of the Kallavere features a variety of decimetre-scale planar and trough cross beds sets and interbedded organic-rich shales and carbonate concretions which likely nucleated on shell debris (Fig. 5.7.). This horizon marks a depositional hiatus and transition in hydrodynamic regime, as the shale interbeds appear to infill the underlying topography. In this 'transition zone' pyrite content increases and tends to form an intergranular cement in the phosphatic biograinstones and appear as laminations in the shale.

The base of the Ordovician.

The *Cordylodus lindstromi* Biozone is the closest traceable level in Baltoscandia approximating the base of the Ordovician, defined by the first appearance of *Iapetognathus fluctivagus* in the GSSP in Green Point, Newfoundland (Puura and Viira 1999). Abundant, early graptolites encountered <0.7m up from the base of the shale indicate that this level in the Turisalu Formation can be assigned to the lower-most Ordovician (~488 Ma). This would suggest that the base of the transitional zone, representing a hiatus and on-lapping of organic-rich shale deposition, would correspond to upper-most Cambrian. The early planktic graptolites from this section have been studied by Kaljo et al. (1986) as Rhabdinopora sp. suggesting that these represent an inner-shelf setting. The interbeds of black shale within the Kallavere exhibit mm-scale burrows and microbial mat features suggesting that the biological activity was prolific during this time (Fig. 5.7.).

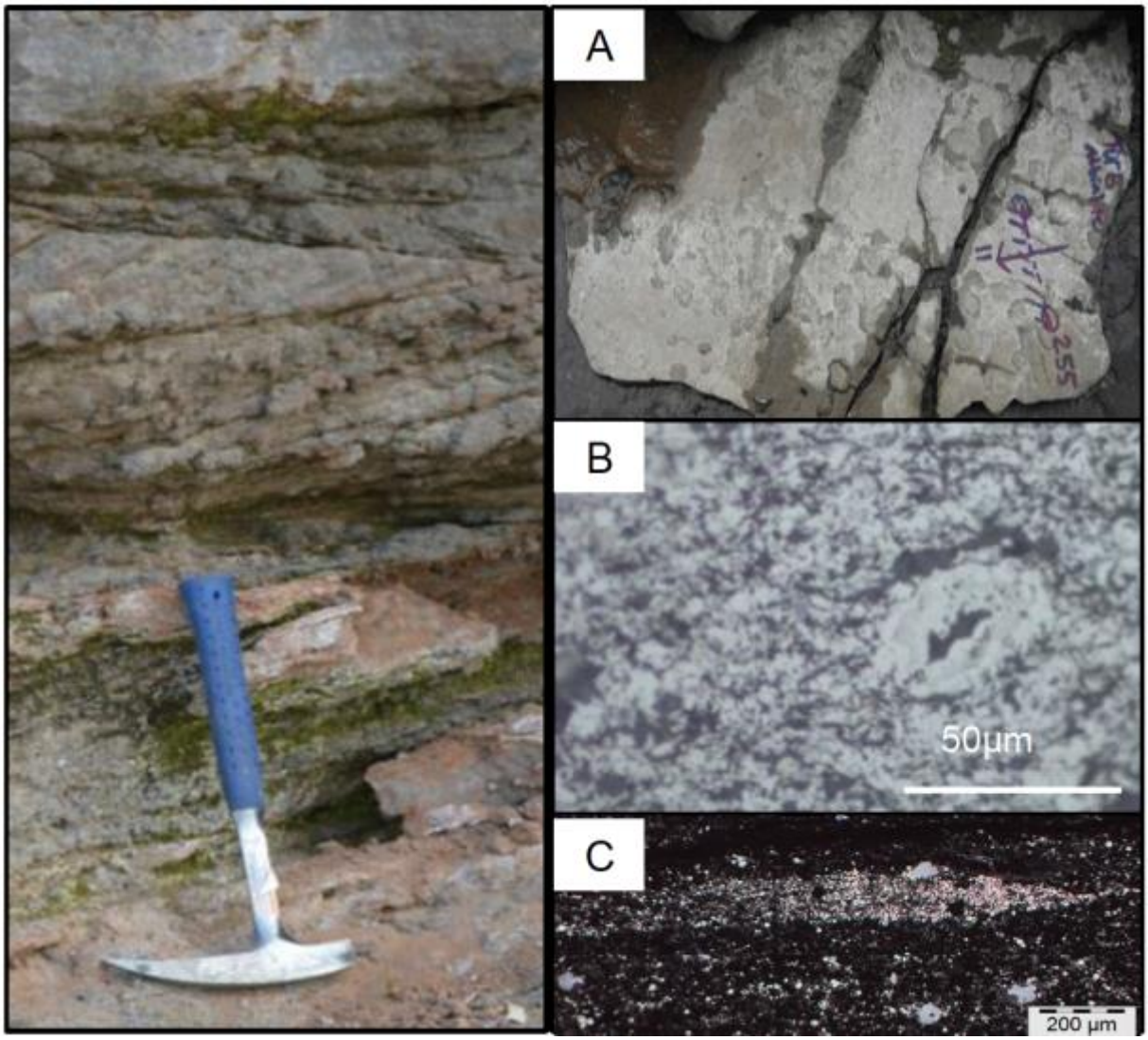

Figure 5.7. Cross bed sets from the upper Kallavere, moving into the transition zone (Site 2, Fig. 5.4). (A) Pyritised microbialite (field of view ~15cm) from the uppermost shale interbed in the transition zone. (B) Reflected light image of the microbialite showing pyrite forming "mounds" and filamentous textures. (C) Cluster and disseminated fine pyrite frambiods in Turisalu Shale (PAK-SHL-5).

The black shale of the Turisalu Formation itself contains fossilised fragments of early planktonic graptolites (Nielsen and Schovsbo, 2011). Fine silt and clay dominates the mineral assemblage along with variable pyrite abundance (~ 2 to 8% and up to 10% in one sample) and is enriched in organic matter. The internal structure of the Turisalu black shale shows a general change from fine, mm-scale lamination, which dominates the lower part to massive fabrics towards the top. According to

Baltoscandian sea level reconstruction of Nielsen (2004), the initial Early Ordovician transgression, which reached its maximum during the interval of Rhabdinopora sp. Biozone (lower part of the Pakerort Stage), was followed by shallowing and then by more moderate sea level rise, which reached a peak during the 'Kiaerograptus Drowning Event' (equivalent to the lower Varangu Stage; Nielsen and Schovsbo, 2011; Nielsen, 2004). Therefore, it is conceivable that the shift from laminated to a more massive character observed in the Turisalu shale can be explained by such a change in relative sea level or a change in environment that may have promoted bioturbation. The upper boundary of the Turisalu Formation comprises a regional unconformity that is capped by organic-poor grey shales or fine, glauconitic sands (Heinsalu, 1980) and marks a sea-level drop that terminated organic-rich mud accumulation in the proximal settings of the Baltic palaeobasin (Ainsaar et al., 2004, Nılvak et al., 2006; Nielsen and Schovsbo, 2011).

Lower Ordovician

Varangu Stage

In the Uuga Cliff section at Pakri Cape (Fig. 5.4, Site 4), the Varangu Stage is represented by a 35cm thick, poorly consolidated, greenish-grey clay and silty-sandstone with abundant glauconite grains.

Hunneberg Stage

In the Pakri Peninsula, the Hunneberg Stage reaches its maximum thickness of 3.9m. This is represented by greenish-grey fine-grained glauconitic sandstone, with intercalations of light grey clay. Both the Varangu and Hunneberg represent deposition in near shore, shallow-water settings.

Billingen Stage

A 35cm thick greenish-grey glauconitic silty-sandstone which is replaced upwards by calcareous silty-sandstones and glauconitic packstone. Phosphatized burrows (3-10 cm in length) are accumulated within very narrow stratigraphic intervals in the upper part of the lower sandstone layer. The presence of glauconite in both of these units suggests these sediments were deposited on a shallow shelf environment under slow accumulation rates and reducing conditions (Chafetz and Reid, 2000).

Middle Ordovician

The carbonates, mainly packstones and wackestones are interpreted to have formed in a temperate climate with low sedimentation rates on a shallow ramp environment; this is in agreement with Nestor and Einasto (1997). The following brief description of the Middle Ordovician units in the Pakri Peninsula is given after Einasto and Mens (1996).

Volkhov Stage

Volkhov Stage is represented by a 1.3m thick, light grey limestone, with intercalations of marls, with glauconite grains. The lower boundary is marked by a distinct discontinuity surface.

Kunda Stage

The Kunda Stage is represented by the ~ 1m thick "kukersite"-containing sandy limestone and limy sandstone (Einasto and Mens, 1996). The rocks of the Kunda are often brecciated towards the top and penetrated by limy-sandstone injections and small burrows.

The uppermost 0.1 m is represented by light grey fine-grained limestone with multiple, phosphatic discontinuity surfaces, interpreted as hard grounds. The upper boundary is marked by an even discontinuity surface, a calcitic hardground with deep (cm-scale) vertical burrows.

Aseri Stage

A 0.2m thick argillaceous, oolitic-limestone with intercalations of marl and ooiids. This horizon represents near-shore tractional depositional processes.

Lasnamagi Stage

Brownish-grey, 2.4m thick, dolomitic, thin to medium-bedded limestone. This unit likely represents deposition within a shallow-water shelf, where relative sea level was higher that during the deposition of the Aseri Stage sediments.

Uhaku Stage

A ~2m thick, packstone limestone with numerous discontinuity surfaces, increasing in frequency upwards. This suggests shallow-water deposition with discrete discontinuity surfaces likely representing moderate variation in relative sea level.

5.2.5. Methodology

Sample collection

A total of 42 samples were collected in order to understand the geochemical conditions present during the time of shale deposition and establish a context for the periods prior to sedimentation and after. Particular emphasis was placed on samples from the Turisalu shale and shale interbeds which were sampled at a high resolution (~ 30cm spacing over 4.5m).

Whole-rock geochemistry

The shale samples were crushed and milled to a fine powder. From these, fusion discs were prepared using the procedure outlined in Robinson (2003) and then analysed for major and trace elements using a PANalytical Axios Advanced X-Ray Spectrometer. Corrections for mass absorption are calculated using PANalytical Super-Q software with its calibration model and alpha coefficients. In house inter-element corrections are also applied. Calibration was conducted using pure element oxide mixes in pure silica, along with international and internal references (Yu et al., 2001; Robinson, 2003).

Carbon and sulfur %

Aliquots of the homogenized material were analysed on an Eltra 2000 C/S analyser. This system allows for simultaneous carbon and sulfur analysis down to the ppm level. The instrument was optimized daily and standards were run every 15 samples to correct for drift. Accuracy and reproducibility, based on international and internal standards was better than 0.05 wt% and 0.1 wt%, respectively. Total carbon and sulfur were analysed first and then TOC % was conducted separately on subsamples which were pre-treated using 6N HCl on a hotplate at 60°C for 24 hours to promote the dissolution of carbonate and the production of CO_2. Inorganic carbon values were obtained by calculating the difference (i.e. total carbon – organic carbon).

Isotope geochemistry

Powdered whole-rock samples were used for $\delta^{13}C$ analysis at the Central Science Laboratory, University of Tasmania. The $\delta^{13}C_{carb}$ component was derived via phosphoric acid treatment (100% H_3PO_4, 50 °C, 24h). The evolved CO_2 is then purified by means of subsequent cold traps (N_2 liq. -196°C and acetone/CO_2 -94 °C) to remove non-condensable reaction by-products and then analyzed using a dual inlet VG Optima. The analytical uncertainty this measurement was less than 0.05‰. Reproducibility based on full duplicate analyses and internal and international standards was better than 0.4‰. The $\delta^{13}C_{org}$ component was derived using the same method as outlined for TOC%, in order to evolve inorganic carbon species and then analysed using an Isoprime 100 PyroCube at the Central Science Laboratory, University of Tasmania.

Some samples (such as the black shales) did not produce enough CO_2 to measure their inorganic component, despite using a large sample amount. The reverse situation occurred for some of the organic lean limestone units with respect to $\delta^{13}C_{org}$.

Sulfur isotope analysis of micro-drilled samples was conducted using an Isoprime 100 PyroCube at the Central Science Laboratory, University of Tasmania and in-situ laser combustion of pyrite was conducted at the N.E.R.C. Isotope Community Support Facility in the Scottish Universities Environmental Research Centre, using the procedure outlined in Kelly and Fallick (1990) and Wagner et al. (2002). Reproducibility based on full duplicate analyses and internal and international standards was better than 0.3‰.

LA-ICP-MS analysis of pyrite

A 2.5 cm-round polished mount was produced, allowing for the petrographic examination using reflected light and then laser ablation of the material. All laser ablation analyses were obtained using a New Wave 193 nm Nd-YAG solid-state laser microprobe coupled to an Agilent 7700 quadrupole ICP-MS. The technique is described in detail by Danyushevsky et al. (2011), and Large et al. (2014). A synopsis and further discussion is provided in the appendix.

5.2.6. Results

Isotope geochemistry

δ^{34}Sulfur

The high-resolution dataset of $\delta^{34}S$ of pyrite compiled here shows distinct variations through the stratigraphy, particularly, in the Lower Ordovician near the boundary with the Cambrian (Fig. 5.8). In a broad sense, four groupings can be made: 1) the foreshore to shallow marine Cambrian Tiskre formation exhibit values of ~24‰. 2) The upper section of the Kallavere, within the interbedded zone exhibit a wide range in $\delta^{34}S$ values ranging from -24‰ to 18‰. 3) The Turisalu black shale exhibits strongly negative $\delta^{34}S$ values (-7 to -30‰). They are most negative and variable in the basal section of the shale and shale interbeds, becoming more clustered above this horizon. 4) Values in upper units of the Lower Ordovician and Middle Ordovician that range from ~ 0 to 15‰.

δ^{13}Carbon

Whole rock samples were analysed for $\delta^{13}C_{carb}$ and $\delta^{13}C_{org}$ isotopes (Fig. 5.8.). The aim was to have corresponding values for each sample however some samples contained not enough inorganic or organic carbon for accurate measurement.

Positive values in $\delta^{13}C$ isotopes (up to +5‰, $\delta^{13}C_{carb}$) was measured in two biograinstone samples from the Upper Kallavere and from the first biograinstone interbed of the transition zone, at the base of the Turisalu Formation. These measurements were repeated in order to confirm their values and were within error of the initial measurements. The $\delta^{13}C_{org}$ values range from between -15 to -30‰ $\delta^{13}C_{org}$ in the lowermost section of the shale, in the interbedded horizon, and between -24 to -29‰ $\delta^{13}C_{org}$ for the rest of the shale sequence. $\delta^{13}C_{carb}$ and $\delta^{13}C_{org}$ values both show similar patterns and maintain a constant fractionation of ~25-28‰ from the carbonate-hosted carbon throughout most of the sequence. Two intervals in the Mid-Ordovician units have minor increases in $\delta^{13}C_{carb,}$ (+3‰, +2.5‰ respectively).

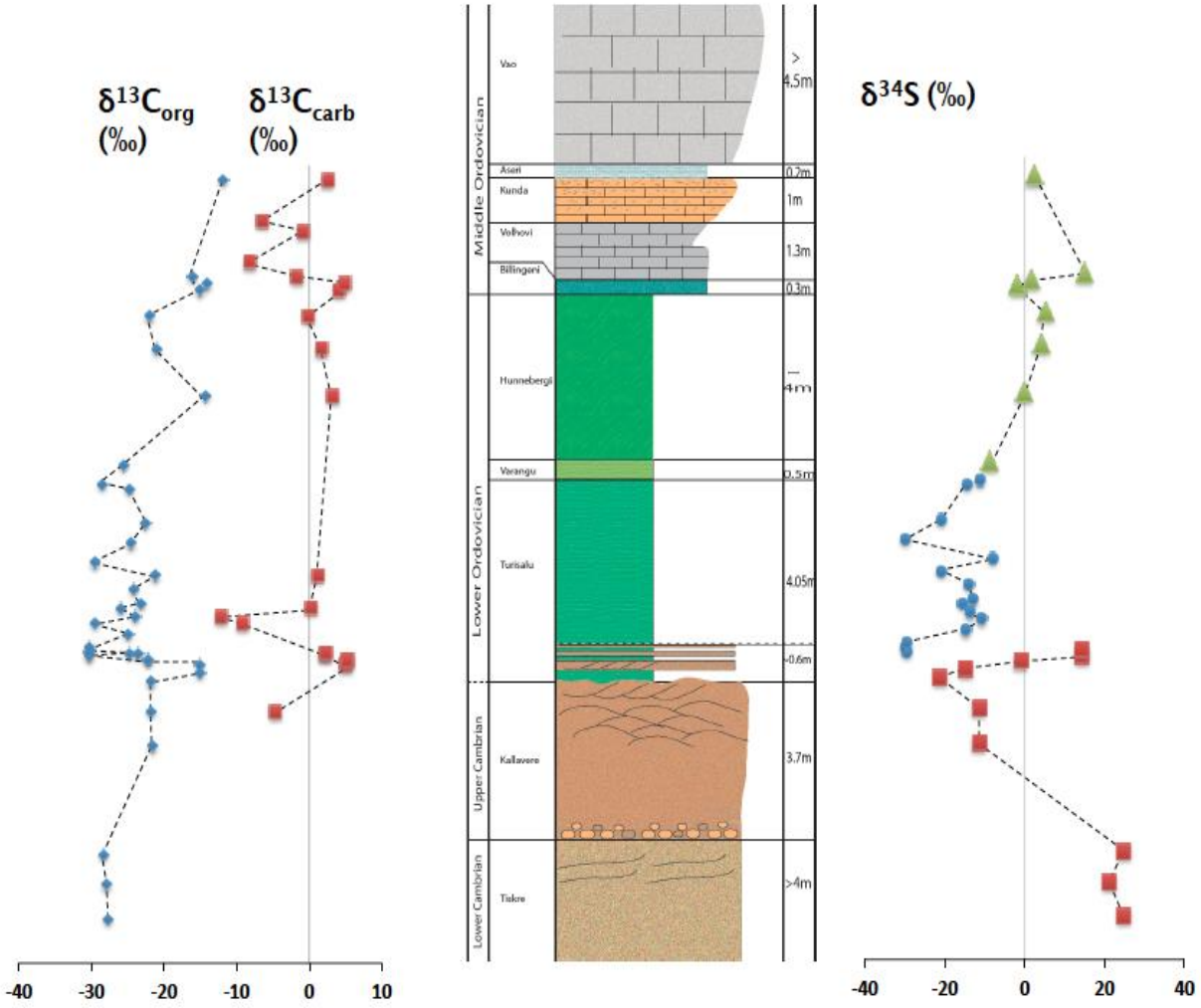

Figure 5.8. Carbon and sulfur isotope profiles through stratigraphy. In the sulfur profile, squares signifies pyrite (grains/ nodules) in the Kallavere and Tiskre, diamonds signify the Turisalua shale and triangles denote pyrite in the rest of the section.

metres through section	Formation	$\delta^{34}S_{Py}$	$\delta^{13}C_{Org}$	$\delta^{13}C_{Calc}$
2	Tiskre	25.0	-27.7	
2.8	Tiskre	21.3	-27.9	
3.5	Tiskre	24.9	-28.2	
6	Kallavere	-11.2	-21.5	
6.8	Kallavere	-11.2	-21.7	-4.68
7.5	Kallavere	-21.2	-21.7	
7.7	Kallavere	-14.6	-15.0	
7.9	Kallavere (Upper)	-0.8	-15.1	5.07
8	Kallevere/Turisalu trasnistion (Interbed)	14.5	-22.2	5.30
8 (Rpt)	Kallevere/Turisalu trasnistion (Interbed)			5.21
8.15	Kallevere/Turisalu trasnistion (Interbed)	14.4	-24.7	2.34
8.15 (Rpt)	Kallevere/Turisalu trasnistion (Interbed)			2.26
8.1	Turisalu	-29.5	-30.1	
8.2	Turisalu	-29.6	-30.3	
8.3	Turisalu	-29.5	-30.2	
8.6	Turisalu	-14.5	-24.8	
8.85	Turisalu	-10.5	-29.5	-9.1
9	Turisalu	-13.5	-23.8	-12.1
9.2	Turisalu	-15.6	-26.0	0.2
9.3	Turisalu	-12.9	-23.2	
9.65	Turisalu	-13.8	-24.1	
9.95	Turisalu	-20.6	-21.1	1.2
10.25	Turisalu	-7.8	-29.5	
10.7	Turisalu	-29.7	-24.5	
11.15	Turisalu	-20.6	-22.5	
11.95	Turisalu	-14.2	-24.6	
12.05	Turisalu	-11.2	-28.4	
12.5	Varangu	-8.7	-25.6	
14.1	Hunnebergi	-0.1	-14.3	3.2
15.2	Hunnebergi	4.2	-20.9	1.7
15.95	Hunnebergi	5.3	-21.9	-0.1
16.55	Billingeni	-1.6	-15.0	4.2
16.7	Billingeni	1.7	-14.0	4.9
16.85	Billingeni	15.0	-16.1	-1.6
17.2	Volhovi			-8.1
17.9	Volhovi			-0.8
18.15	Volhovi			-6.4
19.1	Kunda	2.6	-11.8	2.6

Table 5.1. Sulfur and carbon isotope values through stratigraphy.

Whole rock geochemistry

A wide variety of trace elements are elevated in the Turisalu Shale and have wide variation through the stratigraphy (Fig. 5.9, Table 5.2.). U, V, Ni, Zn, Cu, Se, Mo, Pb, Co, and As are all elevated (up to orders of magnitude) compared to global average shale (WSA; Wedepohl, 1995 and SDO-1; Hyuck, 1989). Element profiles (Fig. 5.9.) show enrichment factors compared to the world shale average (WSA) and normalized to aluminium (i.e. (element $_{sample}$ / Al $_{sample}$) / (element $_{WSA}$ / Al $_{WSA}$) = EF*).

Zinc makes a notable increase (EF*= 22) in the lowermost 1m of the shale at the same level as other trace element and a significant change in the isotopic values of $\delta^{34}S$ and $\delta^{13}C_{org}$. This occurs just above the interbedded horizon of the transition zone. Nickel, uranium and vanadium also exhibit their highest enrichments at this interval, though they also remain comparatively enriched throughout most of the section. Copper and molybdenum are at their highest (Cu EF*= 8 and Mo EF*= 367) in the first shale interbed and decrease up sequence.

The profiles of sulphur, Se and As are similar, exhibiting a decrease after 1m and then attaining their highest concentrations at 3.1m, phosphorous also shows a similar pattern. Barium remains constant through the shale, while cobalt becomes more enriched towards the top of the shale reaching a maximum EF* of 58. Uranium, vanadium and TOC appear to correlate (Fig. 5.10.) and all decrease up section

		% SiO_2	TiO_2	Al_2O_3	Fe_2O_3	MnO	MgO	CaO	Na_2O	K_2O	P_2O_5	TOC (%)	S (%)
SDO-1		**49.3**	**0.71**	**12.3**	**9.3**	**0.042**	**1.50**	**1.10**	**0.40**	**3.40**	**0.11**	**9.9**	**5.4**
WSA		**64.0**	**0.84**	**18.0**	**7.4**	**0.107**	**2.72**	**2.39**	**0.87**	**3.48**	**0.18**	**…..**	**…..**
Sample Pakri Cape	**m (up section from onlapping contact)**												
SHL 1	**0.1**	47.0	0.72	12.1	4.1	<DL	0.58	0.05	0.10	7.43	0.07	14	3
SHL 2	**0.2**	47.9	0.68	12.8	4.6	0.019	1.17	0.21	0.12	7.52	0.18	13	2
SHL 3	**0.3**	45.7	0.69	12.8	4.6	0.020	1.26	0.16	0.10	7.32	0.11	15	2
SHL 5	**0.6**	49.6	0.71	12.7	5.3	0.020	1.18	0.24	0.08	7.57	0.10	12	3
SHL 8	**1**	46.9	0.69	12.3	5.2	0.019	1.18	0.33	0.08	7.15	0.10	13	3
SHL 9	**1.2**	46.5	0.68	12.0	6.1	0.019	1.13	0.27	0.08	7.11	0.11	14	4
SHL 10	**1.3**	48.3	0.74	12.5	4.6	0.019	1.18	0.28	0.08	7.26	0.11	13	3
SHL 11	**1.65**	47.9	0.70	12.6	4.8	0.019	1.14	0.20	0.08	7.43	0.09	14	3
SHL 12A	**1.95**	49.1	0.70	12.2	4.9	0.018	1.07	0.29	0.08	7.35	0.14	13	3
SHL 12B	**2.7**	50.9	0.77	12.9	4.8	0.019	1.17	0.32	0.09	7.64	0.16	10	3
SHL 13	**3.15**	47.9	0.67	11.4	6.8	0.013	0.84	0.34	0.08	7.03	0.07	10	4
SHL 14	**3.95**	52.8	0.72	11.7	4.2	0.014	0.90	0.22	0.09	7.13	0.06	8	2
SHL 15	**4.05**	50.4	0.77	12.6	5.1	0.014	0.92	0.03	0.09	7.73	0.10	10	3
Detection Limits (%)	**0.01**	**0.01**	**0.01**	**0.01**	**0.01**	**0.01**	**0.01**	**0.01**	**0.01**	**0.01**	**0.01**	**2 ppm**	**4 ppm**

		ppm																							
		Sc	Ba	V	Cr	Co	Ni	Cu	Zn	Se	As	Rb	Y	Zr	Mo	Pb	U	Th	La	Ce	Nd
SDO-1		**15**	**397**	**160**	**66**	**47**	**100**	**60**	**64**	**.....**	**69**	**125**	**.....**	**165**	**134**	**28**	**49**	**.....**	**.....**	**.....**	**.....**
WSA		**13**	**580**	**130**	**90**	**19**	**50**	**45**	**95**	**0.6**	**13**	**140**	**26**	**160**	**3**	**20**	**3**	**12**	**.....**	**.....**	**.....**
Sample Pakri Cape	**m**																				
SHL 1	**0.1**	18	466	1,377	80	204	229	295	18	3.6	72	131	13	161	739	118	80	22	37	44	16
SHL 2	**0.2**	12	453	1,400	84	190	210	125	41	3.1	48	141	41	164	457	106	80	16	47	85	48
SHL 3	**0.3**	13	468	1,539	91	76.7	208	135	38	3.4	54	147	23	147	560	104	91	16	41	52	23
SHL 5	**0.6**	13	455	1,183	80	180	330	115	47	4.1	62	135	30	153	164	116	67	14	41	68	34
SHL 8	**1**	15	437	1,434	91	135	426	151	1,633	3.9	55	135	40	148	181	149	89	16	43	72	37
SHL 9	**1.2**	14	447	1,313	83	52	324	136	1,651	4.2	64	132	34	148	192	142	98	16	45	72	39
SHL 10	**1.3**	15	455	1,550	95	81	307	123	51	3.8	57	139	33	163	171	110	122	16	48	78	36
SHL 11	**1.65**	14	442	1,010	91	82	299	165	55	3.4	50	138	34	152	108	159	67	16	47	78	42
SHL 12A	**1.95**	14	428	813	92	194	336	137	49	3.2	50	131	44	161	94	125	47	17	48	88	48
SHL 12B	**2.7**	15	431	1,215	105	124	411	127	49	4.6	54	136	48	180	78	120	65	18	60	113	65
SHL 13	**3.15**	11	415	1,006	80	173	126	57	31	5.4	80	130	15	161	155	162	30	9	36	45	15
SHL 14	**3.95**	12	403	695	82	834	80	60	40	3.2	60	125	16	190	71	99	21	11	31	46	17
SHL 15	**4.05**	13	452	822	91	713	120	106	37	3.3	67	137	14	171	109	76	51	15	35	45	12
D.L (ppm)		**1.5**	**4**	**3**	**1**	**1.5**	**4**	**3**	**1**	**1**	**1**	**1**	**3**	**2**	**0.5**	**1**	**1**	**0.5**	**1**	**2**	**2**

Table 5.2. Whole-rock geochemistry of the Turisalu shale and comparison with shale standards.

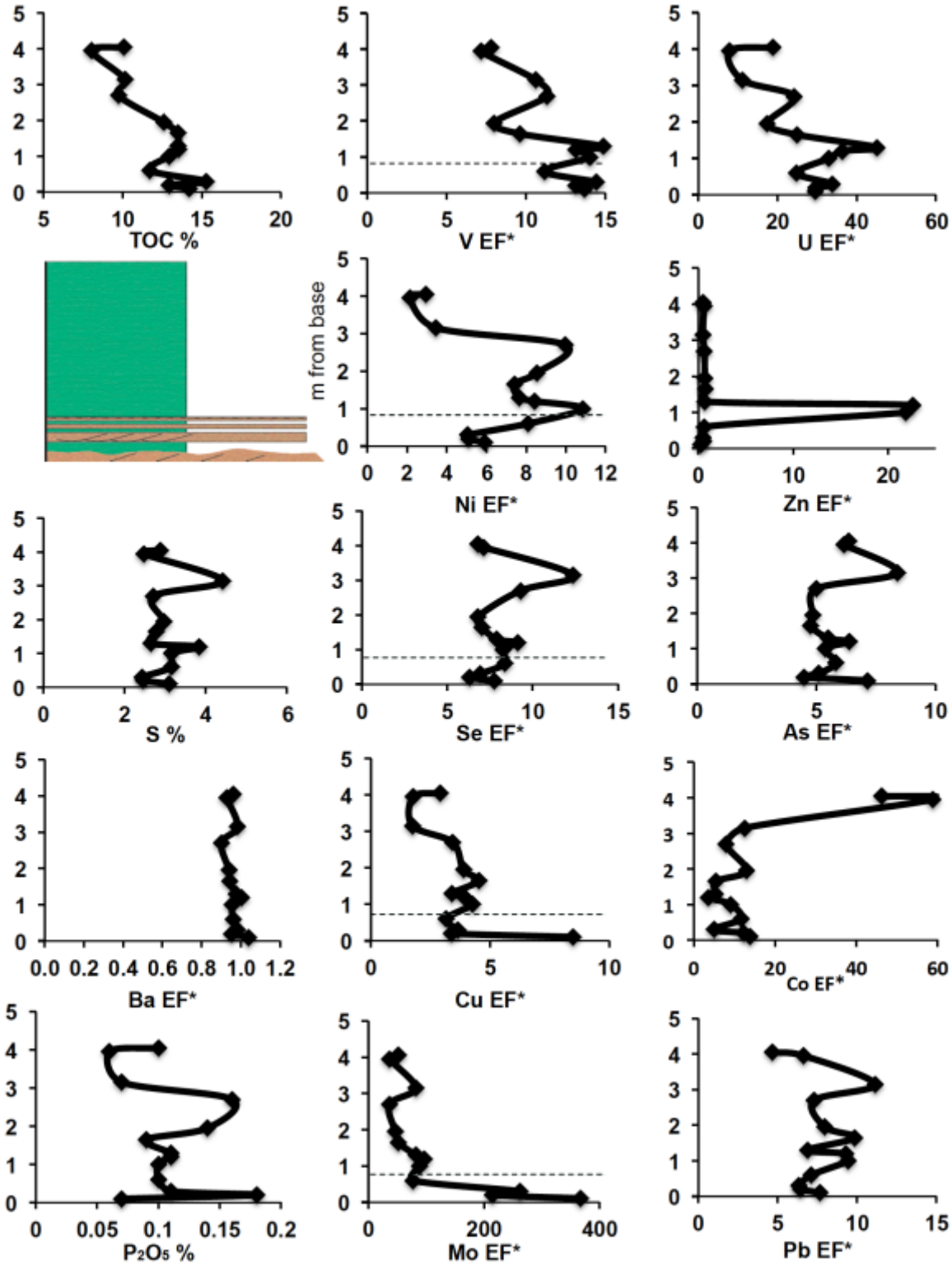

Figure 5.9. Plots of selected trace element enrichments, through the Turisalu shale. Dashed line marks the boundary between the transition zone and Turisalu proper.

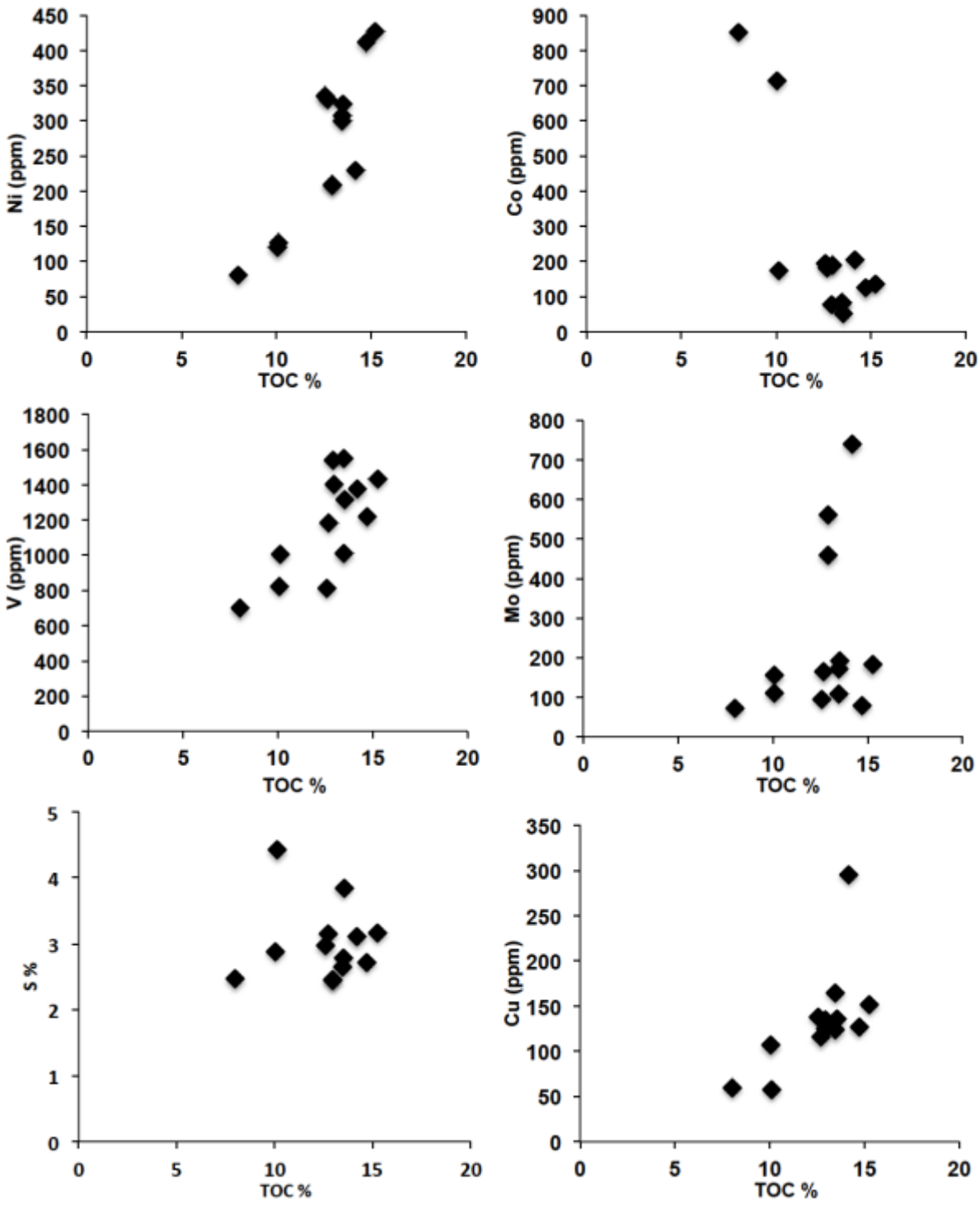

Figure 5.10. Selected paleo-environment indicator elements plotted against total organic carbon.

Pyrite trace element geochemistry

Many paleo-ocean studies have investigated the whole rock TE composition of black shales as a proxy for trace elements (TE) of the ocean in which they were deposited (i.e. Algeo and Maynard, 2004, Tribovillard et al., 2006). However, bulk concentrations in whole-rock shale samples represent mixed signals from terrigenous detrital material, organic matter and authigenic minerals formed during diagenesis. Sedimentary pyrite is formed either in euxinic water columns or shortly after deposition by the bio-mediated reaction of seawater sulfate with reactive iron, forming a monsulfide precursor, and then pyrite (Rickard, 2012). Pyrite has the ability to incorporate many redox-sensitive trace metals during growth, meaning that the trace element content of the pyrite provides potential archive of first-order variations in trace metal content at the time of deposition. This technique has been applied by Berner (2013), Large et al. (2014, 2015), and Gregory et al. (2014; 2015) to show that trace element content of diagentic pyrite can be reflective of the nature of seawater chemistry at the time of formation. Large et al. (2014) showed that there is a positive relationship between TE in recent seafloor pyrite, and TE in the contemporary ocean.

Over 180 analyses of diagenetic pyrite from the Turisalu Shale were made using LA-ICP-MS, and from this data, four key observations can be made (Fig. 5.13):

1) Pyrite in the transition zone, where black shale occurs interbedded with biograinstones, is enriched in a range of trace elements. In some profiles the metal content begins to decrease through the transition zone or remain constant. Zinc, Se, Mo, Ni, As, Th, Co and Pb are recorded in their highest levels in this interval.

2) Pyrite in 1- 2.7m of the Turisalu Shale also displays high metal abundance (Ni, Se, Cu, Zn, Mo). While minor variation occurs (i.e. Se, Mo, Co, Cu) in this part of the shale, the concentrations remain, generally, constant.

3) The upper 1.0 to 1.5m of the shale shows an overall decrease in trace metal abundance in pyrite. This decrease is most prominent in the profiles for (Ni, Zn, Co, Cu, V and Mo). The decrease in metal content also corresponds stratigraphically to a shift in $\delta^{34}S$ and $\delta^{13}C$ isotopic values.

4) Overall, pyrite is enriched in key trace metals by orders of magnitude compared to whole-rock analysis (concentration factors, Table 5.3). The overall trend of the trace metals in pyrite (while variable between individual pyrites) mirrors that of the whole rock analysis, however with much greater sensitivity and resolution, whereby small variations in the element profiles can be discerned using the pyrite method (Fig. 5.11, A5.2). The exception to these is Co and Zn. Cobalt values in the pyrite remain relatively comparable with that of the whole-rock analyses in the lower portion of the shale (CF= ~1). The uppermost 1m of the shale displays a relative enrichment of Co in the whole-rock sample compared to pyrite (CF= 0.05). This level corresponds with a decrease in the majority of trace metals and TOC% and sulphur content. Zinc in the lowermost 1m, directly above the last biograinstone interbed is proportionally higher in whole-rock compared Zn content in pyrite (CF=0.4), this is may be due to minor fine-grained, diagenetic sphalerite formation or a higher proportion of Zn residing in another phase, likely organics. This horizon also marks the full establishment of black shale deposition and also corresponds with a change in the isotopic values with both $\delta^{34}S$ and $\delta^{13}C$ values becoming slightly more negative (for further discussion of this technique, and the data, the reader is referred to the appendix located at the end of this chapter).

No. analyses	Sample	Ni ppm	Co ppm	Cu ppm	Zn ppm	Cd ppm	As ppm	Se ppm	Mo ppm	Au ppm	Ag ppm	Mn ppm	Ba ppm	Pb ppm	Sb ppm	Metres
16	EST-SHL-1_Py Mean	**2372**	**202**	**2982**	**297**	**16**	**1192**	**234**	**8310**	**0.56**	**35**	**919**	**2842**	**993**	**547980**	**0.1**
	Std. Dev.	745	39	808	38	12	302	114	3286	0.76	16	294	1930	332	10717	
	W.R.	229	204	295	51	D.L.	72	4	739	n.d.	n.d.	132	466	118	30995	
	C.F.	**10**	**1**	**10**	**6**	***	**17**	**65**	**11**	***	***	**7**	**6**	**8**	**18**	
26	EST-SHL-3_Py Mean	**2618**	**197**	**3474**	**1045**	**7**	**1604**	**92**	**3856**	**0.15**	**63**	**2524**	**2931**	**1518**	**551982**	**0.3**
	Std. Dev.	891	71	975	597	9	834	60	1155	0.16	66	703	1219	323	31667	
	W.R.	208	77	135	38	n.d.	54	3	560	n.d.	n.d.	151	468	104	24316	
	C.F.	**12.6**	**2.6**	**25.7**	**27.9**	***	**29.5**	**27.0**	**6.9**	***	***	**16.7**	**6.3**	**14.6**	**22.7**	
15	EST-SHL-5_Py Mean	**2579**	**193**	**3537**	**1057**	**7**	**1626**	**90**	**3848**	**0.17**	**61**	**2547**	**3681**	**1555**	**558669**	**0.6**
	Std. Dev.	969	79	1787	743	9	629	50	1226	0.19	57	680	1516	518	24293	
	W.R.	330	180	115	47	D.L.	62	4	164	n.d.	n.d.	152	455	116	31520	
	C.F.	**7.8**	**1.1**	**30.8**	**22.6**	***	**26.4**	**22.1**	**23.5**	***	***	**16.8**	**8.1**	**13.4**	**17.7**	
17	EST-SHL-7_Py Mean	**1963**	**118**	**3480**	**470**	**18**	**1754**	**241**	**3121**	**0.59**	**116**	**2269**	**1641**	**1136**	**536578**	**0.8**
	Std. Dev.	981	86	1215	211	30	928	125	2787	0.51	124	1278	1178	879	24830	
	W.R.	330	180	115	51	D.L.	57	4	171	n.d.	n.d.	148	455	116	26434	
	C.F.	**5.9**	**0.7**	**30.3**	**9.2**	***	**30.7**	**63.4**	**18.3**	***	***	**15.3**	**3.6**	**9.8**	**20.3**	
11	EST-SHL-8_Py Mean	**2672**	**201**	**2389**	**1029**	**6**	**1573**	**93**	**3865**	**0.14**	**65**	**2491**	**2772**	**1468**	**531046**	**1**
	Std. Dev.	814	62	1845	343	9	1016	74	1109	0.12	80	765	1418	476	25980	
	W.R.	426	135	151	1633	n.d.	55	4	181	n.d.	n.d.	150	437	149	31576	
	C.F.	**6.3**	**1.5**	**15.8**	**0.6**	***	**28.7**	**23.9**	**21.4**	***	***	**16.6**	**6.3**	**9.9**	**16.8**	
14	EST-SHL-9_py Mean	**2949**	**194**	**2637**	**727**	**8**	**1228**	**86**	**2124**	**0.14**	**37**	**1521**	**1623**	**1233**	**520967**	**1.2**
	Std. Dev.	898	128	1996	376	16	611	75	1135	0.12	22	884	1256	600	34638	
	W.R.	324	52	136	1651	D.L.	64	4	192	n.d.	n.d.	146	447	142	38343	
	C.F.	**9.1**	**3.8**	**19.4**	**0.4**	***	**19.2**	**20.4**	**11.1**	***	***	**10.4**	**3.6**	**8.7**	**13.6**	
15	EST-SHL-10_Py Mean	**1715**	**132**	**2278**	**436**	**6**	**841**	**83**	**1285**	**0.18**	**38**	**1592**	**2656**	**1482**	**522948**	**1.65**
	Std. Dev.	752	66	857	220	12	197	72	1095	0.14	17	1171	1509	748	24036	
	W.R.	299	82	165	55	D.L.	50	3	108	n.d.	n.d.	147	442	159	27819	
	C.F.	**5.7**	**1.6**	**13.8**	**7.9**	***	**17.0**	**24.4**	**11.9**	***	***	**10.8**	**6.0**	**9.3**	**18.8**	
13	EST-SHL-11_Py Mean	**2421**	**201**	**3212**	**467**	**7**	**1037**	**137**	**2272**	**0.81**	**40**	**2325**	**3033**	**1658**	**559010**	**1.95**
	Std. Dev.	1119	80	2143	212	8	729	120	1360	1.09	41	1111	1838	995	36794	
	W.R.	336	194	137	49	D.L.	50	3	94	n.d.	n.d.	139	428	125	29670	
	C.F.	**7.2**	**1.04**	**23.4**	**9.5**	***	**21.0**	**42.8**	**24.1**	***	***	**16.7**	**7.1**	**13.3**	**18.8**	
19	EST-SHL-12_Py Mean	**1805**	**132**	**2368**	**436**	**6**	**841**	**83**	**1285**	**0.18**	**38**	**1592**	**2656**	**1382**	**532948**	**2.7**
	Std. Dev.	852	86	757	202	15	157	62	1015	0.24	19	1372	1309	848	44036	
	W.R.	411	124	127	49	D.L.	54	5	78	n.d.	n.d.	146	431	120	27114	
	C.F.	**4.4**	**1.1**	**18.6**	**8.9**	***	**15.7**	**18.0**	**16.5**	***	***	**10.9**	**6.2**	**11.5**	**19.7**	
19	EST-SHL-13_Py Mean	**1652**	**142**	**1741**	**369**	**2**	**913**	**164**	**5586**	**0.21**	**33**	**1140**	**2606**	**692**	**578956**	**3.15**
	Std. Dev.	1190	86	805	257	1	332	94	2079	0.22	15	915	1827	442	49475	
	W.R.	126	173	57	31	D.L.	80	5	155	n.d.	n.d.	96	415	165	44172	
	C.F.	**13.1**	**0.8**	**30.4**	**11.7**	***	**11.5**	**30.4**	**36.0**	***	***	**11.9**	**6.3**	**4.2**	**13.1**	
15	EST-SHL-15_PY Mean	**554**	**34**	**1414**	**533**	**11**	**1593**	**86**	**1340**	**0.30**	**40**	**1011**	**3111**	**207**	**573322**	**4.05**
	Std. Dev.	386	31	1296	194	22	599	77	926	0.50	27	690	998	121	13236	
	W.R.	120	713	106	37	D.L.	67	3	109	n.d.	n.d.	112	452	76	28755	
	C.F.	**4.6**	**0.05**	**13.3**	**14.4**	***	**23.7**	**26.1**	**12.3**	***	***	**9.1**	**6.9**	**2.7**	**20.6**	

5.3. Summary of LA-ICP-MS analyses of pyrite and concentration factors compared to whole rock values.

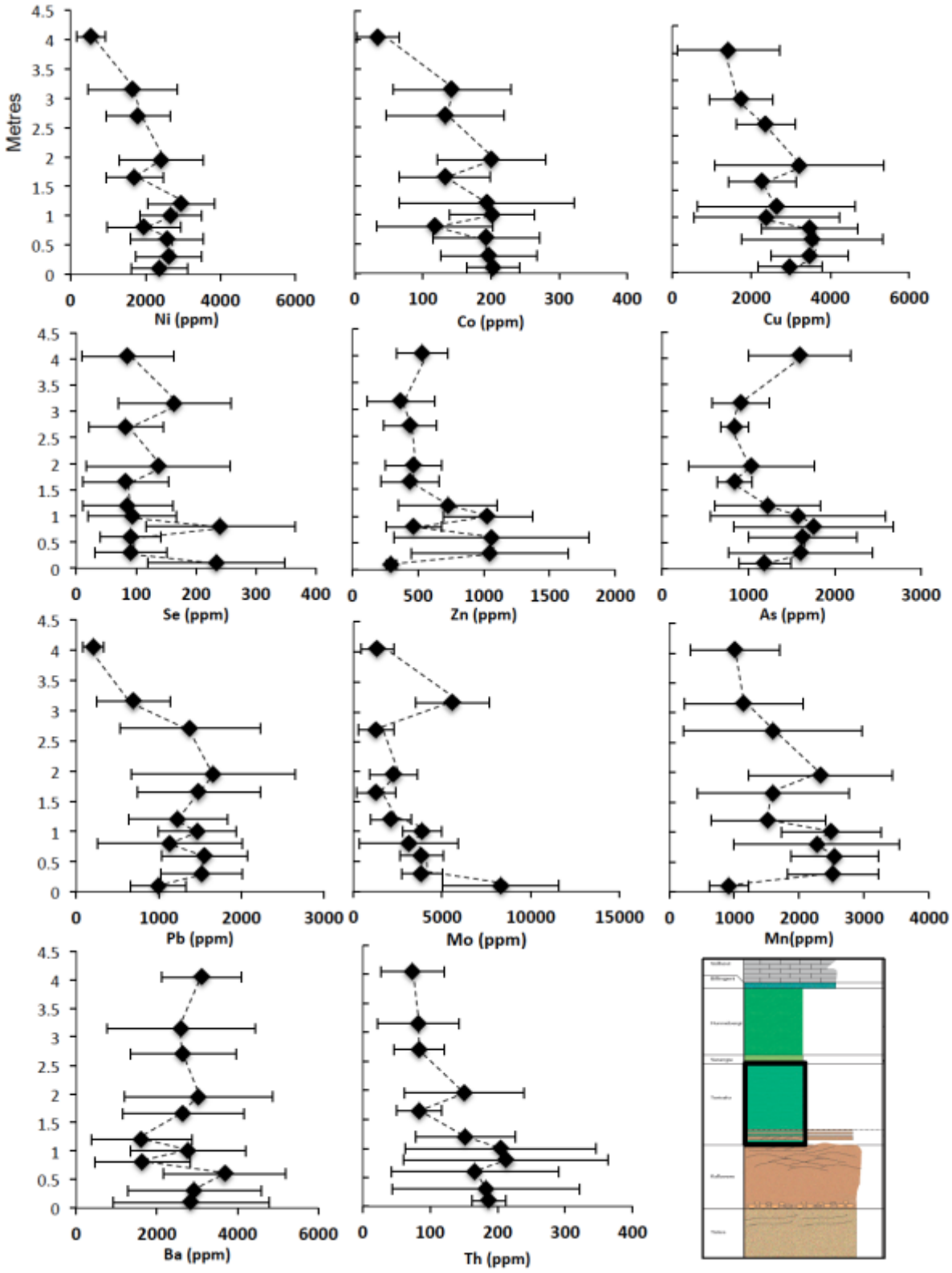

Figure 5.11. Plot of pyrite trace element chemistry from the black shale.

5.2.7. Discussion

Re-evaluating the depositional environment

Detailed sedimentological analysis of the Pakri section, particularly the nature of the contact between the Cambrian Kallavere unit and the lowermost Ordovician Turisalu shales, has added to the depositional models proposed by others (e.g. Nemliher and Puura 1996; Nielsen and Schovsbo 2011). The proposed on-lapping surface between the massive Kallavere and the black shales of the Turisalu Formation represents a large-scale transgression where the cross bed sets in the Upper Kallavere represent periods of high energy before flooding and inundation. Such a transgression likely resulted from a relative sea level rise and may have corresponded to increased erosion (as suggested by the higher energy regime), and then black shale deposition. This observation can place this section in a similar stratigraphic context of other previously studied Late Cambrian SPICE sequences globally. Following an initial rise in sea level, during the deposition of black shale at Pakri, Nielsen (2004) proposed a minor drop is sea level across the Baltica region. The resulting change in hydrodynamic environment may explain the observed change from laminated to massive character toward the top of the shale. As relative sea level began to subside, fine, glauconitic sand and silts of the Varangu and Hunnenberg Formations were deposited, indicative of a low energy, restricted and reducing, shallow water setting. At this time Baltica moved north, towards lower latitudes (Cocks and Torsvik, 2005), leading to more temperate conditions and the deposition of the overlying carbonate-rich shallow water sediments present towards the top of the section.

Basin redox conditions during deposition

Whole rock and pyrite trace element chemistry shows that the Turisalu shales are highly enriched in a range of metals, suggesting that the seawater was low in oxygen in order to facilitate their accumulation (Huerta-Diaz and Morse, 1992). Many trace elements are enriched by many orders compared to WSA and by over 2x compared to SDO-1, conforming to the designation of Hyuck (1989) as being metalliferous. The whole-rock data display a correlation between TOC% and redox sensitive metals, suggesting that organic matter played a role in the overall metal budgeting within the basin and reduced

conditions prevailed. Cobalt increases toward the top of the shale while organic carbon, sulphur, and other metals (i.e. Ni, Zn, Cu) decrease, suggesting a progressive oxygenation of the water column (Saito et al., 2002). Zinc and nickel are notably enriched in both whole-rock and pyrite in the lowermost 1m of the shale which represents the transition from euxinic to anoxic conditions based on U, V, Mo contents. Zinc and nickel sulfides form a solid solution with Fe-sulfides under euxinic conditions but under anoxic conditions where they tend to also form metal-organic clusters and may also partition into organic phases, as they are common nutrients for organic matter (Algeo and Maynard, 2006). This is likely the case here and may suggest that the relative enrichment of Zn and Ni in whole-rock compared to pyrite could be another criterion to fingerprint this transition in ancient sediments. Pyrite trace element content reveals the minor variations through the stratigraphy that are under-represented in whole-rock samples, in particular the cyclic nature (i.e. Se, Ni, Cu, Zn) of enrichment in the lower partition of black shale, corresponding to interbeds of the transition zone (0.1- 1m). This is interpreted to represent a possible episodic expansion of euxinic conditions that coincide with our fluctuations of relative sea level. Selenium shows this cyclicity very well in that it is enriched at the base, becoming more depleted in each of the two other interbeds and then reaching a new maximum above the transition zone. Due to the biologically critical and redox sensitive nature of selenium (Mitchell et al., 2012), it can be inferred that each pulse of enrichment may correspond to a period of increased biological activity and turnover, and potentially the periodic development of euxinic conditions. This proposal fits well with the increased phosphorous content, a common proxy for biological activity, which is also elevated in this zone. The lower portion of the shale is suggested to be euxinic, based on the large Mo and V enrichments (Lyons et al., 2003, Scott et al., 2014). These are trace metals usually associated with the development of euxinic conditions. Critically, a punctuated Mo enrichment in sediments has been suggested to represent localized areas of euxinia in the basin, as widely developed euxinic conditions would likely lead to the dispersion of Mo in the seawater and more uniform enrichments through the shale (Lyons et al., 2009). This portion of the shale is high in pyrite content and records the greatest value of siderophile and chalcophile elements, which is consistent with the interpretation of euxinia (Morse and Luther, 1999). In this instance the use of pyrite chemistry has complimented the traditional

whole-rock method and has allowed for greater resolution as to the dynamic nature of the depositional environment.

Isotopic variation and its implications for the Cambrian- Ordovician as archived in Estonia

The excursion in $\delta^{13}C$ isotopes observed here is similar in scale to the SPICE event (~ 499 Ma ±4 Ma) as archived at other localities on Gondwana and Laurentia (Saltzman et al., 2000; Cocks and Torsvik, 2005). The exact duration of it in the section studied here, however, is not as well constrained. Though, due to the condensed nature of the section it is conceivable that the ~50cm of shallow-water grainstones could easily capture a portion of a millennial-scale isotope excursion. Critically, both $\delta^{34}S_{py}$ and $\delta^{13}C_{org}$ profiles follow a similar pattern in this zone. This fits well with the $\delta^{34}S$ isotope excursion noted by Gill et al. (2011) that accompanied the SPICE event in a section studied in Nevada. In addition, the majority of $\delta^{13}C_{org}$ and $\delta^{13}C_{calc}$ profiles maintain a constant fractionation of ~28‰ which is a typical fractionation factor between organic and inorganic species of carbon. Variation from this is present at a few points in the $\delta^{13}C_{org}$ profile may be attributed to biogenic methane production, which is a common in low oxygen organic shales. This process will cause further fractionation towards more negative $\delta^{13}C$ values in the organic-bound carbon. Based on field and petrographic analysis, there is a distinct lack of thermal maturity or alteration of these units that could affect the isotopic values. In addition, the Alum Shale of Sweden also records the SPICE event as a $\delta^{13}C_{org}$ excursion (Saltzman et al., 2005). Therefore, it may be proposed that the section studied here likely represents the shallow shelf equivalent.

Seawater sulfate concentrations are tied to the redox state of the Earth's atmosphere-ocean system (Canfield, 2005). Fractionation from the seawater sulfate ($\delta^{34}S_{sulfate}$) value recorded in pyrite gives an indicator as to the size of the seawater sulfate reservoir and productivity, therefore, a proxy for the oxidation state of ocean. Shifts in the $\delta^{34}S$ isotope value, linked to productivity within the basin or a change in the sulfate reservoir ($\delta^{34}S_{sulfate}$) may be attributed to the oscillations in the tectonic regime or basin development. Rising and falling of sea level in a basin will alter circulation patterns and oxygen

penetration depths. Variation in oxygen or H_2S levels within a basin will, in turn, dictate trace element budgets and stability of marine species that utilise them as nutrients.

A dramatic shift in all isotope profiles was observed through the lower, interbedded horizon of the transition zone. The mirroring of carbon and sulfur isotopic profiles suggests that this represents a rise in the amount of buried organic matter and pyrite in the sediments. Such a process leads to the removal of ^{12}C and ^{32}S from the ocean as they are buried and metabolised by microbes. This is observed physically by the elevated TOC% and the abundance of pyrite in the lower intervals of the shale. Such parallel burial has been shown to occur in anoxic marine sediments, beneath euxinic water columns (Gill et al., 2011).

The positive $\delta^{34}S$ values for pyrite in the Tiskre Formation are similar to that of Late Cambrian seawater sulfate (Kampschulte and Strauss, 2004). The similar $\delta^{34}S$ values recorded here can be attributed to limited microbial activity, as expressed by the organic-lean nature of the rocks, or very low seawater sulfate content. The uppermost biograinstone of the Kallavere, and in the interbedded zone, exhibit a range of $\delta^{34}S$ values that can be attribute a variety of possible processes. One process may be Rayleigh fractionation within this unit with respect to a closed sulfate reservoir or limited seawater sulphate availability at this time. Rapid sea level rise and inundation of black shale with high microbial activity would result in forming a partially closed system with respect to seawater sulfate. This can explain the pyrite forming an intergranular cement in the pore spaces of this unit, as only sulfate already present or diffusing downwards in the pore waters would be available for reduction, precipitating pyrite when it encounters iron at a suitable redox buffer (Rickard, 2012). The remaining sulfate pool becomes progressively enriched in ^{34}S as ^{32}S is removed. Another process may be the complete reduction of sulfate as the water mass becomes restricted and euxinic conditions dominate. Jorgensen et al. (2004), however, propose that diffusion exchange within sediments towards the overlying water column can produce positive $\delta^{34}S$ values. Their work on the Black Sea and other reduced sedimentary packages suggests that methane-driven sulfate reduction, combined with a trap for the H_2S can produce positive $\delta^{34}S$ values. Their data shows that such positive values also correspond with the sulfate-methane transition in the sedimentary package and may also explain the shift towards more negative $\delta^{13}C_{org}$

values in some of the lowermost black shale samples. Critically, there is no macro- or micro-scale evidence for hydrothermal fluid influx or secondary alteration within this unit, or the rest of the sequence.

The Turisalu shale itself exhibits negative $\delta^{34}S$ values at its base. This corresponds to a fractionation of ~ 38‰ from a proposed seawater sulfate value of ~24‰ (Kampschulte and Strauss, 2004), this fits well with fractionation factors attributed to bacteria sulfate reduction (Canfield and Thamdrup, 1994). It also suggests that productivity was high and that bacteria had an open source to a large sulfate reservoir for the duration of its deposition.

A shift towards more negative values of $\delta^{34}S$, before becoming more positive in the upper 1.5m of the shale, also corresponds to a minor increase in pyrite abundance and is accompanied by a minor change in $\delta^{13}C_{org}$ and trace metal content. It may be that this may represent disproportionation reactions as a new sulfuretum dominates the sulfur reduction process with a contracting sulfate pool and under more oxygenated conditions (e.g. dysoxic) (Canfield and Thamdrup, 1994; Canfield et al., 2010), before progressive oxygenation of the water mass (Fig. 5.12).

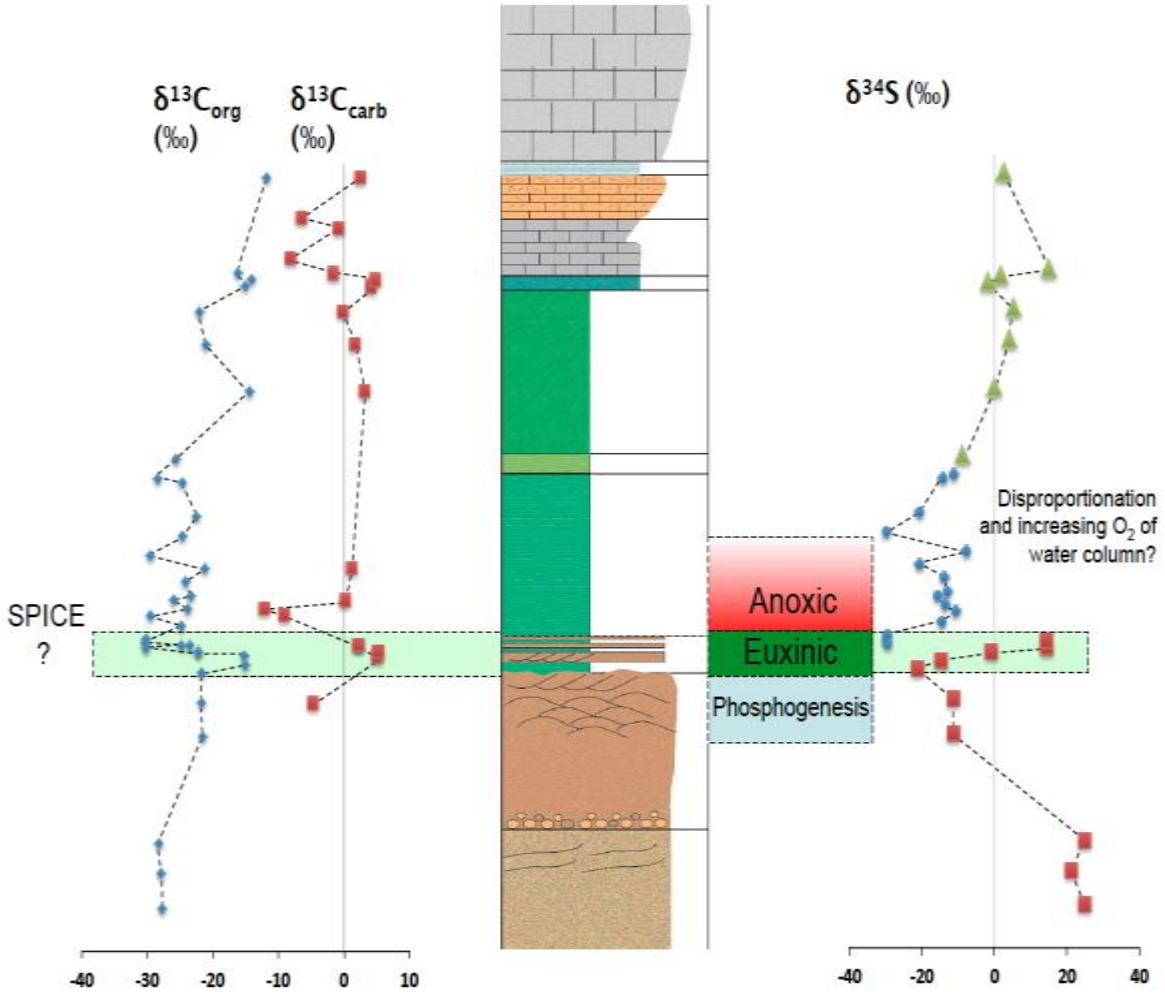

Figure 5.12. Diagram summarizing conditions in the basin during deposition.

Potential drivers for the SPICE event and links to wider geochemical cycles.

The ultimate driver for this dramatic change in sea level, represented by the sedimentological changes discussed here and documented in other localities that archive the SPICE event, remain unclear. Glacial-eustasity provides a framework for both sea level variation and carbon isotope excursions, though there is no evidence of widespread glaciation at this point in Earth History (Saltzman et al., 2004). Annual/ seasonal sea level variation is unlikely to produce the scale of variations in sea level observed here and in other Cambro-Ordovician localities where such a phenomena has been documented. The Pan-African Orogeny (~520- 500; Cawood et al., 2005) had reached its peak prior to

this period, however, far-field tectonic stresses may have still been active and altered ocean circulation patterns may result in relative sea level variations. Sabadini et al. (1990) proposed a non-uniformatarian driver for rapid sea level variations in Earth History, suggesting that true-polar-wander episodes could produce sea level changes of 20-50 m over a period of 1 million years. Evans' (2001) built upon this and proposed a model suggesting that an end-Cambrian true-polar-wander event may manifest itself as a large-scale transgression in Baltica. The models of Evans (2003) and Kirschvinck and Raub (2003) suggest that inertial interchange true polar wander (IITPW), may lead to non-eustatic sea level fluctuations and the alteration of ocean currents, promoting upwelling zones and areas of stagnant water mass. Further investigation of this hypothesis is required, however, such an event may provide a causational framework that can relate the apparent rapid sea level rise and isotope excursion. Despite the governing tectonic driver that may have influenced the event, alteration of water flow and the creation of upwelling zones were likely critical in providing the phosphorous influx to the shallow waters. Increased phosphorous in the prelude to the SPICE has been noted in other localities (i.e. Gill et al., 2011; Sial et al., 2013) and may have triggered a burst of bio-productivity that could have influenced the regulation of the global carbon cycle.

Implications for marine life

Perturbations in the atmosphere-ocean cycle or by geodynamic variation promoting sea level rise inevitably can lead to changes in oxygen levels, trace element input, nutrient content in basins and shelf environments. Some data suggest that such conditions may have led to the decrease in trilobites species that is associated with this time period, as mass burial and dramatic changes in O_2 content within basins would have affected sea-dwelling organisms (Hammer and Harper, 2006; Harper, 2006). A rise in sea level a shift to more restricted conditions with abundant trace elements, which are used as nutrients (e.g. Ni, Se, Cu, Zn), may have led to the dominance of graptolites and sponges whose mode of life may have been better suited to the capture of trace elements in the water column (Harper, 2006; Foote, 1993). Trilobite abundance decreased dramatically at this time and can be related to the effects of dramatic flooding and expansion of oxygen poor conditions into the, once, shallow marine environment in which they thrived. This assumption is supported by the fact that only trilobites that were adapted to

living in deeper waters appeared to survive into the Ordovician (Foote, 1988). It is also possible that the widespread euxinic conditions proposed to have been present at the end Cambrian by Gill et al. (2011), and observed in this study, strengthen the suggestion that dramatic environmental change occurred, promoting a shift to much more unsuitable conditions for trilobite species.

Connections between mass extinctions and isotope excursions occur throughout the Phanerozoic, suggesting the possibility of a common cause. The Cretaceous-Tertiary boundary is the most studied example of this where extinctions are observed soon after the beginning of a $\delta^{13}C$ excursion and continued through its peak. In this example, the extinctions are considered to be due to a disruption of the food chain that was a result of depletion in essential nutrients (Paul and Mitchell, 1994). It is possible to invoke parallels of this mechanism to explain the geochemical evidence presented here and in other studies (Saltzman et al., 2000: Gill et al., 2011; Dahl et al., 2014 and reference therein) and may account for the extinction of many trilobite species during this time.

5.2.8. Conclusion

A focussed study of the Cambrian-Ordovician boundary in Northern Estonia has allowed for a high-resolution geochemical study and further interpretation of the depositional environment. Large geochemical variation is observed through stratigraphy in both whole-rock and pyrite suggesting that, potentially, the seawater was rich in metals and bio-productivity was high. The sedimentary sequence studied records an isotope excursion that is similar in character, magnitude and timing to the SPICE excursion, confirming this event was of a global scale and potentially was more protracted than previously considered. These geochemical changes also correspond to depositional facies changes and a substantial rise in sea level, as noted in other localities (Saltzman et al., 2000). Such changes are likely to be tectonically driven, however, they are required to be geologically rapid to lead to mass deposition and alteration of the global carbon budget. It is proposed that during this time tectonic processes and associated erosional feedbacks coupled with upwelling or altered circulation may have introduced more nutrients to the continental shelf. Zones of upwelling resulted in increased phosphorous being introduced to the shallow shelf, promoting productivity. Since widespread

phosphogenesis has been document in other Late Cambrian localities (e.g. Gill et al., 2011), it is likely that this process promoted increased bio-productivity in a number of shallow-water environments globally, potentially altering the atmospheric carbon budget. In the areas of intensive bio-productivity, the deposition of organic matter may have promoted the local development of euxinia. Conditions prevalent during this time could be analogous to that which occurred during ocean anoxic events of the Mesozoic (Jenkyns, 2010). During such times, the spread of oxygen-depleted waters led to extensive deposition of organic-rich, pyritic sediments in the ocean, and were associated with isotopic shifts in $\delta^{13}C_{org}$ and seawater sulfate (Gill et al., 2011). If the isotopic shifts observed in this study are linked to those documented as the SPICE event then this locality can be related in the geochemical, stratigraphic and biological framework of the SPICE, providing new insight into conditions present during Cambrian-Ordovician times.

The geochemical data suggest that shoaling of oxygen-depleted waters, with punctuated euxinia, onto the shelf may have contributed to the turnover of shelf fauna at this time. This work strengthens the proposal of Gill et al. (2011) that anoxic water masses may have been common in shallow waters of the Late Cambrian. If true, then the high rates of biological turnover and trilobite extinctions documented in Late Cambrian localities can be partially explained by drivers affecting sea level and circulation, culminating in spasmodic expansion of oxygen-depleted waters to shallower shelf environments, high biological turnover and metal enrichments.

5.3. References

Ainsaar, L., Meidla, T. and Martma, T. 2004. The Middle Caradoc Facies and Faunal Turnover in the Late Ordovician Baltoscandian palaeobasin. Palaeogeography. Palaeoclimatology. Palaeoecology, 210, p.119-133.

Algeo, T. J. and Maynard, J.B., 2004. Trace-element behavior and redox facies in core shales of Upper Pennsylvanian Kanas-type cyclothems. Chemical Geology, 206, p. 289-318.

Andersson, A., Dahlman, D., Gee, D. G. and Snall, S., 1985. The Scandinavian alum shales. Sveriges Geologiska Undersokning Ca 56, p. 1-50.

Berner, Z. A., Puchelt H., Noltner, T. and Kramar, U., 2013. Pyrite geochemistry in the Toarcian Posidonia Shale of south-west Germany: Evidence for contrasting trace-element patterns of diagenetic and syngenetic pyrites. Sedimentology, 60, p. 548–573.

Canfield, D. E. and Thamdrup B. 1994. The production of 34S-depleted sulfide during bacterial disproportionation of elemental sulfur. Science, 266, p. 1973–1975.

Canfield, D.E., 2005. The early history of atmospheric oxygen: homage to Robert M. Garrels. Annual Reviews in Earth Planetary Science. 33, p. 1–36

Calvert, S. E. and Pedersen, T. F. 1993. Geochemistry of recent oxic and anoxic marine sediments – implications for the geological record. Marine Geology, 113, p. 67-88.

Cawood, P.A. 2005. Terra Australis Orogen: Rodinia breakup and development of the Pacific and Iapetus margins of Gondwana during the Neoproterozoic and Paleozoic Earth-Science Reviews, 69, p. 249–279.

Chafetz, H.S., Reid, A., 2000. Syndepositional shallow-water precipitation of glauconitic minerals. Sedimentary Geology, 136, p. 29-42

Chappaz, A., Lyons, T. W., Gregory, D. D., Reinhard, C. T., Gill, B.C., Li, C., Large, R. R., 2014. Does pyrite act as an important host for molybdenum in modern and ancient euxinic sediments? Geochimica et Cosmochimica Acta, 126, p. 112-122.

Cocks, L.R.M. and Torsvik, T.H., 2005. Baltica from the late Precambrian to mid Palaeozoic: the gain and loss of a terranes's identity. Earth Science Reviews, 72, p. 39-66.

Danyushevsky, L.V., Robinson, P., Gilbert, S., Norman, M., Large, R., McGoldrick, P., Shelley, M.. 2011. Routine quantitative multi-element analysis of sulfide minerals by laser ablation ICPMS: Standard development and consideration of matrix effects. Geochemistry: Exploration, Environment, Analysis, 11, p. 51-60.

Dahl, T.W., Boyle, R.A., Canfield, D.E., Connelly, J.N., Gill, B.C., Lenton, T.M., Bizzarro, M., 2014. Uranium isotopes distinguish two geochemically distinct stages during the later Cambrian SPICE event. Earth and Planetary Science Letters, 401, p. 313–326.

Dewey, J.F. and Pitman, W.C., 1997. Sea level changes: mechanisms, magnitudes and rates: SEPM Spec. Publ., 58, p. 95-127

Einasto, R. and Mens, K., 1996. Geology. Basement (in Estonia), in Pakri Peninsula–Nature and Human Activity, p. 16–23, ed. Kink, H., Estonian Academy Publishers, Tallinn.

Emerson, S.R, Huested S.S., 1991. Ocean anoxia and the concentrations of molybdenum and vanadium in seawater. Marine Chemistry, 34, p. 177-196

Evans, D.A., 1998. True polar wander, a supercontinental legacy. Earth and Planetary Science Letters, 157, p. 1–8

Evans, D. A., 2003. True polar wander and supercontinents. Tectonophysics, 362, p. 303-320.

Foote, M.,1988. Survivorship analysis of Cambrian and Ordovician Trilobites. Paleiobiology, 14, p. 258- 271.

Foote, M., 1996. Perspective: Evolutionary patterns in the fossil record. Evolution, 50, p. 1- 11.

Gill, B.C., Lyons, T.W., Young, S.A., Kump, L.R., Knoll, A.H. and Saltzman, M.R., 2011. Geochemical evidence for widespread euxinia in the Later Cambrian ocean. Nature, 469, p. 80- 83.

Gregory, D. D., Meffre, S., Large, R. R., 2014. Comparison of metal enrichment in pyrite framboids from a metal-enrichedand metal-poor estuary. American Mineralogist, 99, p. 633- 644.

Gregory, D.D., Large, R.R., Halpin, J.A., Steadman, J.A., Hickman, A.H., Ireland, T.R., Holden, P., 2015. The chemical conditions of the late Archean Hamersley basin inferred from whole rock and pyrite geochemistry with 33S and 34S isotope analyses. Geochimica et Cosmochimica Acta 149, p. 223-250.

Hammer, O. and Harper, D.A.T., 2006. Palentological Data Anlaysis, Blackwell, Oxford, U.K.

Harper, D.A., 2006. The Ordovician biodiversification: Setting an agenda for marine life. Palaeogeography, Palaeoclimatology, Palaeoecology, 232, p.148-166.

Heinsalu, H., Kaljo, D., Kurvits, V., and Viira, V., 2003. The stratotype of the Orasoja Member (Tremadocian, Northeast Estonia): lithology, mineralogy, and biostratigraphy. Proceedings of the Estonian Academy of Sciences: Geology, 52, p. 135–154.

Hints, O. and Nolvak, J., 2006. Early Ordovician scolecodonts and chitinozoans from Tallinn, North Estonia. Review of Palaeobotany and Palynology, 139, p. 189–209.

Hurtgen, M.T., Pruss, S.B. and Knoll, A.H. 2009. Evaluating the relationship between the Carbon and sulfur cycles in the later Cambrian ocean: an example from the Port au Port Group, western Newfoundland, Canada. Earth Planetary Science Letters, 281, p. 288–297.

Huyck, H.L., 1989. When is a metalliferous black shale not a black shale. Metalliferous Black Shales and Related Ore Deposits, Proc. 1989 US Working Group Meet., IGCP, 254, p.42-56.

Jenkyns, H. C., 2010, Geochemistry of oceanic anoxic events. Geochem. Geophys. Geosystems, 11, p. 1-30.

Jones, B. and Manning, D. A. C., 1994. Comparison of geochemical indices used for the interpretation of paleoredox conditions in ancient mudstones. Chemical Geology, 111, p. 111-129.

Jørgensen, B.B., Böttcher, M.E., Lüschen, H., Neretin, L.N. and Volkov, I.I., 2004. Anaerobic methane oxidation and a deep H 2 S sink generate isotopically heavy sulfides in Black Sea sediments. *Geochimica et Cosmochimica Acta*, *68*, p.2095-2118.

Kaljo, D., Borovko, N., Heinsalu, H. Khazanovich, K., Mens, K., Popov, L., Sergejeva, S., and Sobolevskaja, R., 1986. The Cambrian-Ordovician boundary in the Baltic-Ladoga clint area (North Estonia and Leningrad Region, USSR). Proceedings of the Academy of Sciences of the Estonian SSR. 35, p. 97- 108.

Kirschvink, J.L., Ripperdan, R.L., Evans, D.A., 1997. Evidence for large-scale reorganization of early Cambrian continental masses by inertial interchange true polar wander. Science, 277, p. 541–545.

Kirschvink, J.L. and Raub, T.D.2003. A methane fuse for the Cambrian Explosion: Carbon Cycles and True Polare Wander. Comptes Rendus Geosciences. 335, p. 65-78.

Kump, L. R., and Arthur, M. A. 1999. Interpreting carbon-isotope excursions: carbonates and organic matter. Chemical Geology, 161, p. 181-198.

Kampschulte, A. and Strauss, H., 2004. The sulfur isotopic evolution of Phanerozoic seawater based on

the analysis of structurally substituted sulphate in carbonates. Chemical Geology. 204, p. 255-286.

Large, R.R., Halpin, J.A., Danyushevsky, L.V., Maslennikov, V.V., Bull, S.W., Long, J.A., Gregory, D.D., Lounejeva, E., Lyons, T.W., Sack, P.J., McGoldrick, P.J., Calver, C.R., 2014. Trace element content of sedimentary pyrite as a new proxy for deep-time ocean-atmosphere evolution, Earth and Planetary Science Letters, 389, p. 209-220.

Large, R.R., Halpin, J.A., Lounejeva, E., Danyushevsky, L.V., Maslennikov, V.V., Gregory, D.D.,, Sack, P.J., Haines, P.W., Long, J.A., Makoundi, C., Stepanov, A., 2015. Cycles of nutrient trace elements in the Phanerozoic ocean, Gondwana Research, 28, p. 1282–1293.

Longerich, H.P., Jackson, S.E., Günther, D., 1996. Laser ablation inductively coupled mass spectrometric transient signal data acquisition and analyte concentration calculation. Journal of Analytical Atomic Spectrometry, 11, p. 899-904.

Lyons, T.W., Werne, J.P., Hollander, D.J. and Murray, R.W., 2003. Contrasting sulfur geochemistry and Fe/Al and Mo/Al ratios across the last oxic-to-anoxic transition in the Cariaco Basin, Venezuela. Chemical Geology, 195, p.131-157.

Lyons, T.W., Anbar, A.D., Severmann, S., Scott, C. and Gill, B.C., 2009. Tracking euxinia in the ancient ocean: a multiproxy perspective and Proterozoic case study. Annual Review of Earth and Planetary Sciences, 37, p.507-534.

Mens, K., Heinsalu, H., Jegonjan, K., Kurvits, T., Puura, I. and Viira, V., 1996. Cambrian–Ordovician boundary beds in the Pakri Cape section, NW Estonia. Proceedings of the Estonian Academy of Sciences. Geology, 45, p. 9–21.

Mitchell, K., Mason, P. R., Van Cappellen, P., Johnson, T. M., Gill, B. C., Owens, J. D., Diaz, J., Ingall, E.D., Reichart, G.J. and Lyons, T. W., 2012. Selenium as paleo-oceanographic proxy: A first assessment. Geochimica et Cosmochimica Acta, 89, p. 302-317.

Morse J. W. and Luther, G.W. 1999. Chemical influences on trace metal-sulfide interactions in anoxic sediments. Geochimica et Cosmochimica Acta, 63, p. 3373-3378.

Nemliher, J. and Puura, I., 1996. Shell mineralogy of lingulate brachiopods from the east Baltic Cambrian-Ordovician "Obolus phosphorite".In: STOUGE, S. (ed.). WOGOGOB-94 Symposium, Working Group on Ordovician Geology of Baltoscandia, Bornholm-94. Geol. Survey of Denmark and Greenland, Report 98, p. 7989

Nielsen, A.T., 2004. Sea level changes – a Baltoscandian perspective. In B.D. Webby, F. Paris, M.L. Droser and I.G. Percival (eds.): The Great Ordovician Biodiversification Event, 84–93. Columbia University Press, New York.

Nielsen, A.T. and Schovsbo, N.H., 2006. Cambrian to basal Ordovician lithostratigraphy in southern Scandinavia. Bulletin of the Geological Society of Denmark. 53, p. 47–92.

Nielsen, A.T. and Schovsbo, N.H., 2011. The Lower Cambrian of Scandinavia: depositional environment, sequence stratigraphy and palaeogeography. Earth Science Reviews, 107, p. 207- 310.

Nılvak, J., Hints, O., and Mannik, P., 2006. Ordovician timescale in Estonia: recent developments. Proc. Estonian Academy of Science, Geology, 55, p.95-108.

Panchuk, K., Ridgwell, A., and Kump, L. R., 2008. Sedimentary response to Paleocene-Eocene Thermal Maximum carbon release: A model-data comparison. Geology, 36, p. 315-318.

Paul, C.R.C. and Mitchell, S. F. 1994. Is famine a common factor in marine mass extinctions? Geology, 22, p. 679-682

Pedersen, T.F. and Calvert, S.E., 1990. Anoxia vs. productivity: what controls the formation of organic-carbon-rich sediments and sedimentary rocks? AAPG Bulletin, 74, p. 454–466.

Piper, D. Z., 1994. Seawater as the source of minor elements in black shales, phosphorites and other sedimentary rocks. Chemical Geology, 114, p. 95-114.

Piper, D. Z., and Isaacs, C. M.,1995. Minor elements in Quaternary sediment from the Sea of Japan: A record of surface-water productivity and intermediate-water redox conditions. Geological Society of America Bulletin, 107, p. 54-67.

Pitman, W. C. (1978), Relationship between eustacity and stratigraphic sequences of passive margins, Geological Society of America Bulletin, 89, p. 1389–1403

Puura, I. and Viira, V. 2004. Tracing the base of the Ordovician System in Baltoscandia. In Hints, O. and Ainsaar, L., (eds): WOGOGOB-2004 Conference Materials. Tartu University Press.

Rimmer, S., 2003. Geochemical paleoredox indicators in Devonian-Mississippian black shales, Central Appalachian basin (USA). Chemical Geology 206, p. 373–391

Robinson P. 2003. XRF analysis of flux-fused discs. Geoanalysis 2003, Analysis of Geological and Environmental Materials, Abstracts, 90.

Rothman, D.H., Fournier, G.P., French, KL, Alm, E.J., Boyle, E.A., Cao, C., Summons, R.E., 2014. Methanogenic burst I the end-Permian carbon cycle. Proceedings of the National Academy of Science, USA, 111, p. 5462–5467.

Sabadini, R., Doglioni, C. and Yuen, D.A., 1990. Eustatic sea level fluctuations induced by polar wander, Nature, 345, p. 708-710.

Saito, M.A., Moffett, J.W., Chisholm, S.W., Waterbury, J.B., 2002. Cobalt limitation and uptake in Prochlococcus. Limnol. Oceanogrography, 47, p. 1629–1636.

Saltzman, M.R., Runnegar, B. and Lohmann, K.C., 1998. Carbon isotope stratigraphy of Upper Cambrian (Steptoean Stage) sequences of the eastern Great Basin: Record of a global oceanographic event. Geological Society of America Bulletin, 110, p. 285-297.

Saltzman, M.R., Ripperdan, R.L., Brasier, M.D., Lohmann, K.C., Robison, R.A., Chang, W.T., Peng, S., Ergaliev, E.K. and Runnegar, B., 2000. A global carbon isotope excursion (SPICE) during the Late Cambrian: relation to trilobite extinctions, organic-matter burial and sea level. Palaeogeography, Palaeoclimatology, Palaeoecology, 162, 3, p.211-223.

Saltzman, M.R., Cowan, C.A., Runkel, A.C., Runnegar, B., Stewart, M.C. and Palmer, A.R., 2004. The Late Cambrian Spice (13C) Event and the Sauk II-SAUK III Regression: New Evidence from Laurentian Basins in Utah, Iowa, and Newfoundland. Journal of Sedimentary Research, 74, 3, p.366-377.

Saltzman, M.R., 2005. Phosphorus, nitrogen, and the redox evolution of the Paleozoic oceans. Geology, 33, p. 573-576.

Scott, C.T., Slack, J.F., and Kelley, K.D., 2014, An aqueous sulphide control for hyper-enrichments of trace metals in black shales [abs.]: Geological Association of Canada-Mineralogical Association of Canada, Program with Abstracts, v. 37.

Sial, A. N., Peralta, S., Ferreira, V. P., Toselli, A. J., Aceñolaza, F. G., Parada, M. A., Gaucher, C., Alonso, R. N. and Pimentel, M. M., 2008. Upper Cambrian carbonate sequences of the Argentine Precordillera and the Steptoean C-Isotope positive excursion (SPICE). Gondwana Research, 13, p. 437-452.

Sial, A. N., Peralta, S., Gaucher, C., Toselli, A. J., Ferreira, V. P., Frei, R., Parada, M.A., Pimental, M. M. and Pereira, N. S., 2013. High-resolution stable isotope stratigraphy of the upper Cambrian and Ordovician in the Argentine Precordillera: Carbon isotope excursions and correlations. Gondwana Research, 24, p. 330-348.

Southgate, P.N. and Shergold, J.H. 1991. Application of sequence stratigraphic concepts to Middle Cambrian phosphogenesis, Georgina Basin, Australia. Journal of Australian Geology and Geophysics. 12, p. 119-144

Thickpenny, A. 1987. Palaeooceanography and depositional environment of the Scandinavian Alum shales: sedimentological and geochemical evidence. In J. K. Leggett and G.G. Zuffa (eds.): Marine Clastic Sedimentology–Concepts and Case Studies, p. 156–171. Graham and Trotman, London.

Tribovillard, N., Algeo, T.J., Lyons, T.W. and Riboulleau, A.,2006. Application of trace metals as paleoredox and paleoproductivity proxies. Chemical Geology. 232, p. 12–32.

Veski, R.; Palu, E. 2003. Investigation of Dictyonema oil shale and its natural and artificial transformation products by a vankrevelenogram. Oil Shale. 20, p. 265–281

Viira, V., Mens, K. and Nemliher, J. 2006. Lower Ordovician Leetse Formation in the North Estonian Klint area. Proceedings of the Estonian Academy of Sciences, Geology, 55, p. 156-174.

Voolma, M., Soesoo, A., Hade, S., Hints, R. and Kallaste, T. 2013. Geochemical heterogeneity of Estonian graptolite argillite. Oil Shale, 30, p. 377- 401.

Wagner, T., Boyce, A.J., Fallick, A.E. 2002. Laser combustion analysis of $\delta^{34}S$ of sulfosalt minerals: determination of the fractionation systematics and some crystal-chemical considerations. Geochimica et Cosmochimica Acta, 66, p. 2855-286.

Wedepohl, K.H. 1995. The composition of the continental crust. Geochemica, Cosmochemica Acta, 59, p. 1217- 1232.

Yu, Z., Robinson, P. and McGoldrick, P., 2001. An Evaluation of Methods for the Chemical Decomposition of Geological Materials for Trace Element Determination using ICP-MS. Geostandards Newsletter, 25, p.199-217.

5.4. Appendix to Chapter 5

5.4.1.Summary of sedimentary units with facies descriptions

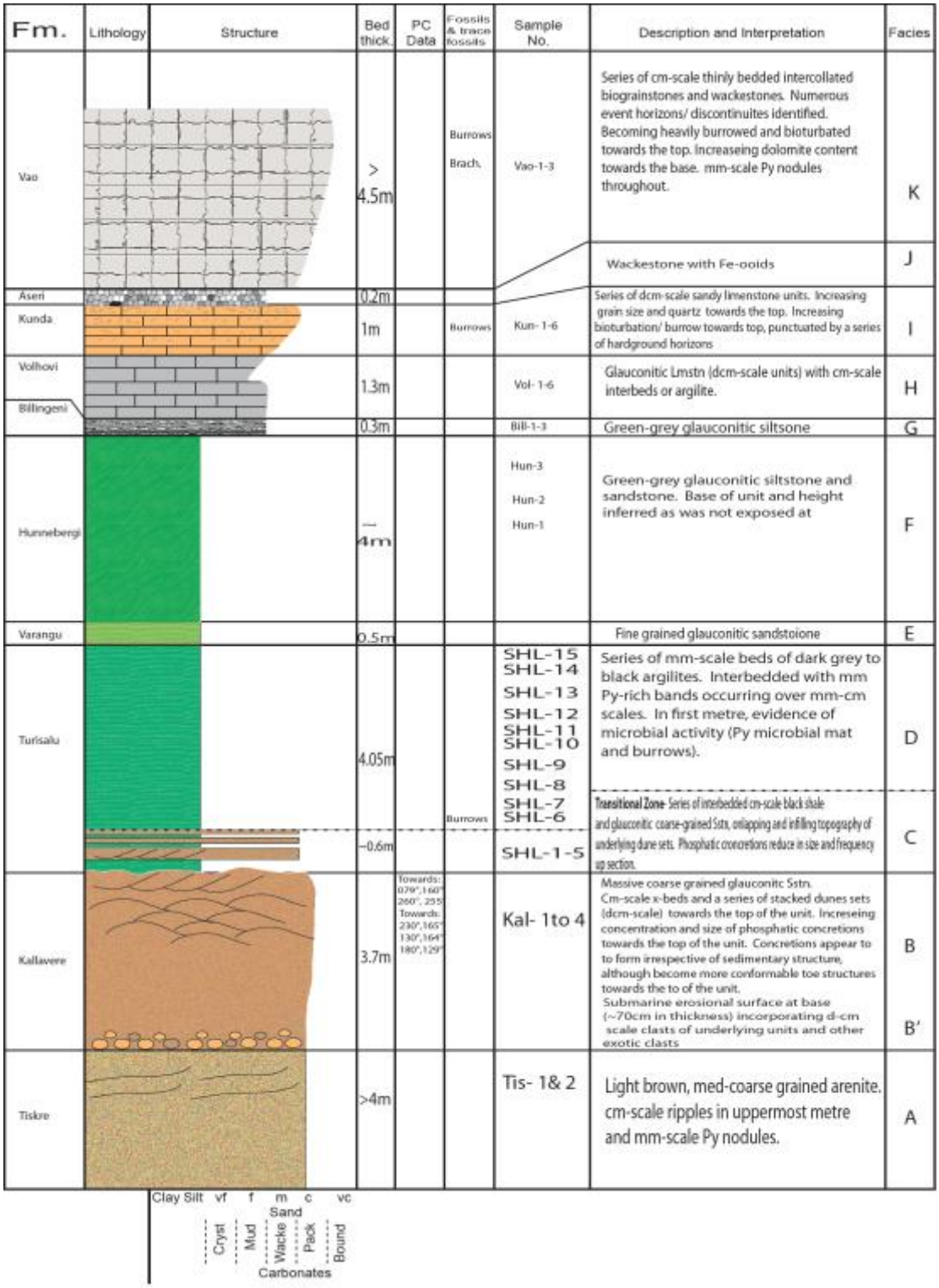

Figure 5.A.1. Summary of sedimentary units with facies descriptions.

5.4.2. Pyrite and whole-rock trace element geochemistry- methods, rationale and evaluation

Method

The laser is equipped with an in-house, small volume ablation cell with a <1-s response time and <2-s washout delay. Ablation was performed in pure He. The aerosol carried by the He gas was immediately mixed with Ar after exiting the cell and then passed through a pulse-homogenizing device before entering the ICP-MS. Optimization of the ICP-MS took place every day in order to maximize sensitivity toward mid- to high atomic mass isotopes (a.m.u. ranging from 130-240).

Trace element analyses were performed by ablating spots between 40 and 20μm in diameter, depending on sulfide grain size repeating at a rate of 5 Hz for 60 seconds. Total analysis time was ~90 seconds per spot, including a pre-ablation and background measurement period. Element acquisition times were controlled by element type: major silicate/ carbonate elements were set at 0.005 seconds, minor silicate/carbonate elements at 0.01 seconds, in addition to Fe and As; transition metals (e.g., Co, Ni, Zn, and Mo) at 0.02 seconds; Te and Pt at 0.05 seconds; Au at 0.1 second; and all other elements at 0.02 seconds, for a total of 45 elements.

Data reduction was achieved using standard procedures (Longerich et al., 1996), using Fe as the internal standard. The primary standards (STDGL2b2 and GSD-1G; Danyushevsky et al., 2011) were analyzed twice each after every 30 unknowns with a 100-μm beam size at a frequency of 10Hz to correct for instrument drift. The porous nature of syngenetic and diagenetic pyrite results in a variable amount of matrix also being ablated. Quantification of the mixed pyrite/matrix signal was conducted by analyzing all major elements in the mix and normalizing the total of the analysis to 100 % (g/g). The composition of the silicate matrix was determined in each sample by analyzing several spots around the diagenetic pyrite. With the composition of the matrix known, the compositions of pyrite were derived from the analysis of the mix with a standard mass-balance approach. Concentrations of all major silicate elements, but Fe (i.e., Al, Mg, K, Na, Si, Ti) were used to estimate the proportion of matrix in each analysis by a least squares method. All analyses with silicate matrix over 50%, or analyses where the method for estimating the amount of matrix gave large errors, were excluded from the data set. Pyrite

data that showed large inclusions of other sulphides was also excluded, when Zn and Pb > 20,000 ppm, Cu > 30,000 ppm, As > 10 wt% or 0.5<Fe/S<1.2.

Rationale

Analysis of the trace element content of pyrite provides a context to study the chemistry at the time of deposition as this would represent the conditions within the basin. It is observed that the syn-sedimentary to early diagenetic pyrite here hold an abundance of trace metals suggesting that the metals were present in the water column during the time of the pyrite formation. The ultimate source of these metals may be debated (i.e. Lehmann et al., 2007) however, the elements enriched in the shale and the pyrite (Ni, Zn, Cu and Co) are the same elements commonly enriched in black shales formed in anoxic to euxinic basins (Claver and Pedersen, 1993).

The use of pyrite chemistry to infer the conditions present during deposition is a relatively new method (Large et al., 2014, Gregory et al., 2015) that may have merits over the traditional whole rock geochemical method. Namely, this approach negates the complications of differing mineralogical components within which trace elements can partition. Sediment source, bio-productivity, basin architecture and the types of organisms that are present in the water column, and the upper sedimentary layers can heavily influence the differing mineral assemblages of black shale. This means that comparisons of whole-rock geochemical data from different localities could be problematic when building a regional to global framework.

The analysis of syn-/diagenetic pyrite by LA-ICPMS has a number of potential advantages over traditional whole rock geochemistry. First, there is no dissolution of the sample; thus there is no associated dilution, allowing for greater sensitivity. This allows the analysis and quantification of a wider range of elements that would be below detection limits using traditional techniques. Secondly, the majority of redox sensitive metals traditionally used to interpret paleo-ocean conditions (Ni, Zn, Cu, Pb, Se, Mo, Th, Mn, Co) all show a high affinity to be incorporated into pyrite, usually at 2–3 orders of magnitude more than is present in whole-rock analyses (Large et al., 2014).

Evaluation

Whole-rock trace element analyses, normalized to Al, which has been the established method to display trace element data and, in turn, has be proven to be reflective of conditions present during deposition, was compared to pyrite In the same way that Al is used to normalize whole-rock data, the sulfur content of pyrite has been to normalize our pyrite trace element data, since the majority of trace elements replace the Fe site in the pyrite lattice (Huerta-Diaz and Morse, 1992). Once both sets are normalized, the relative enrichments of the majority of elements are very similar (within one order of magnitude, Fig. 5.A.2.). The exception to this is Ba and Co, which is likely due to them being held within pyrite as well as other mineral phases (e.g. Ba in feldspars and micas, and Co within clastic material, complexed with organic matter or, potentially, hindered by slow reaction kinetics with pyrite, leading it to form its own CoS phase under reduced conditions; Bishop, 1988; Huerta-Diaz and Morse, 1992).

Zinc makes a notable shift in both whole-rock and pyrite in the lowermost 1m of the shale, which represents the transition from euxinic to anoxic conditions. Zinc forms a solid solution with Fe-sulfides under euxinic conditions where it is limited by Fe and H_2S production or, to a lesser degree, may form its own sulfide phase (Huerta-Diaz and Morse, 1992). Whereas under anoxic conditions, it tends to form metal-organic clusters and would partition into organic phases (Huerta-Diaz and Morse, 1992; Algeo and Maynard, 2006). This may explain the range in Zn values in this interval. Manganese shows less correlation moving up stratigraphy however this can be explained by progressive oxygenation of the water column or changes in detrital input where Mn is held within Mn-Fe hydroxide detritus (Huerta-Diaz and Morse, 1992). Ni and Co show an inverse pattern which can be attributed to contrasting redox potential i.e Ni increases during reduced conditions and Co increases with increasing oxidized conditions where it is held in hydroxide detritus. Normalised values for Mo in pyrite directly follow that of whole-rock, suggesting that Mo is exclusively held within pyrite. The profiles of the sulfide forming elements are similar, or close, to that of whole- rock normalized profiles, especially in the lower intervals where euxinic conditions are interpreted to have dominated. This matches with the expectation that sulfide forming chalocphile and siderophile elements would strongly partition into pyrite under euxinic conditions and less so under anoxic but non-sulfidic conditions.

The potential issue of variation in sulfur content in pyrite (attributed to As and Se replacing S in the structure of pyrite; Deditius et al., 2008) and the large deviations (up to 10%) in our ability to quantify sulfur effectively is acknowledged. However, the data is still comparable with the whole-rock Al normalized points and further development of the data reduction method to mitigate quantification errors will only improve this methodology. We have been able to show that the same redox-sensitive trace element enrichments used by many previous workers can be mirrored or better resolved using this pyrite method. With careful sample collection and analysis, the ubiquitous occurrence of pyrite in many black shales can be utilized to great effect.

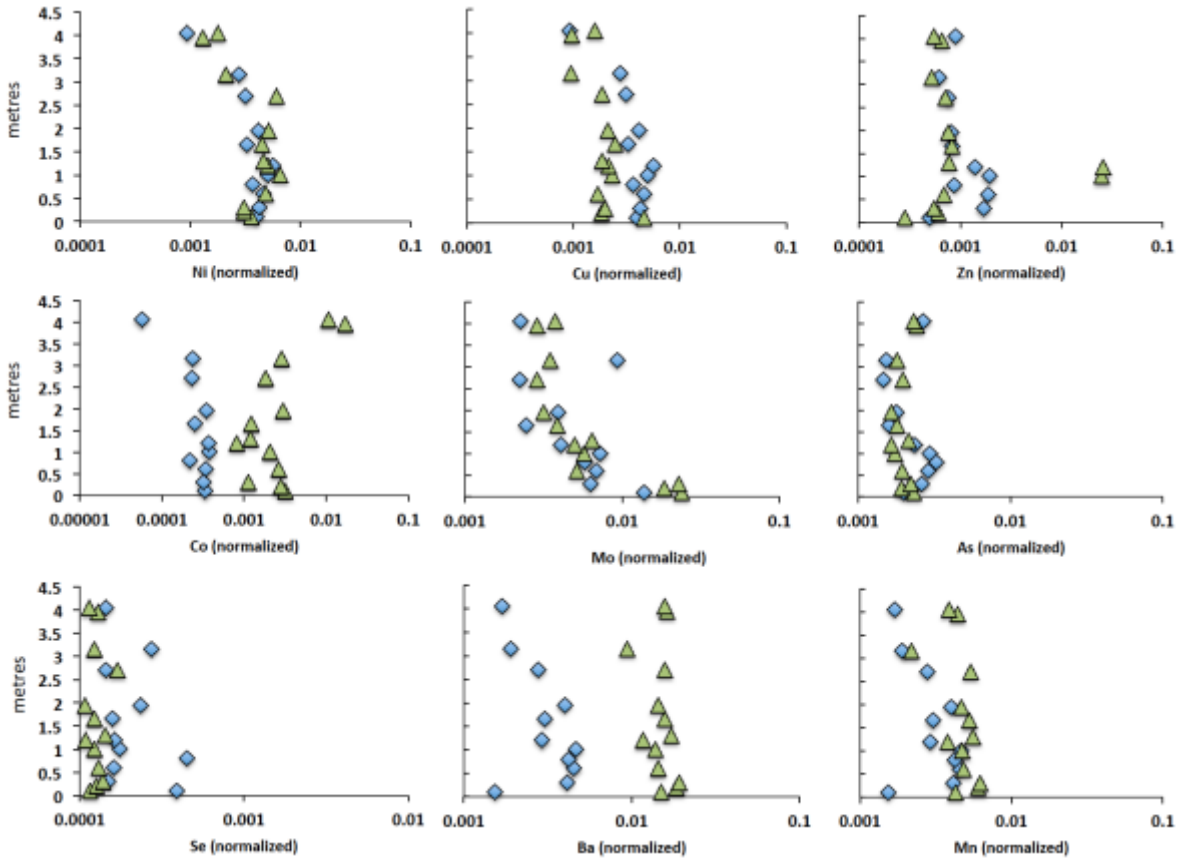

Figure 5.A.2. Plot of normalized (*S) pyrite chemistry (diamonds) and normalized (*Al) whole-rock chemistry (triangles).

Chapter 6

Primary metal enrichments and metamorphic effects in the formation of the world's largest poly-metallic black shale deposit.

6.1. Foreword

This chapter focuses on the origin and metal enrichment mechanisms at the Talvivaara Ni-Zn-Cu-Co deposit, Finland. The Paleoproterozic Talvivaara deposit is, by volume, the world's largest black shale-hosted deposit. This presents a unique opportunity to understand the metal enrichment processes that may have contributed to its formation. The deposit shares some commonalities with the Cambro-Ordovician Turisalu Formation discussed in the last chapter, as both were deposited during periods of anoxia in the wake of global carbon perturbations. The Talvivaara black shale host rocks were deposited ~2.0 Ga, in the wake of the Great Oxidation Event and towards the end of the largest Carbon isotope excursion recorded in the geological record- the Lumagundi-Jatuli (~2.1 to 2.0 Ga), and is coeval with mass accumulations of organic matter- the Shunga Event (~2.0Ga to 1.98 Ga). The curious occurrence of metal-rick black shale during this period of perturbation suggests that there may be a causal relationship. Furthermore, since the deposit has been metamorphosed, this study provides a challenge as to whether various paleo-environmental techniques can still be used and, critically, what effects does metamorphism have on the black shales and their enrichments. A version of this chapter has been reviewed by Dr. Iain Pitcairn and Prof. Sarah Gleeson for publication in Economic Geology. The reviewers felt aspects of the rock descriptions, sedimentology and zircon geochronology would be better served in a separate publication that focused on the regional and deposit-scale geology. The revised version is presented below but the zircon geochronology has been included in the chapter as it is of importance.

6.2. Understanding the depositional environment, metal enrichment and metamorphic effects at the Paleoproterozoic Talvivaara Ni-Zn-Cu-Co deposit, Finland.

6.2.1. Abstract

The Paleoproterozoic amphibolite-grade, black schist-hosted Talvivaara Ni-Zn-Cu-Co deposit appears unique in regards to its metal endowment and formation. Presented here are whole rock geochemistry, in-situ trace element data, and $\delta^{34}S$ values of sulfides through the stratigraphy of the deposit. Deposition of the Talvivaara shales took place in a rift basin at ~ 2.0 Ga. The host-rock comprises of thick homogenous black shale (now schist) with intermediate cm and decimeter- scale, medium-grained sandy horizons, interpreted to relate to mass flow depositional sequences. Whole-rock geochemistry display high concentrations in a range of redox sensitive and bio-essential trace metals. This is similar to other metal-rich black shales deposited during Phanerozoic anoxic events. Analysis of early diagenetic and metamorphic sulfides show that the earliest pyrite is enriched in range of trace elements compared to those that formed during metamorphism. It is proposed that the metal enrichment can be linked to primary enrichment due to the redox state of the seawater and the basin, facilitated by perturbations in the atmosphere-seawater cycle. Here it is suggested that the Talvivaara deposit represents an extreme end-member of metal-rich black shales, governed by similar primary metal enrichment processes as Phanerozoic examples. However, Talvivaara developed on a more profound scale in the wake of the Great Oxidation Event, when enhanced oxidative weathering delivered more metals and bio-essential elements to ocean basins, effectively, preconditioning the basin with metal–rich sediments. Metamorphism led to the breakdown and recrystallization of the majority of primary pyrite and organic matter, liberating trace elements that formed additional sulfide phases.

6.2.2. Introduction

Black shales are fine-grained, laminated, siliciclastic deposits that contain appreciable amounts of organic carbon and pyrite. They are deposited under low-oxygen bottom water conditions on continental shelfs and marine basins. They are commonly enriched in a range of redox-sensitive and bio-essential trace elements (TE) including P, Mo, Ni, Co, Zn, As, Cu, Se, U, or V. The metal enrichment can be a function of a combination of processes, including: (1) up-take from seawater by phytoplankton and related species; (2) direct absorption onto organic matter and detrital particles; and (3) incorporation of important trace metals Ni, Co, Mo, Zn, As, Se, Cu, Pb, and Sb into sedimentary pyrite during sedimentation and early diagenesis (Huerta-Diaz and Morse, 1992; Piper and Merando, 1994; Mao, et al., 2002; Tribovillard et al., 2006; Gregory et al., 2014). Metal enrichment requires conditions conducive to the accumulation of a large amount of organic matter (such as low oxygen) and slow accumulation rates in order to maximize the concentration of trace metals (Algeo, 2004; Perkins et al., 2008). Due to their large extents, and in many cases significant metal endowments, black shales present important economic targets as well as being critical source rocks for orogenic-style mineralization (Large et al., 2007; Pitcairn et al., 2010; Cave et al., 2015).

In comparison to other shales or average crustal rocks, black shales show significant enrichment in organic carbon, sulfur and redox-sensitive metals, such as P, U, V as well as those that can be sulfide-forming (i.e. Mo, As, Cd, Cu, Ni, Zn, Pb, and Co) (Vine and Tourtelot, 1970, Algeo, 2004, Tribovillard et al., 2006). Trace metals such as Mo, Cu, Ni and Zn also play an integral role in many biological processes and are common in organisms such as nitrogen-fixing bacteria and algae (Anbar, 2004). Redox sensitive metals (i.e. Mo, Zn, Cu, U) have higher rates of transfer to the sediment at lower redox potentials due to uptake by organic matter or authigenic minerals (Morford and Emerson, 1999), therefore, the redox state of the overlying seawater can exert a strong influence on metal concentrations in shale.

The Paleoproterozoic period is characterized as having enhanced global ocean redox stratification, driven by the profound changes in atmospheric, ocean and bio-geochemistry that occurred in the wake of the Great Oxidation Event (GOE) (Melezhik et al., 2013).

Geological and geochemical data from the Talvivaara deposit in Finland, the world's largest black schist-hosted poly-metallic deposit (Loukola-Ruskeeniemi and Lahtinen, 2012) is presented and evaluated. Since Talvivaara is considerably larger than any other metal-rich black shale of the Phanerozoic, and formed in the wake of the Great Oxidation Event, it may provide significant insight as to the environmental conditions at this critical time in Earth history, and specifically whether there was a fundamental change in the processes that form metal-rich shales in the Precambrian, compared to the Phanerozoic. In order to understand its formation, three key aspects of the deposit genesis: 1) the age and nature of deposition of the shale host rock; 2) the origin and processes of metal enrichments in the shale, and 3) the processes by which the deposit formed and the relative timings of metal input.

6.2.3. Geology

Geological history

The Fennoscandian Shield (Fig. 6.1.) has been extensively studied due to its high metal endowment and its complex, long-lived history. The Archean-age Karelian and Kola cratons have archived some of the most profound changes in Earth's evolution, including the first supercontinent "Kenorland" (~ 2.7 to 2.4 Ga; Williams et al., 1991; Huhma et al., 2011); the rise and aftermath of atmospheric oxygen (Great Oxidation Event, ~2.4Ga, Holland, 2002), the first large-scale glaciations (2.3- 2.2 Ga, Melezhik et al., 2006), oxidized red beds, the first large-scale phosphogenesis event, the largest carbon isotope anomaly in geological history (2.1 – 2.05 Ga) and mass accumulation of organic carbon (Shunga Event, ~ 2.0Ga) (Melezhik et al., 2013). The Karelia and Kola cratons have been the focus of study to try to understand these changes (Melezhik et al., 2013 and references therein). The region itself is noted for its array of ore deposits, most of which formed between the Archean and Neoproterozoic (Huhma et al., 2011; Eilu et al., 2012).

The Shield is dominated by Archean igneous rocks (3.7-2.5 Ga). The period from 2.5-2.1 Ga was one of stable cratonic sedimentation, interrupted by episodes of extension and related mafic magmatism (Eilu et al., 2012). The first organic carbon rich sediments appear as thin layers near the top of dolomitic and tuffaceous strata of 2.3- 2.1 Ga "Jatuli" Stage rocks (Fig. 6.2.). The Proterozoic black shales of the

Kainuu region (Lower Kaleva Stage, 2.1- 1.95 Ga) represent the first abundant deposition of organic-rich sediments, characterized by quartz-rich wackes and pelites, representing mass flows, with local phosphorite-banding, silicate–magnetite intercalations and high organic carbon contents.. These sediments are thought to have been deposited on the margins of a rift basin that formed from the breakup of the Kenorland supercontinent continent (Barkley et al., 2005; Ramo et al., 2005; Eilu et al., 2012). Proterozoic strata were then deformed and metamorphosed to greenschist – amphibolite grade during the 1.91–1.78 Ga Svecofennian Orogeny (Eilu et al., 2012).

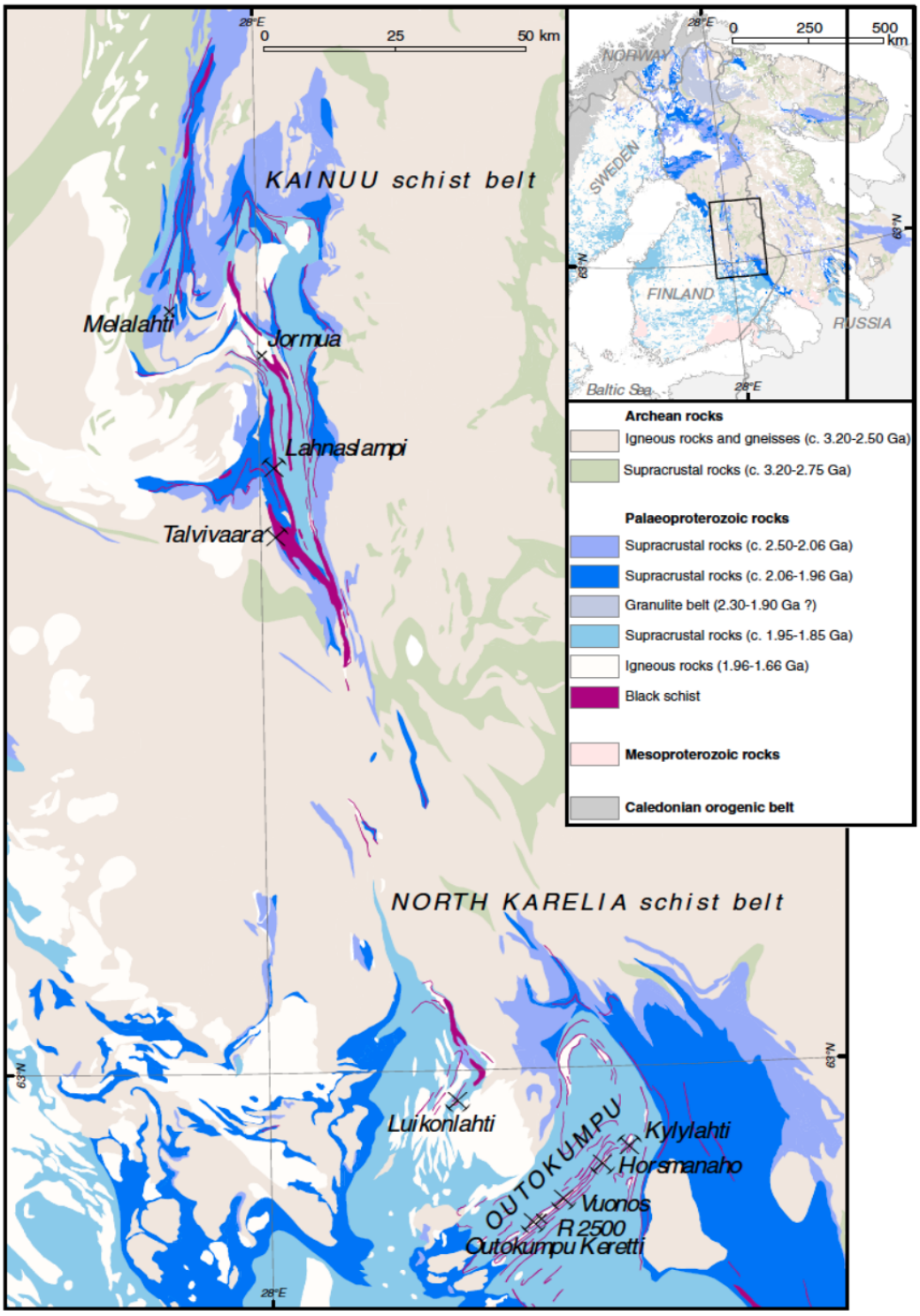

Figure 6.1. Geological map of the Talvivaara region showing distribution of Paleoproterozoic strata, particularly, black shale and major metal occurrences. From Young et al. (2013).

Deposit Geology

Talvivaara is a giant, low-grade, polymetallic (Ni-Zn-Cu-Co) black schist-hosted deposit. It is located in an extensively folded and faulted amphibolite-grade belt of Palaeoproterozoic units, bounded by the Archean crust of Fennoscandania. (Eilu et al., 2012). The lower amphibolite facies conditions (550°C and ~ 4-6 Kbar, Santti et al., 2006) and complex structures and juxtapositions produced as a result of the Svecofennian Orogeny (1.9- 1.78 Ga), make the identification of original sedimentary units and stratigraphy problematic. The estimated size of the deposit is 2053 Mt with 0.22% Ni, 0.13% Cu, 0.02% Co, and 0.49% Zn, as defined under the JORC code (Talvivaara Mining Company, 2013). The Talvivaara mine comprises two ore bodies, Kuusilampi and Kolmisoppi (Fig. 6.2.). The Kuusilampi ore body is 2.8 km long, the width varies from 40 m to 600 m and the maximum depth reached by drilling is 800 m. The Kolmisoppi ore body is 2.5 km long, the width of the ore horizon varies from 30 m to 450 m and the maximum depth obtained so far by drilling is 800 m, however, mineralization still considered to be present below this depth.

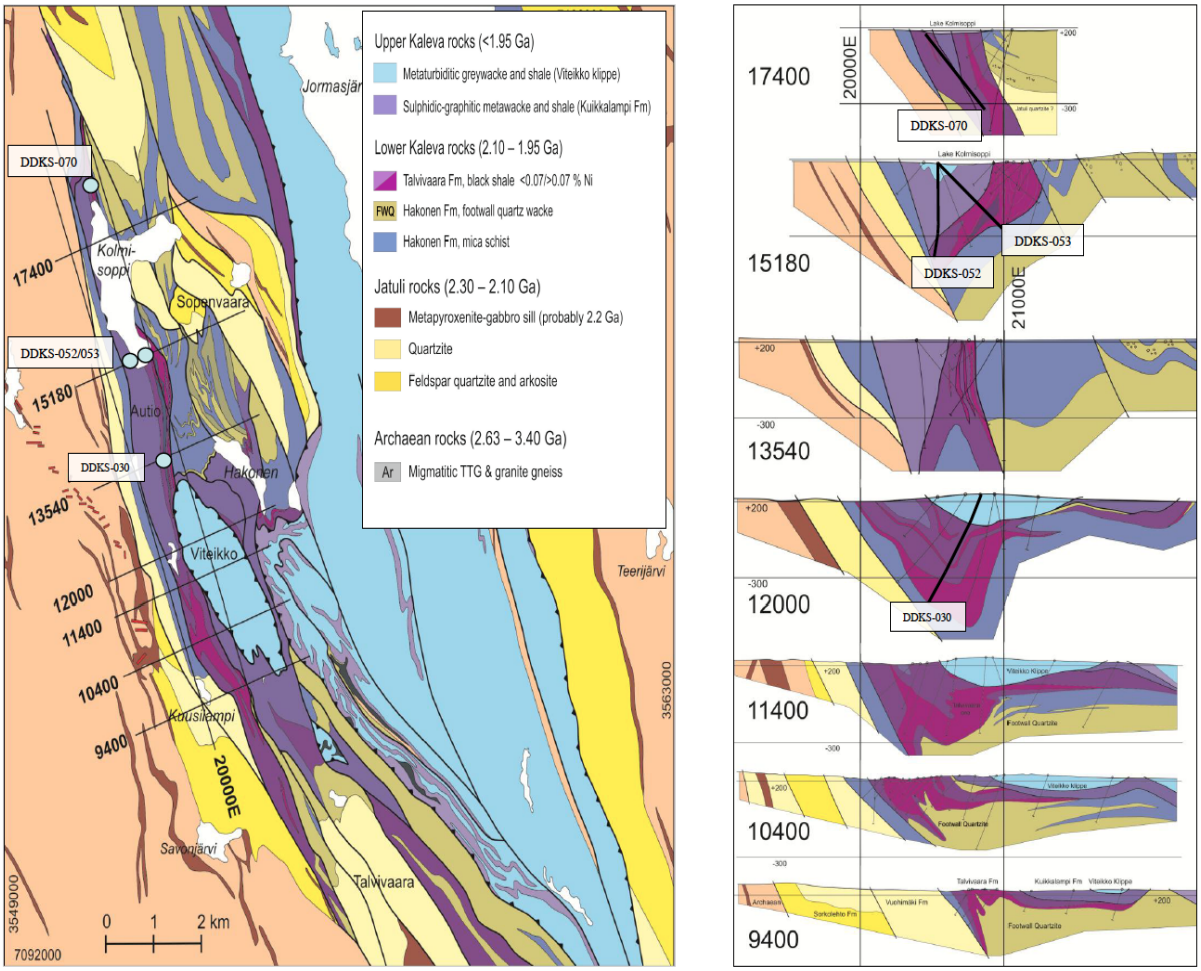

Figure 6.2. Geological map and cross sections of the deposit geology (After Kontinen et al., 2013). Circles represent collar locations of drill cores sampled.

The lithostratigraphy of the Talvivaara deposit and surrounding area is based on extensive field mapping and drilling by the Geological Survey of Finland (Kontinen et al., 2013) and indicates that the lithostratigraphy of the deposit is as follows (listed from oldest to youngest) (Loukola-Ruskeeniemi and Lahtinen, 2012; Eilu et al., 2012, and references therein: Kontinen et al., 2013. Fig. 6.3):

1. Archean gneissic- migmatitic basement.

2. "Jatuli" stage (2.3-2.1 Ga) shallow water quartzites, consisting of two main units; the Sorkolehto Formation with cross- to parallel- bedded feldspathic quartzites; and the Vuohimaki Formation containing mature, fine-grained, and often bedded, orthoquartzites. It also contains shallow water

carbonate horizons, which are time equivalents of similar rocks in the Pechenga region that record the largest known positive carbon isotope excursion- the Lomagundi event (Melezhik et al., 2013 and references therein)

3. The Lower Kaleva stage (c. 2.1- 1.95 Ga) comprises the Hakonen Formation of medium to thinly bedded metawackes, metacarbonates and metapelites with metre-scale interbeds of quartz sands and matrix-supported conglomerates, considered remnants of a series of mass flow events during the pelagic sedimentation.

4. Overlying the Hakonen Formation are the metal-rich black schists of the Talvivaara Formation. Laminated pyritic meta-mudstones and manganese-rich black schists are found in the upper parts of this formation, meta-carbonates and mass flow-related coarse-grained sands increase towards the base. The highly metal enriched black schists in lower part of the Talvivaara Formation denote the Talvivaara ore horizon.

5. The Upper Kaleva stage (1.95-1.90 Ga) constituting the Kuikkalampi Formation is chiefly composed of medium to thinly bedded massive black to dark grey feldspathic metawackes with frequent, laminated, pyritic black shale interbeds.

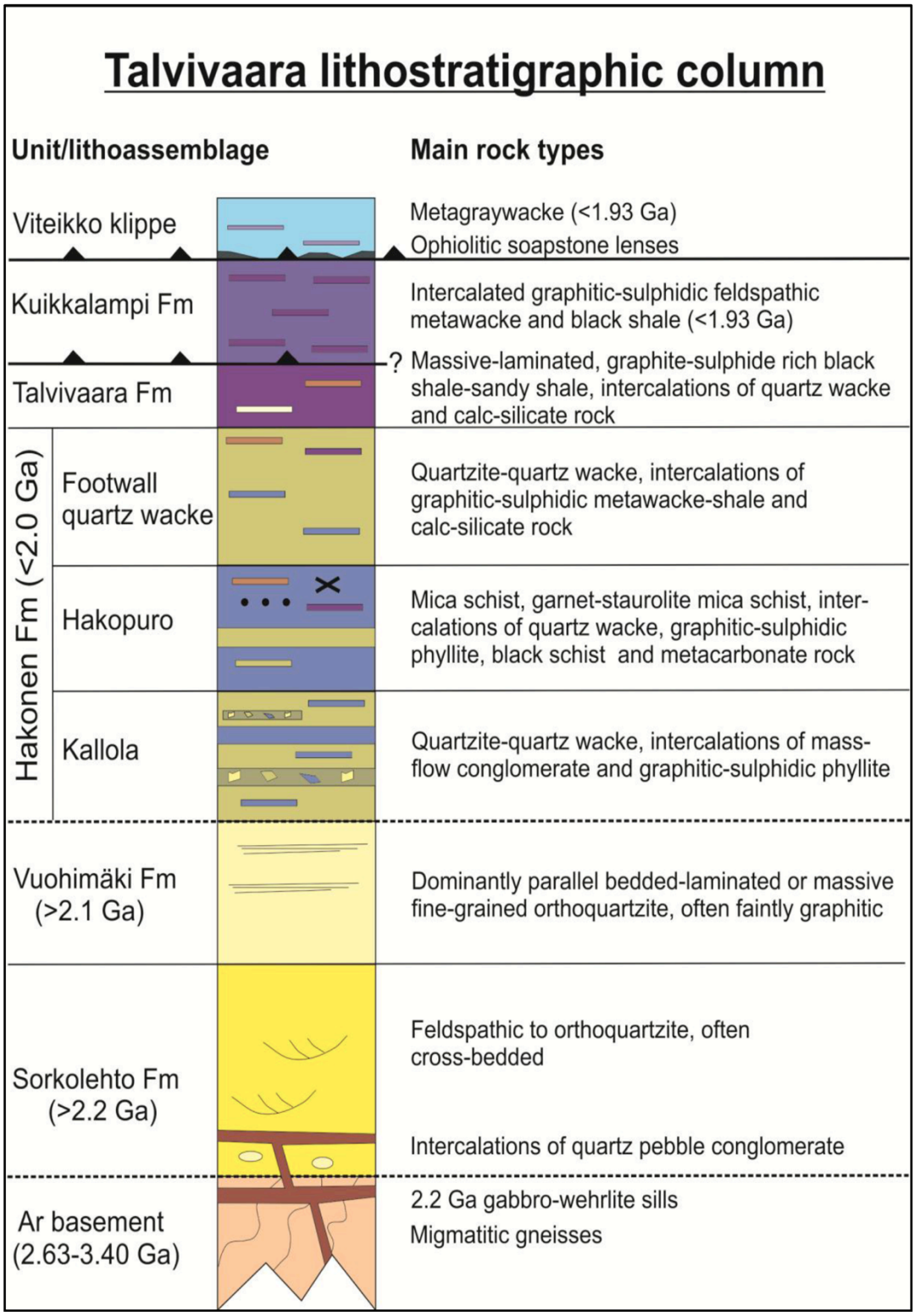

Figure 6.3. Summary stratigraphic log of deposit geology (adapted from Kontinen et al., 2013).

6.2.4. Previous work

The black schists of Finland were initially studied due to their proximity to the mineralized ultramafic rocks of the Jorma- Outokumpu Ophiolites and its potential connection to the base metal enrichemnts in the black schists (Loukola-Ruskeeniemi, 1991). The depositional age of the host rocks to the deposit have been constrained as between 2.05 to 1.95 Ga (Kontinen and Hanski, in press., Lehtinen, et al., 2008, Humma et al. 2008). If this age is accurate, this would be coeval with many major events in Earth history, notably the termination of the Lomagundi- Jatlui Carbon Isotope Excursion (Martin et al., 2013) where enhanced productivity and mass burial of organic matter occurred in the wake of this perturbation of the global carbon cycle.

Comprehensive studies have been conducted at Talvivaara (Loukola-Ruskeeniemi, 1991; Loukola-Ruskeeniemi, 1998; Loukola-Ruskeeniemi and Heino, 1996), from which it is clear that the metal enrichments appear to be syn-sedimentary. Recently, Young et al. (2013) conducted a multi-sulfur isotope study and suggested that the hydrothermal fluids were prevalent at the time of deposition.

6.2.5. Methodology

Sample collection

Four drill cores (DDKS: 030, 052, 053 and 070) that gave good lateral and vertical context of the Kolmisoppi orebody (Fig. 6.2.) were sampled (approx. 20 cm length of split core per sample) to give a representative data set for throughout the stratigraphy (n=67). From these, samples were further screened and prioritized for study based on: location in the stratigraphy, drill logs, and consultation with mine geologists in order to gain the most representative samples of hanging wall, footwall and the ore zone; mineralogy, i.e. horizons in which pyrrhotite was dominant and those in which pyrite was dominant; texture and effects of deformation, i.e. laminated pyrite, massive, fine grained black shale and highly complex, coarse grained and cross-cutting sulfides. Drill core DDKS-052 captured a thick sequence of hanging wall, ore zone, and footwall lithologies as well as displaying the least deformation out of all the cores sampled. Therefore, 16 samples were selected as the best representation of the overall stratigraphy and submitted for geochemical analysis. Additional samples from the other drill

cores were selected for major and trace element chemistry based on similar stratigraphic level to previously selected samples, varied sulfide mineralogy, pXRF values (i.e. >3000ppm Ni, >2000ppm Zn) and texture in order to augment the stratigraphic profile captured in DDKS-052, paying particular focus to the ore horizon. Samples were processed for whol-rock geochemistry and polished thin sections, and mounts, were made for a paragenetic study, in-situ trace element analysis and isotope geochemistry.

Zircon geochronology

Previous work has helped to constrain the depositional age as being ~ 2.05 to 1.95 Ga. However much of this is based on precise age constraints of the overlying and under-lying rock units and limited detrital zircons recovered from within the deposit itself. Therefore efforts were focused on sampling some of the well-developed coarse-grained interbeds within the ore zone. The Laser ablation (LA-) ICP-MS method used in this study is now widely employed for measuring U, Th and Pb isotopic data (e.g. Fryer et al., 1993; Black et al., 2003; Kosler and Sylvester, 2003; Jackson et al., 2004; Chang et al., 2006; Harley and Kelly 2007). The zircons were first imaged using cathode-luminescence (CL) in order to ascertain the internal complexity and zonation of the zircon grains in order to target their cores for analysis.

The analyses in this study were performed on an Agilent 7500cs quadrupole ICP-MS with a 193 nm Coherent Ar-F gas laser and a Resonetics S155 ablation cell at the University of Tasmania. Down hole fractionation, instrument drift and mass bias correction factors were calculated using 2 analyses on the primary 91500 standard (Wiedenbeck et al., 1995) and 1 analysis on each of the secondary standard zircon standards Temora (Black et al., 2003) and JG1 (Jackson et al., 2004) taken every 15 samples. Additional secondary standards (The Mud Tank Zircon of Black Gulson (1978), Penglai zircons of Li et al. (2010), and the Plesovice zircon of Slama et al. (2008)) were also analyzed. The correction factor for the $^{207}Pb/^{206}Pb$ ratio was calculated using NIST610, analyzed after every 30 unknowns, and corrected using the values of Baker et al. (2004).

Zircons were sampled using 32 micron spots at 5 Hz and a density of approximately 2 J/cm^2. The data reduction used was based on the method outlined in detail in Meffre et al. (2008) and Sack et al. (2011).

Sulfur isotope analysis

In-situ sulfur isotopic ($\delta^{34}S$) measurements were conducted on a range of ore sulfide minerals. Analyses were conducted at the N.E.R.C. Isotope Community Support Facility in the Scottish Universities Environmental Research Centre using the procedure outlined in Fallick et al. (1992). All sulfur isotope results are expressed in the conventional delta ($\delta^{34}S$) value, as per mil (‰) deviations relative to Cañon Diablo Troilite (CDT). Reproducibility, based on duplicate analyses as well as internal and international standards, was better than 0.3‰. The sulfur dioxide produced was purified via a series of cryogenic separations before being introduced directly and analyzed on-line by a duel-inlet VG SIRA 2 mass spectrometer. Correction factors were applied for laser-induced, mineral-specific fractionation during the combustion process using the values of Wagner et al. (2002).

Whole-rock geochemistry

Whole-rock geochemistry was conducted on samples that were crushed and milled to a fine powder. From these, fusion discs were prepared and then analyzed for major and trace elements using a PANalytical Axios Advanced X-Ray Spectrometer at the University of Tasmania. Corrections for mass absorption were calculated using PANalytical Super-Q software with its calibration model and alpha coefficients. In house inter-element corrections were also applied. Calibration was conducted using the procedure outlined in Robinson (2003). For trace elements and REE, solution ICP-MS was used. Powdered samples were digested and then analyzed on an Agilent 7700 ICP-MS with a 3rd Generation Octopole Reaction System using the procedures outlined in Yu et al. (2001).

C/S % analysis

Aliquots of homogenized material were analyzed on an Eltra 2000 C/S analyzer that was optimized daily. Standards were run every 15 samples to account for potential instrument drift. Accuracy and reproducibility, was better than 0.05 wt% for carbon and 0.1 wt% for sulfur, respectively. For analysis of total S and total C, between 100- 200mg of powdered sample were combusted at ~1200°C for 55

seconds where the gases were purified and analyzed in real time via four infra-red detectors. Corg % (total C – $C_{carbonate}$ = Corg (organics+ graphite)) was conducted in the same way, however the powdered samples were pre-treated using an acid treatment of 6N HCl on a hotplate at 70°C for 12 hours to promote the dissolution of carbonate carbon species but preserve graphite and organic phases, then rinsed with deionized water and oven-dried overnight.

In-situ trace element geochemistry of pyrite and pyrrhotite phases

All laser ablation analyses were conducted on 2.5cm polished mounts at CODES, University of Tasmania using a New Wave 193 nm Nd-YAG solid-state laser microprobe coupled to an Agilent 7700 quadrupole ICP-MS. The method is described in detail by Danyushevsky et al. (2011). Data reduction was achieved using standard procedures (Danyushevsky et al., 2011, after Longerich et al., 1996), using Fe as the internal standard. The primary standard was a Li borate fused glass developed at CODES (STDGL2b2; Danyushevsky et al., 2011).

Element maps of selected areas were obtained by ablating a series of parallel lines to raster across a sample. Lines were rastered at a speed double that of the beam diameter (i.e., 70 μm/s for a 35 μm spot). A set of 42 elements was chosen for imaging, with acquisition time for most elements set to 0.002 seconds. Certain elements of interest (Ni, Se, Co, Cu, Zn and Au) were analyzed for longer periods. Background levels and instrument drift were measured before and after each image. Processing of the image involved applying a median filter in order to reduce artifacts, subtraction of background from filtered counts, replacement of filtered counts below background values with the standard deviation value for that element, and the production of a logarithmic color-scale image for each element.

6.2.6. Results

Lithology

The Hakonen Formation, which sits below the Talvivaara Formation is dominated by massive quartzite-psammite with intercalations of metre scale conglomeratic horizons and sulphidic-graphitic mica schist horizons which are on the order of tens of metres in size (Fig. 6.3.). There is a gradational contact between the Hakonen and the overlying Talvivaara sequence from quartz-wacke to the massive black schists that comprise the majority of the unit. Varying proportions of quartz, microcline, anorthite, phlogopite and muscovite dominate the schists. Carbon occurs mainly as crystalline flakes of graphite throughout the rock mass, or as bitumenous coatings on uraninite (Lecomte et al., 2014). In the lower parts of the Talvivaara Formation calc-silicate intercalations are common which often include tremolite, garnet and chlorite. Manganese-rich spessartine garnet is also found here, associated with the calc-silicate horizons (Kontinen and Hanski, in press). Alabandite is found associated with carbonate veins in calc-silicate intercalations and it most common in the upper portion of the unit. However alabandite can be found in varying amounts throughout the stratigraphy. Moving up through the Talvivaara Formation, cm-scale bands of black phosphatic beds are found. These tend to be found in the lower portions of the metal-rich black schists and also above the main ore zone. Minor graphite-quartz-dominated horizons also occur, within cm to dcm-scale, medium-grained, psammitic units. These units are often coarser towards the base and likely represent former mass-flow deposits. Textures in the black schists, in the main ore horizon, are variable depending on the degree of deformation. In the least deformed zones, thin beds of laminated, fine-grained, pyrite are often found here and increase in frquencys towards the top of the Talvivaara Frm (Fig. 6.4). Massive, thickly-bedded black schists are also common in the main ore zone. They often include dispersed, fine-grained sulfide minerals, usually pyrite, pyrrhotite and sphalerite. In more deformed areas, reworking and mobilization of sulfides into coarse blebs and veinlets are common (Fig. 6.4; Kontinen et al., 2013; Loukola-Ruskeeniemi and Lahtinen, 2012). In this zone pyrrhotite, and minor chalcopyrite stringers, are much more common than pyrite. The overlying Kuikkalampi Formation is lithologically similar to the Talvivaara Formation, as graphitic-sulfidic micas schists are also dominant (Kontinen et al., 2013). Towards the top of the

sequence there is an increase in quartz content, possibly reflecting changes in the nature of deposition. Minor minerals present throughout the stratigraphy include apatite, monazite, rutile, tourmaline and zircon. In zones of greatest deformation, leucosome-style quartz- mica-plagioclase veins occur. These are associated with the presence of coarse-grained pyrite.

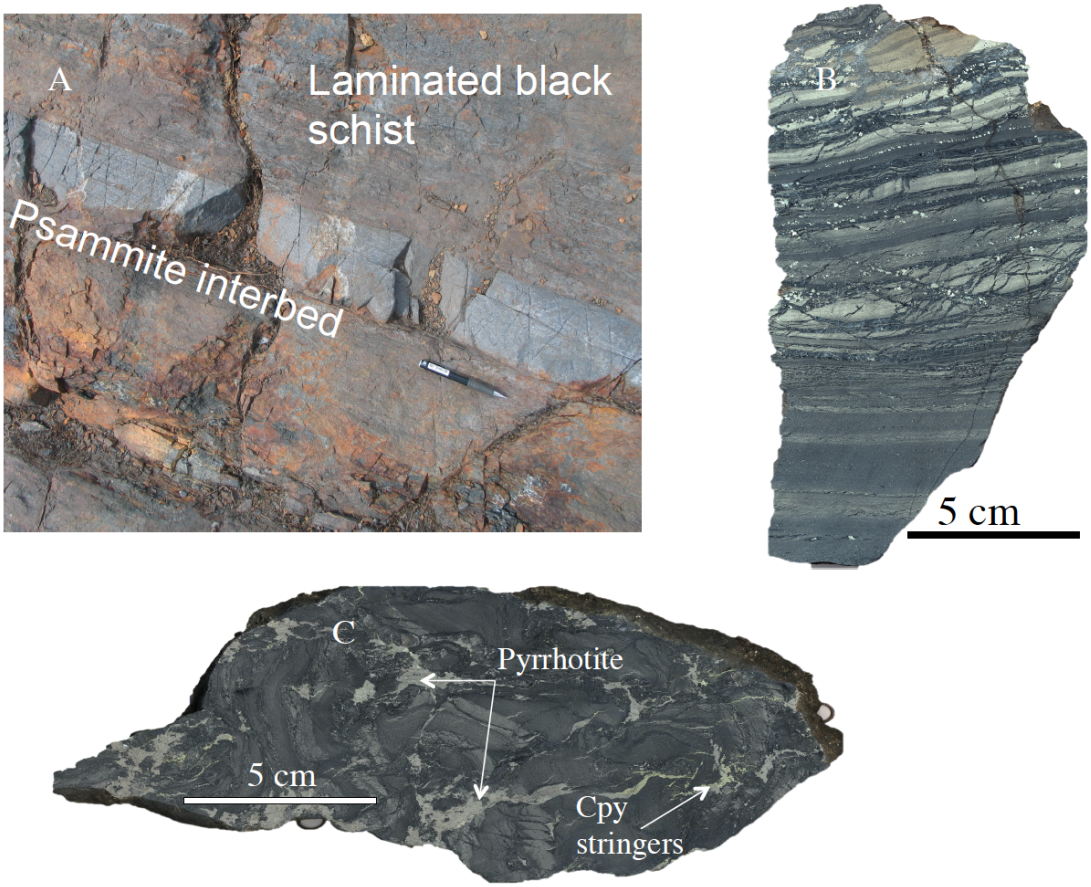

Figure 6.4. Examples of macroscale textures. (A)Outcrop photograph of Talvivaara host rocks. Finely laminated black schists with a quartz-rich interbed, likely representing periods of mass flow deposition. (B) laminated pyritic black schist above main ore horizon. (C) deformed pyritic laminated black shales with semimassive, disseminated and coarse 'blebby' pyrrhotite and chalcopyrite stringers

Sulfide paragenesis

A variety of textures are observed in hand-specimens and in thin-section (Fig. 6.4, 6.5, 6.6) these range from, relatively, undisturbed pyritic laminations and disseminated, fine-grained pyrite in less deformed zones to intensely veined, highly deformed, massive sulfide with multiple sulfide minerals and generations. The main sulfide mineral assemblage contains abundant pyrite and pyrrhotite, as well as pentlandite, sphalerite, chalcopyrite, alabandite, molybdenite and minor galena. Detailed microscopy suggests 4 main stages of sulfide. These stages are described below and examples are shown in Figures 6.5 and 6.6:

Stage 1. Early (diagenetic/ syn-sedimentary) fine grained (<20μm) spherical pyrite. In drill core and thin section, these often appear laminated or occur parallel to interpreted relic bedding. These pyrites (Py1) are interpreted to represent syn-sedimentary to early-diagenetic pyrite formation (i.e relic pyrite frambiods). The majority of pyrite is less than 10 μm, this has been suggested to represent original frambiodal pyrite formation in an euxinic water column (Wilkin et al., 1996).

Stage 2. Prograde metamorphic sulfides. Fine to medium grained (> 50 μm to <200 μm) pyrite (Py2), minor, fine grained galena, sphalerite, chalcopyrite, alabandite, molybdenite pyrrhotite and pentlandite. Pyrite in this stage (Py2) is coarser and euhedral compared to those of Py 1. Pyrite tends to form along the metamorphic fabric as a result of recrystallized clusters of earlier pyrite or as porphyroblasts (Fig. 6.5.A.). Often small amounts of graphite and metamorphic silicates form in pressure shadows around the margins of Py2. Pyrrhotite varies in texture from very fine disseminations to coarse blebs or aggregates in zones of higher deformation. Pyrrhotite commonly displays pentlandite exsolutions and inclusions. Medium-grained, euhedral, pyrite (Py2), sphalerite, alabandite, and galena are often found with increasing pyrrhotite size and abundance. Sphalerite ranges in size from very fine, when present in less deformed zones, to coarse grained in areas of increased deformation (Fig. 6.6.B). Chalcopyrite is often found associated with the assemblage defined here and is most abundant in highly deformed areas, where pyrrhotite is dominant. Chalcopyrite is mechanically weakest of the sulfides present and

therefore tends to occur as mm-scale stringers or veins (Fig. 6.6.C). Alabandite occurs predominantly as coarse clusters in zones of higher sulfide abundance and deformation (Fig. 6.F). Molybdenite is rare but when it occurs it is often as fine grains and associated with graphite flakes.

Stage 3. Retrograde pyrite formation (Fig. 6.5.C; 6.5.D; 6.6.E). Pyrite (Py3) in this category overgrow, or cross-cut, stage 1 and 2 minerals. Pyrite 3 often forms as coarse (0.5 to 5mm), solitary, blebs, often overgrowing or associated with pyrrhotite margins.

Stage 4. Late-stage, vein-associated pyrite (Fig. 6.5.D.). Large (sub-mm to mm scale) euhedral pyrite grains (Py4) commonly associated with quartz veins which appear to cross cut the relic bedding and all previous genetic stages.

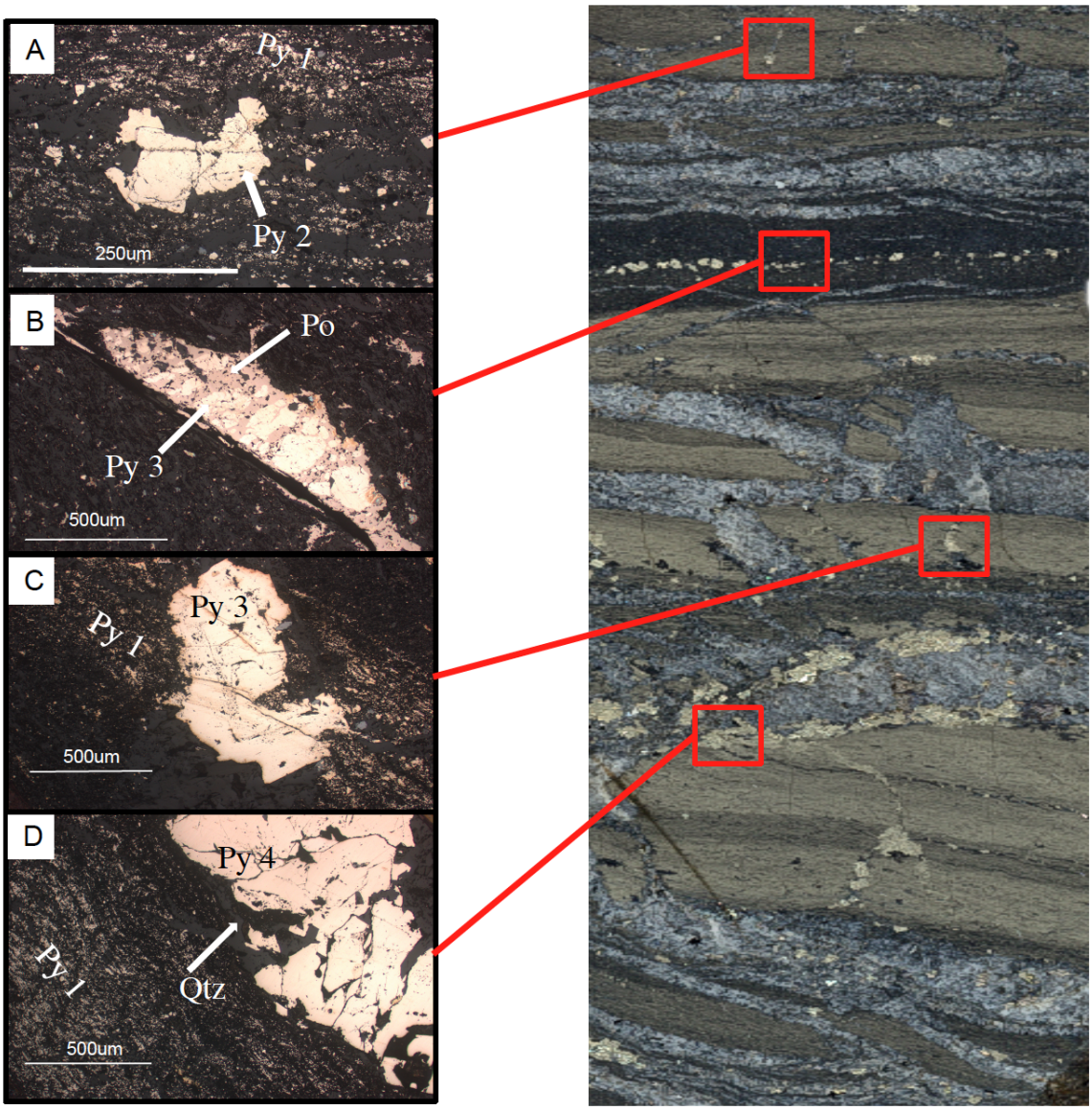

Figure 6.5. Scanned image of drill core and photomicrographs displaying examples of the range in mineral textures and relationships. Large image of core sample displaying Laminated pyritic schist disrupted by quartz veining and late stage, coarse grained sulfides. (A) Fine grained, diagenetic pyrite (Py1) along metamorphic fabric, defecting around syn-metamorphic, porphyroblastic pyrite (Py2). (B) 'blebby' pyhrrotite, pentlandite and pyrite (Py3). (C) Pyrite (Py3) cross-cutting metamorphic fabric and overgrowing Py1. (D) Late stage, coarse grained pyrite (Py4) associated with late-stage, quartz vein, cross cutting original, and metamorphic, features.

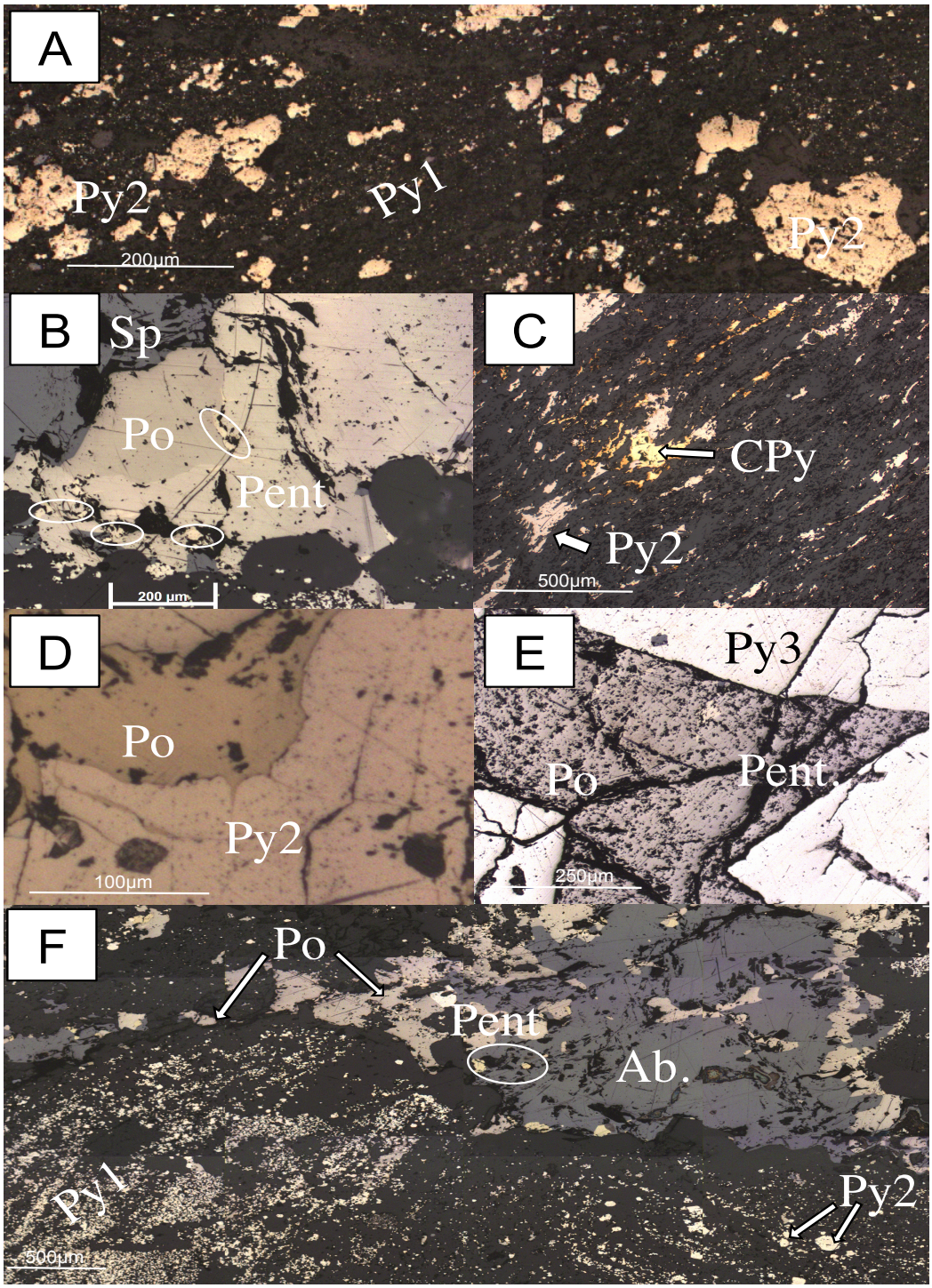

Figure 6.6. Photomicrographs of the metamorphic mineral assemblage. (A) Dispersed fine-grained Py1 and coarser, metamorphic Py2. (B) Sphalerite, pyrrhotite with dispersed pentlandite inclusions. (C) Metamorphic Py 2 and chalcopyrite stringers occurring parallel to metamorphic fabric. (D) Pyrrhotite intergrown at the edge of a larger Py2. (E) Pyrrhotite with dispersed pentlandite, overgrown by coarse, euhedral Py 3. (F) Coarse, alabandite and pyrrhotite, with pentlandite. Fine-grained Py1 and coarser Py2.

Zircon Geochronology

Due to the fine-grained nature of the black schist host rock, zircon recovery efforts were focused upon two of the cm-scale, coarse-grained, psammitic interbeds that occur within the Talvivaara ore unit (DDKS-052, 528m and DDKS-070, 465m). Seventy-eight individual analyses of zircon cores were conducted using the method detailed previously. Samples exhibiting common lead problems or loss were omitted from the final dataset which eventually numbered 49 cores with an age of 2723 ±27 Ma (Fig. 6.7.) for the average of the youngest coherent population. The zircons show a well-defined, unimodal distribution (Fig. 6.8.). There is also a distinct lack of Paleoproterozoic zircons with over 85% of analyses falling within 2.7-2.8 Ga range.

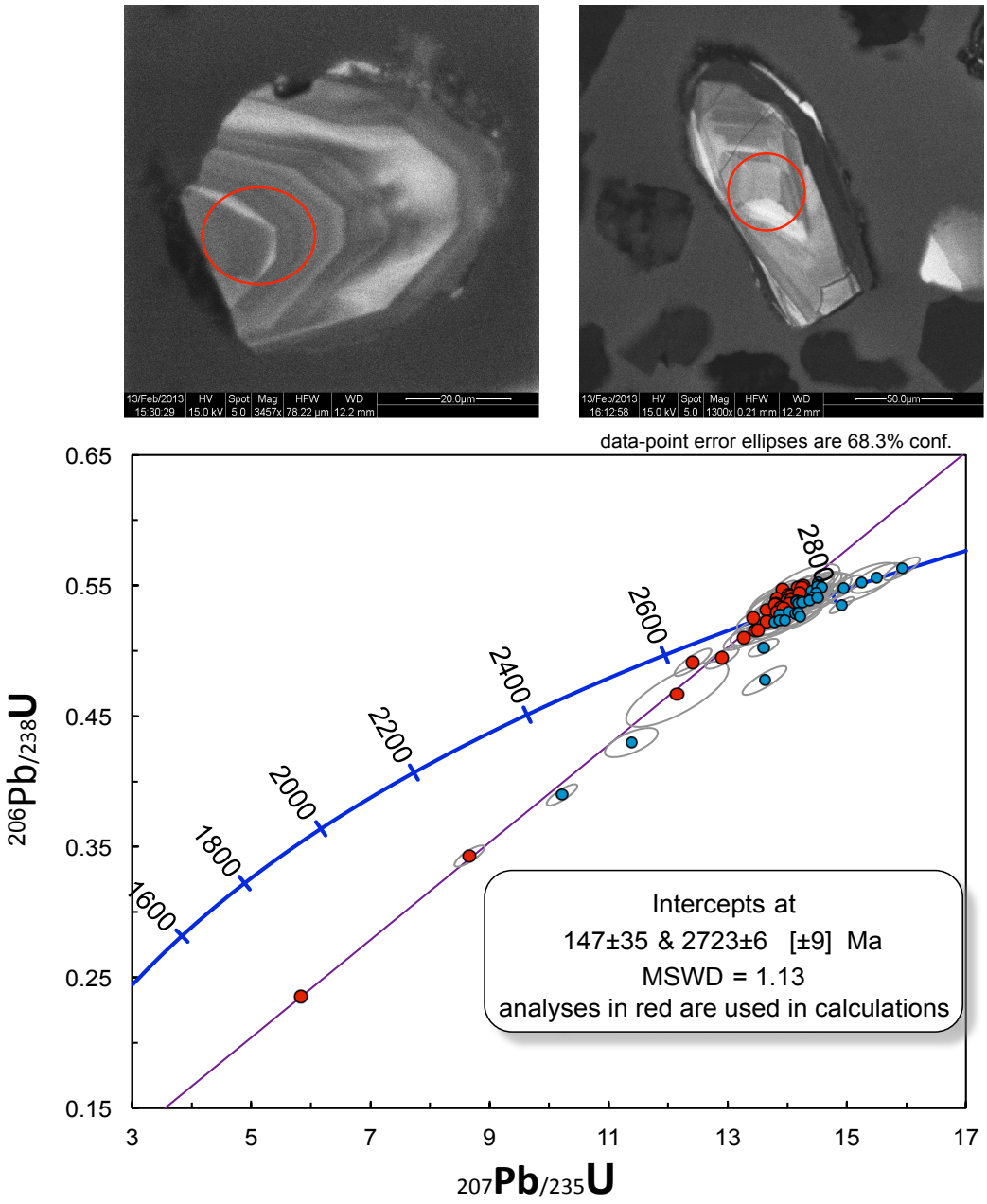

Figure 6.7. U/Pb ages of detrital zircons from within the Talvivaara metal-rich zone with CL-images of the zirons analyzed in their internal structure.

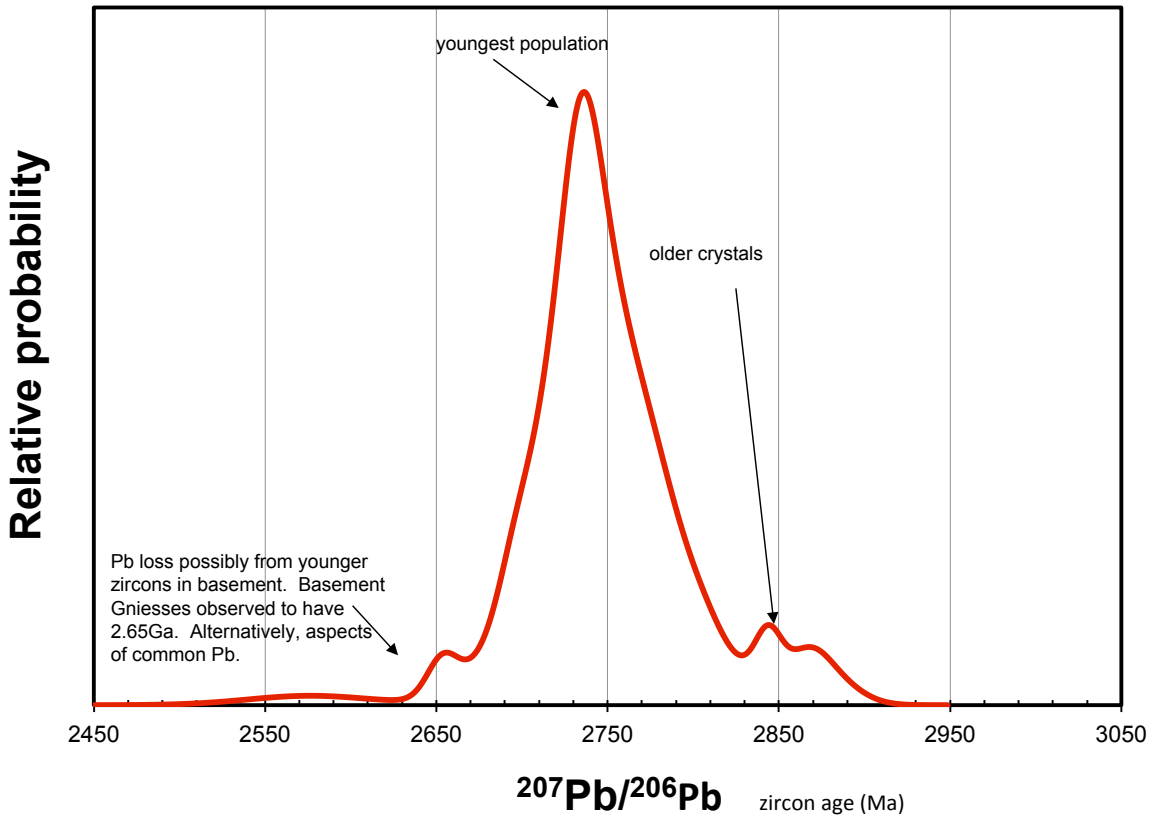

Figure 6.8. Distribution of Talvivaara zircon ages in this study.

Whole-rock geochemistry

DDKS-052 Lithogeochemistry- Major elements

Whole-rock geochemical results and corresponding sample descriptions are presented in Table 6.1. Much of the stratigraphy is dominated by SiO_2 (25-50 wt%), Al_2O_3 (7-14 wt%), FeO_2 (10-30 wt%), organic carbon (4- 15 wt%) and S (4-10 wt%). These constituents are common for black shales. CaO, K_2O and MgO are an order of magnitude higher than Na_2O. S/Fe ratios are predominantly lower than 1.15, the stoichiometric value in pyrite. Mn/Al values are mostly low throughout the stratigraphy, except for directly above and below the Talvivaara ore horizon (486m and 623m). The highly Mn-rich lower horizon corresponds with spessartine garnets that are found in greatest abundance at the base of

the Talvivaara Formation (Kontinen and Hanski, in press). P_2O_5 averages ~ 0.2 wt% throughout the most of the stratigraphy, with a high of 0.8 wt% occurring just below the ore horizon at 623m.

DDKS-052 Lithogeochemistry-Trace elements

Nickel averages >1000ppm through the entire stratigraphy, reaching >200 ppm in the Talvivaara ore horizon (Table 1.). There appears to be an inverse correlation between Ni and Mn at the top and base of the ore layer (Fig. 6.9). Molybdenum is higher in Kuikkalampi Formation where it averages >100 ppm and reaches 300 ppm in one sample, compared ~60 ppm in the underlying Talvivaara Formation. Zinc is high throughout the stratigraphy with an average of 5775 ppm, with the highest values (>10,000 ppm) encountered in the uppermost horizons of the Talvivaara formation. Copper averages >1,500 ppm in the Talvivaara Formation. compared to 445 ppm in the overlying Kuikkalampi. Vanadium, lead, selenium, and uranium are relatively uniform through stratigraphy with means of 893 ppm, 48 ppm, 39 ppm and 13 ppm, respectively.

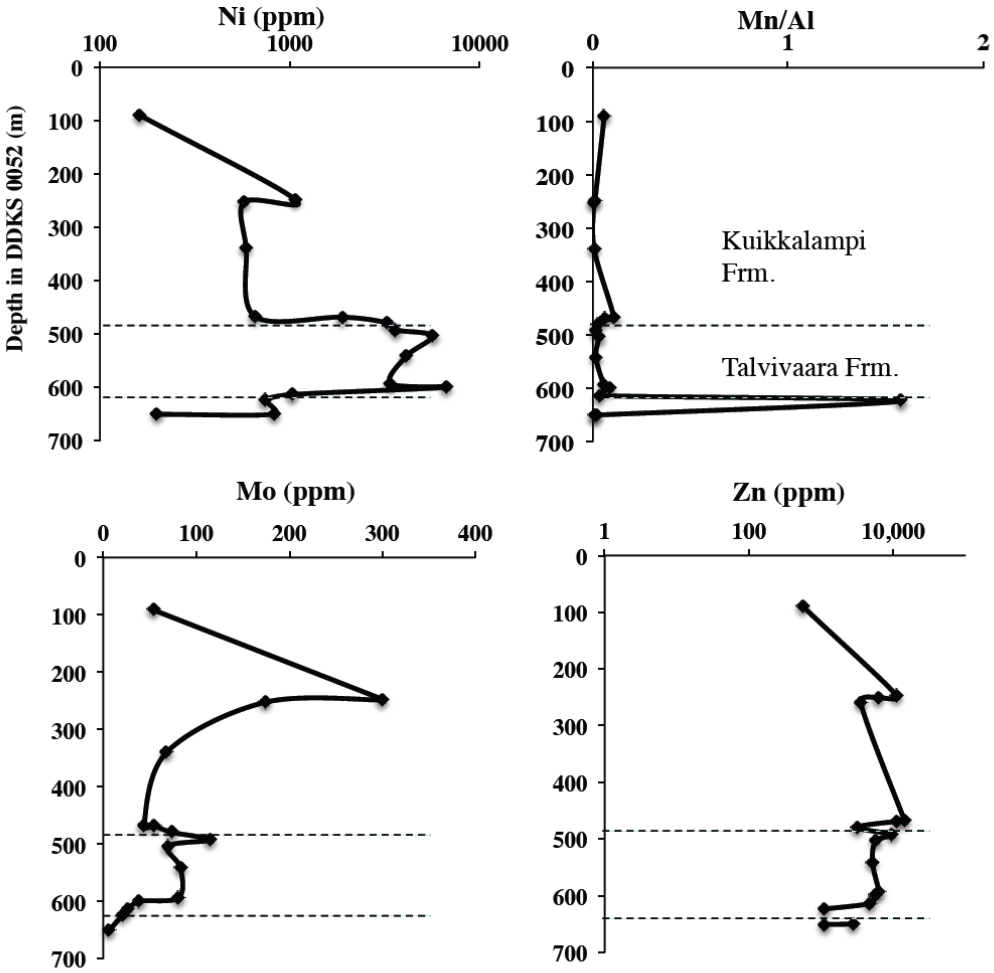

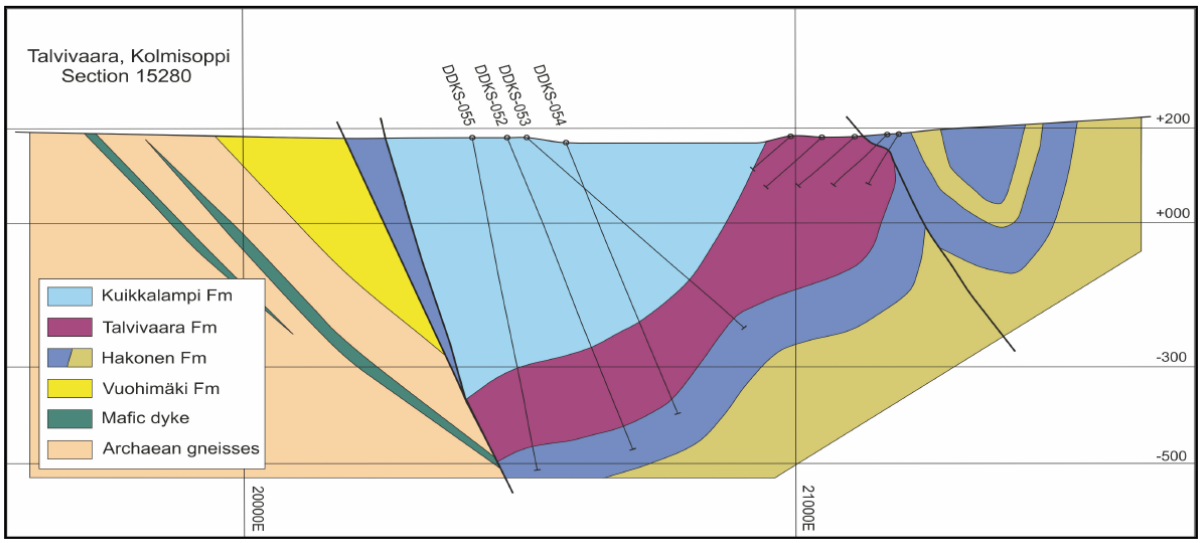

Figure 6.9. Plots of whole rock geochemistry vs depth in DDKS052.

DDKS-052 Lithochemistry-REEs

In previous studies (Loukola-Ruskeeniemi and Lahtinen, 2012; Young et al., 2013) have proposed that an Eu anomaly present at Talvivaara is evidence of a hydrothermal fluid source for the metals contained within the deposit. The transect captured by DDKS-052 offered the opportunity to investigate this in a stratigraphic context. REE concentrations have been normalized by two different references, the North America Shale Composite (NASC), which has been used in previous studies of Talvivaara, and also by Chondrite (Fig. 6.10.). The rationale for this is that NASC will show enrichments in comparison to average shale, while chondrite will be reflective of hydrothermal fluids (e.g. Douville et al., 2002). The NASC normalized REE pattern in the data remains relatively flat with a minor increase in HREEs. Only one sample, in the footwall stratigraphy, exhibits a minor Eu enrichment. In the chondrite-normalized plot a very minor Eu enrichment is observed in the same sample. This sample had garnet, rutile and was coarser grained in comparison to the overlying black schists. REE do not show any systematic correlation with base metal content (Fig. 6.10).

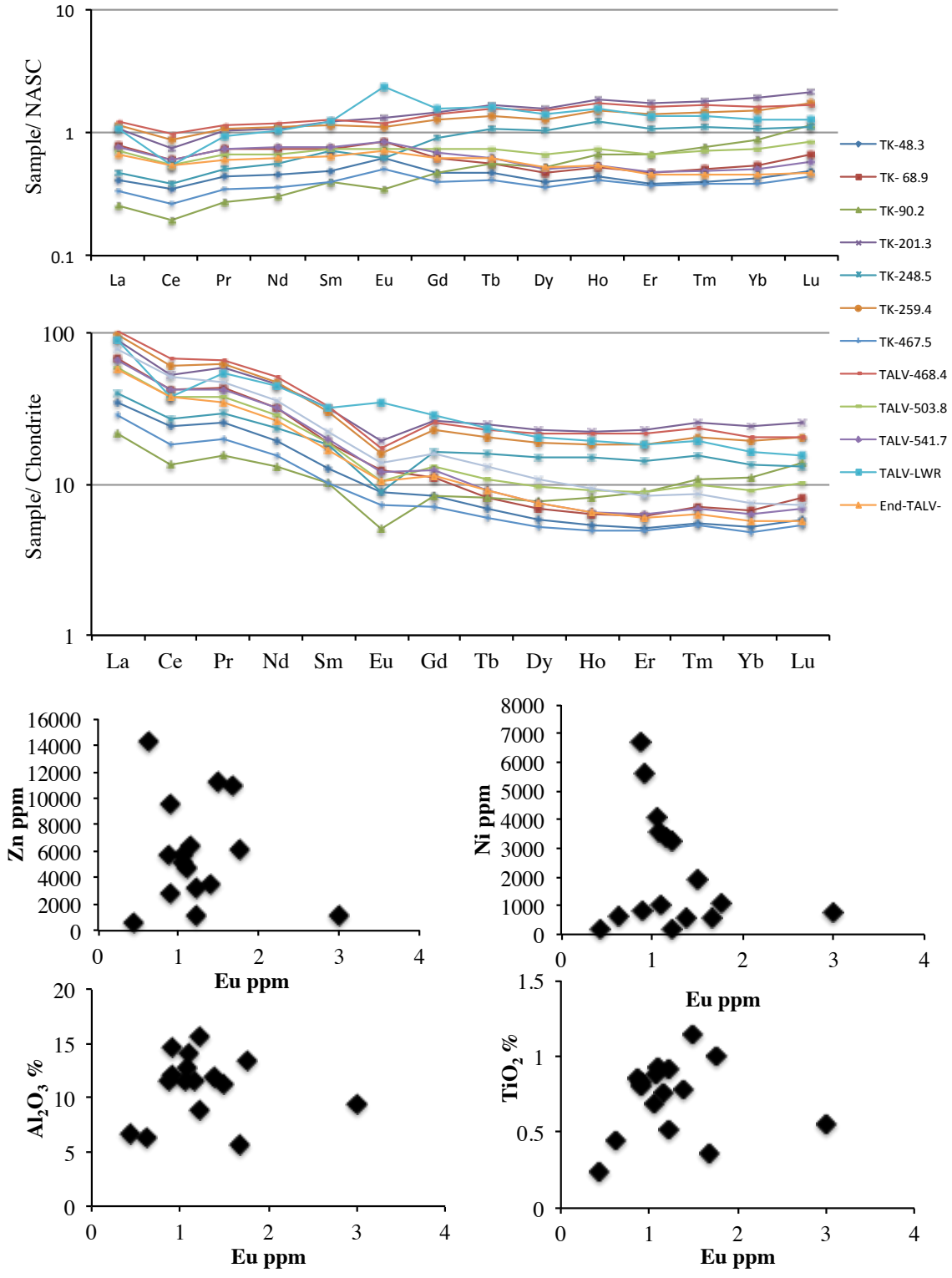

Figure 6.10. REE patterns downhole in DDKS052, normalized to Devonian Shale standard (NASC) and Chondrite. Cross plots of Eu vs key metals in the deposit- Zn and Ni, and Eu vs Al_2O_3% and TiO_2%.

Gd/Yb ratios have been successfully applied to other sedimentary sequences of potentially mixed provenance (McLennan, 1993). A spread in these values can be attributed to mixing of felsic and mafic components. Gd/Yb ratios plotted against Eu from DDKS-052 cluster in the 1- 2.5 Gd/Yb and 0.6- 1.6 Eu space (Fig. 6.11). Based on the dominance of 2.7 Ga zircons found in this study, a sample of base metal-rich Fennoscandian igneous suites of a similar age we have also been plotted for comparison. The Vetereny Belt from N. Russia is comprised of a series of Mg-rich mafics and ultramafics, this sample fits well within the range for Talvivaara sediments in terms of Gd/Yb but is slightly lower in terms of Eu content. Average komatiite composition sits lower in Eu vs. Gd/Yb space, while the Finnish Lozo Dolerite (Kapyako et al., 2006) has the highest Eu and Gd/Yb values. Other intermediate- felsic rocks (Kapyako et al., 2006) have similar Eu values but higher Gd/Yb than the Talvivaara suite and are closer in composition to average Finnish crust.

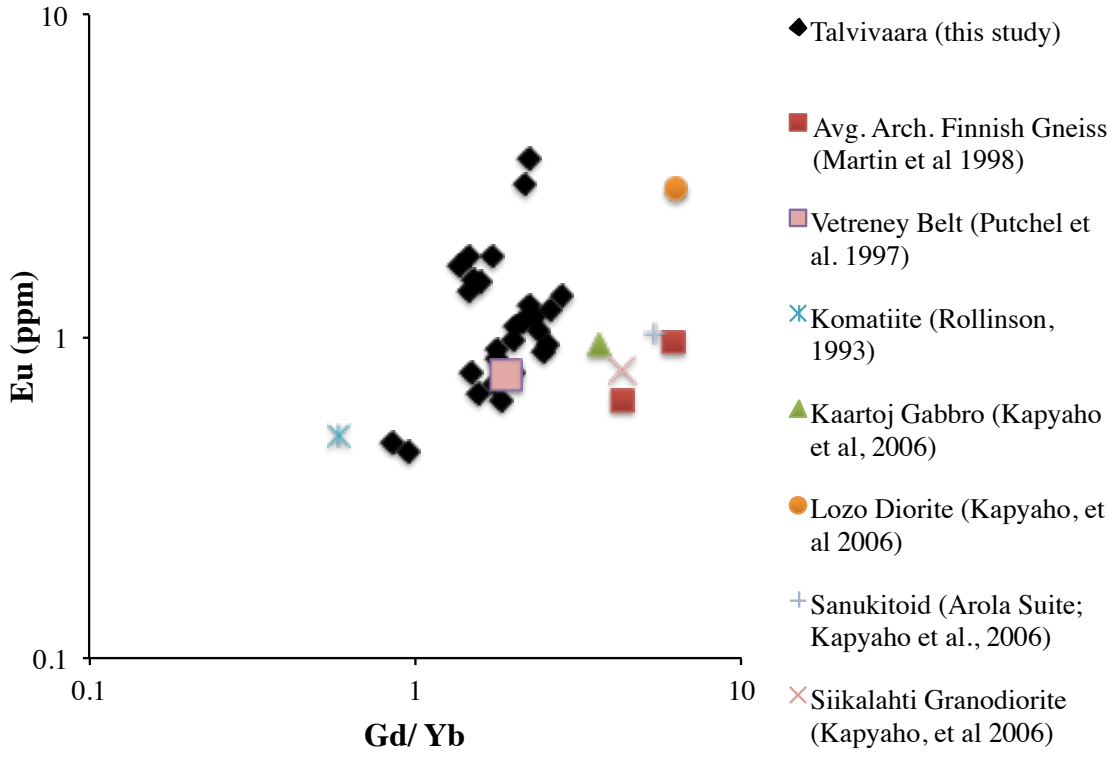

Figure 6.11. Eu/(Gd/Yb) of Talvivaara stratigraphy (DDKS052) with respect to potential 2.7 Ga source rocks of Fennoscandia.

			Wt % SiO_2	TiO_2	Al_2O_3	Fe_2O_3	MnO	MgO	CaO	Na_2O	K_2O	P_2O_5	TOC %	S %
		Dectetion Limit	0.01	0.01	0.01	0.01	0.01	0.01	0.01	0.01	0.01	0.01	2 ppm	5 ppm
DDKS-052														
	Core depth (m)	Sample Description												
Kuikkalampi Frm.														
T-K-6	90	Black schist with a series of mm-scale, quartz-wacke interbeds and disseminated, fine-grained sulfides (Py 1 & 2).	23	0.25	6.7	11	0.27	10	20	0.20	2.5	0.10	11	8.5
T-K-8	246	Black schist with fine-grained sulfides (Py1, Py2 & Po).	25	0.37	5.7	37	0.04	1.5	0.75	0.22	3.0	0.06	10	3.9
T-K-9	250	Massive black schist with fine grained sphalerite, pyrite (Py 1 & 2) and pyrrhotite cross cut by mm- to cm-scale, quartz veins with coarse pyrite (Py4).	41	1.0	13	8	0.06	4.7	3.1	0.53	4.8	0.12	7.0	10
T-K-10	259	Series of intercollated schist and quartz-wacke with mm-scale, pyrrhotite blebs along boundaries.	33	0.79	12	22	0.06	3.3	0.29	0.23	4.6	0.10	13	11
T-K-14	467	Massive black schist with minor disseminated, fine-grained sulfides (Po, Py 1 & 2, Sph). Phosphorous rich, cm-scale meatwacke horizon.	36	0.45	6.4	33	0.47	3.2	0.61	0.08	2.6	0.31	9.0	10
Talvivaara Frm														
TALV-01	468	Start of Talvivara ore horizon. Massive black schist with fine, disseminated sulfides (Py1, Py2 & Po).	52	1.1	11	13	0.47	4.7	0.94	0.12	4.3	0.11	6.7	6.3
TALV-02	479	Black schist with abundant laminated pyrite (Py 1).	28	0.52	8.8	30	0.16	2.6	0.76	0.09	3.1	0.11	11	12

TALV-03	**493**	Massive black schist with v. fine, disseminated sulfides (Py1, Py2 & Po).	**43**	**0.83**	**12**	**16**	**0.14**	**2.4**	**0.87**	**0.17**	**4.0**	**0.13**	**12**	**7.0**
TALV-04	**503**	Black schist with fine grained sulfides(Po, Py1 & Py2), mm-scale 'blebs' of pyrrhotite and chalcopyrite stringers.	**45**	**0.88**	**13**	**13**	**0.27**	**4.1**	**1.64**	**0.27**	**4.0**	**0.13**	**12**	**4.5**
TALV-05	**542**	Black schist with laminated pyrite (Py2), sub-mm euhedral pyrite following lamination (Py2) and mm-scale pyrite occuring at an angle to it (Py4).	**34**	**0.69**	**12**	**23**	**0.13**	**3.9**	**1.82**	**0.16**	**3.5**	**0.17**	**12**	**6.9**
TALV-06	**593**	Black schist with cm-scale quartz-rich wacke intercalactions. Fine, disseminated sulfides in black schist portition, cross cut by quartz vein and coarse pyrite.	**52**	**0.76**	**12**	**15**	**0.45**	**3.1**	**1.32**	**0.21**	**4.2**	**0.24**	**9.0**	**7.5**
TALV-07	**600**	Massive black schist with v. fine, disseminated sulfides (Py1, Py2 & Po). with 8cm section of multi-generation sulfides. Pyritite laminations, cross cut by oblique orientated coarse-grained pyrite	**29**	**0.85**	**12**	**35**	**0.68**	**1.7**	**1.03**	**0.29**	**4.8**	**0.10**	**13**	**7.4**
TALV-08	**613**	Black schist with cm-scale, quartz-rich, wacke intercalactions. Fine, disseminated sulfides in black schist (Py1), cross cut by multiple, mm-scale, quartz shear veins and coarse pyrite (Py4).	**58**	**0.93**	**14**	**8**	**0.36**	**2.9**	**1.2**	**0.73**	**4.7**	**0.18**	**6.9**	**16**
TALV-LWR	**623**	Black schist with mm-scale, psammitc intercalations with coarse pyrrhotite, mm-scale spessartine garnet porphyroblast.	**35**	**0.55**	**9.4**	**25**	**10**	**6.3**	**4.9**	**0.02**	**0.7**	**0.83**	**6.3**	**3.6**
Hakonen Frm.														
FT-TALV-1	**650**	Black schist with micaceous bands and mm-scale, garnet porphyroblasts. Minor, stringer-style pyrite along garnet boundaries.	**59**	**0.80**	**15**	**10**	**0.10**	**2.4**	**0.79**	**0.40**	**4.5**	**0.15**	**2.5**	**10**
FT-TALV-2	**651**	Black schist and mm-scale, psammitic laminations. Minor disseminated sulfides throughout	**56**	**0.91**	**16**	**9**	**0.23**	**5.7**	**1.35**	**0.74**	**5.0**	**0.21**	**3.4**	**4.4**

DDKS-053												
Kuikkalampi Frm.												
T-K-6	**192**	Black schist with fine-grained, pyrite laminations.	**25**	**1.21**	**6.0**	**32**	**0.04**	**8.4**	**8.3**	**0.32**	**2.7**	**0.08**	**6.9**
T-K-9	**308**	Black schist with a series of mm-scale, quartz-wacke interbeds, and disseminated, fine-grained sulfides (Py1, Py2, Py3 & Po).	**30**	**0.87**	**14**	**23**	**0.17**	**3.8**	**3.7**	**0.21**	**2.5**	**0.17**	**12**
T-K-11	**395**	Cm-scale quartz wacke horizon in black schist, with re-worked coarse, blebby Po along boundary.	**28**	**0.65**	**12**	**22**	**0.36**	**3.0**	**2.3**	**0.27**	**3.1**	**0.09**	**13**
Talvivaara Frm												
TALV-4	**491**	Massive black schist with fine grained sulfides.	**28**	**0.76**	**13**	**23**	**0.38**	**3.1**	**1.5**	**0.26**	**4.1**	**0.34**	**14**
TALV-8	**616**	Black schist with disseminated sulfides (Py1, Py2, Py3 & Po) and a cm-scale, quartz-wacke horizon.	**36**	**0.83**	**14**	**15**	**0.11**	**2.9**	**1.7**	**0.37**	**3.2**	**0.21**	**9.0**
DDKS-030												
Kuikkalampi Frm.												
T-K-4	**118**	Black schist with minor, cm-scale quartz-wacke interbed and disseminated, fine-grained sulfides.	**32**	**0.47**	**7.3**	**11**	**0.08**	**3.2**	**3.7**	**0.13**	**4.4**	**0.20**	**5.3**
T-K-5	**121**	Black schist with minor, cm-scale, quartz-wacke interbed and disseminated, fine-grained sulfides.	**52**	**1.04**	**11**	**35**	**0.12**	**3.3**	**3.0**	**0.18**	**3.2**	**0.10**	**9.5**
T-K-8	**163**	Black schist with grey, fine-grianed, quartz-wacke interbed, with cm-scale, black shale clast.	**36**	**0.50**	**15**	**8**	**0.38**	**2.7**	**1.3**	**0.16**	**4.1**	**0.18**	**10**

DDKS-070													
Kuikkalampi Frm.													
T-K-5	**201**	Black schist with mm-scale pyrite lamination, distrupted by cross-cutting quartz veins with associated coarse grained pyrite.	**45**	**0.80**	**11**	**21**	**0.03**	**3.2**	**5.1**	**0.29**	**3.9**	**0.21**	**9.5**	**7.5**
T-K- 9	**270**	Massive black schist with pyrite laminations and coarse grained pyrite porphyroblasts.	**35**	**0.83**	**13**	**19**	**0.10**	**2.5**	**2.3**	**0.21**	**3.1**	**0.14**	**13.3**	**8.4**
T-K-10	**281**	Pyrite laminated black shale with interspersed mm- to cm-scale quartz veining.	**41**	**0.88**	**11**	**26**	**3.48**	**2.8**	**0.92**	**0.24**	**3.8**	**0.13**	**13.8**	**7.2**
Talvivaara Frm													
TALV-1	**393**	Start of ore horizon. Massive black schist with fine-grained sulfides. Cm-scale, black, phosporous-rich bands.	**28**	**0.55**	**11**	**25**	**0.21**	**2.4**	**1.4**	**0.68**	**4.2**	**0.71**	**12**	**9.3**
TALV-2	**407**	Massive black schist with fine grained sulfides and mm-scale blebs of Pyrrhotite and chalocpyrite stringers.	**30**	**0.62**	**12**	**32**	**0.33**	**3.4**	**1.5**	**0.13**	**0.9**	**0.15**	**15**	**10**
TALV-4	**439**	~10cm thick psammitic horizon with quartz veining and mm-pyrite veining.	**50**	**0.59**	**13**	**23**	**0.18**	**5.3**	**1.7**	**0.29**	**4.3**	**0.27**	**9.7**	**8.3**
TALV-6	**456**	~20cm thick, medium grained, clastic horizon with mm-scale black shale clast.	**51**	**0.75**	**15**	**18**	**0.21**	**4.2**	**1.3**	**0.62**	**4.7**	**0.23**	**8.7**	**4.3**
TALV-9	**467**	Massive black shale with disseminated sulfides(Py1, Py2, Py3 & Po) and chalcopyrite stringers.	**27**	**0.81**	**13**	**21**	**0.13**	**3.1**	**1.2**	**0.32**	**2.7**	**0.12**	**13**	**8.5**
North American Shale Composite (NASC) (Gromet, 1984)			**65**	**0.78**	**17**	**8.1**	**0.06**	**2.9**	**3.6**	**1.2**	**4.0**	**0.11**	**…..**	**…..**
Upper Kaleva meta-schists (Kontinen & Hanksi, in press)			**59**	**0.85**	**17**	**8.5**	**0.07**	**3.8**	**2.0**	**2.5**	**4.1**	**0.16**	**…..**	**0.36**
World Shale Average (WSA) (Wedepohl, 1978)			**64**	**0.84**	**18**	**7.4**	**0.11**	**2.7**	**2.4**	**0.87**	**3.5**	**0.18**	**…..**	**…..**

		ppm Sc	Ba	V	Cr	Co	Ni	Cu	Zn	As	Se	Rb	Sr	Y	Zr	Mo	Pb	Bi	U	Th
DDKS-052		**0.008**	**0.050**	**0.01**	**0.03**	**0.003**	**0.01**	**0.078**	**0.04**	**2**	**2**	**0.008**	**0.004**	**0.006**	**0.030**	**0.020**	**0.018**	**0.001**	**0.001**	**0.003**
Kuikkalampi Frm.	**Core depth (m)**																			
T-K-6	**90**	**7**	**120**	**447**	**63**	**15**	**163**	**67**	**554**	**84**	**9**	**148**	**87**	**25**	**68**	**54**	**24**	**0.28**	**9.4**	**5.8**
T-K-8	**246**	**34**	**457**	**2,729**	**367**	**27**	**576**	**417**	**11,001**	**8**	**19**	**169**	**59**	**66**	**162**	**300**	**53**	**0.86**	**33**	**11.1**
T-K-9	**250**	**8**	**277**	**843**	**117**	**75**	**1,069**	**863**	**6,196**	**19**	**57**	**98**	**47**	**32**	**70**	**130**	**22**	**2.21**	**15**	**8.9**
T-K-10	**259**	**25**	**479**	**1,554**	**224**	**21**	**589**	**327**	**3,538**	**10**	**38**	**170**	**30**	**49**	**156**	**174**	**59**	**4.19**	**22**	**12.3**
T-K-14	**467**	**10**	**139**	**500**	**98**	**36**	**657**	**550**	**14,342**	**33**	**74**	**97**	**24**	**13**	**68**	**68**	**66**	**DL**	**3.8**	**2.9**
Talvivaara Frm																				
TALV-01	**468**	**24**	**253**	**903**	**181**	**39**	**1,909**	**2,837**	**11,317**	**38**	**27**	**145**	**31**	**73**	**102**	**44**	**34**	**0.36**	**19**	**7.0**
TALV-02	**479**	**19**	**196**	**707**	**113**	**159**	**3,256**	**555**	**3,158**	**407**	**48**	**85**	**25**	**15**	**74**	**55**	**82**	**DL**	**8.3**	**4.1**

DDKS-053																				
Kuikkalampi Frm.																				
T-K-6	**192**	**29**	**326**	**269**	**289**	**10**	**200**	**447**	**544**	**6**	**23**	**133**	**87**	**25**	**68**	**54**	**21**	**0.24**	**22**	**3.5**
T-K-9	**308**	**21**	**212**	**2,729**	**150**	**25**	**1,240**	**1,490**	**2,915**	**5**	**18**	**103**	**59**	**66**	**162**	**300**	**46**	**0.50**	**17**	**9.1**
T-K-11	**395**	**16**	**408**	**1,123**	**130**	**98**	**2,171**	**2,157**	**964**	**<2**	**54**	**48**	**47**	**32**	**70**	**100**	**67**	**0.60**	**29**	**7.7**
Talvivaara Frm																				
TALV-4	**491**	**24**	**125**	**707**	**156**	**105**	**4,019**	**2,716**	**9,382**	**10**	**64**	**125**	**30**	**49**	**156**	**174**	**34**	**0.32**	**9.5**	**4.1**
TALV-8	**616**	**27**	**193**	**1,049**	**181**	**64**	**2,243**	**2,164**	**4,045**	**39**	**30**	**63**	**24**	**13**	**68**	**68**	**51**	**0.46**	**13**	**8.5**
DDKS-030																				
Kuikkalampi Frm.																				
T-K-4	**118**	**27**	**128**	**387**	**47**	**34**	**287**	**353**	**4,823**	**62**	**50**	**66**	**25**	**15**	**74**	**55**	**54**	**0.47**	**4.0**	**10.4**
T-K-5	**121**	**13**	**314**	**843**	**93**	**79**	**3,256**	**732**	**4,749**	**30**	**37**	**51**	**60**	**21**	**124**	**39**	**67**	**0.36**	**16**	**4.9**
T-K-8	**163**	**19**	**292**	**472**	**165**	**102**	**3,595**	**1,398**	**9,056**	**107**	**36**	**60**	**20**	**51**	**79**	**27**	**125**	**0.34**	**9.4**	**6.7**

TALV-04	503	29	275	1,049	183	139	3,595	1,362	5,713	191	50	98	45	17	110	74	76	DL	13	5.8
TALV-05	542	26	251	875	158	138	4,098	1,427	5,150	285	47	101	54	30	109	69	51	0.47	12	3.9
TALV-06	593	22	221	775	152	98	3,400	2,425	6,337	<2	36	115	37	27	113	83	61	0.40	15	5.8
TALV-07	600	26	292	888	158	109	6,684	710	5,692	34	81	120	76	10	118	81	99	DL	16	7.1
TALV-08	613	24	280	734	165	97	1,026	709	4,808	<2	21	121	60	21	124	39	37	DL	12	7.9
TALV-LWR	623	11	21	472	130	258	741	1,680	1,126	5	32	40	20	51	79	27	12	0.12	10	8.4
Hakonen Frm.																				
FT-TALV-1	650	26	297	398	158	86	830	473	2,787	<2	19	92	42	19	107	21	13	0.32	6.8	5.4
FT-TALV-2	651	28	207	289	169	47	200	304	1,129	<2	9	138	68	28	117	7	13	0.16	4.6	8.5

DDKS-070																															
Kuikkalampi Frm.																															
T-K-5		**201**		**19**	**305**	**398**	**137**	**158**	**1,026**	**1,311**	**2,406**	**16**	**19**	**132**	**42**	**19**	**107**	**21**	**15**	**0.72**	**9.4**	**6.9**									
T-K- 9		**270**		**14**	**212**	**289**	**46**	**49**	**6,684**	**522**	**1,395**	**23**	**22**	**115**	**68**	**28**	**117**	**7**	**33**	**0.75**	**15**	**8.0**									
T-K-10		**281**		**15**	**333**	**903**	**301**	**86**	**5,256**	**754**	**5,097**	**340**	**28**	**127**	**31**	**73**	**102**	**44**	**123**	**0.59**	**6.8**	**6.3**									
Talvivaara Frm																															
TALV-1		**393**		**22**	**105**	**1,554**	**128**	**45**	**4,098**	**1,472**	**7,710**	**<2**	**34**	**109**	**64**	**30**	**120**	**115**	**35**	**0.25**	**10**	**2.7**									
TALV-2		**407**		**20**	**197**	**888**	**154**	**136**	**5,632**	**794**	**5,028**	**60**	**52**	**57**	**45**	**17**	**110**	**74**	**44**	**1.19**	**11**	**6.0**									
TALV-4		**439**		**26**	**184**	**2,729**	**179**	**159**	**2,540**	**781**	**2,569**	**86**	**50**	**82**	**54**	**30**	**109**	**69**	**129**	**0.29**	**16**	**4.9**									
TALV-6		**456**		**24**	**197**	**447**	**113**	**175**	**2,256**	**867**	**4,287**	**12**	**29**	**76**	**37**	**27**	**113**	**83**	**93**	**1.02**	**5.5**	**5.8**									
TALV-9		**467**		**25**	**182**	**775**	**142**	**98**	**5,632**	**3,904**	**11,468**	**413**	**28**	**70**	**76**	**10**	**118**	**81**	**110**	**0.54**	**4.4**	**5.2**									
	North American Shale Composite		**15**	**636**	**.....**	**127**	**26**	**58**	**.....**	**.....**	**28**	**.....**	**125**	**142**	**.....**	**200**	**.....**	**.....**	**.....**	**.....**	**2.7**	**12**									
	Upper Kaleva meta-schists		**24**	**.....**	**188**	**147**	**24**	**83**	**62**	**166**	**.....**	**0.2**	**161**	**170**	**24**	**145**	**.....**		**0.20**	**2.9**	**10**									
	World Shale Average (WSA)		**13**	**580**	**130**	**90**	**19**	**50**	**45**	**95**	**13**	**0.6**	**140**	**170**	**26**	**160**	**3**	**20**	**0.43**	**2.7**	**12**									

Table 6.1. Whole-rock geochemistry, sample descriptions, and comparisons with Upper-Kaleva shale and Phanerozoic standards NASC and WSA.

Environmental and depositional proxies

To augment the stratigraphic profile collected from DDKS052, additional samples were analyzed to understand the conditions of deposition of the Talvivaara sediments (total n= 32). In order to address this, a variety of geochemical proxies were employed. Analysis from throughout the deposit stratigraphy, show that base metal enrichment is not a unique feature of the ore horizon (Fig. 6.12; Table 6.2; 6.3). The entire stratigraphy is enriched in metals (i.e. 2642 ppm Ni, 1272 ppm Cu and 5276 ppm Zn in the hanging wall) compared to typical Phanerozoic shales (i.e. world shale average (WSA) and North American Shale Composite (NASC); Table 1 and 2). The metal, Ni, plotted against total organic carbon (TOC) % shows moderate correlation and Mo, Zn and U, normalized to Alx10^{-4} display similar patterns to those deposited under mixed anoxic-euxinic waters during the Phanerozoic (Algeo and Maynard, 2004). Commonly used element concentrations, and metal ratios, for paleo-redox studies are shown in Table 2. In addition, calculated enrichment factors (i.e. (element $_{sample}$ / Al $_{sample}$) / (element $_{WSA}$ / Al $_{WSA}$) = EF*) are presented in Table 6.3. The Talvivaara Formation has higher V/Cr, Ni/Co and U/Th ratios and much lower Cr/Ni values compared to the Phanerozoic samples (NASC and WSA; Table 2). Vanadium, nickel, molybdenum, and uranium enrichments are often considered as a function of the redox state of the water column, where as Cr and Co are usually a proxy for high detrital content or hydrothermal input (Lyons et al., 2003; Tribovillard et al., 2006; Scott et al., 2014). Cu/Zn ratios are similar to NASC and WSA, but the metals themselves are highly enriched by comparison with EF*max= 185 for Ni, and 22 for Cu, respectively. Chromium, Co, and Mn generally exhibit low EF*. V/ (V+Ni) has been commonly used to elucidate the oxygen content in the water column during deposition of Phanerozoic black shales (Rimmer et al., 2004). The data shows a bimodal distribution between dysoxic and anoxic/euxinic based on the thresholds outlined (Rimmer et al., 2004).

The chemical index of alteration (CIA- 100* Al_2O_3/ (Al_2O_3+CaO+Na_2O+K_2O); Nesbitt Young, 1982) can be used to determine the degree of weathering of source sediments (ranging in intensity from low: 1, to high: 100). The majority of samples for the Talvivaara Formation fall with the range of 60-75, this is similar to that of NASC, WSA and the overlying black schists. Th/Sc (0.2-1) and Zr/Sc (4-10) ratios

are slightly lower than NASC and WSA. These ratios are used to identify sediment recycling and sorting processes (McLennan et al., 1993).

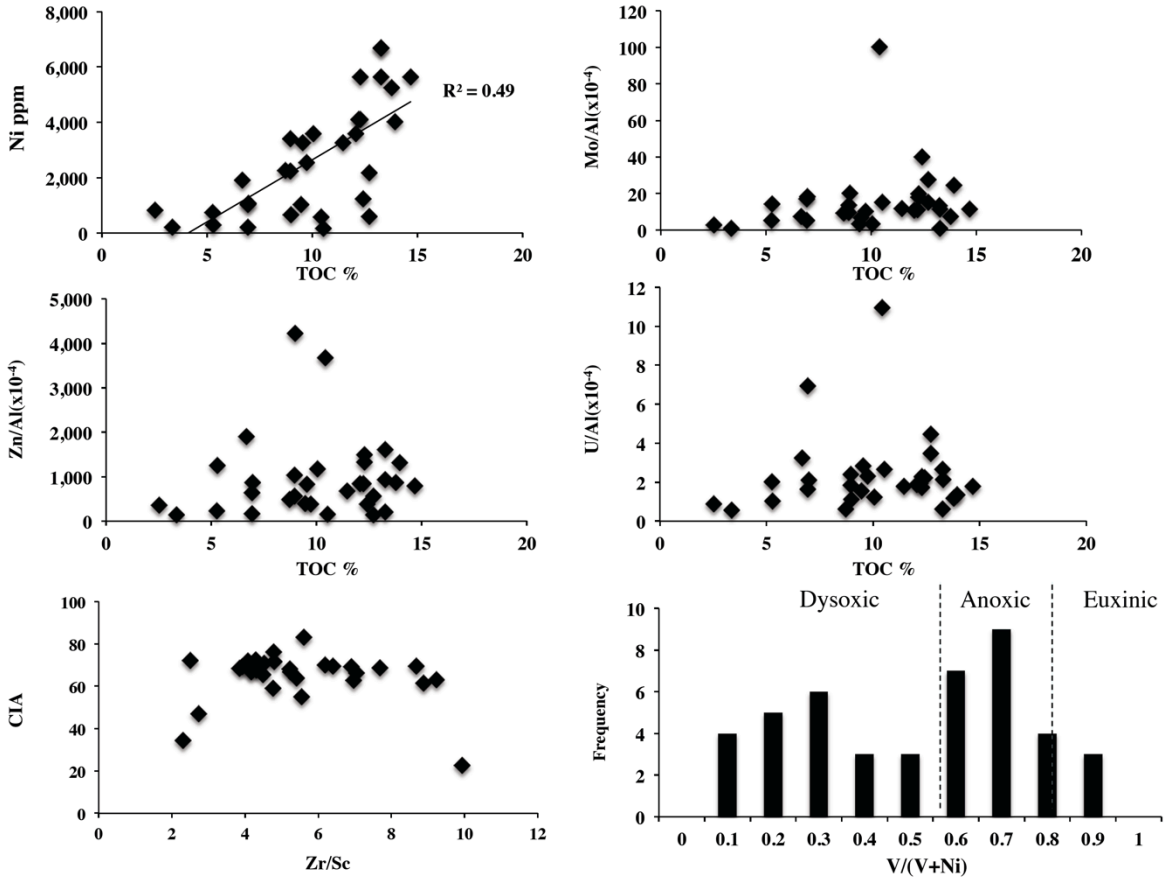

Figure 6.12. Element ratio plots (all samples) for depositional environmental analysis.

		Ni/Co	Cu/Zn	Cr/Ni	V/Cr	U/Th	V/Sc	Th/Sc	Zr/Sc	Fe/S	CIA	V/(V+Ni)
DDKS-052												
Kuikkalampi Frm.	**Depth (m)**											
	90	**11**	**0.1**	**0.4**	**7.0**	**1.6**	**66**	**0.8**	**9.9**	**0.9**	**23**	**0.73**
	246	**21**	**0.0**	**0.6**	**7.4**	**3.0**	**80**	**0.3**	**4.8**	**8.4**	**59**	**0.83**
	250	**14**	**0.1**	**0.1**	**7.2**	**1.7**	**107**	**1.1**	**8.9**	**0.2**	**61**	**0.44**
	259	**28**	**0.1**	**0.4**	**7.0**	**1.8**	**61**	**0.5**	**6.2**	**1.5**	**70**	**0.73**
	467	**18**	**0.0**	**0.1**	**5.1**	**1.3**	**52**	**0.3**	**7.1**	**1.5**	**66**	**0.43**
Talvivaara Frm												
	468	**49**	**0.3**	**0.1**	**5.0**	**2.7**	**38**	**0.3**	**4.3**	**1.4**	**68**	**0.32**
	479	**21**	**0.2**	**0.0**	**6.3**	**2.0**	**38**	**0.2**	**3.9**	**1.0**	**69**	**0.18**
	493	**43**	**0.4**	**0.0**	**5.3**	**2.1**	**43**	**0.3**	**4.5**	**1.6**	**71**	**0.17**
	503	**26**	**0.2**	**0.1**	**5.7**	**2.2**	**37**	**0.2**	**3.9**	**0.8**	**68**	**0.23**
	542	**30**	**0.3**	**0.0**	**5.5**	**3.0**	**33**	**0.1**	**4.1**	**2.3**	**68**	**0.18**
	593	**35**	**0.4**	**0.0**	**5.1**	**2.6**	**36**	**0.3**	**5.2**	**0.6**	**67**	**0.19**
	600	**62**	**0.1**	**0.0**	**5.6**	**2.3**	**34**	**0.3**	**4.5**	**3.3**	**65**	**0.12**
	613	**11**	**0.1**	**0.2**	**4.4**	**1.6**	**31**	**0.3**	**5.2**	**0.3**	**68**	**0.42**
	623	**2.9**	**1.5**	**0.2**	**3.6**	**1.2**	**41**	**0.7**	**7.0**	**4.9**	**63**	**0.39**
Hakonen Frm.												
	650	**9.6**	**0.2**	**0.2**	**2.5**	**1.3**	**15**	**0.2**	**4.1**	**0.7**	**72**	**0.32**
	651	**4.3**	**0.3**	**0.8**	**1.7**	**0.5**	**10**	**0.3**	**4.2**	**1.5**	**69**	**0.59**
DDKS-053												
Kuikkalampi Frm.												
	192	**19**	**0.8**	**1.4**	**0.9**	**6.2**	**9.1**	**0.1**	**2.3**	**4.4**	**34**	**0.57**
	308	**49**	**0.5**	**0.1**	**18**	**1.8**	**129**	**0.4**	**7.7**	**1.3**	**69**	**0.69**
	395	**22**	**2.2**	**0.1**	**8.7**	**3.8**	**69**	**0.5**	**4.3**	**1.9**	**69**	**0.34**
Talvivaara Frm												
	491	**38**	**0.3**	**0.0**	**4.5**	**2.3**	**29**	**0.2**	**6.4**	**1.4**	**70**	**0.15**
	616	**35**	**0.5**	**0.1**	**5.8**	**1.6**	**38**	**0.3**	**2.5**	**1.0**	**72**	**0.32**
DDKS-030												
Kuikkalampi Frm.												
	118	**8.5**	**0.1**	**0.2**	**8.2**	**0.4**	**14**	**0.4**	**2.7**	**0.9**	**47**	**0.57**
	121	**41**	**0.2**	**0.0**	**9.1**	**3.3**	**63**	**0.4**	**9.2**	**2.4**	**63**	**0.21**
	163	**35**	**0.2**	**0.0**	**2.9**	**1.4**	**26**	**0.4**	**4.3**	**0.9**	**72**	**0.12**
DDKS-070												
Kuikkalampi Frm.												
	201	**6.5**	**0.5**	**0.1**	**2.9**	**1.4**	**21**	**0.4**	**5.5**	**2.0**	**55**	**0.28**
	270	**46**	**0.4**	**0.0**	**6.3**	**1.8**	**21**	**0.6**	**8.7**	**1.6**	**70**	**0.04**
	281	**29**	**0.1**	**0.1**	**3.0**	**1.1**	**61**	**0.4**	**6.9**	**1.6**	**69**	**0.15**
Talvivaara Frm												
	393	**91**	**0.2**	**0.0**	**12**	**3.7**	**70**	**0.1**	**5.4**	**1.9**	**64**	**0.27**
	407	**41**	**0.2**	**0.0**	**5.8**	**1.9**	**45**	**0.3**	**5.6**	**2.2**	**83**	**0.14**
	439	**42**	**0.3**	**0.0**	**15**	**3.2**	**104**	**0.2**	**4.2**	**1.9**	**67**	**0.52**
	457	**30**	**0.2**	**0.0**	**3.9**	**1.0**	**19**	**0.2**	**4.8**	**3.8**	**72**	**0.17**
	467	**58**	**0.3**	**0.0**	**5.5**	**0.8**	**32**	**0.2**	**4.8**	**1.2**	**76**	**0.12**
NASC*		**2.3**	**.....**	**2.2**	**.....**	**0.2**	**.....**	**0.8**	**13.4**	**.....**	**66.0**	**.....**
Upper Kaleva^		**3.5**	**0.4**	**1.8**	**1.3**	**0.3**	**7.8**	**0.4**	**6.0**	**.....**	**65.8**	**0.69**
WSA#		**2.6**	**0.5**	**1.8**	**1.4**	**0.2**	**10.0**	**0.9**	**12.3**	**.....**	**72.8**	**0.72**

Table 6.2. Whole-rock trace element ratios from Talvivaara, Upper Kaleva, and reference standards.

DDKS-052	Core depth (m)	Ni EF*	Zn EF*	Cu EF*	Mo EF*	U EF*	Mn EF*	V EF*	Co EF*	Cr EF*	Se EF*
Kuikkalampi Frm.											
T-K-6	90	9	2	3	56	9	7	9	2	2	41
T-K-8	246	37	14	21	367	39	1	67	5	13	100
T-K-9	250	29	12	4	67	7	1	9	5	2	126
T-K-10	259	18	5	6	102	12	1	18	2	4	95
T-K-14	467	37	16	4	74	4	12	11	5	3	345
Talvivaara Frm											
TALV-01	468	61	48	2	27	11	7	11	3	3	73
TALV-02	479	133	12	2	43	6	3	11	17	3	163
TALV-03	493	168	65	4	66	8	2	13	10	4	132
TALV-04	503	101	20	2	40	7	4	11	10	3	117
TALV-05	542	127	23	2	41	7	2	10	11	3	121
TALV-06	593	106	40	3	50	9	7	9	8	3	94
TALV-07	600	208	12	3	49	9	10	11	9	3	210
TALV-08	613	26	9	1	19	6	4	7	6	2	45
TALV-LWR	623	28	34	1	20	7	182	7	26	3	103
Hakonen Frm.											
FT-TALV-1	650	21	6	1	10	3	1	4	6	2	39
FT-TALV-2	651	5	4	0	3	2	2	3	3	2	18
DDKS-053											
Kuikkalampi Frm.											
T-K-6	192	12	14	4	63	24	1	6	2	10	117
T-K-9	308	32	20	8	147	8	2	27	2	2	38
T-K-11	395	63	33	3	55	16	5	12	7	2	129
Talvivaara Frm											
TALV-4	491	108	38	5	90	5	5	7	7	2	142
TALV-8	616	60	30	2	35	7	1	11	4	3	65
DDKS-030											
Kuikkalampi Frm.											
T-K-4	118	14	9	3	52	4	2	7	4	1	206
T-K-5	121	108	13	1	25	10	2	11	7	2	102
T-K-8	163	89	18	1	13	4	4	4	7	2	75
DDKS-070											
Kuikkalampi Frm.											
T-K-5	201	32	22	1	13	5	0	5	13	2	49
T-K- 9	270	185	8	0	4	8	1	3	4	1	52
T-K-10	281	171	13	2	27	4	53	11	7	5	76
Talvivaara Frm											
TALV-1	393	134	25	4	72	6	3	20	4	2	94
TALV-2	407	169	13	2	42	6	5	10	11	3	130
TALV-4	439	72	12	2	38	8	2	30	12	3	117
TALV-6	456	55	11	2	39	2	2	4	11	2	59
TALV-9	467	151	55	2	42	2	2	8	7	2	63

Table 6.3. Enrichment factors of characteristic trace elements used in paleo-redox studies compared to WSA.

Sulfur Isotopes

Previous sulfur isotope work on the deposit has focused on whole rock or micro-drilling methods. Pyrite and pyrrhotite have been the sole focus of study with reported ranges from -7.1 to +20.8‰ across the whole deposit and medians of –5.2‰ for pyrrhotite and –4.3‰ for pyrite (Loukola-Ruskeeniemi and Lahtinen, 2012). However, little focus has been paid to the accessory sulfides or establishing a relationship between these values and mineral paragenesis.

Results from in-situ analysis of $\delta^{34}S$ values of a variety of sulfides in this study can be placed into three groupings (Fig. 6.13).

1. A negative $\delta^{34}S$ values (-5 to -12.5‰) are found in the earliest pyrite (Py 1) and defines stage 1 of the proposed genetic history.
2. Stage 2, encompassing the syn-metamorphic mineral assemblage displays a range of negative values (-1 to -13‰) with the exception of one pyrrhotite analysis (+0.6‰). Sphalerite has the most variation in $\delta^{34}S$ values (between -1 and 13‰) but the majority of analyses are below -10‰. Pyrrhotite, pentlandite, chalcopyrite and galena all fall within the range of Pyrite 2 (Fig. 6.14). Alabandite values (n=3) display very little variation (-1.8 to -2.8‰).
3. A less variable but distinct group of $\delta^{34}S$ values (-1.5 to +3‰) are encountered in the medium to coarse Pyrite 3, which is interpreted to represent retrograde mineral formation.
4. The final group encompasses a large range of positive $\delta^{34}S$ values (1 to 13.6‰) that correspond to coarse pyrite (Py 4) associated with late-stage, cross cutting veins.

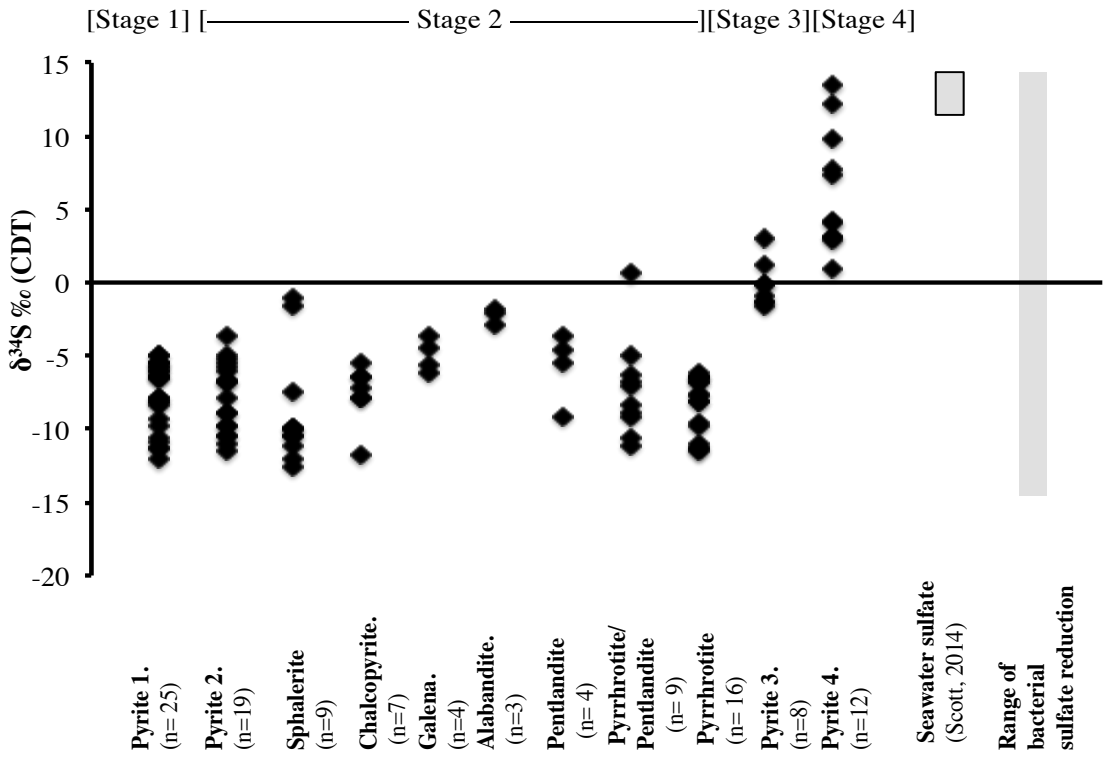

Figure 6.13. Summary of the range of $\delta^{34}S$ values.

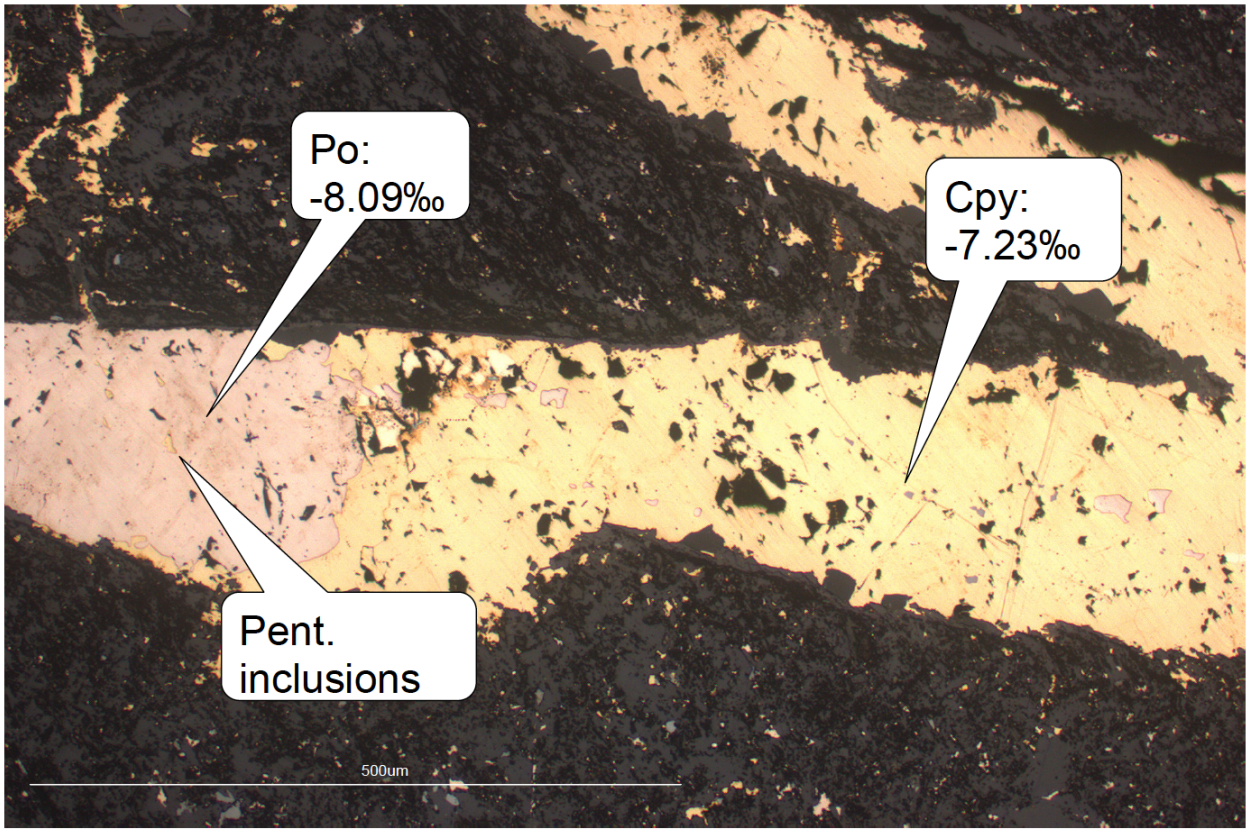

Figure 6.14. Image of pyrrhotite (and pentlandite) and chalcopyrite stringer with corresponding $\delta^{34}S$ isotope values superimposed (sample: 70-Talv-2).

Trace element geochemistry- LA-ICP-MS in-situ analysis

Over 220 analyses were conducted on pyrite and pyrrhotite from 12 samples representing diagenetic pyrite (Py1), syn-metamorphic pyrite (Py 2) and pyrrhotite, retrograde pyrite (Py 3) and late-stage, vein-associated pyrite generation (Py 4). Their trace element concentrations were plotted to give the schematic in Figure 6.15 and summarized in Table 3. Pyrite 1 is the most enriched in a range to trace elements compared to all other Fe-sulfide phases. In particular, Zn, Cd, Mn, Au, Ag, and Mo are lower, by over an order of magnitude, in the later stage pyrites (Py2, Py3, and Py4) and pyrrhotite. Nickel concentrations remain relatively constant through each of the Fe-sulfide phases. Cobalt displays a wide range of values in pyrrhotite (0.01 to 1928ppm), compared to pyrite. It also appears in high abundance (median, 1037ppm) in Py 3, a post-peak metamorphic sulfide stage. Selenium shows a moderate

variation (within one order of magnitude) through each stage with a minor increase in the Py 3, Py 4 and pyrrhotite. Element mapping (Fig. 6.16, 6.17, and 6.18) shows that U, V, Cr and Mn appear to be heavily associated with the matrix component. High Mo, Cu, and Zn concentrations on in the maps correspond to accessory molybdenite, chalcopyrite and sphalerite. Precious metals (Au and Pt) are in low abundance and are exclusively associated with the earliest pyrite stage. Microscopy confirms that high Ag is associated with the early pyrite, galena, and as Ag-sulfosalts within the matrix. Cadmium is likely associated with sphalerite as it is strongly correlated with Zn.

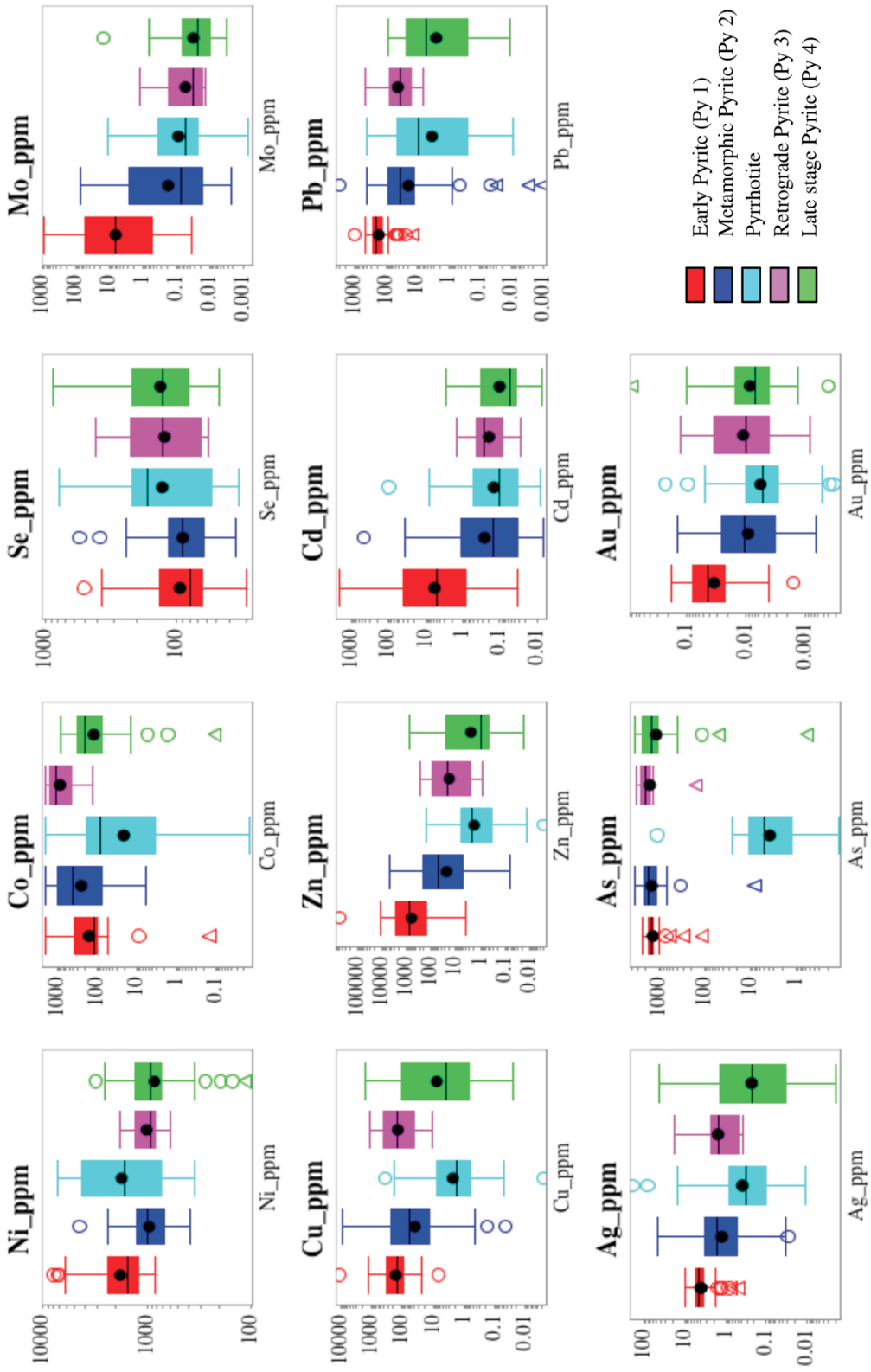

Figure 6.15. Trace element content of minerals with respect to the paragenetic sequence. Dots represent means, lines represent median values and the box spans Q1 to Q3 values.

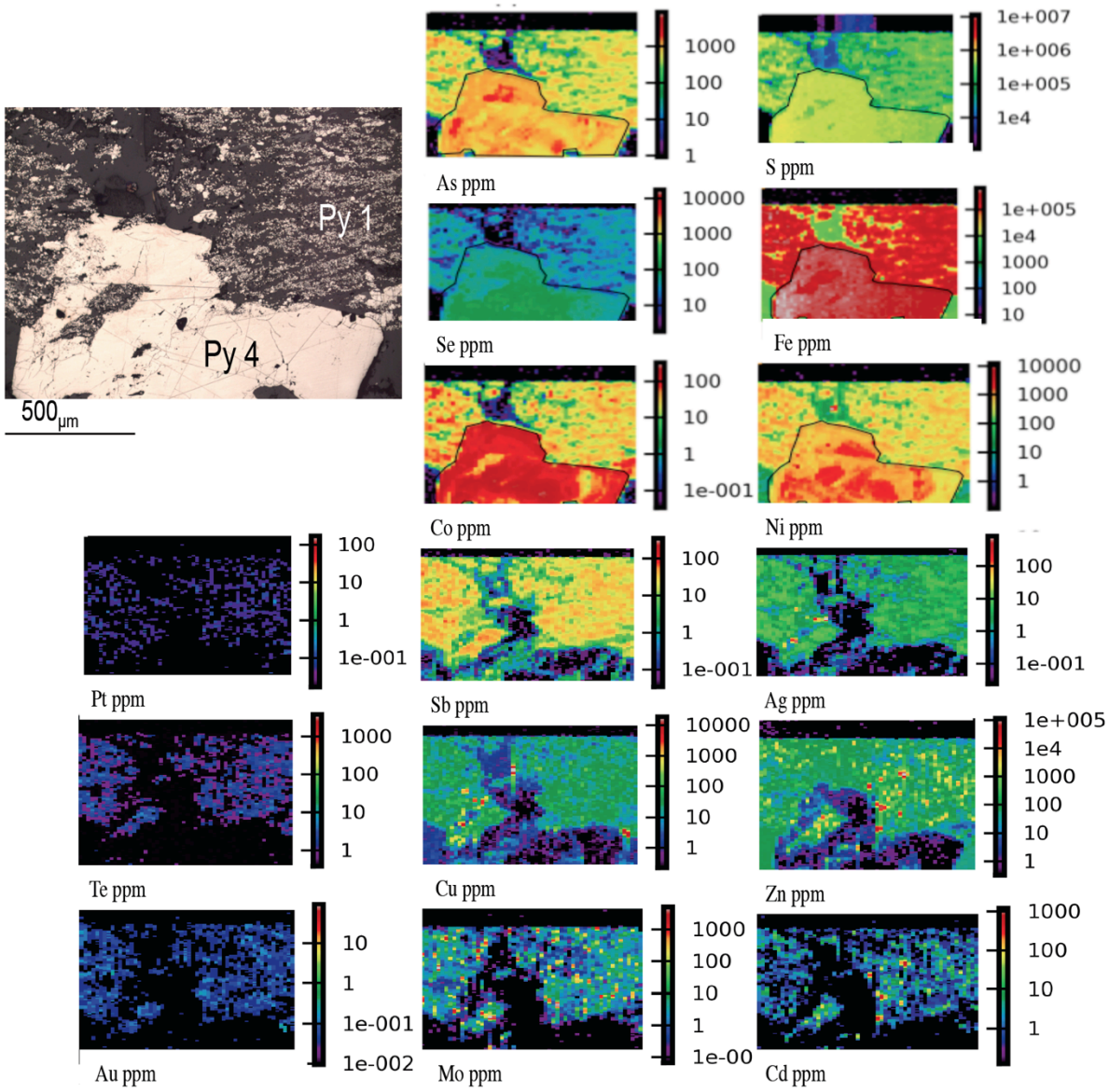

Figure 6.16. Trace element map of late stage, vein pyrite (Py 4) overprinting early, fine-grained sulfides (53-Talv-4). Individual element highs correspond to other sulfide mineral grains (e.g. chalcopyrite, sphalerite, molybdenite).

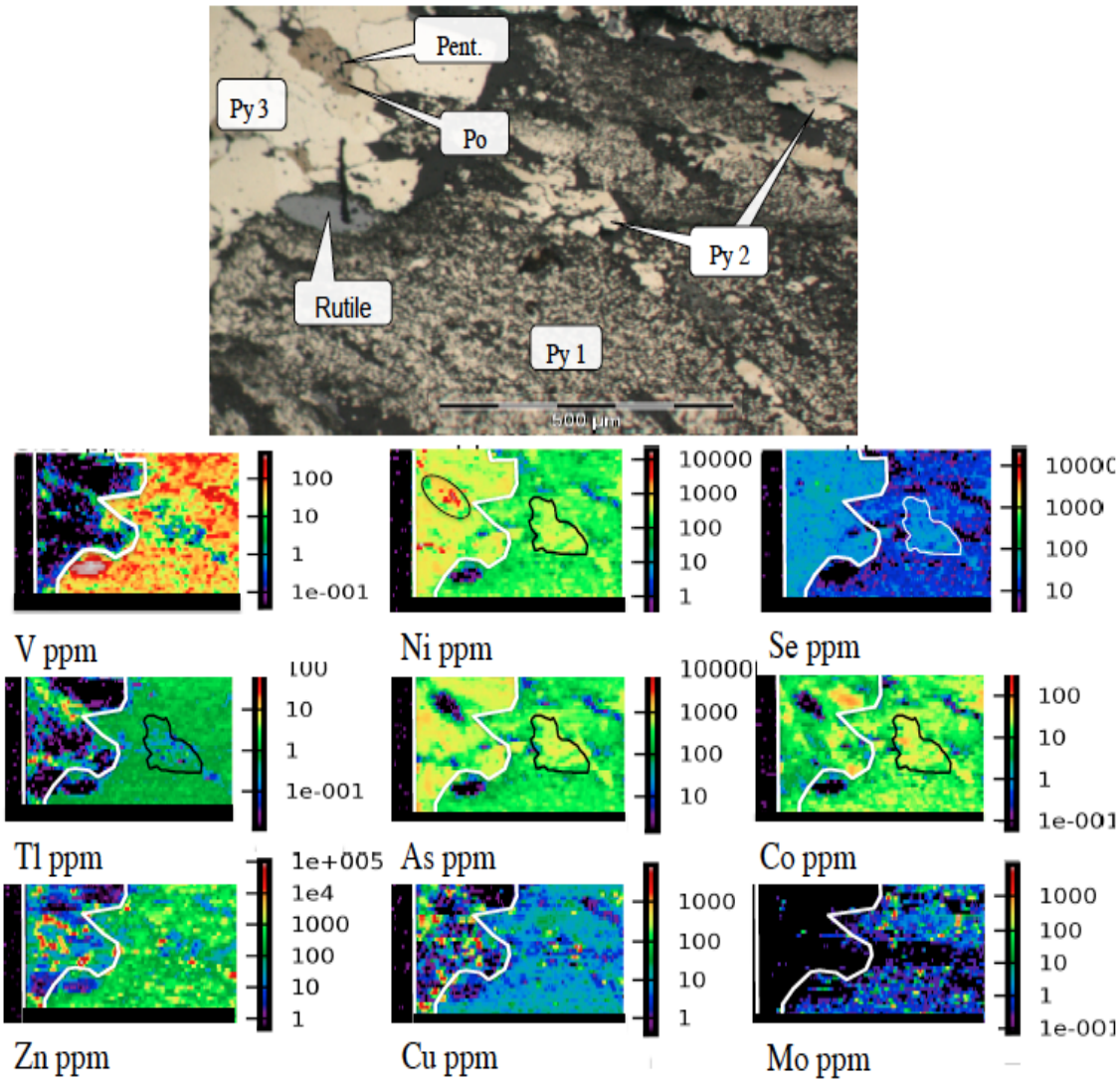

Figure 6.17. Trace element maps of retrograde pyrite (Py3) surrounding pyrrhotite and over growing fine-grained Py 1 and syn-metamorphic Py 2 (sample 52-Talv-8).

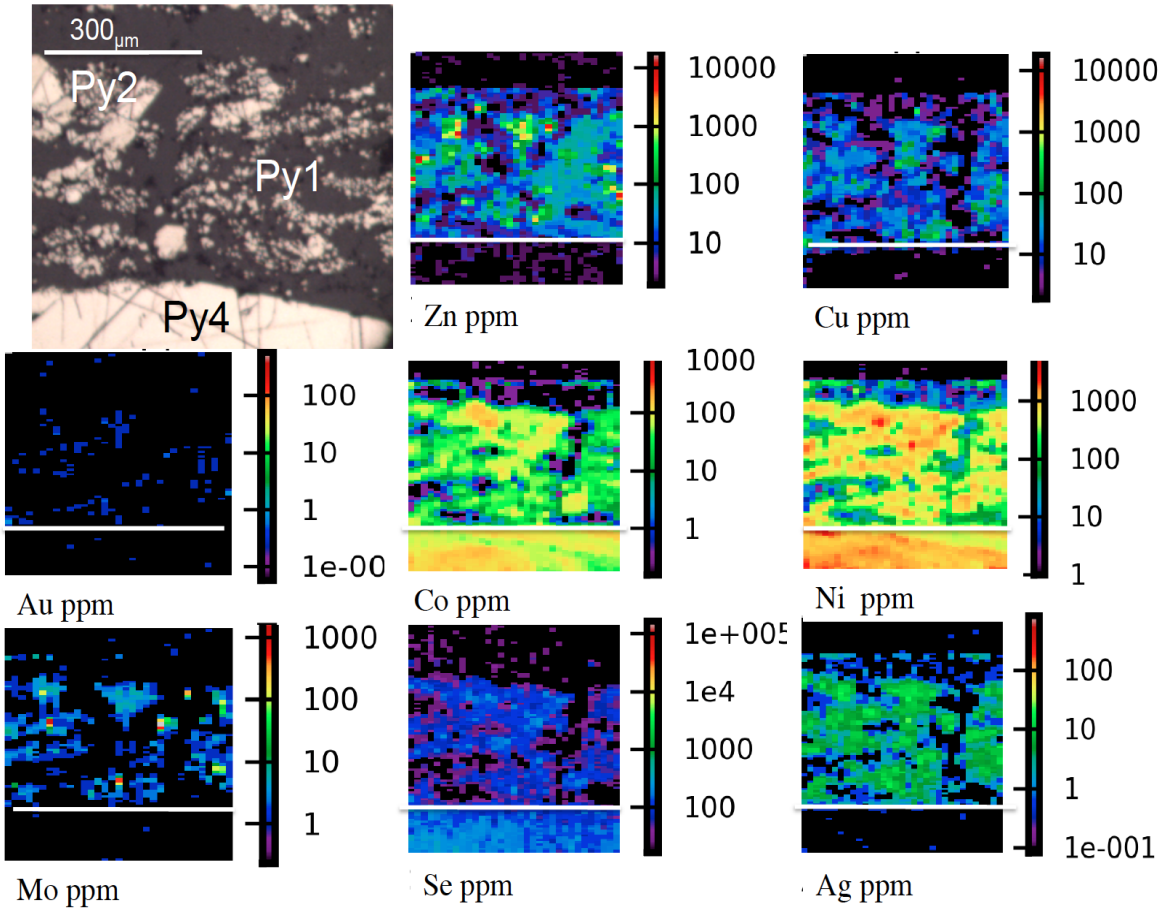

Figure 6.18. Trace element map across matrix, fine-grained sulfides (Py 1) and the boundary with late stage pyrite (Py 4; white line) using a $10_{\mu m}$ spot size (sample 53-Talv-4).

Table 6.4. Trace element content of pyrite and pyrrhotite from LA-ICP-MS analyses.

Mineral		ppm Ni	Co	Cu	Zn	Cd	Se	As	Mo	Mn	Ag	Tl	Pb	Au	Pt	Bi	Ba	V	Sn	Sb	W	Th
Fine Pyrite (Py 1)																						
n= 55	Minimum	834	55	24	4	0.03	30	936	0.04	3.92	1.75	0.22	85	DL	0.09	0.64	0.33	9.48	0.12	10.0	0.01	DL
	Maximum	7890	1950	1206	11337	2081	371	2295	896	1214	10	79	496	0.18	0.16	6.6	2823	13299	12	50	38	1.75
	Mean	**1800**	**157**	**163**	**630**	**6**	**95**	**1373**	**7**	**83**	**4**	**8**	**174**	**0.03**	**0.05**	**2.7**	**110**	**552**	**1.1**	**26**	**4.1**	**0.17**
	Median	1513	114	153	725	5	81	1494	7	63	5	13	213	0.04	0.05	3.0	407	1905	1.38	**33**	10	0.33
Metamorphic Pyrite (Py 2)																						
n= 28	Minimum	375	5.86	0.43	0.06	0.02	35	692	DL	0.03	0.03	1.11	0.78	DL	0.02	0.02	DL	DL	0.01	0.14	0.03	DL
	Maximum	2396	1964	4522	4522	26	246	3477	74	294	46	46	424	0.14	0.25	4.03	214	936	5.29	66	1.66	1.41
	Mean	**949**	**247**	**40**	**24**	**1.81**	**91**	**1460**	**0.18**	**6**	**1.25**	**5.06**	**20**	**0.01**	**0.02**	**0.36**	**13**	**58**	**0.23**	**5**	**0.04**	**0.54**
	Median	976	415	62	50	4.30	95	1666	0.09	13	1.59	5.18	37	0.01	0.04	0.52	39	159	0.26	8	0.02	0.21
Pyrrhotite (Po)																						
n=61	Minimum	349	0.01	0.05	0.02	0.03	34	0.12	DL	DL	0.01	0.10	0.27	DL	DL	DL	0.04	0.01	DL	0.09	DL	DL
	Maximum	7255	1928	184	214	1.03	784	25	11	36	16	1.0	403	0.01	0.01	3.13	0.12	0.47	4.77	2.42	0.12	1.22
	Mean	**2096**	**21**	**2**	**67**	**0.61**	**130**	**4**	**0.12**	**4**	**0.39**	**0.45**	**3.49**	**0.006**	**0.005**	**0.04**	**0.03**	**0.23**	**0.14**	**0.90**	**0.03**	**0.09**
	Median	1652	82	2	101	0.52	168	5	0.07	10	0.31	0.44	9.67	0.006	0.01	0.03	0.07	0.23	0.08	0.52	0.06	0.05
Retrograde Pyrite (Py3)	Minimum	585	126	10	0.82	0.03	57	1380	0.01	3.6	0.38	0.06	6.67	DL	DL	0.14	DL	DL	0.01	1.22	0.03	DL
n= 33	Maximum	1791	1964	1077	299	1.5	417	3231	12	288	18	7.10	486	0.13	0.05	2.06	127	936	2.53	35	1.66	1.41
	Mean	**1005**	**851**	**142**	**19**	**0.20**	**125**	**1614**	**0.06**	**24**	**1.55**	**0.75**	**43**	**0.01**	**0.02**	**0.60**	**11**	**58**	**0.46**	**8**	**0.07**	**0.05**
	Median	925	1037	149	20	0.26	130	2063	0.03	22.48	1.52	0.55	37.62	0.01	0.01	0.74	19	159	0.39	12	0.04	0.21
Late Pyrite (Py 4)																						
n=55	Minimum	346	13.91	0.03	0.02	DL	49	409	DL	0.03	DL	DL	0.01	DL	DL	DL	1.66	DL	DL	DL	DL	DL
	Maximum	2524	790	1511	757	3	873	3491	1	514	42	24	86	0.10	0.09	2.74	72	240	3	50	1.8	0.91
	Mean	**846**	**119**	**8**	**2**	**0.10**	**134**	**1168**	**0.03**	**2**	**0.23**	**0.89**	**3**	**0.01**	**0.01**	**0.38**	**3**	**11**	**0.13**	**0.70**	**0.05**	**0.03**
	Median	916	200	4	1	0.05	124	1469	0.02	2	0	3.10	6	0.01	0.02	0.70	11	40	0.09	1.44	0.07	0.15

* Minimum and maximum values correspond to whiskers value of box plots, not statistical outliers.

6.2.7. Discussion

Sediment deposition and primary metal enrichment processes at Talvivaara.

Based on work presented here it is deduced that the stage 1 pyrite is syn-sedimentary/ early-diagenetic in origin, as is typical for black shale deposition. This is represented as the fine-grained pyrite often found along well-preserved laminations. The high thermal stability of pyrite (710°C; Lambert et al., 1998), and its dominance in zones of less strain, suggests that the fine-grained, laminations are likely to be of primary or early-diagenetic in origin. This conclusion is in agreement with the previous work of Loukola-Ruskeeniemi and Heino (1996) and Loukola-Ruskeeniemi and Lahtinen, (2012). The preservation of fine-grained, laminated, syn-sedimentary/ early-diagenetic pyrite provides a context to study the seawater chemistry at the time of deposition. Recently, Large et al. (2014) proposed that sedimentary pyrite could be used as a first-order proxy for ocean chemistry through time. Trace elements are adsorbed onto pyrite as it forms in the water column or in the uppermost layers of sediments during diagenesis, providing an ability to record a 'snapshot' of the seawater chemistry at the time of deposition. Therefore, periods of high concentration of certain metals in seawater are recorded via the incorporation of high metal contents of sedimentary pyrite (Gregory et al., 2013: 2015). Applying this hypothesis to the early, well-preserved, pyrite (Py1), the data suggests that significant metal enrichment was prevalent in the seawater and/or uppermost pore waters during the deposition of the Talvivaara black shales. As stated previously, the majority of early pyrite (Py1) is <10 μm, suggesting that the majority of the pyrite formed in the water column (Wilkin et al., 1996). Nickel, Zn, Cu, Pb, Se, Mo and Co are all bio-essential trace elements and can occur in high abundance in shale deposited in a low-oxygen, biomass-rich, marine environment (Huerta-Diaz and Horse 1992; Large et al., 2014).

Whole-rock geochemistry (Table 6.1, 6.2, 6.3) show that Mn is elevated above and below the main ore horizon. However the lower Mn enrichment is likely influenced by the presence of garnet in that particular sample. Manganese enrichments can be related to periods of basin deepening (Large et al., 1998). Alternatively, these enrichments may represent Mn-oxide accumulation as a result of periods where the water column became more oxic. Another option may be that in the development of euxinic

conditions with high productivity, Mn can become concentrated below the chemocline where euxinic waters strongly sequester Fe but not Mn (Lyons and Severmann, 2006). The V/(V+Ni) ratios (Fig. 6.12) also suggest that the water column varied between anoxic, sulfide, and dysoxic states. High phosphorous values are also present above and below the ore horizon. Phosphorous concentrations are higher throughout the Talvivaara ore horizon, compared to the overlying Kuikkalampi Formation. Since phosphorous is a critical nutrient these horizons may represent periods of increased bio-productivity during the deposition of the Talvivaara sediments, facilitated by increased nutrient supply. Critically, bio-essential elements (i.e., Mo, Se, Zn, Cu, and Ni), as well as U and V that are often fixed by organic matter (Wackett et al., 2004) are all enriched by orders of magnitude in Talvivaara, compared to WSA. However elements such as Cr, Co, Mn, overall, display low enrichment factors. These are elements usually associated with hydrothermal environments (i.e. Von Damm, 1995).

High CIA values suggest that the source material to the basin was highly weathered and are comparable to Phanerozoic examples (e.g. Slack et al., 2015). Zr/Sc ratios do not suggest sufficient recycling of the source material before deposition.

Previous studies of the Talvivaara deposit have favored the role of hydrothermal fluids as a metal source, based on a positive Eu anomaly encountered associated with the ore horizon (Young et al., 2013; Loukola-Ruskeeniemi and Heino 1996). The data does not show any significant, nor systematic, variation in Eu when normalized to both chondrite and NASC. It is proposed that the positive Eu signature in their samples and the single, moderate enrichment in the dataset compiled in this study, may be related to detritus or early diagenetic processes within sediments with sulfidic pore waters, rather than hydrothermal processes (Slack et al., 2015). Gd/Yb vs Eu ratios for a range of Fennoscandian rocks of similar age to detrital zircon populations of 2.7 Ga show either comparable values or that a mixing of these sources could account for similar Eu enrichments. Th/Sc and Zr/Sc suggest very little sedimentary reworking but that there is the potential for a mix of mafic and felsic provinces. Shields and Stille (2001) showed, in great detail, that many REE budgets are linked to detrital input and that diagenesis and post- depositional alteration can affect their signal. Europium does not show a correlation with the ore metals but does show a weak correlation with TiO_2, suggesting that

phases such as metamorphic rutile may partly account for the REE budget of the rock. In addition, the influence of amphibolite grade metamorphism on redistributing or homogenizing the REE signature cannot be ruled out.

Metamorphism at Talvivaara

Observations by Santti et al. (2006) based on mineral assemblages in units proximal to the deposit suggest peak metamorphic temperatures of 550°C. Long-term high temperature equilibrium of the rocks at Talvivaara has influenced both the sulfide and silicate phases. With the exception of pyrite (Py1) and zircon, all minerals are considered to be metamorphogenic in origin.

Elemental partitioning during metamorphism can be attributed to the breakdown and recrystallization of early pyrite. At temperatures of greenschist facies and above, pyrite can recrystallize to form a metamorphic pyrite or pyrrhotite, each of these transitions is associated with the loss of the trace elements form the original pyrite (Craig and Vokes, 1993; Large et al., 2007; Pitcairn et al., 2010). Pyrrhotite is the most common ore mineral in the deposit. This suggests that much of the early pyrite has been converted to pyrrhotite. In a closed system, the reduction from pyrite to pyrrhotite (as expressed below) leads to the loss of sulfur via a variety of potential reactions. Experimental studies suggest this occurs when sulfur atoms combine on free surfaces and begin to desorb or react with a fluid. Iron, now out of equilibrium, begins to diffuse inwards until the original pyrite breaks down or is completely replaced by pyrrhotite (Lambert et al., 1998). The similar range in $\delta^{34}S$ values in the pyrrhotite as in pyrite 1 and 2 supports the suggestion that pyrrhotite is derived in this manner. A variety of reactions (Eq. 1- 5, after Hall et al., 1998) are possible, based on the likely composition of the host rock. Each of these is capable of liberating a large quantity of reduced sulfur during metamorphism, from either the original pyrite or from organic matter. This process may allow for sulfur to be then utilized in the formation of other metal sulfides, e.g. pentlandite, chalcopyrite, molybdenite and sphalerite.

$$2\ \text{Pyrite} + 2H_2O + C\ (\text{organics}) \rightleftharpoons 2\text{Pyrrhotite} + 2H_2S + CO_2 \quad (1)$$

$$8\ \text{Pyrite} + 3CH_4 + 6\ \text{Siderite} = 2\ \text{Pyrrhotite} + 9CO_2 + 12H^+(aq) \quad (2)$$

$$\text{Pyrite} + H_2 \rightarrow 2\ \text{Pyrrhotite} + 12HS^-_{(aq)} \quad (3)$$

$$14\ \text{Pyrite} + 3CH_4 \rightarrow 2\ \text{Pyrrhotite} + 3C + 12HS^-_{(aq)} \quad (4)$$

$$7\ \text{Pyrite} + 6CO + 6H_2O \rightarrow \text{Pyrrhotite} + 6CO_2 + 6H_2S_{(aq)} \quad (5)$$

The reactions were likely facilitated by the concurrent break down of organic components along pyrite grain boundaries, leading to the desorbtion of sulfur and consumption of pyrite by pyrrhotite. In addition, much of the whole-rock Fe budget was likely sulfidized during the metamorphic process as silicate minerals also destabilized. This, along with the high thermal stability of pyrite (710°C), may explain the preservation of the original pyrite as it may have been in excess to that required to balance the incorporation of silicate-hosted iron into the newly forming pyrrhotite. Given the destruction of the primary mineral assemblages during metamorphism, such a mechanism can only be indirectly deduced but fits well with experimental work (Lambert et al., 1998).

The accessory sulfide phases; sphalerite, galena, molybdenite, chalcopyrite and alabandite, commonly associated with pyrrhotite likely formed via liberation of metals from the earliest pyrite and organic matter which combined with sulfur (also liberated from the breakdown of the original rock mass) to form their own distinct phases. Similar associations between pyrrhotite development and Zn-, Cu- and As-sulfides have been noted by Craw et al., (2002), Large et al., (2007), and Pitcairn et al. (2010). The main ore minerals, pentlandite and pyrrhotite, likely formed in a similar fashion via unmixing of metastable Ni-(Co)-Fe-S, derived from the breakdown of Py 1, at peak metamorphic temperatures. The blebby texture of pyrrhotite and its dominance in the most deformed areas of the deposit support the idea that it is derived via exsolution processes and small-scale mobility at peak metamorphic conditions. However, the pyrrhotite is often observed in a layered or bedding-bound nature, usually on the scale of a few centimeters. This negates the possibility of large-scale mobility as a deposit-wide process. Due to the structure of pyrrhotite only Ni, Co and Se are common constituents, as other chalcophile elements do not fit well within the Fe and S lattice sites of pyrrhotite (Morimoto et al., 1975; Harries et al., 2011).

Previous studies have suggested that sulfide minerals quickly re-equilibrate during retrograde reactions, often observed as the sulfidation of pyrrhotite to pyrite (Barton, 1970; Hall et al., 1987). The formation of pyrite 3 can be attributed to this process where the addition of sulfur to the system, possibly derived from metamorphic fluids or the breakdown of organics, facilitated the growth of pyrite 3. Previous studies by Craig and Vokes (1993) and Pitcairn et al. (2010) observe a similar pattern where metamorphic homogenization of the early sulfur source occurs during prograde metamorphism followed by retrograde pyrite formation, carrying a positive signature due to the residual sulfur becoming available. We suggest that as the Ni-(Co)-Fe-S metastable solution began to unmix and form the nickel-rich phases (pentlandite and pyrrhotite), Co behaved in a more refractory sense, preferentially partitioning into Pyrite 3 which began to form during retrograde metamorphism. It is also possible that additional sulfur converted some pyrrhotite to pyrite (Py 3) or altered S fugacity sufficiently to promote pyrite growth and trace metal incorporation (Hall et al., 1987). This can account the variability of Co in pyrrhotite and its moderate increase in Pyrite 3. A similar process can also be invoked for the minor increases in Cu and Pb in Pyrite 3. Since chalcopyrite and galena are mechanically weak it is possible that they were affected during peak metamorphic conditions or leached by metamorphic fluids and began to release Cu and Pb back into the system. Alternatively, a change in physio-chemical conditions as a function of retrograde sulfur fugacity changes may also have promoted Cu and Pb uptake by Pyrite 3.

Pyrite 4, associated with late-stage veining, holds the lowest of metal contents of any pyrite from the genetic stages and likely formed under metal-depleted conditions. The association with late stage veining would suggest that the pyrite formed via residual metamorphic fluids at the retrograde stage (Fig. 6.19).

The whole-rock S% content does not show any systematic variation based on the dominance of late stage pyrite (Py 3 and Py 4) compared to early or prograde sulfides, suggesting that most of the sulfur produced by metamorphic desulfidation reactions was contained within the rock and not mobilized on a large scale, nor was a significant volume of sulfur added.

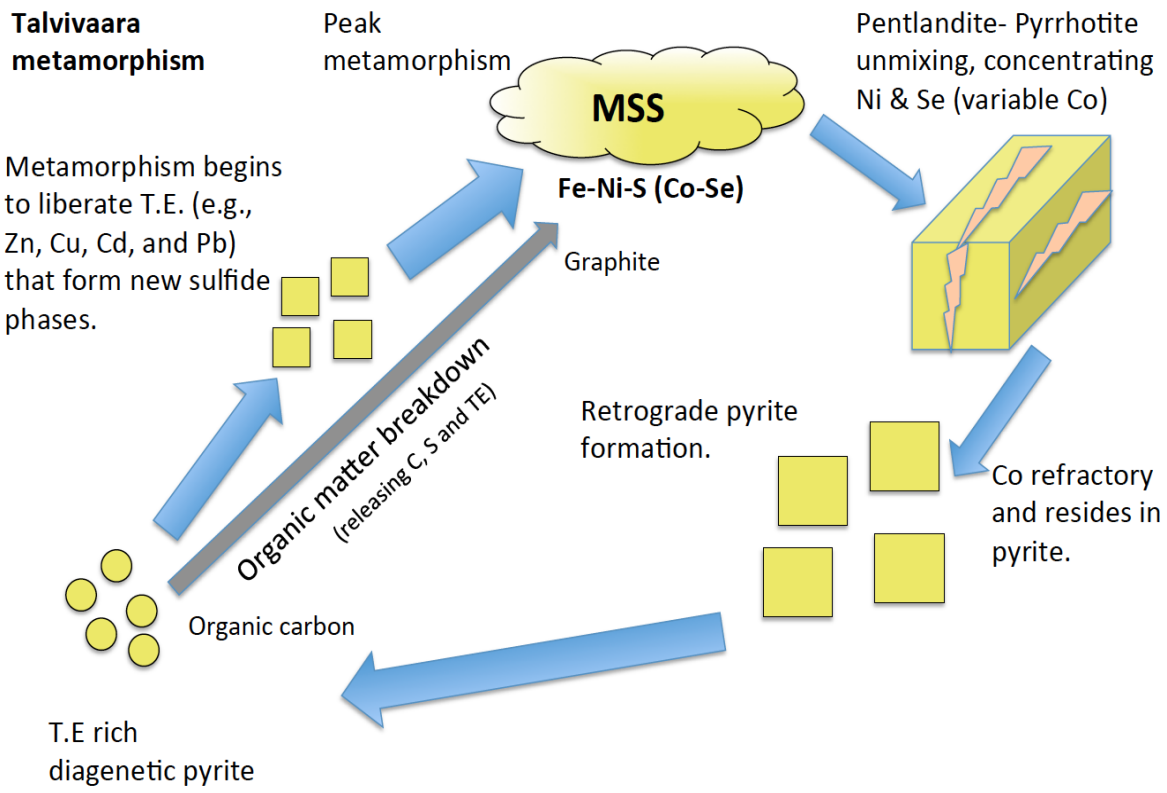

Figure 6.19. Schematic interpretation of sulfide paragenesis through metamorphism and the timing of trace metal release.

Sources of sulfur

Using a proposed ocean $\delta^{34}S$ sulfate value at the end of the GOE of ~10-14‰ (Schroder et al., 2008; Scott et al., 2014), suggests an average fractionation between the original sulfide (Py 1) and sulfate of ~20‰, consistent with open, or partly open, system BSR of seawater sulfate (Canfield, 2005). Importantly, there is no evidence in the sulfur isotope data to suggest an exotic hydrothermal sulfur source at the time of sedimentation and early sulfide formation.

Recent work (Scott et al., 2014) has suggested a dramatic increase in marine sulfate abundance during and towards the end of the GOE, hence, seawater is the likely source for sulfur in the Talvivaara rocks.

Scott et al. (2014) also proposed that the sulfate reservoir then began to contract around 2.0 Ga as evidenced by the narrowing in the range of $\Delta^{34}S$ reported by Anbar and Knoll (2008). Schroder et al. (2008) proposed that this may be due to increased pyrite burial, which could help to explain the high abundance of laminated sedimentary pyrite (Py1) preserved at Talvivaara and the high sulfur content of the rocks.

The isotopic data suggests that the early and prograde sulfides formed via a common bacteriogenic source. The data suggest that the initial diagenetic sulfides were produced by H_2S from sulfate reduction by bacteria, and this signature is retained during closed system metamorphism, recrystallization, and formation of other prograde metamorphic sulfide phases, including the key ore mineral, pentlandite. It is likely that during the reduction to pyrrhotite, the accessory sulfide minerals utilized both the released metals (Zn, Cu, Mo, Ni, Mn) and the liberated sulfur in their formation of sphalerite, chalcopyrite, molybdenite, pentlandite and alabandite, respectively.

The prograde mineral assemblage exhibits a narrower range in negative values and is likely an effect of metamorphic homogenization. Fractionation vectors between Py 2 and Po, Py2 and sphalerite, and sphalerite and galena, broadly correspond to those expected at temperatures of 450 to 550°C (Seal, 2006).

Pyrite 3 and 4 have positive $\delta^{34}S$ values that may be attributed to the introduction of an metamorphic fluid. Alternatively, the signature may be attributed to residual positive ^{34}S in the system, leading to the sulfidation of pyrrhotite to pyrite. This process has been observed in many high-grade metamorphic rocks (Hall et al., 1987; Pitcairn, et al., 2010) and is supported by the previous work of Craig and Vokes (1993) who state that metamorphic homogenization of the early bacteriogenic sulfur source occurs during prograde metamorphism is followed by retrograde pyrite formation, carrying a positive signature due to the residual, heavy sulfur available. The positive sulfur signature may be derived from the release of organic-bound sulfur during the breakdown of organic matter, changes in the physio-chemical state of the rock mass, or from seawater sulfate preserved within the rock or from pyrite which formed during partially closed system BSR. A combination of all of these factors is possible, through the latter two are less likely as a primary mix of positive and negative $\delta^{34}S$ values in the initial rock mass would

likely result in homogenization of both signatures at high temperatures, whereas the release of ^{34}S from organic matter converting to graphite close to peak metamorphism may account for the later stage input. Another possibility is that the sulfur source is from external hydrothermal or metamorphic fluids, though the data does not show significant whole-rock S% increases corresponding the dominance of Py 3 or Py 4 phases.

Critically, the lack of notable increase in the main ore elements (i.e. Ni, Cu, Zn) in late stage pyrites compared to those of the prograde assemblage suggests that this later sulfur source did not add significant metal to the overall ore budget.

Young et al. (2013) conducted a multi-sulfur isotope study of organic-rich rocks of the Karelia and Kola regions, including Talvivaara. Their study suggested that thermochemical sulfate reduction (Watanabe et al., 2009) was dominant; they also reported a minor mass-independent sulfur isotope fractionation (MIF-S), in some of the pyrites studied, which is unusual for strata post GOE. ^{33}S or ^{36}S data is required in order to comment fully on this idea, however, the majority of sulfur isotopic data presented here does not display any signatures consistent with hydrothermal fluids being associated with sedimentation or early metal input. Bacteriogenic sulfate reduction of MIF-S carrying sulfate, derived from an Archean source, however, might account for slight variations in $\Delta^{33}S$, such as those documented by Young et al. (2013). Reinhard et al. (2013) term this a "crystal memory effect" where anomalous $\Delta^{33}S$ can be recycled over long time scales. It is also noteworthy that the level of oxygen present in the atmosphere during this period (~2.0 Ga) is still a matter of debate (i.e. Bekker and Holland, 2012). A variety of published data show slight variations in $\Delta^{33}S$ during this time (~ 2.3-1.8 Ga) which can be attributed to the notion that atmospheric oxygen could have reached above PALx10^{-5} (PAL= present atmospheric level), the level of O_2 where MIF stops in experimental studies (Wing et al., 2005 and references therein) but remained below PAL x10^{-3}, the level of O_2 modeled to be required in order to fully establish an O-zone layer which would block the UV required to cause this fractionation (Segura et al., 2003). The effects of metamorphism at amphibolite grade may also play a role in the minor fractionations observed in their study. Additional multi-S isotopic work is planned in order to understand this in the context of the new data presented here.

Depositional environment and links to Paleoproterozoic seawater

The preservation of fine-grained, metal-rich, laminated pyrite at Talvivaara provides a context to study the state of seawater at the time of deposition as this may represent the conditions within the basin. The earliest pyrite (Py1), interpreted to be of syn-sedimentary or diagenetic origin, have the highest concentration of trace metals, suggesting that the metals were present in the basin during the time of the pyrite formation. The ultimate source of these metals is open to debate. However:

1) High TOC % content suggests that bio-productivity was high at the time of metal enrichment.
2) The elements enriched in the ore (Ni, Zn, Cu, Co, U, V and P) are the same bio-essential elements commonly enriched in black shales formed in anoxic to euxinic basins (Claver and Piper, 1984).
3) Detrital zircons, REE and metal ratios suggest that the ultimate source of the detrital input may be from mafic Archean igneous rocks.
4) CIA values suggest that intensive weathering of the parental material occurred.

A hydrothermal metal source (Loukola-Ruskeeniemi and Heino 1996) is a plausible scenario for metal enrichments in black shales. However the data suggests that an alternate model where the metal enrichment was a primary function of the nature of the deposition environment may also be a valid hypothesis.

Here, an alternate scenario where metal enrichment is related to the larger scale geodynamic fluxes occurring over this time period is proposed. Black shales with high metal content are commonly found in the geological record during periods of increased anoxia in the ocean. High trace elemental fluxes to basins can be attributed to an increase in oxygen, facilitating weathering and promoting nutrient uptake due to enhanced productivity (e.g., Anbar and Knoll, 2002; Parnell et al., 2012; Large et al., 2014; 2015). It is possible that the same mechanisms that promote metal enrichments in Phanerozoic black shales and sapropels (such as the Black Sea or during marine anoxic periods in the Phanerozoic; Lyons et al., 2003, Lehmann et al., 2007; Pasava et al., 2008; Jenkyns, 2010) are also what controlled the enrichment at Talvivaara, however, Talvivaara represents this process on a larger and more dramatic scale. During the Paleoproterozoic, large climatic and geochemical fluctuations occurred where the

dramatic rise of oxygen in the atmosphere (GOE, ~2.3- 2.4 Ga) promoted increased weathering of continental crust and oxidation of minerals, such as sulfides, that were formerly stable under a reduced atmosphere. This led to an increase in sulfate concentrations in the ocean and oxygenation of shallow waters promoting a strongly redox stratified ocean (Canfield, 2005). Bekker et al. (2008) argues that oxygen may have 'overshot' for a brief period and quickly risen higher than conventional models suggest at ~2.1 Ga, before dropping again for most of the Meso- and Neoproterozoic. In this context, intense oxidative weathering of metal-rich rocks may liberate a variety of trace metals, such as Ni, Zn, Cu, Cd and Se, which act as nutrients for photic-zone dwelling organisms in marine surface waters and are then deposited in the low oxygen (anoxic to euxinic) bottom waters as decaying organic matter (Fig. 6.20).

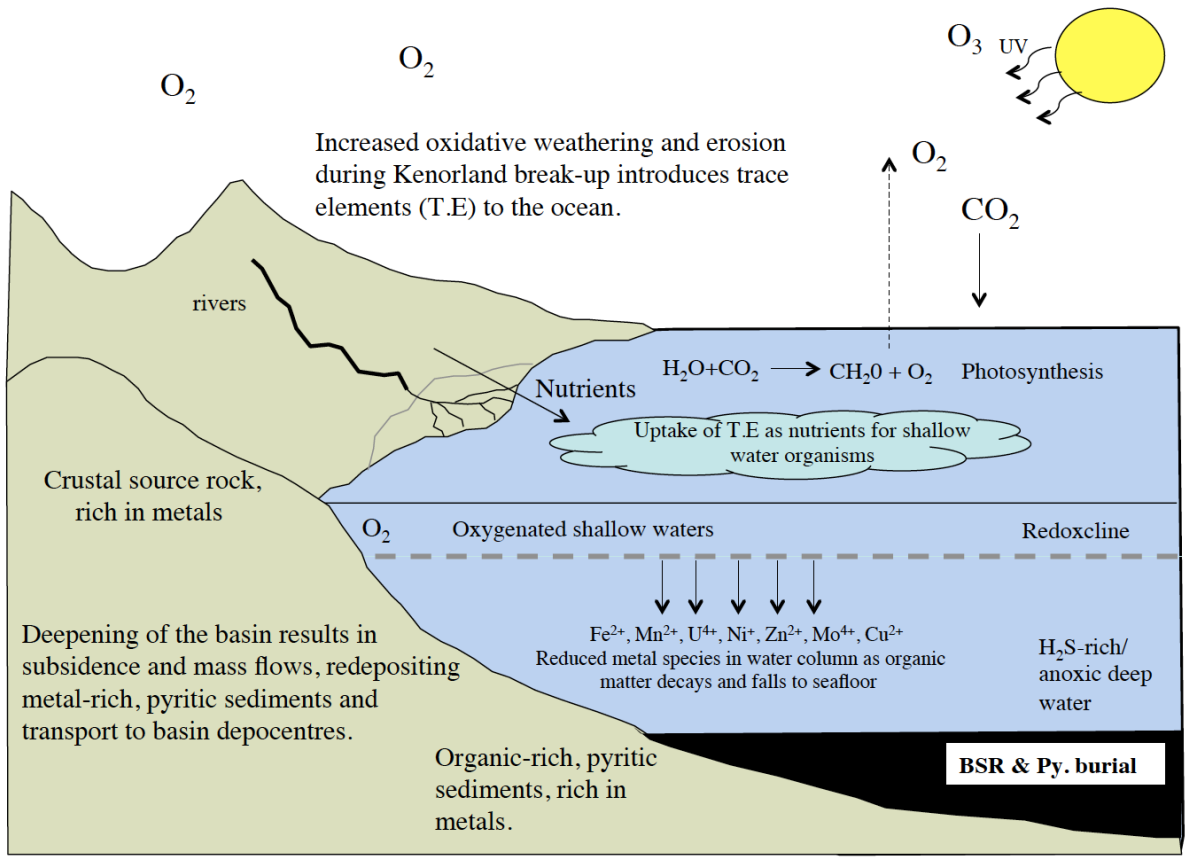

Figure 6.20. Schematic interpretation of the deposition environment of the Talvivaara sediments.

In order to understand the feasibility of this proposal a simple mass balance calculation was conducted (Table 4). Using the current area of the deposit (10kmx 2kmx1km) and average density of sedimentary rocks (2.7gcm^{-3}) as representing the basin sediments, along with the average composition of Py 1 (rounded to the nearest 0.05 wt%) as representing an initial composition, though this can be much higher based on the range of values reported for Py 1. From this calculation an initial composition of ~30% pyrite and 45% organic matter can produce the metal budget at Talvivaara. While this may represent an extreme end-member of black shale composition, it is also likely that organic matter may have held high amounts of Ni and Zn, given its propensity to sequester these elements (i.e. Gluskoter et al., 1977; Lewan and Maynard, 1982, Brumsack, 1989). Enrichments in TOC of this magnitude have been reported for other rocks of similar age across Fennoscandia (i.e. >50% in the Onega region; Melezhik et al., 2004), and many Phanerozoic black shales have also reported values of this magnitude (i.e. >55% in parts of the Mecca Quarry shale; Coveney et al., 1987; up to 35% in the Tollebuc Formation; Lewis et al., 2010; and 45% for the Hatteras Formation, deposited during Cretaceous Anoxic Event 2; Trabucho-Alexandre, 2010). This value only represents an initial organic component at the time of deposition but euxinic environments, such as those suggested as being prevalent during the deposition of the Talvivaara shales, would act to maximize the preservation potential and concentration of metals (Lyons et al., 2009). In addition, given the low-oxygen conditions during the time of formation, the original sulfide content may have been a mix between pyrite and other sulfide phases (i.e. Ni-rich monosulfides) that were consumed during metamorphism. The integration area selected is based on current exposure of the Talvivaara black schist in the area of deposit and it is extremely likely that the basin in which the muds collected was significantly larger, likely by orders of magnitude than the scale for which this model has been constructed. When this is considered, it is conceivable that enhanced black shale enrichment processes can easily facilitate the accumulation of metal equal to, and more, than that contained at Talvivaara.

Based on the diversity and chemistry of Fennoscandian rocks, all of these metals can conceivably be sourced from rocks that were exposed on the continent at the time. These two conclusions would

suggest that enhanced weathering and bio-productivity were both thriving as this time. These conditions are sufficient to facilitate increased pyrite burial and accumulation of organic matter, accounting for the high metal budget in the basin.

Base metal ratios at Talvivaara are similar to other sulphidic-graphitic shales of similar age across Fennoscandia (Kontinen et al., 2013). Furthermore, despite being Ni and Cu enriched by orders of magnitude compared to Phanerozoic shales, their ratios are similar to other Phanerozoic shales and that of recent planktonic species (e.g. Gluskoter et al., 1977; Brumsack, 1989). Since Ni and Cu contents are believed to reflect original organic matter accumulation (Tribovillard et al., 2005), this suggests that the primary metal concentration may be typical black shale deposition but in an environment where the metals were temporally and abnormally enriched. The enrichment is likely to have been on a large scale in order to facilitate the huge magnitude of metals stored in both the Talvivaara deposit and the associated, overlying black shales that are also enriched relative to average shale. Given the emphasis placed on Fennoscandian rocks of this age as an archive of global scale processes (Melezhik et al., 2013 and references therein), it is feasible to suggest that the metal enrichment in seawater during the period of Talvivaara black shale deposition may have been widespread, and potentially linked to global ocean conditions.

	Total (Mt) 2055	Mt	Metal content of Py1 (Avg. Wt%)	Deposit Area = 2km x 10km x 1km
				Density of Avg. Shale
Ni	0.20%	4.11	0.2	**2.7g/cm3**
Zn	0.50%	10.28	0.2	for 20 km3 **5.40E+03** **Mt**
Cu	0.13%	2.67	0.02	
Co	0.02%	0.41	0.01	

Metal content at Talvivaara (2055 Mt)	**17.47**

% Py in Blk Shl	Py in shale (Mt)	0.2% Ni	0.2% Zn	0.02% Cu	0.01% Co	Total (Mt)
2%	108	0.22	0.22	0.02	0.01	**0.5**
5%	270	0.54	0.54	0.05	0.03	**1.2**
10%	540	1.08	1.08	0.11	0.05	**2.3**
20%	1080	2.16	2.16	0.22	0.11	**4.6**
30%	**1620**	**3.24**	**3.24**	**0.32**	**0.16**	**7.0**
40%	2160	4.32	4.32	0.43	0.22	**9.3**

Organics in black shale	Organics in shale (Mt)					
10%	540	1.08	1.08	0.11	0.05	**2.3**
20%	1080	2.16	2.16	0.22	0.11	**4.6**
30%	1620	3.24	3.24	0.32	0.16	**7.0**
40%	2160	4.32	4.32	0.43	0.22	**9.3**
45%	**2340**	**4.68**	**4.68**	**0.47**	**0.23**	**10.1**
50%	2700	5.4	5.40	0.54	0.27	**11.6**

Table 6.5. Summary of mass balance calculations.

6.2.8. Conclusions

The base metal-rich Talvivaara deposit in Finland is a type locality and is, by size, the largest metalliferous black shale deposit in the world. The majority of the key metals in the deposit are mainly associated with fine-grained, diagenetic pyrite and metamorphic pyrrhotite, pentlandite, sphalerite, galena, chalcopyrite, alabandite and minor molybdenite. Using in-situ sulfur isotopes, and LA-ICP-MS element budgets within pyrite and pyrrhotite, and the dynamics of sulfide evolution through the metamorphic sequence have been tracked. Nickel, and other metal enrichments are associated with early stage pyrite, interpreted to be of a syn-sedimentary or diagenetic origin. It is likely that metals were also associated with organic matter that has since been lost. This implies that significant metal enrichment was present in the basin on a large scale at the time of sedimentation. This enrichment is likely related to 'supercharged' black shale enrichment mechanisms, pertaining the wake of the GOE, where water column chemistry was significantly different from those of the Phanerozoic, helping to facilitate and preserve such a high metal concentration. This may explain why there are no equivalents to Talvivaara in terms of size and grade forming at other periods of Earth History, as Talvivaara represents an exclusive combination of conditions specific to the Paleoproterozoic. The rise of oxygen in the atmosphere would have led to aggressive oxidative weathering of the Fennoscandian Shield during that time, yielding detritus into the ocean, where trace elements acting as essential nutrients, drove high biological productivity. Decaying organisms, along with a strong redox gradient between the oxygenated surface and anoxic deep waters, helped to deliver a vast quantity of metals to the seafloor and provide adequate conditions for their accumulation. Such processes and depositional environment effectively preconditioned the basin with metal-rich sediments. High-grade metamorphism during the Svecofennian Orogeny led to the break down and recrystallization of the majority of the original assemblage and liberation of metals during the transformation of pyrite to pyrrhotite and organic phases to graphite. The metals and sulfur released were utilized to form the resultant metal-sulfide assemblage of the or**e.**

6.3 References

Algeo, T. J. Maynard, J.B., 2004. Trace-element behavior and redox facies in core shales of Upper Pennsylvanian Kanas-type cyclothems. Chemical Geology, 206, p. 289-318.

Anbar, A.D., Knoll, A.H., 2002, Proterozoic ocean chemistry and evolution: A bioinorganic bridge? Science, 297, p.1137–1142.

Baker, J., Peate, D., Waight, T., Meyzen, C., 2004. Lead isotopic analysis of standards and samples using a Pb-207-Pb-204 double spike and thallium to correct for mass bias with a double focusing MC-ICP-MS. Chemical Geology, 211, p. 275-303.

Barley, M.E.,Bekker, A. Krappez, B., 2005. Late Archean to Early Paleoproterozoic global tectonics, environmental change and the rise of atmospheric oxygen. Earth and Planetary Science Letters, 238, p.156-171.

Barton, P.B., 1970. Sulfide petrology. Mineralogical Society of America special paper, 3, p. 187-198.

Bekker, A., Holland, H.D., 2012. Oxygen overshoot and recovery during the early Paleoproterozoic. Earth and Planetary Science Letters, 317, p. 295-304.

Berner, R.A. 1984. Sedimentary pyrite formation: an update. Geochimica Cosmochimica Acta, 48, p. 605- 615.

Black, L.P., Kamos, L., Allen, C.M., Aleinkoff, J.N., Davis, D.W., Korsch, R.J., Foudoulis, C., 2003. TEMORA 1: a new zircon standard for Phanerozoic U-Pb geochronology. Chemical Geology, 200, p. 155-170.

Black, L.P., Gulson, B.L., 1978. The age of the Mud Tank Carbonatite, Strangways Range, Northern Territory. Journal of Australian Geology and Geophysics, 3, 227-232.

Brumsack, H.J., 1989. Geochemistry of recent TOC-rich sediments from the Gulf of California and the Black Sea. Geoligische Rundschau. 78, p. 851–882.

Calvert, S.E., Piper, D.Z. 1984. Geochemistry of ferromanganese nodules from DOMES Site A, Northern Equatorial Pacific: Multiple diagenetic metal sources in the deep sea. Geochemica et Cosmochemica Acta, 48, p. 1913-1928.

Canfield, D.E., 1998. A new model for Proterozoic ocean chemistry. Nature, 396, p. 450-453.

Canfield, D.E., 2005. The early history of atmospheric oxygen. Annual Reviews in Earth and Planetary Science 33. 1-36.

Cave, B. J., Stepanov, A. S., Craw, D., Large, R. R., Halpin, J. A. Thompson, J. 2015. Release of trace elements through the sub-greenschist facies breakdown of detrital rutile to metamorphic titanite in the Otago Schist, New Zealand. The Canadian Mineralogist, 53, p. 379-400.

Chang, Z., Large, R.R., Maslennikov, V., 2008. Sulfur isotopes in sediment-hosted orogenic gold deposits: Evidence for an early timing and a seawater sulfur source. Geology, 36, p. 971-974.

Craig, J.R Vokes F.M.,1993. The metamorphism of pyrite and pyritic ores: an overview. Mineralogical Magazine. 57, 3-18.

Craw, D. 2002. Geochemistry of late metamorphic hydrothermal alteration and graphitisation of host rock, Macraes gold mine, Otago Schist, New Zealand. Chemical Geology, 191, p. 257-275.

Danyushevsky, L.V., Robinson, P., Gilbert, S., Norman, M., Large, R., McGoldrick, P., Shelley, M., 2011. Routine quantitative multi-element analysis of sulphide minerals by laser ablation ICPMS: Standard development and consideration of matrix effects. Geochemistry: Exploration, Environment, Analysis, 11, p. 51-60.

Douville, E., Charlou, J.L., Oelkers, E.H., Bienvenu, P., Colon, C.J., Donval, J.P., Fouquet, Y., Prieur, D. and Appriou, P., 2002. The rainbow vent fluids (36 14'N, MAR): the influence of ultramafic rocks and phase separation on trace metal content in Mid-Atlantic Ridge hydrothermal fluids. Chemical Geology, 184, p. 37-48.

Emerson, S. R., Huested, S.S. 1991. Ocean anoxia and the concentrations of molybdenum and vanadium in seawater. Marine Chemistry, 34, p. 177– 196.

Eilu, P., Ahtola, T., Äikäs, O., Halkoaho, T., Heikura, P., Hulkki, H., Iljina, M., Juopperi, H., Karinen, T., Kärkkäinen, N., Konnunaho, A., Kontinen, A., Kontoniemi, O., Korkiakoski, E., Korsakova, M., Kuivasaari, T., Kyläkoski, M., Makkonen, H., Niiranen, T., Nikander, J., Nykänen, V., Perdahl, J.-A., Pohjolainen, E., Räsänen, J., Sorjonen-Ward, P., Tiainen, M., Tontti, M., Torppa, A., Västi, K., 2012. Metallogenic areas in Finland. Mineral Deposits and Metallogeny of Fennoscandia. Geological Survey of Finland. Special Paper 53, p. 207–342.

Fallick, A.E., McConville, P., Boyce, A.J., Burgess, R., Kelley, S.P., 1992. Laser microprobe stable isotope measurements on geological materials: Some experimental considerations (with special reference to δ34S in sulphides) Chemical Geology, 101, p. 53–61.

Gluskoter, H.J., Ruch, R.R., Miller, W.G., Cahill, R.A. and Dreher, G.B., 1977. Trace elements in coal: occurrence and distribution. Final report, June 1974--June 1976 (No. PB-270922). Illinois State Geological Survey, Urbana (USA).

Gregory, D.D., Meffre, S, Large, R.R. 2013. Mineralogy of metal contaminated estuarine sediments, Derwent estuary, Hobart, Australia: Implications for metal mobility. Australian Journal of Earth Science. 60, p. 589-603.

Gregory, D.D., Large, R.R., Halpin, J.A., Lounejeva, E., Lyons, T.W., Wu, S., Danyushevsky, L.V., Sack, P., Chappaz, A., Maslennikov, V.V., 2015. Trace element content of sedimentary pyrite in black shales. Economic Geology, 110, p. 1389- 1410.

Hall, A.J, Boyce, A.J. and Fallick, A.E., 1987. Iron sulphides in metasediments: isotopic support for retrogressive pyrrhotite to pyrite reaction. Chemical Geology, 65, p. 305-310.

Harries D., Pollok K., and Langenhorst F., 2011. Translation interface modulation in NC-pyrrhotites: Direct imaging by TEM and a model toward understanding partially disordered structural states. American Mineralogist 96, p. 716–731.

Holland, H. D., 1984. The Chemical Evolution of the Atmosphere and Oceans. Princeton Univ.Press, Princeton, USA.

Holland, H.D. 2002. Volcanic gases, black smokers and the Great Oxidation Event. Geochimica et Cosmochimica Acta, 66, p. 3811-3826.

Huhma, H., O'Brien, H., Lahaye, Y. and Mänttäri, I. 2011. Isotope geology and Fennoscandian lithosphere evolution. Geological Survey of Finland Special Paper 49, p. 35-48.

Jackson, S.E., Pearson, N.J., Griffin, W.L., Belousova, E.A. 2004. The application of laser ablation inductively coupled plasma-mass spectrometry to in-situ U-Pb zircon geochronology. Chemical Geology, 211, p. 47-69.

Käpyaho, A., Mänttäri, I., and Huhma, H. 2006. Growth of Archaean crust in the Kuhmo district, eastern Finland: U-Pb and Sm-Nd isotope constraints on plutonic rocks. Precambrian Research, 146, p. 95-119.

Käpyaho, A., Hölttä, P., Whitehouse, M.J. 2007. U-Pb zircon geochronology of selected Archaean migmatites in eastern Finland. Bulletin of the Geological Society of Finland, 79, p. 95-115.

Kontinen, A.T., Hanski, E. In Press. The Talvivaara black-shale hosted Ni-Zn-Cu-Co deposit, eastern Finland. In Maier, W., Lahtinen, H and O'Brien, H. eds. Mineral Deposits of Finland. Elsevier.

Kontinen, A.T., Sorojen-Ward, P., Huhma, H., Lahtinen, H., 2013. Lithostratigraphy, sedimentary environment and origin of the Talvivaara black schist hosted Ni-Zn-Cu- Co deposit. Geological Survey of Finland, Report 198.

Kosler, J., 2001, Laser-ablation ICPMS study of metamorphic minerals and processes. In: Sylvester P. J. ed. Laser-ablation-ICPMS in the earth sciences; principles and applications Mineralogical Association of Canada Short Course Handbook 29, p.185-202.

Lahtinen, R., Huhma, H., Kohonen, J., Kontinen, A., Sorjonen-Ward, P. 2010. New constraints for the source characteristics, deposition and age of the 2.1-1.9 Ga metasedimentary cover at the western margin of the Karelian Province. Precambrian Research 176, p. 77–93.

Lambert, J.M., Simkovich, G., Walker, P.L. 1998. The kinetics and mechanism of the pyrite to pyrrhotite transformation. Metalurgical and materials transactions. 29B, p. 385-396.

Large, R.R., Bull, S.W., Cooke, D.R., and McGoldrick, P.J, 1998. A genetic model for the HYC deposit, Australia, based on regional sedimentology, geochemistry, and sulfide-sediment relationships: Economic Geology, 93, p. 1345–1368.

Large, R.R., Maslennikov, V.V., Robert, F., Danyushevsky, L.V., Chang, Z., 2007. Multistage sedimentary and metamorphic origin of pyrite and gold in the giant Sukhoi Log deposit, Lena gold province, Russia. Economic Geology, 102, p. 1233-1267.

Large, R.R., Danyushevsky, L., Hollitt, C., Maslennikov, V., Meffre, S., Gilbert, S., Bull, S., Scott, R., Emsbo, P., Thomas, H., Singh, B., Foster, J., 2009. Gold and trace element zonation in pyrite using a laser imaging technique: Implications for the timing of gold in orogenic and Carlin-style sediment-hosted gold deposits. Economic Geology, 104, p. 635-668.

Large, R.R., Halpin, J.A., Danyushevsky, L.V., Maslennikov, V.V., Bull, S.W., Long, J.A., Gregory, D.D., Lounejeva, E., Lyons, T.W., Sack, P.J., McGoldrick, P.J., Calver, C.R., 2014. Trace element content of sedimentary pyrite as a new proxy for deep-time ocean-atmosphere evolution, Earth and Planetary Science Letters, 389, p. 209-220.

Lehmann, B., Nagler, T.F., Holland, H.D., Willie, M., Mao, J., Pan, J., Dongsheng, M., Dulski, P., 2007. Highly metalliferous carbonaceous shale and Early Cambrian seawater. Geology, 35, p. 403-406.

Leventhal, J., 1987. Carbon and sulfur relationships in Devonian shales from the Appalachian basin as an indicator of environemnet of deposition. American Journal of Science, 287, p. 33-49.

Lewan, M.D., Maynard, J.B. 1982. Factors controlling enrichment of vanadium and nickel in the bitumen of organic sedimentary rocks. Geochimica et Cosmochimica Acta Vol. 46, p. 2547-2560

Li, X., Long, W.G., Li, Q.L., Liu, Y., Zheng, Y.F., Yang, Y.H., Chamberlain, K.R., Wan, D.F., Guo, C.H., Wang, X.C., Tao, H., 2010. Penglai Zircon Megacrysts: A Potential New Working Reference Material for Microbeam Determination of Hf-O Isotopes and U-Pb Age. Geostandards Geoanalysis Research, 34, p. 117-134.

Longerich, H.P., Jackson, S.E., Günther, D., 1996. Laser ablation inductively coupled mass spectrometric transient signal data acquisition and analyte concentration calculation. Journal of Analytical Atomic Spectrometry, 11, p. 899-904.

Loukola-Ruskeeniemi, K., 1991. Geochemical evidence for the hydrothermal origin of sulphur, base metals and gold in Proterozoic metamorphosed black shales, Kainuu and Outokumpu areas, Finland. Mineralium. Deposita. 26, p. 152–164.

Loukola-Ruskeeniemi, K., Heino, T., 1996. Geochemistry and genesis of the black shale hosted Ni–Cu–Zn deposit at Talvivaara, Finland. Economic Geology. 91, p. 80–110.

Loukola-Ruskeeniemi, K., 1999. Origin of black shales and the serpentinite-associated Cu–Zn–Co ores at Outokumpu in Finland. Economic. Geology. 94, p. 1007–1028.

Loukola-Ruskeeniemi, K., Lahtinen, H. 2013. Multiphase evolution in the black schist hosted Ni-Cu-Zn-Co deposit at Talvivaara, Finland. Ore Geology Reviews, 52, p. 85-99.

Lyons, T.W., and Severmann, S., 2006. A critical look at iron paleoredox proxies: New insights from modern euxinic marine basisns: Geochimica et Cosmochimica Acta, 70, p. 5698–5722.

Lyons, T.W., and Severmann, S., 2006. A critical look at iron paleoredox proxies: New insights from modern euxinic marine basisns: Geochimica et Cosmochimica Acta, 70, p. 5698–5722.

Martin, A.P., Condon, D.J., Prave, A.R., Melezhik, V.A., Lepland, A. and Fallick, A.E., 2013. Dating the termination of the Palaeoproterozoic Lomagundi-Jatuli carbonisotopic event in the North Transfennoscandian Greenstone Belt. PrecambrianResearch, 224, p.160-168.

McLennan, S. M., Hemming, S., Mcdaniel, D. K., 1993. Geochemical approaches to sedimentation, provenance and tectonics. Processes Controlling the Composition of Clastic Sediments (Jonhanson, M. J. et al., eds.), Geological Society of America Special Paper, 284, p. 21–40.

Meffre, S., Large, R.R., Scott, R., Woodhead, J., Chang, Z., Gilbert, S.E., Danyushevsky, L.V., Maslennikov, V., Hergt, J.M., 2008. Age and pyrite Pb-isotopic composition of the giant Sukhoi Log sediment-hosted gold deposit, Russia. Geochimica et Cosmochimica Acta, 72, p. 2377-2391.

Melezhik, V.A., Filippov, M.M. and Romashkin, A.E., 2004. A giant Palaeoproterozoic deposit of shungite in NW Russia: genesis and practical applications. Ore Geology Reviews, 24, p.135-154.

Melezhik, V.A. 2006. Multiple Causes of Earth's earliest global glaciation. Terra Nova, 18, p. 130-137.

Melezhik, V. A., Prave, A., Fallick, A.E., Kump, L., Struass, H., Lepland, A., Hanski, E., (Eds), 2013. Reading the Archive of Earth's oxygenation. Volume 1.: The Paleoproterozoic of Fennoscandia as Context for the Fennoscandian Arctic Russia Drilling Early Earth Project. Frontiers in Earth Sciences. Springer, Hiedelberg.

Morimoto, N., Gyobu, A., Mukaiyama, H. and Izawa, E., 1975. Crystallography and stability of pyrrhotites. Economic Geology, 70, p. 824-833.

Nesbitt, H.W. Young G.M. 1982. Early Proterozoic climates and plate motions inferred from major element chemistry of lutites. Nature, 299, p. 715-717.

Pasava, J., Kribek, B., Vymazalova, A., Sykorova, I., Zak, K., Orberger, B., 2008. Multiple sources of metals of mineralization in Lower Cambrian black shales in south China: evidence from geochemical and petrographic study. Resource. Geology. 58, p. 25–42.

Paton, C., Woodhead, J.D., Hellstrom, J.C., Hergt, J.M., Grieg, A., Maas, R., 2010. Improved laser ablation U-Pb zircon geochronology through robust down-hole fractionation correction. Geochemistry, Geophysics, Geosystems, 11.

Pitcairn, I.K., Olivo, G.R., Teagle, D.A.H., Craw, D., 2010. Sulphide evolution during prograde metamorphism of the Otago and Alpine Schists, New Zealand. Can. Mineral. 48, p. 1267–1296.

Puchtel, I. S., Haase, K. M., Hofmann, A. W., Chauvel, C., Kulikov, V. S., Garbe-Schönberg, C.D. Nemchin, A. A. 1997. Petrology and geochemistry of crustally contaminated komatiitic basalts from the Vetreny Belt, southeastern Baltic Shield: evidence for an early Proterozoic mantle plume beneath rifted Archean continental lithosphere. Geochimica et Cosmochimica Acta 61, p. 1205–1222.

Raghavan, V., 2004. Fe-Ni-S (Iron-Nickel-Sulfur), J. Phase Equilibria and Diffusion, 25, p. 373-381.

Rämö, O.T., Halla, J., Nironen, M., Lauri, L.S., Kurhila, M.I., Käpyaho, A., Sorjonen-Ward, P., Äikäs, O., 2005. EUROGRANITES 2005— Proterozoic and Archean Granites and Related Rocks of the Finnish Precambrian. Eurogranites 2005 Field Conference, September 11–17.

Reinhard, C.T., Raiswell, R., Scott, C., Anbar, A.D., Lyons, T.W., 2009, A late Archean sulfidic sea stimulated by early oxidative weathering of the continents. Science. 326, p. 713–716.

Reinhard C.T., Planavsky, N.J., Lyons, T.W., 2013. Long-term sedimentary recycling of rare sulphur isotope anomalies. Nature, 497, p. 100-103.

Rimmer, S.M., 2004. Geochemical paleoredox indicators in Devonian–Mississippian black shales, central Appalachian Basin (U.S.A.). Chemical Geology 206, p. 373- 391.

Robinson P. 2003. XRF analysis of flux-fused discs. Geoanalysis 2003, Analysis of Geological and Environmental Materials, Abstracts, 90.

Rollinson, H.R., 1993. *Using geochemical data: evaluation, presentation, interpretation*, Longman Group UK.

Sack, P.J., Berry, R.F., Meffre, S., Falloon, T.J., Gemmell, J.B., Friedman, R.M., 2011. In-situ location and U-Pb dating of small zircon grains in igneous rocks using laser ablation inductively coupled plasma-quadrupole mass spectrometry. Geology, Geophysics, Geosystems, 12.

Santti, J., Kontinen, A., Sorojonen-Ward, P., Johanson, B., Pakkanen,L., 2006. Metamorphism and chromite in serpentinized and carbonate-silica-altered peridotites of the Paleoproterozoic Outokumpu-Jorma ophiolite belt, Eastern Finland. International Geology Review, 48, p. 494-546.

Schröder, S., Bekker, A., Beukes, N. J., Strauss, H. and Van Niekerk, H. S., 2008. Rise in seawater sulphate concentration associated with the Paleoproterozoic positive carbon isotope excursion: evidence

from sulphate evaporites in the ~ 2.2–2.1 Gyr shallow-marine Lucknow Formation, South Africa. Terra Nova. 20, p. 108-117.

Scott, C.T., Wing, B.A., Bekker, A., Planavsky, N.J., Medvedev, P., Bates, S.M., Yun, M., Lyons, T.W., 2014. Pyrite multiple-sulfur isotope evidence for rapid expansion and contraction of the early Paleoproterozoic seawater sulfate reservoir. Earth and Planetary Science Letters, 389, p. 95-104.

Seal, R.R., 2006. Sulfur isotope geochemistry of sulphide minerals. Reviews in mineralogy Geochemistry, 61, p. 633-677.

Segura, A., Krelove, K., Kasting, J.F., Sommerlatt, D., Meadows, V., Crisp, D., Cohen, M., Mlawer, E. 2003. Ozone concentrations and Ultraviolet Fluxes on Earth-like Planets around other stars. Astrobiology, 3, p. 689-708.

Slama, J., Kosler, J., Condon, D.J., Crowley, J.L., Gerdes, A., Hanchar, J.M., Horstwood, M.S.A., Morris, G.A., Nasdala, L., Norberg, N., Schaltegger, U., Schoene, B., Tubrett, M.N., Whitehouse, M.J., 2008. Plesovice zircon - A new natural reference material for U-Pb and Hf isotopic microanalysis. Chemical Geology, 249, p. 1-35.

Trabucho Alexandre, J., Tuenter, E.,. Henstra, G. A., van der Zwan, K. J., van de Wal, R. S. W., Dijkstra H. A., and de Boer, P. L., 2010. The mid-Cretaceous North Atlantic nutrient trap: Black shales and OAEs, Paleoceanography, 25, PA4201.

Tribovillard, N., Ramdani, A., Trentesaux, A., 2005. Controls on organic accumulation in Late Jurassic shales of northwestern Europe as inferred from trace-metal geochemistry. In: Harris, N. (Ed.), The Deposition of Organic-Carbon-Rich Sediments: Models, Mechanisms, and Consequences. SEPM Spec. Pub., 82, p. 145–164.

Von Damm, K.L., 1995. Controls on the chemistry and temporal variability of seafloor hydrothermal fluids. *Seafloor Hydrothermal Systems: Physical, Chemical, Biological, and Geological Interactions*, p.222-247.

Vine, J.D., Tourtelot, E.B. 1970 Geochemistry of black shale deposits; a summary report. Economic Geology, 65, p. 253-272.

Wackett, L.P., Dodge, A.G. and Ellis, L.B., 2004. Microbial genomics and the periodic table. Applied and environmental microbiology, 70, p. 647-655.

Wagner, T., Boyce, A.J., Fallick, A.E. 2002. Laser combustion analysis of δ34S of sulfosalt minerals: determination of the fractionation systematics and some crystal-chemical considerations. Geochimica et Cosmochimica Acta, 66, p. 2855-286.

Watanabe, Y., Farquhar, J., Ohmoto, H., 2009. Anomalous fractionations of sulfur isotopes during thermochemical sulfate reduction. Science, 324, p. 370-373.

Weidenbeck, M.,Alie, P., Corfu, F, Griffin, W.L., Meier, M., Oberli, F., Vonquadt, A., Roddick, J.C., Speigel, W., 1995. 3 natural zircon standards for U-Th-Pb-Lu-Hf, trace element and REE analyses. Geostandards Newsletter, 19, p. 1-23.

Williams, H., Hoffman, P.F., Lewry, J.F., Monger, J.W.H., Rivers, T., 1991. Anatomy of North America: thematic portrayals of the continent. Tectonophysics 187, p. 117–134.

Wilkin, R.T., Barnes, H.L. and Brantley, S.L., 1996. The size distribution of framboidal pyrite in modern sediments: an indicator of redox conditions. Geochimica et Cosmochimica Acta, 60, p. 3897-3912.

Wing, B., Lyons, J.R., Ono, S., Farquhar, J., Jonasson, I., Kaufman, A.J. 2005. Reconciling isotope effects of SO2 photolysis with Archean record of sulfur multiple isotopes. Geochemica et Comochimica Acta, 69, A451.

Young, S.A., Loukola-Ruskeeniemi, K., Pratt, L.M., 2013. Reactions of hydrothermal solutions with organic matter in Palaeoproterozoic black shales at Talvivaara, Finland: evidence from multiple sulfur isotopes. Earth and Planetary Science Letters, 367, p. 1-14.

Yu, Z., Robinson, P. and McGoldrick, P., 2001. An Evaluation of Methods for the Chemical Decomposition of Geological Materials for Trace Element Determination using ICP-MS. Geostandards Newsletter, 25, p.199-217.

Chapter 7

The transformation of pyrite to pyrrhotite in black shales and its role in metal-enrichments

7.1. Foreword

The ability of pyrite to sequester and then release trace elements during metamorphism has been discussed in pervious chapters. Many workers consider the transition of pyrite to pyrrhotite during greenschist metamorphism, and above, as a critical mechanism in the formation of orogenic gold deposits (Pitcairn et al., 2006; 2010; Large et al., 2011). This chapter outlines aspects of the pyrite to pyrrhotite conversion in black shales and trace element mobility as a function of this reaction. Trace element release during the metamorphic conversion of pyrite to pyrrhotite has previously been studied, particularly the mobility of arsenic and gold during greenschist facies metamorphism (i.e. Pitcairn et al., 2006; 2010; Tomkins, 2010; Thomas et al, 2011, Large et al, 2012). This chapter documents the results of an experimental study and then examines real-world examples from metamorphosed sulphide-rich rocks to demonstrate that the conversion to pyrrhotite occurs at temperatures lower than previously documented. A hypothesis is presented and discussed that suggests that the organic-rich nature of the shales are able to reduce pyrite to pyrrhotite at lower temperatures than in less organic rich rocks. The chapter also explores the concept that the heat released during the reaction may help to progress the transformation on the mineral scale and, potentially, on the scale of the rock mass. These two concepts may have important implications for the formation of ore deposits worldwide.

7.2. Low temperature pyrite to pyrrhotite reduction in black shales: implications for ore deposit models.

7.2.1. Abstract

Pyrite and pyrrhotite are common sulfide minerals in marine black shales and their metamorphic equivalents. During metamorphism desulfidation reactions can lead to breakdown of pyrite to form pyrrhotite. Although pyrite is capable of reducing to pyrrhotite at room temperature in a hydrogen atmosphere, in geological systems the transformation is often only considered relevant at middle-greenschist facies temperatures (i.e. >300°C, Toulmin and Barton, 1964; Craig and Vokes, 1993; Pitcairn et al., 2006; Large et al., 2011). However, paleomagnetic studies have recognized pyrrhotite-borne magnetic characteristics in carbonaceous sediments from throughout geological history and in rocks of low thermal maturities (e.g. Weaver et al., 2002; Fischer et al., 2014). Due to advancements in analytical techniques, we can now investigate both geochemical and magnetic variation within rocks and minerals at a fine scale. Here a controlled laboratory rock magnetometry detection test and in-situ geochemistry for a series of real-world examples of pyrite converting to pyrrhotite at conditions below greenschist facies metamorphism are presented. The experiments suggest that low temperature transformation of pyrite to pyrrhotite lies in mineral-scale solid state diffusion-limited reactions, or in the formation of pyrrhotite inclusions or domains within pyrite. It is proposed that the concurrent breakdown of organic matter in the shale during catagenetic to low-metamorphic conditions aids in producing sufficient reduction potential for the transformation. Since the breakdown of pyrite during metamorphism of black shales has been a suggested source for many orogenic gold deposits, and since the loss of Au is one of the first stages of the pyrite reduction process, there is the potential for many sub-greenschist settings to be prospective for large tonnage low-grade gold deposits.

7.2.2. Introduction

Pyrite and pyrrhotite are the two most common naturally occurring sulfides on the planet. Pyrite is a common constituent in sediments deposited below low-oxygen water columns. It has also been shown to incorporate a variety of trace metals into its structure, forming a substantial host of refractory gold in many ore deposits (e.g. Pitcairn et al., 2010; Large et al., 2012).

The thermal decomposition of pyrite has been investigated by many researchers, as has its capacity to release metals during metamorphism (e.g. Pitcairn et al., 2010; Large et al., 2012). Experimental studies report activation energies for this reaction in the range from 70 to 200kJ/mol (Toulmin and Barton, 1964; Guha and Narsimhan, 1972; Lambert et al., 1998) with the rate-determining step proposed as the dissociation of sulfur anions in the pyrite structure, accompanying lattice destruction and the movement of the pyrite/pyrrhotite interface on the mineral scale. Therefore, it stands to reason that the reduction potential of a rock mass many exert influence on sulfur mobility within the structure of the pyrite, facilitating the conversion to pyrrhotite, and the release of trace elements and sulfur.

Paleomagnetic studies have documented pyrrhotite-borne magnetizations in thermally-immature carbonaceous and reduced sedimentary rocks from throughout geological history (e.g. Weaver et al, 2002; Fischer et al., 2014). Since pyrrhotite has ferromagnetic characteristics whereas pyrite is only weakly paramagnetic, rock magnetic techniques are capable of detecting pyrrhotite as well as, potentially, characterizing its full crystal morphometrics in a sample at the ppm to ppt range, depending on the sensitivity of the magnetic techniques applied. At such trace levels, pyrrhotite domains may not be recognizable using bulk or even micron-scale compositional analysis of pyrite.

Presented here is an experimental magnetic study of a pyrite sample and how its magnetic characteristics vary as a function of increasing temperature in order to ascertain potential mineral-scale transitions. This is supplemented by the trace element geochemistry of two real-world examples of pyrrhotite forming in low concentrations in black shales that have only experienced sub-greenschist facies metamorphism. A new, conceptual model suggesting that the transition to pyrrhotite, and release of trace elements can be facilitated at lower temperatures is presented. This model proposes that local heat flux within the rock mass may lead to the breakdown of organic matter, creating sufficient reduction

potential, as well as the mineral-scale reactions, that may help to facilitate the conversion at temperature below 300°C. This proposal may have implications for mineral exploration (especially Au), in that low grade, but potentially large deposits in sedimentary basins may have been be overlooked based on previous exploration criteria.

7.2.3. Previous work

The simple desulfidation reaction that occurs during prograde metamorphism, that of pyrite breaking down to form pyrrhotite, has been recognized for many years (e.g. Toulmin and Barton, 1964). Other studies have looked at the processes and conditions of the pyrite to pyrrhotite conversion, particularly in terms of ore deposits (Craig and Vokes, 1993; Pitcairn et al., 2006; Tomkins et al., 2006; Large et al., 2011; Tomkins, 2013). The work of Craig and Vokes (1993) addressed the conversion and elucidated upon the partitioning of metals among the sulfide phases. This idea has since been expanded greatly, owing to advanced analytical methods, allowing for greater quantification of a range of trace elements and their concentrations in various Fe-sulfide phases that may form during metamorphism and implications for the genesis of orogenic gold deposits (Pitcairn et al., 2006; Thomas et al., 2011; Large et al., 2011).

The exact mechanisms by which pyrite becomes enriched in trace elements remains a matter of debate. Experiments and observations by Morse and Luther (1999) suggest that metals are taken up by sedimentary pyrite, based on the degree to which elements are pyritized: Hg > As = Mo > Cu ≥ Co > Ni >> Mn > Zn > Cr = Pb > Cd. Their observations where based on a kinetic and a thermodynamic approach. The presence of As in pyrite has been proposed as an important influence for the incorporation of other trace elements as it can enhance their uptake in pyrite (Deditius et al., 2008). The substitution of As for S is often accompanied by the uptake of elements with similar ionic radius and charge to Fe(II) (e.g., Co(II), Ni(II), Cu(II), Zn(II); Michel et al., 1994; Deditius et al., 2008, 2011). The substitution of As for Fe enhances the uptake of larger cations (e.g., Au(I), Ag (I), Pb (II); (Deditius et al., 2008, 2011;). It has been demonstrated by Pitcairn et al., (2006, 2010) Large et al. (2011) and Thomas et al. (2006; 2010) that Au, As and other trace metals can be released form pyrite during the

metamorphic desulfidation reaction to pyrrhotite, meaning that this transition can be viewed as the critical factor in the formation of orogenic gold deposits.

Lambert et al. (1998) conducted an experimental study of the transition using thermogravimetric analysis of a pyrite sample at various temperatures ranging from 620 to 973K, and in atmospheres of He, H_2, Ar and *in vacuo*. They proposed that the thermal reduction of pyrite to pyrrhotite in inert atmospheres follows a process in which pyrite begins to lose sulfur, and the Fe (now out of equilibrium) begins to diffuse inwards, resulting in an intermediate FeS phase between pyrite and newly formed pyrrhotite (Fig. 1, eq. 1):

$$FeS_2 \rightarrow FeSx\ (2\text{-}x) \qquad (1)$$

However, they found that with the presence of hydrogen at temperatures below 775K, the rate of sulfur removal increases. In this scenario, the sulfur is liberated from the pyrite and then diffuses through the FeS_x layer, maintaining the FeS_2/FeS_x equilibrium, leading to an increased S concentration gradient in the pyrrhotite zone, and is removed at the exterior surface. These findings suggest that the presence of H_2, and potentially other reductants, can exert greater influence on the conversion of pyrite, via sulfur diffusion and loss, rather than temperature alone. In order to test this proposal samples of oil shale, where reduced gases have already been produced with the rock mass were targeted in order to investigate whether this reactions can be preserved in natural samples. In addition, samples of concretions that contain pyrrhotite rims, believed to be of catagenetic origin were also selected for study.

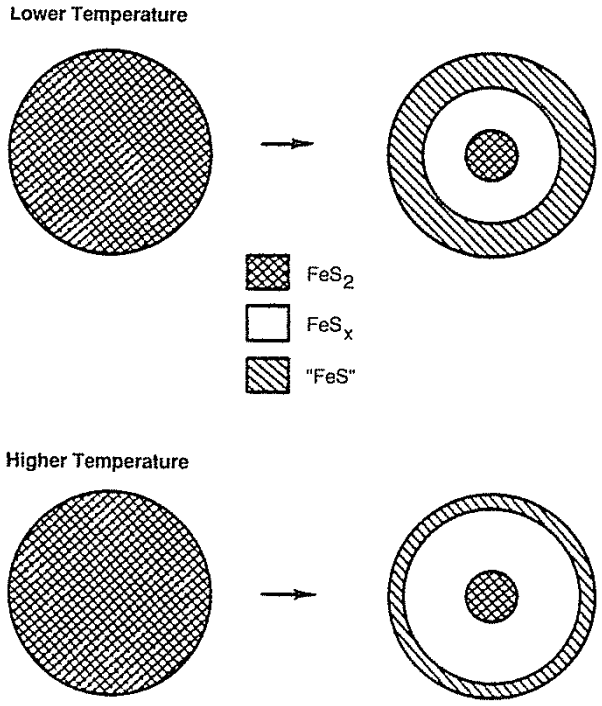

Figure 7.1. Schematic illustration of pyrite decomposition and the formation of pyrrhotite at different temperatures (698K and 808 K, respectively) from Lambert et al., (1998).

7.2.4. Data collection and methodology

Experimental design

Since pyrite and pyrrhotite have vastly differing magnetic properties, the aim of this experiment was to monitor the magnetic characteristics of pyrite as a function of increasing temperature in order to, potentially, identify pyrrhotite formation at trace levels.

A sample of pyrite from the Mina Ampliación a Victoria deposit, about 4 km north of the village of Navajún, in the La Rioja province, Spain was used in our study. The well-developed pyrites from this area are of museum quality, have been well characterized by other workers and used in other studies (Calvo et al., 1989: Lodders et al., 1998; Alonso Azcárate et al., 1999). They have previously been used in experiments due to their large crystal sizes and relative geochemical homogeneity. The sample used in this study was cut into wafers (~2mm x 25mm) and analyzed at the California Institute of Technology

Paleomagnetics laboratory. The equipment, methods, and specifications utilized in this study are discussed in detail by Kirschvink et al. (2007, 2008) and Kopp et al. (2006). The procedure involves the use of a high-resolution superconducting quantum interference devise (SQUID) that allows for very low levels of detection of mineral magnetic remanence. The sample wafers were heated in a controlled-atmosphere, magnetically shielded furnace for a total of 20 minutes. The sample was then measured for isothermal remnant magnetization (at conditions of ~$1e^{-8}$ emu). The furnace was evacuated of air and flushed with a small amount of hydrogen and argon in order to dissipate any O_2 before heating, ensuring a controlled atmosphere to mitigate against the formation of Fe-oxide phases. This was conducted five times for each temperature step. Blanks (quartz glass holders at conditions of ~$1e^{-9}$ emu) were measured three times before and three times after the set of 5 analyses in order to establish background values and monitor for drift. The samples were heated in increments of ~20 to 30°C, covering a range of values typical of diagenesis and catagenesis/ metagenesis (~ 50 to 220 °C). The final output is a unit-less 'magnetic change factor' that is calculated as a function of intensity of magnetic response, compared to background values and proportional to the mass of the sample.

LA-ICP-MS analysis

Four samples of oil shale from the Narva deposit, Estonia were collected. The Lower- Mid Ordovician Narva oil shales are found further inland and to the east, compared to the black shales of the Turisalu discussed in Chapter 5. The organic-rich shales, termed "Kukersite" were deposited in a shallow-water environment and are often found interbedded with the organic-rich shales. Estonian kukersite deposits (Fig. 7.2.) are one of the world's highest-grade oil shale deposits, with organic carbon content varying from 15% to 55% (average > 40%), low sulfur contents (<1 to 2%) and comprise of varying amounts of quartz, feldspar and micas (Lille, 2003). These were targeted in order to test the extent to which reduced gases generated from the thermal decay of organic matter and sub-greenschist temperatures may influence pyrite degradation and whether this reaction can be preserved in natural samples.

Samples of diagenetic to catagenetic sulfide concretions were also studied from the Pechenga Belt in NW Russia (Fig. 7.2.). Melezhik et al. (1998) studied these concretions in great detail. While the Belt

itself has experienced pumpellyite to lowermost-greenschist facies metamorphism, they presented full mineralogical, morphological and isotopic evidence that suggests the sulfide concretions are diagenetic in origin with catagenetic pyrite and pyrrhotite rims. Using their criteria the morphology of the concretions comprise of: 1) a concentrated core of fine-grained pyrite which appears closely compacted (Py1); 2) a mass of fine grained disseminated pyrite across the main body of the concretion (Py2); 3) a coarse grained, aggregate of pyrite radiating from the center of the concretion (Py3); and 4) a rim comprising of pyrrhotite (Po). Each of these likely represents different growth stages and chemical environments for the concretion and was studied for their trace element signature via LA-ICP-MS. These concretions were specifically targeted as the pyrite core and pyrrhotite rims are similar to the conceptual diagrams of Lambert et al. (1998; Fig 7.1.) and may provide a natural analogue of their proposed process and may aid understanding of trace element variation across each phase.

A 2.5 cm-round "disc" was drilled out with a hollow diamond-bit drill, mounted in epoxy, and then polished, allowing for the petrographic examination phase and then laser ablation of the material. All laser ablation analyses were obtained at CODES, University of Tasmania using a New Wave 193 nm Nd-YAG solid-state laser microprobe coupled to an Agilent 7700 quadrupole ICP-MS. The method is described by Danyushevsky et al. (2011).

Optimization of the ICP-MS took place every day in order to maximize sensitivity toward mid- to high atomic mass isotopes (a.m.u. ranging from 130-240). Production of molecular oxide species (e.g., $^{232}Th^{16}O/^{232}Th$) and doubly charged ionic compounds (e.g., $^{124}Ce^{2+}/^{140}Ce$) was kept to <0.2%. No correction was needed for signal intensities caused by the presence of interfering species that are produced, as they occurred at very low levels. Every analysis was run in time-resolved mode, which comprises sequential peak cycling through the mass spectrum.

Trace element analyses were performed by ablating spots between 40 and 10μm in diameter, depending on sulfide grain size, repeating at a rate of 5 Hz for 60 seconds; laser energy density was maintained between 3.5-4.5 J/cm^2. Total analysis time was 90 seconds, which included a 30-second pre-ablation and background measurement period and a 60-second ablation period.

Element acquisition times were controlled by element type: major silicate/ carbonate elements (e.g., Na, Mg, Al, Si, Ca, and Mn) were set at 0.005 seconds, along with S; minor silicate/carbonate elements (e.g., Zr, Ba, and U) at 0.01 seconds, in addition to Fe and As; transition metals (e.g., Co, Ni, Zn, and Mo) at 0.02 seconds; Te and Pt at 0.05 seconds; Au at 0.1 second; and all other elements at 0.02 seconds, for a total of 42 elements.

Data reduction was achieved using standard procedures (Longerich et al., 1996), using Fe as the internal standard. The primary standard was a Li-borate fused glass of a pyrite mixture, developed at CODES (STDGL2b2; Danyushevsky et al., 2011). This was analyzed once every 90 minutes with a 100-μm beam size at a frequency of 10Hz to correct for instrument drift.

Imaging of the sulfide material consisted of ablating a set of parallel lines to raster across a sample. A spot size of 35μm was used to give a good resolution over the size of area to be mapped (~ 2 x 2 mm) lines were rastered at a speed double that of the beam diameter (i.e., 70 μm/s for a 35 μm spot), operating at a rate of 20 Hz.

A set of 32 elements was chosen for imaging, with acquisition time for most elements set to 0.002 seconds. Certain elements of interest (Ni, Se, Co, Cu, Zn and Au) were analyzed for longer periods. Total sweep time was ~0.2 s. A 15-second delay was factored in at the end of each line to allow for cell washout. Background levels and instrument drift were measured before and after each image. Mapping was designed to finish within a ~ 90 minute time window in order to diminish the effect of drift in sensitivity of the ICP-MS on the quality of the image. Processing of the image involved applying a median filter in order to reduce artifacts, subtraction of background from filtered counts, replacement of filtered counts below background values with the standard deviation value for that element, and the production of a logarithmic color-scale image for each element. Interference of the signal caused by sample “splatter”, or re-deposition of ablated material on the surface, was avoided by pre-ablating each line.

Figure 7.2. Map of northern Europe showing the Estonian and Russian sample locations.

7.2.5. Results

Magnetic characteristics

Pyrite from the Mina Ampliación a Victoria deposit in our experiment displayed a low magnetic response during each step heating cycle with a magnetic fraction change factor of between 1 S.I. and 2 S.I., suggesting that the sample at these temperatures is, essentially, non-magnetic in that the response of the magnetometer signal is less than 10 times above background. Trace responses may be present but

would require more highly sensitive magnetometers than currently available in order to confirm this. Values close to background continued for samples until temperatures of above ~178°C. At higher temperatures the magnetic change factor increased to 9.8 S.I. at 189°C, and to over 21 S.I. at 208°C (Fig. 7.3.).

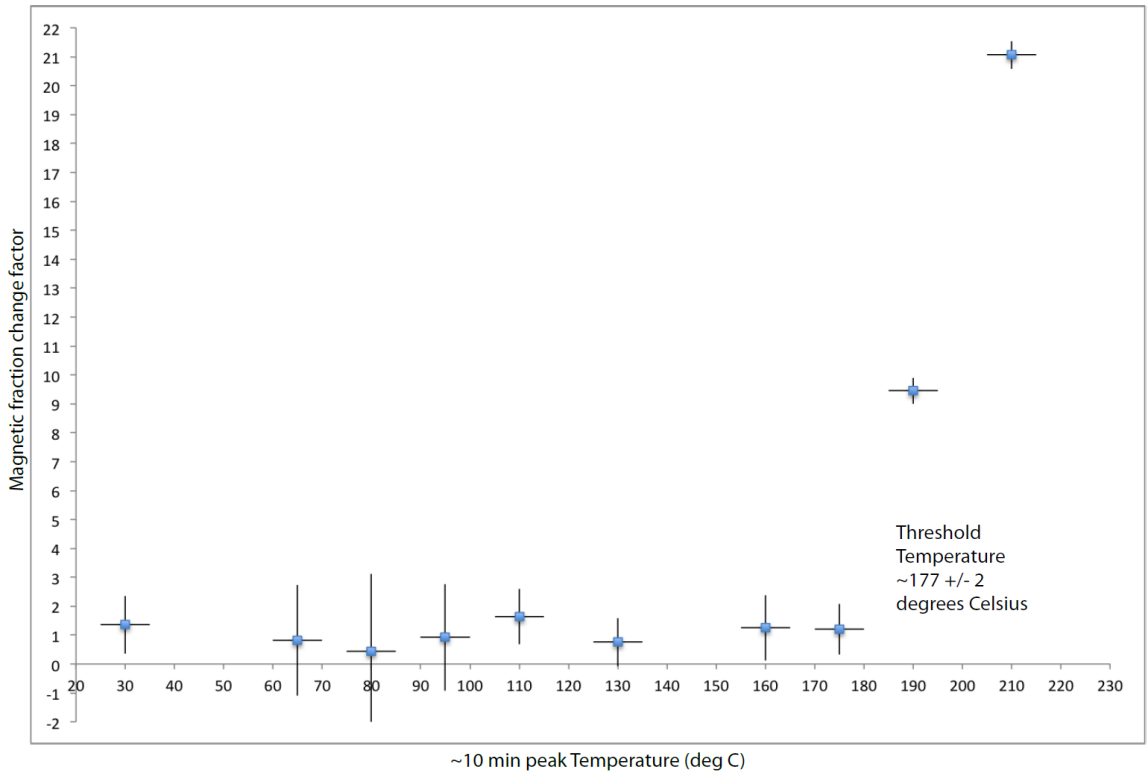

Figure 7.3. Results of temperature vs magnetism for samples of La Rioja pyrite. Error bars represent 1 standard deviation from the mean values.

Trace element content of pyrite and pyrrhotite

The pyrrhotite analyzed in the Kurkisite oil shale samples shows that it has significantly less trace elements present in comparison to the pyrite (Table 7.1; Fig. 7.4.). Nickel, cobalt and selenium were the only trace elements found in appreciable amounts in the pyrrhotite (means: 1,554 ppm Ni, 174 ppm Co and 196 ppm Se, respectively). In comparison, the Kurkisite pyrites have high concentrations of molybdenum, zinc and copper (means: 1,421ppm Mo, 1,533ppm Zn, 1,982ppm Cu, respectively) and generally show a wider range in values compared to pyrrhotite. These elements tend to be elevated in

oil shale and hydrocarbon-rich material rocks (Duyck et al., 2002). A comparison of pyrite and pyrrhotite suggests that Ni, Co, Se, Cd, Tl and Ag are similar to the values of the original pyrite. However the Cd and Ag values are low in both the pyrite and pyrrhotite phases. While other metals such as Mn, Pb, Zn, As, Au, Mo and Cu all decrease dramatically in the pyrrhotite phase (Fig. 7.4.). These results match that of Large et al. (2011) and Thomas et al. (2011) who suggested that these elements are not easily substituted into the pyrrhotite structure.

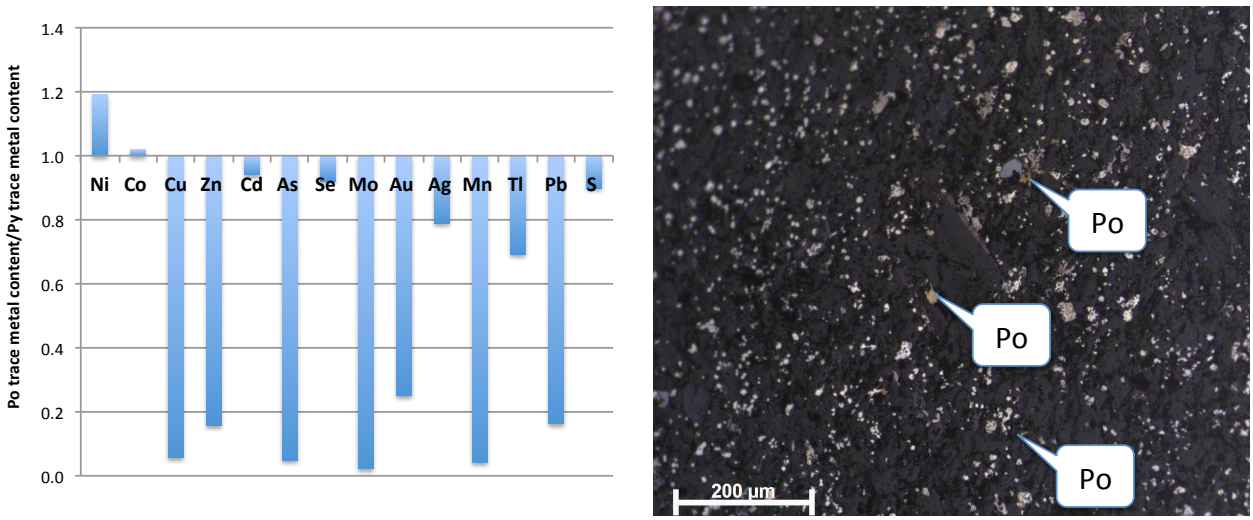

Figure 7.4. Photomicrograph of pyrite and minor pyrrhotite dispersed in Kurkisite shale and relative metal enrichments between the pyrite and pyhrrotite phases.

No. analyses	Sample	Ni (ppm)	Co (ppm)	Cu (ppm)	Zn (ppm)	Cd (ppm)	As (ppm)	Se (ppm)	Mo (ppm)	Au (ppm)	Ag (ppm)	Mn (ppm)	Tl (ppm)	Pb (ppm)	S (ppm)
22	**EST-Kurk-OS-Py : Mean**	**1472**	**182**	**1982**	**1533**	**52**	**1942**	**213**	**1421**	**0.16**	**35**	**259**	**136**	**214**	**548780**
	Std. Dev.	244	59	808	38	28	302	92	316	0.76	16	134	23	113	10213
14	**EST-Kurk-OS-Po : Mean**	**1754**	**186**	**114**	**242**	**49**	**93**	**196**	**34**	**0.04**	**28**	**11**	**94**	**35**	**493322**
	Std Dev.	284	29	95	84	13	49	59	6	0.05	13	34	38	19	14237
	Po/Py	**1.2**	**1.0**	**0.1**	**0.2**	**0.9**	**0.05**	**0.9**	**0.02**	**0.3**	**0.8**	**0.04**	**0.7**	**0.2**	**0.9**

Table 7.1. Concentrations of trace elements in pyrite and pyrrhotite from the Kurkisite oil shale.

The analyses of the pyrite and pyrrhotite concretions from the Pechenga sample (Fig. 7.5.) exhibit the same overall trend from high concentrations of a variety of elements in the early pyrite phase to lower, or more limited, trace element concentrations in the pyrrhotite (Fig. 7.6). Fine-grained pyrite in the core of the concretions (Py1) exhibits the highest trace metal mean out of all the phases present in the concretions. Dispersed, fine grained pyrite (Py 2) shows similar means but a much wider range in values (except for As), whereas the coarse, radial Py3 exhibits much lower concentrations and smaller range in the majority of elements, with the exception of As. Pyrrhotite at the rim of the concretions has similar Ni, Co and Se content to the other pyrite phases but is strongly depleted in most other elements. Trace element distribution maps (Fig.7.7.) show that the majority of elements are higher in the core of the concretions, while high values towards the rim can be attributed to the presence of other metal sulfide phases (i.e. Zn in sphalerite and Mo in molybdenite). Nickel and selenium appear to be evenly distributed through the concretion, while Co remains high in Py 1 and Py 2, it is lower in Py3 and appears to become highly concentrated in Py2 and Po at the boundary between the two phases.

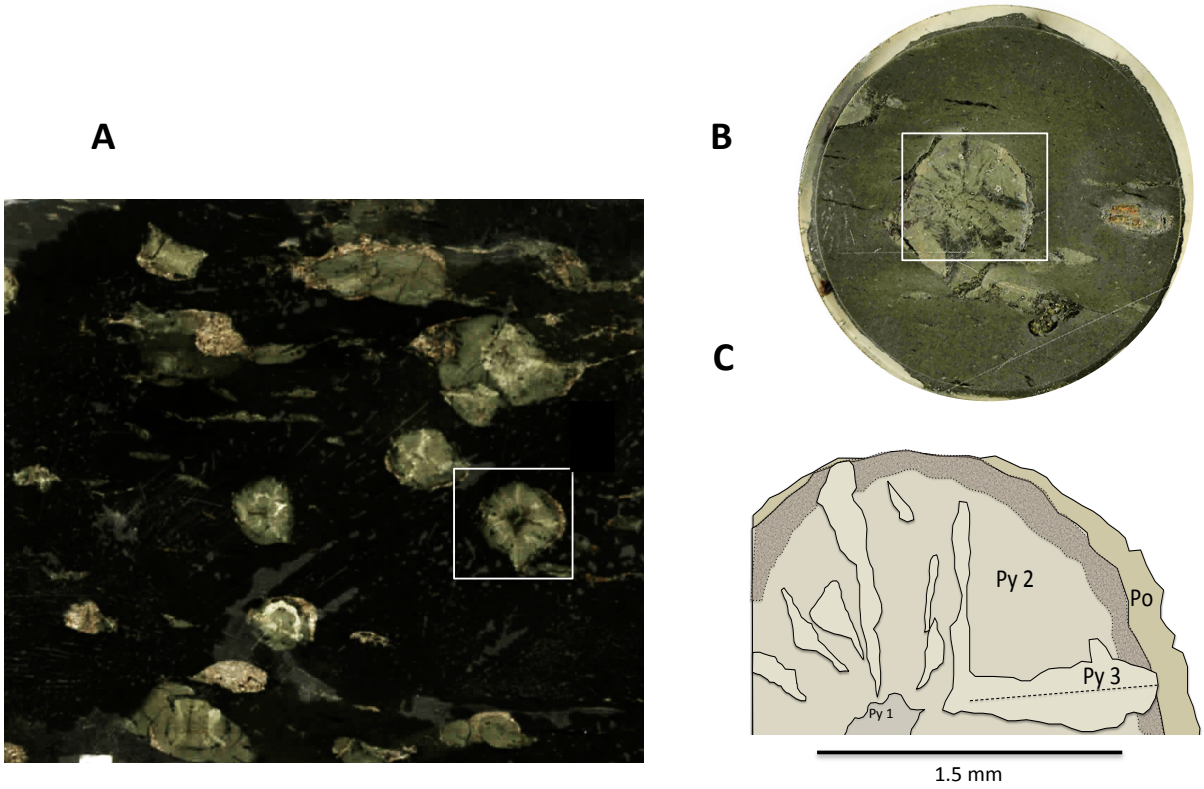

Figure 7.5. (A) Polished slab of black shale with pyritic concretions with pyrrhotite rims (approx. 11cm). (B) ~ 25mm mount of concretion. (C) stylized illustration of concretion morphology.

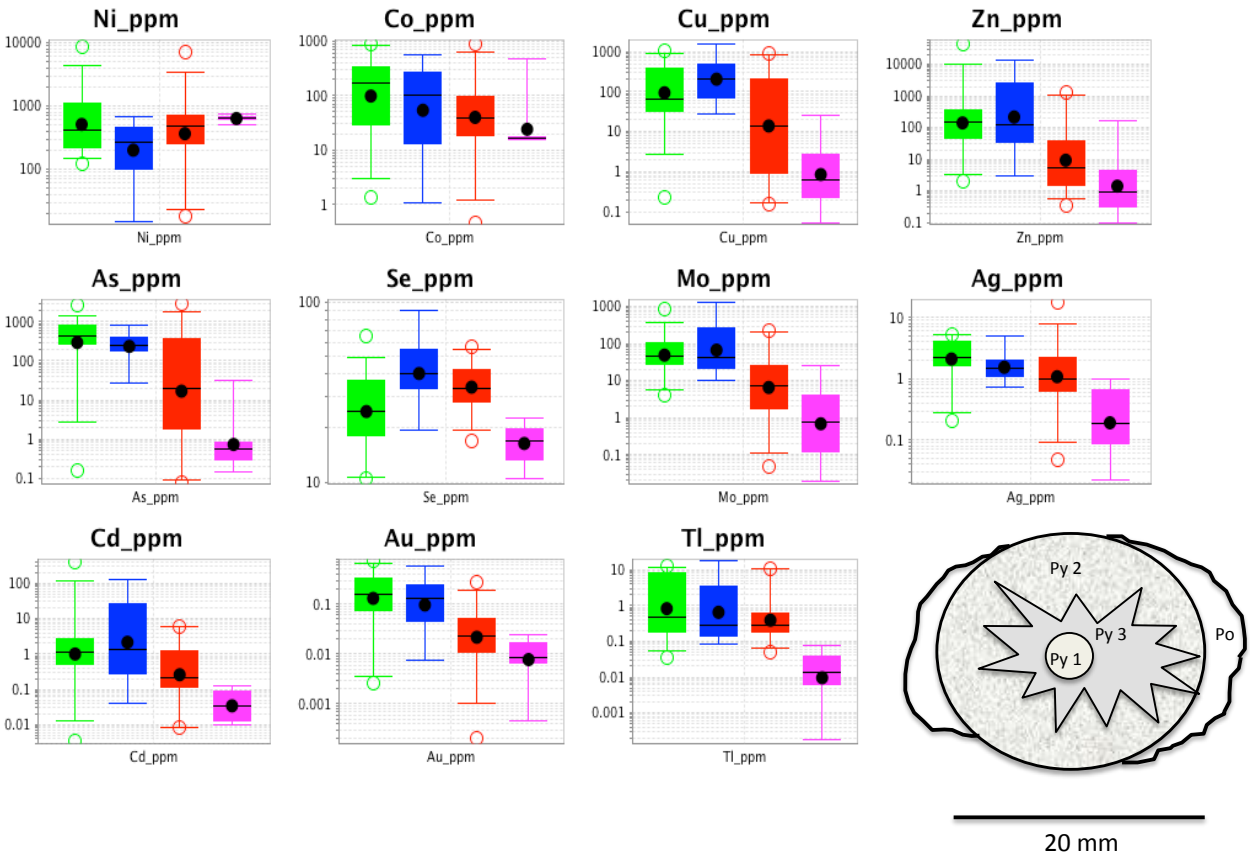

Figure 7.6. Summary of trace element content from transects across 4 concretions. Pyrite in the core (Py1, green, n=32), dispersed fine grained pyrite across the concretions (Py2, blue, n=43), coarse-grained radiating pyrite (Py3, red, n= 38) and the pyrrhotite rim (Po, pink, n=21).

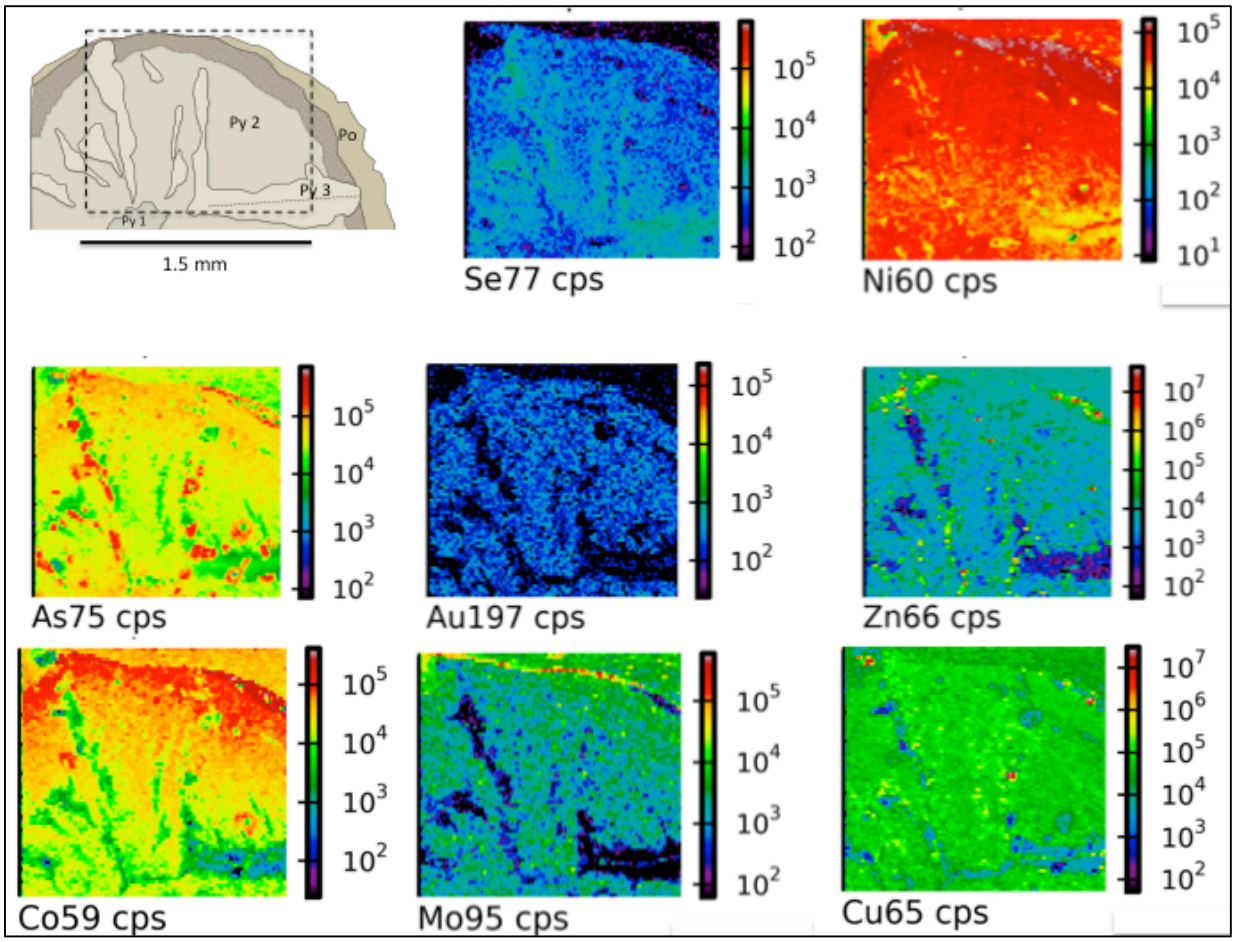

Figure 7.7. Trace element distribution map of a segment of concretion with stylized illustration of its morphology (sample- Pech-7-1).

7.2.6. Discussion

Mechanisms for low temperature conversion

During diagenesis and catagenesis a variety of volatiles can be liberated from organic matter, and other mineral transformations, these include CO_2, hydrogen gas, methane and water. The combination of these volatiles can help to facilitate the reduction of pyrite to pyrrhotite via a variety of potential reactions (Eq. 2 to 6, after Hall et al., 1998):

$$14Py + 3CH_4 \rightarrow 2Po + 3C + 12HS^-_{(aq)} \quad (2)$$

$$8Py + 3CH_4 + 6Sid \rightarrow 2Po + 9CO_2 + 12H^+_{(aq)} \quad (3)$$

$$Py + H_2 \rightarrow 2Po + 12HS^-_{(aq)} \quad (4)$$

$$7Py + 6CO + 6H_2O \rightarrow Po + 6CO_2 + 6H_2S_{(aq)} \quad (5)$$

$$7Py \rightarrow Po + 6S \quad (6)$$

Each of these pathways would not require significant heat in order for the reactants to be produced in a black shale package (Hall et al., 1998). Rather, catagenetic conditions are capable of breaking down the organic matter and producing high amounts of methane, hydrogen, and carbon monoxide that may exert influence over the rate of sulfur diffusion and desorption in pyrite.

The trace element content of pyrite decreases during the reduction to pyrrhotite with Au and As commonly being considered to be the first metals released from the pyrite structure (Pitcairn et al., 2006; Tomkins et al., 2006, 2010; Large et al., 2012). Since Au and As are considered to be one of the first elements to be released from the pyrite structure during metamorphism, and have lower propensity to being held within pyrite (Morse and Luther, 1999; Pitcairn et al., 2006; Deditius et al., 2008; Large et al., 2011; Large et al., 2012), and As has been considered a controlling factor in the incorporation of other trace elements (Deditius et al., 2008), that the rate at which they diffuse from the pyrite structure may effect the efficiency of this reaction and the secondary release of other trace metals. Zinc, Cu, Mo and Cd may follow a similar process, especially when S content reaches sufficient levels to preferentially stabilize their own metal sulfide phases (Morse and Luther, 1999). Nickel, cobalt and

selenium are capable of forming their own sulfide phases but it may be that the required fS_2, fO_2, and reaction kinetics are not achieved during this reaction (i.e. Yamamoto et al., 1968; Chouinard et al., 2005).

Since the transition from pyrite to pyrrhotite involves formation intermediate FeSx it may be possible that the zone of dispersed pyrite near the pyrrhotite rim of the concretions is an expression of this affect. This may explain the wide range in trace element values for Py2, as the sulfur and Fe are diffusing so are the other metals, leading to variable compositions of Fe-S in this zone along with the presence of other metal sulfides (i.e. Co, Zn). Furthermore, Py3 may represent zones of recrystallized phases of pyrite where the majority of trace elements are lost along the reaction pathway from core to rim.

Previous studies of the kinetics and mechanisms of the conversion have eluded that the impurity level or crystallographic defects can influence the rates and efficiency of the conversion (Morimoto et al., 1975; Crerar et al., 1978; Hall et al., 1986; Lambert et al., 1998; Chouinard et al., 2005). Therefore, it can be proposed that the trace element content, and the location of the substituted elements in the pyrite can influence the reaction. Furthermore, diagenetic pyrite with high Au and As, for example, may convert more easily to pyrrhotite, when coupled with degrading organic matter, than a pyrite with a much lower trace element content.

Heat generation during the reduction reaction

Many previous workers have discussed regional-scale heat generation as means to facilitate the pyrite to pyrrhotite reduction, namely greenschist and amphibolite facies metamorphism. However little attention has been paid to mineral scale heat transfer during the transition. Recent studies of the thermal conductivity of pyrite and pyrrhotite suggest that their difference is one of the largest of any related mineral species (Py, 26.8W/m*k; Popov et al., 2013; and Po ($Fe_{0.8}$), 4.18W/m*k; Clauser and Huenges, 1995). This, along with Gibbs free energy values (Toulmin and Barton, 1964), suggests that the reduction process itself may also release sufficient heat in order to progress the reaction (Fig. 7.8.) as the move from lower order cubic symmetry to higher order monoclinic/hexagonal symmetry would result in a net entropy increase.

Therefore, it may be possible that in a rock mass with high pyrite content, during the transition of pyrite to pyrrhotite, the huge decrease in thermal conductivity may create an upward-self-propagating thermal front, above which the reaction continues to proceed. At temperature/ depth conditions that allows for the vigorous transformation between the two phases, if the pyrite was in sufficiently appreciable levels, the local temperature of the rock mass may increase as the lower thermal conductivity creates a shallower-than-equilibrium thermal front in the underlying pyrrhotite zone, and a steeper-than-equilibrium dynamic thermal front in the closely-overlying pyrite zone. This may move the overlying layer into the pyrrhotite zone, which will decrease the thermal conductivity, raising the local geotherm in the layer above it. This could lead to progressive desulfidation and conversion within the rock mass. This may explain the observation of upward-shoaling pyrrhotite fronts in the gold deposits of the Otago Schist, Bendigo and Sukhoi Log (Pitcairn et al., 2006, 2010; Thomas et al., 2011; Large et al., 2011; 2012). Tomkins et al. (2006) noted that conditions generated by pyrite breakdown along the pyrite-pyrrhotite buffer lead to the either the melting of arsenopyrite or its conversion to lollingite and pyrrhotite in massive sulfide deposits, depending on the $f(S_2)$. The result of this reaction in ore deposits would create pyrite-rich massive sulfides were this reaction has not occurred with localized pyrrhotite zones of former arsenopyrite where desulfidation has occurred.

The release of sulfur during this reaction will also affect the pH and Eh of the local rock mass (e.g. Tomkins et al., 2006, 2010; Pitcairn et al., 2006, 2010). This means that additional physio-chemical reactions are likely occurring concurrently. While the breakdown of pyrite to pyrrhotite is considered the biggest control on fugacity, the surrounding mineralogy can influence the efficiency of the pyrite to pyrrhotite conversion. For example, the breakdown of barite may promote conditions of high $f(S_2)$, while the sequestering of S by Fe-silicates, and oxides, can form pyrrhotite very efficiently and may cease the breakdown of pyrite (Tracy and Robinson, 1988; Tomkins et al., 2006; 2010).

If the conversion to pyrrhotite is potentially a rapid geological process within the lower basin stratigraphy where dehydration reactions are also occurring, then it may account for the very rapid generation of a Au-As-S ore fluid, capable of forming the Au-As-rich rims seen in pyrites from orogenic gold deposits and terranes (i.e. Sukhoi Log and Bendigo; Large et al., 2007; 2011, Thomas et al., 2011).

The H_2O produced during the dehydration of organic-rich mudstones at higher temperatures can dissolve S, leading to the consumption of pyrite in order to maintain equilibrium, leading to higher $f(S_2)$, the breakdown of pyrite and the release of As and other trace metals (Connolly and Cesare, 1993; Tomkins, et al., 2006). The As-rich fluid that may form can be highly effective in mobilizing other metals, especially Au (Tomkins et al., 2006). The increased porosity and permeability, as a function of the breakdown of organic matter, may aid in fluid migration and coupled dissolution-substitution reactions along pyrite grain boundaries that may have been in contact with the degrading organic matter (Bell & Cuff, 1989; Puntis and Austrheim, 2010). Such mechanisms may also explain the preferential occurrences of pyrrhotite-rich laminations or concentrations along bedding in zones that are predominantly pyrite-laminated. Features such as this are common in many orogenic/ metamorphogenic deposits with organic carbon-rich precursor rocks but the nature of their formation has been debated (e.g. Hansley & Spirakis, 1992; Cline et al., 2002; Thomas et al., 2011; Steadman et al., 2015). It may be that these particular bedding planes had a higher organic matter content than those surrounding it, allowing for increased, localized, fluid movement and more efficient reaction fronts along the pyrite boundaries, leading to more pervasive pyrrhotization along a particular bedding plane (Wheeler, 1987; Bell & Cuff, 1989; Bell & Hayward, 1991; Hansley & Spirakis, 1992). While additional experiment work is required to fully explore the influence this process may have on an entire rock mass and at varying scales, this conceptual model may be useful to consider it in terms of mineral scale processes, especially during organic matter breakdown at lower temperatures.

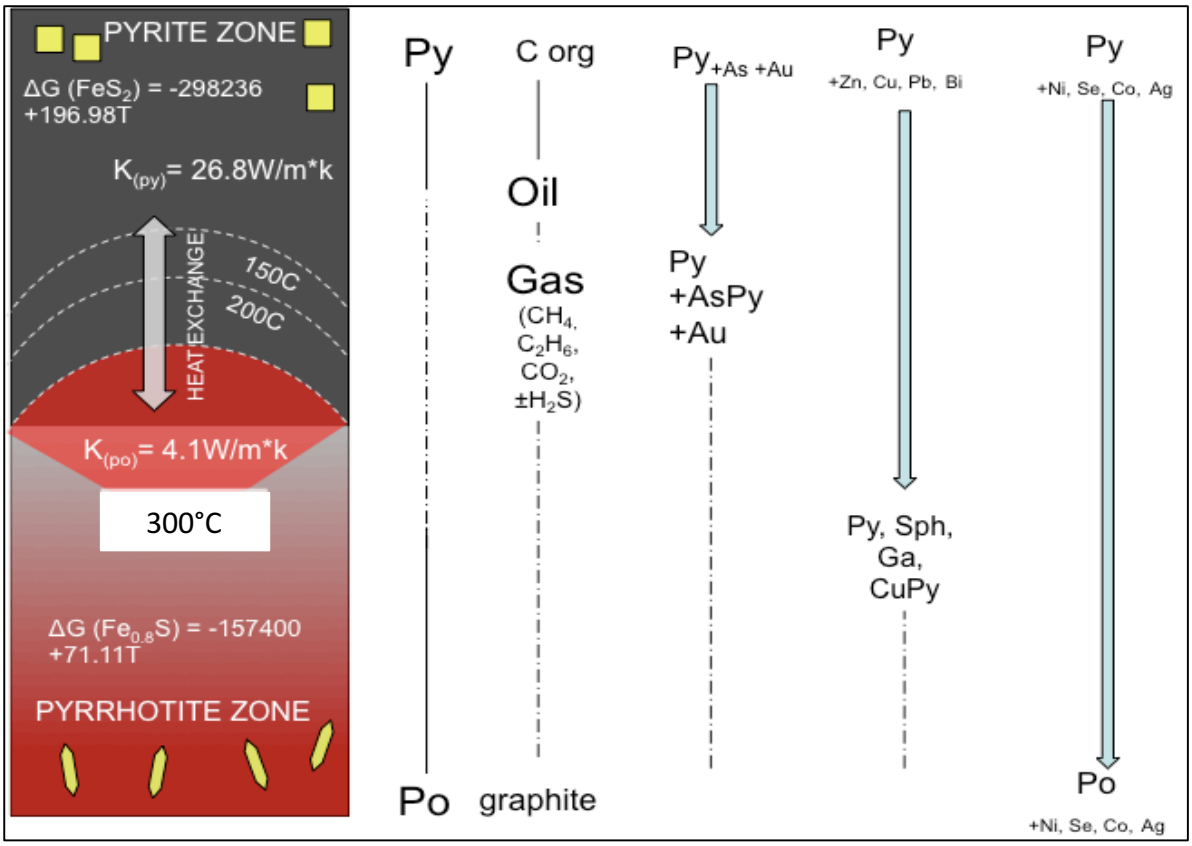

Figure 7.8. Schematic diagram depicting metals released from pyrite as a function of temperature during the pyrite to pyrrhotite conversion.

7.2.7. Conclusion

Sensitive rock magnetic and in-situ geochemical techniques are capable of quantifying and qualifying pyrite to pyrrhotite systematics and occurrences in rock of lower thermal maturity than previously considered. We have shown evidence that mineral-scale transformations occur in a pyrite standard at temperatures far lower than previously quoted in the literature. We attribute this low temperature reaction to a combination of mineral-specific and localized reactions and conditions. 1) Our lab experiment of a pure pyrite standard suggest that discernable trace levels of pyrrhotite form at ~ 180°C. However the trace element content of pyrites found in black shales can be variable and may exert influence over the exact temperature of the transition. 2) In black shales, the breakdown of organic phases can release a variety of reductants that can also drive the transition at low temperatures as well as increased fluid movement and potential surface substitute reactions at pyrite grain boundaries that may

be in contact with the organic phases. 3) The large contrast in thermal conductivity between pyrite and pyrrhotite suggest that the heat generation attributed to this reaction may help to facilitate further transformation on a mineral scale, or potentially larger.

A variety of elements are often found in sedimentary pyrite and have varying affinities to being held within the pyrite structure during metamorphism. Elements such as S, Au and As are likely the first to be liberated in early stages of reduction to pyrrhotite, followed by Cu, Zn, Pb, Bi and Cd. Nickel, Co and Se, as well as minor Ag, are suggested to remain within the pyrite and the resultant pyrrhotite. These metals can substitute readily into the structure of both minerals unless sufficient buffering factors are overcome such as temperature, $f(S_2)$, $f(O_2)$, and Fe content which might promote the formation of their own phase (Morse and Luther, 1999; Tomkins et al., 2006). Given the affinity for the released metals to form their own sulfides it is likely that the desulfidation of pyrite and breakdown of surrounding organic components may lead to accessory sulfide formation during metamorphism. This has implications for ore deposit formation as well as introducing the potential to open exploration interest in sub-greenschist black shales terrains as a source for low-grade but economically viable orogenic gold deposits.

7.3. References

Alonso Azcárate, J., Boyce, A.J., Bottrell, S.H., Macaulay, C.I., Rodas, M., Fallick, A.E., Mas, J.R., 1999. Development and use of in situ laser sulfur isotope analyses for pyrite-anhydrite geothermometry: An example from pyrite deposits of the Cameros Basin, NE Spain. Geochimica et Cosmochimica Acta, 63, p. 509-513.

Arvo, O., 2007. Estonian oil shale properties and utilization in power plants. Energetika, 53, p. 8-18.

Bell, T.H. and Cuff, C., 1989. Dissolution, solution transfer, diffusion versus fluid flow and volume loss during deformation/metamorphism. Journal of Metamorphic Geology, 7, p. 425-447.

Bell, T.H. and Hayward, N., 1991. Episodic metamorphic reactions during orogenesis: the control of deformation partitioning on reaction sites and reaction duration. Journal of Metamorphic Geology, 9, p. 619-640.

Birch, F., 1942. Thermal conductivity and diffusivity. Geological Society of America Special Papers, 36, p. 243-266.

Calvo, M. and Sevillano, E.,1989. Pyrite crystals from Soria and la Rioja provinces, Spain. The Mineralogical Record, 20, p. 451-456.

Chouinard, A., Paquette, J. and Williams-Jones, A.E., 2005. Crystallographic controls on trace-element incorporation in auriferous pyrite from the Pascua epithermal high-sulfidation deposit, Chile–Argentina. The Canadian Mineralogist, 43, p. 951-963.

Clauser, C. and Huenges, E., 1995. Thermal conductivity of rocks and minerals. Rock physics & phase relations: A handbook of physical constants, p. 105-126.

Cline, J.S., 2001, Timing of gold and arsenic sulfide mineral deposition at the Getchell Carlin-type gold deposit, north-central Nevada. Economic Geology, 96, p. 75–90.

Connolly, J.A.D. and Cesare, B., 1993. C-O-H-S fluid composition and oxygen fugacity in graphitic metapelites. Journal of metamorphic geology, 11, p. 379-388.

Crerar, D.A., Susak, N.J., Borcsik, M. and Schwartz, S., 1978. Solubility of the buffer assemblage pyrite+ pyrrhotite+ magnetite in NaCl solutions from 200 to 350 C. Geochimica et Cosmochimica Acta, 42, p. 1427-1437.

Danyushevsky, L.V., Robinson, P., Gilbert, S., Norman, M., Large, R., McGoldrick, P., Shelley, M., 2011. Routine quantitative multi-element analysis of sulphide minerals by laser ablation ICPMS: Standard development and consideration of matrix effects. Geochemistry: Exploration, Environment, Analysis, 11, p. 51-60.

Deditius, A.P., Utsunomiya, S., Renock, D., Ewing, R.C., Ramana, C.V., Becker, U. and Kesler, S.E., 2008. A proposed new type of arsenian pyrite: Composition, nanostructure and geological significance. Geochimica et Cosmochimica Acta, 72, p. 2919-2933.

Deditius, A.P., Utsunomiya, S., Reich, M., Kesler, S.E., Ewing, R.C., Hough, R. and Walshe, J., 2011. Trace metal nanoparticles in pyrite. Ore Geology Reviews, 42, p. 32-46.

Duyck, C., Miekeley, N., da Silveira, C.L.P., Aucelio, R.Q., Campos, R.C., Grinberg, P. and Brandao, G.P., 2007. The determination of trace elements in crude oil and its heavy fractions by atomic spectrometry. Spectrochimica Acta Part B: Atomic Spectroscopy, 62, p.939-951.

Fischer, W.W., Fike, D.A., Johnson, J.E., Raub, T.D., Guan, Y., Kirschvink, J.L. and Eiler, J.M., 2014. SQUID–SIMS is a useful approach to uncover primary signals in the Archean sulfur cycle. Proceedings of the National Academy of Sciences, 111, p. 5468-5473.

Guha, B.K. and Narsimhan, G., 1972. Control regimes and particle temperature gradients during decomposition of pyrites. The Chemical Engineering Journal, 3, p. 145-155.

Hall, A.J., 1986. Pyrite-pyrrhotine redox reactions in nature. Mineralogical Magazine 50, p. 223-229.

Hall, A.J., Boyce, A.J. and Fallick, A.E., 1987. Iron sulphides in metasediments: isotopic support for a retrogressive pyrrhotite to pyrite reaction. Chemical Geology, 65, p. 305-310.

Hansley, P.L. and Spirakis, C.S., 1992. Organic matter diagenesis as the key to a unifying theory for the genesis of tabular uranium-vanadium deposits in the Morrison Formation, Colorado Plateau. Economic Geology, 87, p. 352-365.

Kirschvink, J.L., 1981. Rock and Paleomagnetism. In Weinstock, H and Overton, W.C., eds. SQUID Applications to Geophysics. Society for Exploration Geophysics.

Kirschvink, J. L., and Isozaki. Y. 2007.Extending the sensitivity of paleomagnetic techniques: magnetostratigraphy of weakly-magnetized, organic-rich black limestone from the Permian of Japan. In AGU Fall Meeting Abstracts, 1, p. 1223.

Kirschvink, J. L., Kopp, R. E.. Raub, T. D. Baumgartner, C. T and Holt, J. W., 2008. Rapid, precise, and high-sensitivity acquisition of paleomagnetic and rock-magnetic data: Development of a low-noise automatic sample changing system for superconducting rock magnetometers, Geochem. Geophys. Geosyst., 9, Q05Y01.

Klshima, N., 1989. A thermodynamic study on the pyrite-pyrrhotite-magnetite-water system at 300–500 C with relevance to the fugacity/concentration quotient of aqueous H2S. Geochimica et Cosmochimica Acta, 53, p. 2143-2155.

Kopp, R. E.,. Nash, C. Z. Kobayashi, A. Weiss, B. P Bazylinski, D. A, .and Kirschvink, J. L., 2006. Ferromagnetic resonance spectroscopy for assessment of magnetic anisotropy and magnetostatic interactions: A case study of mutant magnetotactic bacteria, Journal of Geophysical Research, 111, B12S25.

Lambert Jr, J.M., Simkovich, G. and Walker Jr, P.L., 1998. The kinetics and mechanism of the pyrite-to-pyrrhotite transformation. Metallurgical and Materials Transactions B, 29, p. 385-396

Large, R.R., Maslennikov, V.V., Robert, F., Danyushevsky, L.V. and Chang, Z., 2007. Multistage sedimentary and metamorphic origin of pyrite and gold in the giant Sukhoi Log deposit, Lena gold province, Russia. Economic Geology, 102, p. 1233-1267.

Large R.R., Danyushevsky L., Hollit C., Maslennikov V., Meffre S., Gilbert S., Bull S., Scott R., Emsbo P., Thomas H., Singh B., Foster J., 2009. Gold and trace element zonation in pyrite using a laser imaging technique: Implications for the timing of gold in orogenic and carlin-style sediment-hosted deposits. Economic Geology, 104, p. 635–668.

Large, R.R., Bull, S.W. and Maslennikov, V.V., 2011. A carbonaceous sedimentary source-rock model for Carlin-type and orogenic gold deposits. Economic Geology, 106, p. 331-358.

Large, R., Thomas, H., Craw, D., Henne, A. and Henderson, S., 2012. Diagenetic pyrite as a source for metals in orogenic gold deposits, Otago Schist, New Zealand. New Zealand Journal of Geology and Geophysics, 55, p. 137-149.

Lille, Ü. 2003. Current knowledge on the origin and structure of Estonian kukersite kerogen. Oil Shale, 20, p. 253–263.

Lodders, K., Klingelhofer, G., Kremser, D. T., 1998. Chloritoid inclusions in pyrite from Navajun, Spain. Canadian Mineralogist, 36, p. 137-145.

Longerich, H.P., Jackson, S.E., Günther, D., 1996. Laser ablation inductively coupled mass spectrometric transient signal data acquisition and analyte concentration calculation. Journal of Analytical Atomic Spectrometry, 11, p. 899-904.

Melezhik, V.A., Grinenko, L.N. and Fallick, A.E., 1998. 2000-Ma sulphide concretions from the 'Productive' Formation of the Pechenga Greenstone Belt, NW Russia: genetic history based on morphological and isotopic evidence. Chemical Geology, 148, p. 61-94.

Möller P., Kersten G., 1994. Electrochemical accumulation of visible gold on pyrite and arsenopyrite surfaces: Mineralium Deposita, 29, p. 404–413.

Morimoto N., Gyobu A., Mukaiyama H., and Izawa E., 1975. Crystallography and stability of pyrrhotites. Economic Geology, 70, p. 824–833.

Morse, J.W. and Luther, G.W., 1999. Chemical influences on trace metal-sulfide interactions in anoxic sediments. Geochimica et Cosmochimica Acta, 63, p. 3373-3378.

Pitcairn I.K., Teagle D.A.H., Craw D., Olivo G.R., Kerrich R., Brewer T.S., 2006. Sources of metals and fluids in orogenic gold deposits: Insights from the Otago and Alpine Schists, New Zealand: Economic Geology, 101, p. 1525–1546.

Pitcairn, I.K., Olivo, G.R., Teagle, D.A. and Craw, D., 2010. Sulfide evolution during prograde metamorphism of the Otago and Alpine Schists, New Zealand. The Canadian Mineralogist, 48, p .1267-1295.

Pitcairn, I.K., Craw, D. and Teagle, D.A., 2014. The gold conveyor belt: Large-scale gold mobility in an active orogen. Ore Geology Reviews, 62, p.129-142.

Popov, P. A., Fedorov, P. P., Kuznetsov, S. V., 2013. Thermal conductivity of FeS_2 pyrite crystals in the temperature range 50-300 K. Crystallography Reports, 58, p. 319-321.

Puntis, A. & Austrheim, H. 2010. Fluid-induced processes: metasomatism and metamorphism. Geofluids, 10, p. 254-269.

Thomas, H.V., Large, R.R., Bull, S.W., Maslennikov, V., Berry, R.F., Fraser, R., Froud, S. and Moye, R., 2011. Pyrite and pyrrhotite textures and composition in sediments, laminated quartz veins, and reefs at Bendigo gold mine, Australia: insights for ore genesis. Economic Geology, 106, p. 1-31.

Tomkins, A.G., Frost, B.R. and Pattison, D.R., 2006. Arsenopyrite melting during metamorphism of sulfide ore deposits. The Canadian Mineralogist, 44, p. 1045-1062.

Tomkins, A.G., 2010. Windows of metamorphic sulfur liberation in the crust: Implications for gold deposit genesis. Geochimica et Cosmochimica Acta, 74, p.3246-3259.

Tomkins, A.G., 2013. On the source of orogenic gold. Geology, 41, p. 1255-1256.

Toulmin, P. and Barton, P.B., 1964. A thermodynamic study of pyrite and pyrrhotite. Geochimica et Cosmochimica Acta, 28, p. 641-671.

Tracy, R.J. and Robinson, P., 1988. Silicate-sulfide-oxide-fluid reactions in granulite-grade pelitic rocks, central Massachusetts. American Journal of Science, 288, p. 45-74.

Tsatis, D.E., Thermal expansion of pyrrhotite (Fe7S8), 1987. Journal of Physics and Chemistry of Solids, 48, p. 489-490.

Weaver, R., Roberts, A.P. and Barker, A.J., 2002. A late diagenetic (syn-folding) magnetization carried by pyrrhotite: implications for paleomagnetic studies from magnetic iron sulphide-bearing sediments. Earth and Planetary Science Letters, 200, p. 371-386.

Wheeler, J., 1987. The significance of grain-scale stresses in the kinetics of metamorphism. Contributions to Mineralogy and Petrology, 97, p. 397-404.

Wu, M., Rhee, J., Emge, T.J., Yao, H., Cheng, J.H., Thiagarajan, S., Croft, M., Yang, R. and Li, J., 2010. A low band gap iron sulfide hybrid semiconductor with unique 2D [Fe16S20] 8– layer and reduced thermal conductivity. Chemical communications, 46, p. 1649-1651.

Yamamoto, M., Ogushi, N. and Sakai, H., 1968. Distribution of sulfur isotopes, selenium and cobalt in the Yanahara ore deposits, Okayama-Ken, Japan. Geochemical Journal, 2, p. 137-156.

Chapter 8

Metalliferous black shale deposition and periods of increased atmospheric oxygen: A synthesis

8.1. Foreword

Chapter 8 aims to present an overview and discuss potential mechanisms of black shale enrichments as a function of geodynamic processes, and how the influence and drivers of these processes may have changed over the course of Earth history. Emerging from this is the proposal of a new classification- 'highly-metalliferous black shale'. This classification applies to <5% of global black shales, many of which occur at prominent periods of Earth History suggesting interplay between geodynamics, biogeochemistry and black shale enrichments. Aspects of the work and ideas presented here are being formulated into a manuscript.

8.2. Highly-metalliferous black shales: an archive of periods of peak O_2 and bio-productivity

8.2.1. Abstract

Presented here is a compilation of pyrite and whole-rock geochemical data for a variety of metal-rich black shales through Earth evolution. The designation of 'highly metalliferous black shales' (HMBS) has been assigned to those shales that contain mean whole-rock contents of Mo + Ni + Zn + Se + V > 1500 ppm. Pyrite trace element contents of these shales are also high with mean concentrations of 1700 ppm Ni, 1400 ppm Zn, 890 ppm Se, 860 ppm Cu, 820 ppm Mo, 180 ppm Ag, and 70 ppm Cd, respectively. These shales appear to be deposited at particular periods of Earth's history, and are coeval with peaks in the atmospheric oxygen record. A concept is proposed whereby metal enrichment is linked

to tectonic activity and increased atmospheric O_2, with related feedbacks helping to precondition the water column and basin that facilitate metal enrichment. Discussed is the idea that the nature of these HMBS has also changed through time, from thin, concentrated horizons in the Late Paleozoic to thick sequences of lower grades in the Pre-Cambrian. This may be attributed to the changing nature of Earth's atmospheric/ ocean redox state through time.

8.2.2. Metaliferrous black shales and bio-productivity

Black shale deposition, and enrichment, has been discussed throughout this thesis, as has the association between metals and biological activity. Huyck (1989) proposed a definition for metalliferous black shales as "black shale that is enriched in metal by a factor of 2x (except for beryllium, cobalt, molybdenum, and uranium, for which 1x is sufficient) relative to the U.S. Geological Survey Standard SDO-1". Many of the trace elements (TE) often enriched in black shales are bio-essential (i.e. P, Mo, Ni, Co, Zn, As, Cu, Se, U, or V). This suggests that bio-productivity, trace element uptake by organic matter, and the metal content of the seawater are critical factors that influence the final metal budget of the black shale. While some black shale enrichments are related to hydrothermal input, (either syn-sedimentary or epigenetic), nevertheless, the processes that pre-condition the basin for hydrothermal input, and metal enrichment, are ultimately tied to increased bio-productivity, and the development of conditions that enhance organic matter preservation. Therefore, understanding the periods and causes of increased productivity in the oceans can aid in identifying and understanding the formation and distribution of metal-rich black shales. It is this rationale that has driven the investigations contained within this thesis, and has led to the discussions presented in the chapter.

8.2.3. Highly-metalliferous black shales

Using the definition of Hyuck (1989), many black shales can be classed as metalliferous. Some of these occurrences reach grades high enough to be economic targets but most are sub-economic. Apprtoximately, 25% of the black shales compiled in the dataset of Large et al. (2014; 2015) fit within the Hyuck (1989) criteria. Many of these appear to be randomly distributed through geological time,

and are variable in terms of their depositional setting. This suggests that additional means of classification may be required in order to better define and classify those black shales that are important metal resources, their formation, and whether there are critical metallogenic shale epochs.

The association of bio-productivity, ocean anoxia, with redox-sensitive and bio-essential elements, appears to be intimately related to primary enrichments in black shales. Therefore, the main redox-sensitive, and bio-essential elements, (i.e. Ni, Mo, Zn, Se, V) as well as organic carbon content were deemed as being critical components in any selection criteria. The main global black shale metal resources and the highest trace element values of the Large et al. (2014; 2015) dataset were identified and evaluated. These black shales are all highly enriched in organic carbon and the critical trace elements denoted above. In addition, it appears that these black shales can be constrained to particular periods of Earth history, namely; the Middle- Late Paleoproterozoic, Cambrian-Early Ordovician, Middle Devonian, Carboniferous, Middle Permian, and short periods of the Cenozoic.

Here, the classification of 'highly-metalliferous black shales (HMBS)' is proposed to describe these occurrences. This designation can be assigned to those shales that have mean whole-rock contents of Mo + Ni + Zn + Se + V > 1500 ppm, 3x that of SDO-1, and TOC% of > 2% (Table 8.1). In comparison, the world shale average (WSA) has Mo + Ni + Zn + Se + V of 280 ppm, the USGS SDO-1 has a value of 460 ppm, and Black Sea sapropels average 550 ppm (Table 8.1). The new criteria restricts HBMS to <5% of all black shale stratigraphic units in the dataset of Large et al. (2015) and specifically includes major black shale-hosted deposits and districts. Due to their high organic carbon content, (2 to >20 wt % TOC, average ~10 wt %; Table 8.1, Fig.8.1.), most HMBS are also potential hydrocarbon targets.

In terms of depositional setting, most of the HMBS listed were deposited in continental margin, shelf, slope, or basin environments; however, a few examples occur in intercontinental shallow (epeiric) sea. While the host black shale may be on the order of 100s m thick, the HMBS member is commonly on the order of meters. The most metal-rich examples (Ni-Mo unit in the Cambrian Niutitang Formation, South China and Nick unit in the Devonian Canol Formation, Yukon) are stratiform, pyrite-rich strata only a few centimeters to 0.5 m thick and extend laterally for 100s to 1000s of kilometers (Hulbert et al., 1992; Lehmann, 2016).

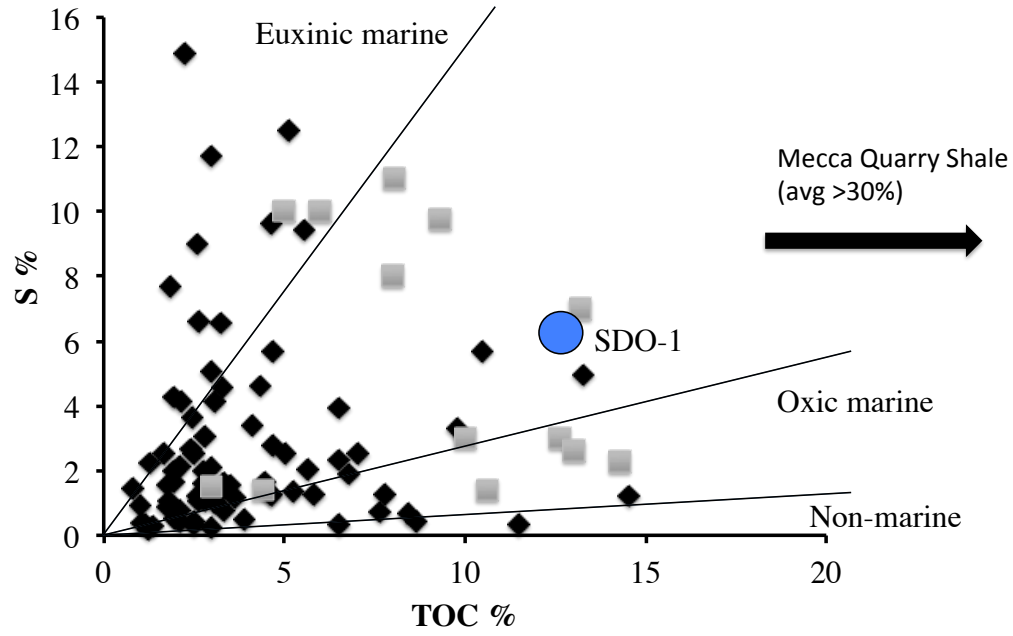

Figure 8.1. Total organic carbon (TOC) % vs S% for all black shale samples in the database of Large et al., 2015 (diamonds), HMBS (squares) and SDO-1. Thresholds are based on that of Raiswell, 1983.

Previous work (e.g. Large et al., 2014; 2015; Gregory et al., 2015), and in this thesis, suggest that the concentration of trace elements in sedimentary pyrite in black shales can reflect changes in ocean-atmosphere conditions. For example, the concentrations of Ni, Mo, Cu, Zn, Se, and Cd in marine pyrite have been proposed as a proxy for ocean nutrients, and the Se/Co ratio appears to correlate with modelled peaks in atmospheric pO_2 (Berner, 2006; Large et al., 2014; 2015, Long et al., 2015).

The nutrient TEs listed above (with the exception of Co and Mn) are highly enriched in the pyrite from the HMBS in comparison to the mean contents of pyrites from 'normal' black shale (Table 8.2). HMBS pyrite has mean concentrations of 1700 ppm Ni, 1400 ppm Zn, 890 ppm Se, 860 ppm Cu, 820 ppm Mo, 180 ppm Ag, and 70 ppm Cd (Table 8.2). Selenium, Mo, Cd, and Ag have the highest concentration factors (Table 8.2) compared to average marine pyrite. While Ni, Co, Cu, and Mn display the lowest concentration factors. In terms of Se, and the general nutrient proxy elements (Ni+Mo+Se+Zn+V; Large et al., 2015), HMBS pyrites plot toward the maximum end of the range for pyrite in black shales (Fig.

8.2). On the Neoproterozoic to Recent atmospheric pO_2 proxy diagram (Fig. 8.3), HMBS occurrences plot at intervals that coincide with periods of high-pO_2. In summary, the pyrite, and whole-rock chemistry suggests HMBS formation under conditions of maximum nutrient supply at times when atmospheric pO_2 was at, or close to, maximum levels for the Phanerozoic (current levels and above). The actual pO_2 levels during HMBS deposition cannot be ascertained with confidence, but based on the model of Berner (2009), values of 25 to 35 % atmospheric O_2 may be a suitable estimate.

A similar pattern between black shale enrichment and atmospheric oxygen is observed in the Paleoproterozoic where black shale occurrences are found in the rocks deposited in the wake of the Great Oxidation Event (G.O.E.), culminating in the formation the deposition of the Talvivaara, and Poorman metal-rich shales, followed by a large organic matter burial event ('Shunga Event'; Melezhik et al., 2004). In the wake of this event, black shale deposition and enrichments appear to decrease during the period 1.8 to 0.8 Ga, while atmospheric oxygen is argued to have remained low and stable.

Table 8.1. Summary of whole rock geochemistry of HMBS and black shale standards

	Paleoproterozoic Talvivaara, ~2.0Ga, Finland (n=40)	Paleoproterozoic Poorman Formation ~2.0 Ga, USA (n=5)	Lower Cambrian Ni-Mo South China Huangjiawan, Guizhou Mao et al. (2002)	Lower Cambrian Ni-Mo Guizhou S. China Coveney (pers. comm.)	Middle Cambrian Hot Shale Arthur Ck Fm TODD1 - HR1(n=1)	Late Cambrian Alum Shale Billingen Area Leventhal, 1991	Early Ordovician Turisalu Estonia (n=14)	Middle Devonian UM Popovich Fm. Carlin GA54c/1460ft. (n=1)	Middle Devonian Nick Horizon Yukon Sack (pers. comm.)	M-L Carboniferous Lisburne Group Alaska. Slack et al., 2015	M-L Carboniferous UM Heath Fm USA Kelley et al. (2015)	M-L Carboniferous Mecca Quarry Shale Illinois Coveney et al., 1987	M Cretaceous Julia Creek Shale Qld, Australia Lewis et al., 2010	black shale USGS SDO-1 Standard Huyck (1989)	WSA World Shale Avg. Wedepohl (1995)	Sapropel Black Sea Baturin (2011)
	Cont. margin, anoxic/euxinic basin	Cont. margin, anoxic/euxinic basin	*Cont. margin. Transistion to deep ocean*	passivel margin, transitional between platform & deep ocean	Anoxic shallow shelf	Anoxic shallow shelf	Anoxic shallow shelf	Continental margin, anoxic slope and basin	restricted basin with euxinic deepwater	continental margin, outer ramp anoxic deep water	epicratonic continental margin	continental interior shallow anoxic basins	epeiric anoxic sea			
wt %	**wt %**	**wt %**	**wt %**	**wt %**	**wt %**	**wt %**	**wt %**	**wt %**	**wt %**	**wt %**	**wt %**	**wt %**	**wt %**	**wt %**	**wt %**	**wt %**
SiO2	40.54	nd	nd	nd	nd	45.4	48.52	nd	nd	40.6	39	28.5	33.0	49.3	63.99	nd
TiO2	0.73	0.10 as Ti%	nd	nd	nd	nd	0.71	0.13	nd	0.29	0.38	0.4	0.3	0.71	0.84	nd
Al2O3	11.09	4.28 as Al%	nd	0.5	1.22	6.3	12.35	3.0	nd	5.5	8.3	9.1	6.3	12.3	18.03	nd
Fe2O3	19.92	15.41 as Fe%	nd	16.3	1.23	5.9	4.99	1.2	18.8	2.0	3.4	4.9	3.1	9.3	7.39	nd
MgO	3.91	1.56 as Mg%	nd	0.18	1	nd	1.06	7.5	0.02	1.2	1.8	1.1	0.6	1.5	2.72	nd
CaO	2.6	2.08 as Ca%	nd	3.68	8.87	nd	0.23	13.4	0.26	17.6	14.4	1.0	21.0	1.1	2.39	nd
Na2O	0.28	0.30 as Na%	nd	0.32	0.057	nd	0.09	0.05	0.015	0.3	0.5	0.3	0.6	0.4	0.87	nd
K2O	3.77	1.95 as K%	nd	0.14	0.51	4.4	7.36	1.1	0.12	1.5	1.4	2.2	0.9	3.4	3.48	nd
P2O5	0.19	0.05 as P%	2.0 as P%	>1.0	nd	nd	0.11	0.6	0.127	4.0	0.4	0.9	0.4	0.11	0.18	nd
TOC	8.05	9.3	nd	nd	3.0	13.2	12.6	4.4	4.3	10.6	14.3	31.9	13.0	9.9	0.2	2 to > 10
Tot S	11.05	9.77	nd	>10	1.51	7	3.0	1.4	2.1	1.4	2.3	2.5	2.6	5.4	0.24	nd
ppm	**ppm**	**ppm**	**ppm**	**ppm**	**ppm**	**ppm**	**ppm**	**ppm**	**ppm**	**ppm**	**ppm**	**ppm**	**ppm**	**ppm**	**ppm**	**ppm**
Ag	2.8	1.8	75	90	4.3	nd	nd	3.9	8.2	29.4	2.6	6.2	nd	0.13	nd	0.3
As	92	13.6	17,000	>10000	40.8	nd	59	50	3410	36.3	nd	30.8	37	68.5	13	22
Au ppb	nd	36	320	0.9	0.2	nd	nd	6	0.2	8.2	nd	2.3	nd	2.8	nd	4.6
Ba	257	294	800	24.3	104	630	442	590	6.6	372	99.3	412.7	350	397	580	1240
Bi	0.84	0.98	nd	8.4	0.55	nd	<2	0.1	1.5	<1	0.2	n.a.	nd	5	0.4	0.3
Co	91	74	185	198	5.6	29	35	3	289	3.9	12	23.7	10	47	19	26
Cd	nd	7	nd	nd	8.4	nd	nd	nd	nd	nd	71.5	nd	25	nd	nd	1.6
Cr	144	88	107	33	188	64	88	260	234	1104	310	524.8	65	66	90	57
Cu	1188	211	2600	3270	187	130	133	108	394	181	80	166.7	180	60	45	140
Mn	1631	1970	320	144	88	250	137	139	196	161	241	304.6	410	325	852	225
Mo	78	49	57,000	>10,000	54	260	236	120	2050	75.1	328	1354	190	134	2.6	110
Ni	1801	175	36,000	>10000	176	290	261	235	>10,000	399	238	344.5	180	100	50	132
Pb	71	55	504	517	19.6	45	121	8	110	12.4	26	74.0	17	28	20	10
Sb	5	11	550	440	5.4	nd	nd	30	76	10.0	32	46.4	nd	4.5	nd	3.8
Se	38	10	1655	1000	11.4	nd	3.78	42	>1000	56.4	nd	184.9	nd	nd	0.6	7
Sn	3.1	2.3		2.7	1.2	nd	nd	nd	8	<1	1.5	n.d.	nd	29	nd	1.3
Te	0.6	0.77	nd	0.79	0.17	nd	nd	0.2	3.7	0.3	nd	n.d.	nd	nd	nd	0.2
Tl	11	3	nd	64	0.05	nd	nd	2.5	211	2.7	7	n.d.	nd	8.3	nd	0.7
U	22	24	140	280	28	390	70	20	145	36.2	32	107.0	nd	49	2.7	17.8
V	796	508	1200	774	923	845	1181	2190	218	1305	890	2633	1670	160	130	256
W	nd	nd	na	2.3	0.94	nd	nd	0.5	4.2	<1	0.6	2.5	nd	3.3	nd	2
Zn	4809	1320	2950	924	863	335	287	1900	>10000	1968	1702	2190	910	64	95	48
Zr	100	43	nd	7.7	10.5	nd	161	nd	8.4	85	77	71.5	76.0	165	160	80
V+Mo+Se	7521	2069	98655	>23,000	2027	1730	1969	4487	>24,000	3803	3157	6706	>2950	458	279	553
Strongly enriched TE; TE > 2X SDO-1	Cr, Cu, Mn, Ni, Pb, V, Se, Zn	Ag, Au, Cu, Mn, Pb, Sb, V, Zn	Ag, As, Au, Ba, Co, Cu, Mo, Ni, Pb, Sb, Se, U, V, Zn	Ag, As, Co, Cu, Mn, Mo, Ni, Pb, Sb, Se, U, V, Zn	Ag, Cr, V, Zn	Cr, Cu, Mn, Mo, Ni, Pb, U, V, Zn	Cu, Mn, Ni, Pb, V, Zn	Au, Ag, Cr, Mn, Ni, Mo, Sb, Se, V, Zn	Ag, As, Co, Cr, Cu, Mo, Ni, Pb, Sb, Se, Tl, U, V, Zn	Ag, Au, Cr, Cu, Mn, Ni, Sb, Se, V, Zn	Ag, Cr, Mo, Ni, Sb, V, Zn	Cr, Mo, Ni, Sb, Se U, V, Zn	Cu, V, Zn			Cu

Nutrient trace element	HMBS pyrite mean	global marine pyrite mean	pyrite concentration factors
	ppm	ppm	
	n = 230	n = 5300	
Cd	73	6	12.2
Se	890	90	9.9
Ag	180	20	9.0
Mo	820	100	8.2
Zn	1400	210	6.7
Cu	860	450	1.9
Ni	1700	1100	1.5
Mn	1070	740	1.4
Co	62	480	0.1

Table 8.2. Mean concentrations of nutrient trace elements in pyrite from HMBS compared to the global marine pyrite data set (Large et al., 2015

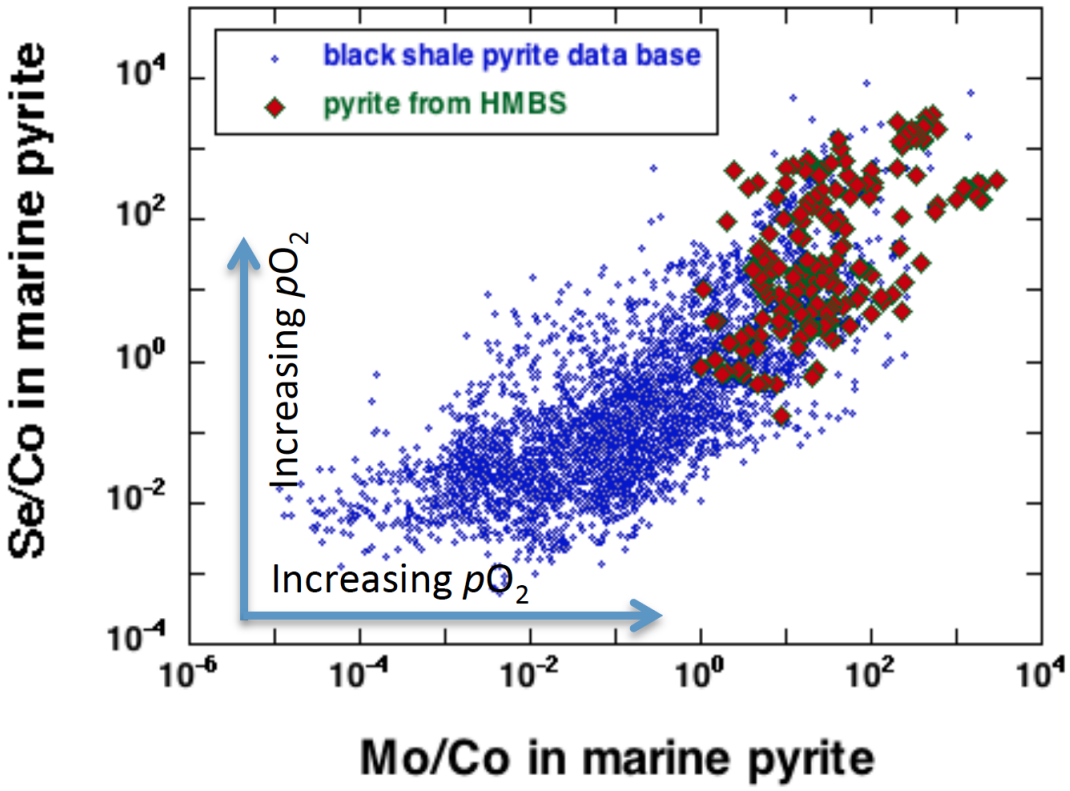

Figure 8.2. Mo/Co vs Se/Co ratios of pyrite.

8.2.4. Phanerozoic geodynamics, oxygenation and enrichment mechanisms

The secular distribution of HMBS in the Phanerozoic and peaks in the atmospheric oxygen record suggests that there may be a causational relationship. In the following section, a review of the dynamics of this Eon is presented, and the potential influences that such geodynamic fluctuations may have had on black shale enrichments are discussed. Since the peaks in HMBS appear to emerge over 100.m.y cycles and coincide with peaks of atmospheric oxygen, potential drivers and feedback mechanisms are presented, culminating in a framework for the development of HMBS during the Phanerozoic.

Following the last major global oxygenation event (G.O.E.2), the Phanerozoic Eon is a period of greater geochemical stability in comparison to the Archean and Proterozoic. The rise of animal life and the colonization of land plants led to the establishment of atmospheric O_2 concentrations near to that of present day, along with relative climate stability (Berner et al., 2009; Glasspool and Scott, 2010). This period archives the formation and break up of two supercontinents (Gondwana and Pangea) along with many orogenic events (Evans et al., 2003; Cawood, 2005; Cawood and Hawkesworth, 2014). The

cyclic nature of supercontinental cycles over 100 m.y. wave lengths appears to differentiate the Phanerozoic from the more stagnant tectonism of the Pre-Cambrian. HMBS also appear to be distributed in a similar fashion. Along with this, the Eon experienced various greenhouse and icehouse states. However, none of which culminated in large-scale glaciation like in the Precambrian. This is likely due to a more stable balance of oxygen and greenhouse gases in the atmosphere (Claire et al., 2006). Despite this apparent stability, changes in the burial rates of organic carbon and sulfur have affected changes in the level of atmospheric O_2, by as much as 40% in the case of the Carboniferous period (Berner et al., 2009). Changes in the burial rates are ultimately tied to changes in the productivity and life cycles of the biomass, and as such, can influence the accumulation of black shales. Understanding the interplay of these features may help to elucidate our understanding of black shale deposition during these intervals and explain their secular distribution.

Large et al. (2015), using the trace element content of sedimentary pyrite, argued that the influx of bio-essential elements was cyclic during the Phanerozoic where periods of low nutrient abundance correspond to periods of mass extinction, while periods of high nutrient abundance correspond to periods of enhanced bio-productivity and radiations. These peaks broadly correspond to the periods of HMBS enrichment; Cambrian, Middle-Devonian, Carboniferous, Middle-Permian, with minor peaks in the Cenozoic. Coeval with these time periods are major tectonic regime changes and orogenesis. Large et al. (2015) proposed that during periods of continental collision increased detritus would stimulate photic zone organisms and lead to increased bio-productivity and increased atmospheric O_2 as a result of feedbacks associated with this. The secular trends of nutrient trace elements in pyrite, modeled atmospheric O_2 cycles and the Sr record (e.g. Burke et al., 1982; Long et al., 2015) all lend support to this proposal. The idea can be further elaborated to suggest that HMBS form at the peaks of these processes.

Increased weathering and detrital input during such events may lead to enhanced nutrient uptake and spur bio-productivity. With increased nutrient supply and bio-productivity, CO_2 is sequestered and net O_2 increases as a function of photosynthesis. This, in turn, may lead to more aggressive oxidative weathering and greater nutrient input. As a result organic matter assimilates trace metals and transfers

them to the seafloor where they are deposited. The burial, degradation and oxidation of the deposited organic matter may lead to the development of euxinia, helping to increase transfer of the metals to the sediments (Scott et al., 2014).

Phanerozoic HMBS horizons tend to be high grade but only on the order of a few meters, the shale package hosting them, however, can be widespread and on the order of hundreds of meters thick. This suggests that the bio-essential TE supply and bio-productivity was fairly continuous and generally exceeded the drawdown of organic matter, and metals, into the marine muds, leading to the formation thick black shale packages. The HMBS horizons within the packages likely represent the maxima in these cycles where supply, productivity, and basin anoxia were all at optimal levels to enhance metal endowment, explaining their thin occurrences.

While the ultimate source of the metal enrichments is enhanced weathering as a result of increased atmospheric O_2, other factors such as high ocean TE inventory and low sedimentation rate are required in order to account for the extreme metal enrichment observed in examples such as at the Nick horizon, Yukon Territory, Canada (Hulbert et al., 1992) and the Ni-Mo horizon, South China (i.e. Mao et al., 2002). Locally, euxinic basins occurring within greater, generally oxic or at least non-sulfidic oceans, enhance the redox gradient at the basin depo-center and can allow for greater concentration of TE. A similar process can be invoked in order to explain such high concentrations in these HMBS examples. A modern example is the Cariaco Basin, where concentrations of Mo are 1 to 2 times the SDO-1 standard (mean of 128 ppm Mo, across 65 cm; Piper and Dean, 2002), although sedimentation deposition rates are too high in the Cariaco to achieve concentrations exhibited by HMBS intervals (Mao et al., 2002). Therefore slow and sustained black shale sedimentation is required in order to ensure greatest concentration potential in the metal-rich horizons. Furthermore, the development of local euxinic conditions and high organic matter content will act as an effect trap site for hydrothermal, metal-rich fluids that may exhale or be introduced along basin margins or via hydrothermal venting (e.g Mao et al., 2002). However these fluids tend to contain a different element suite and are distinguishable from much of the sedimentary pyrite data presented here (e.g., Steiner et al, 2001, and Jiang et al, 2007)

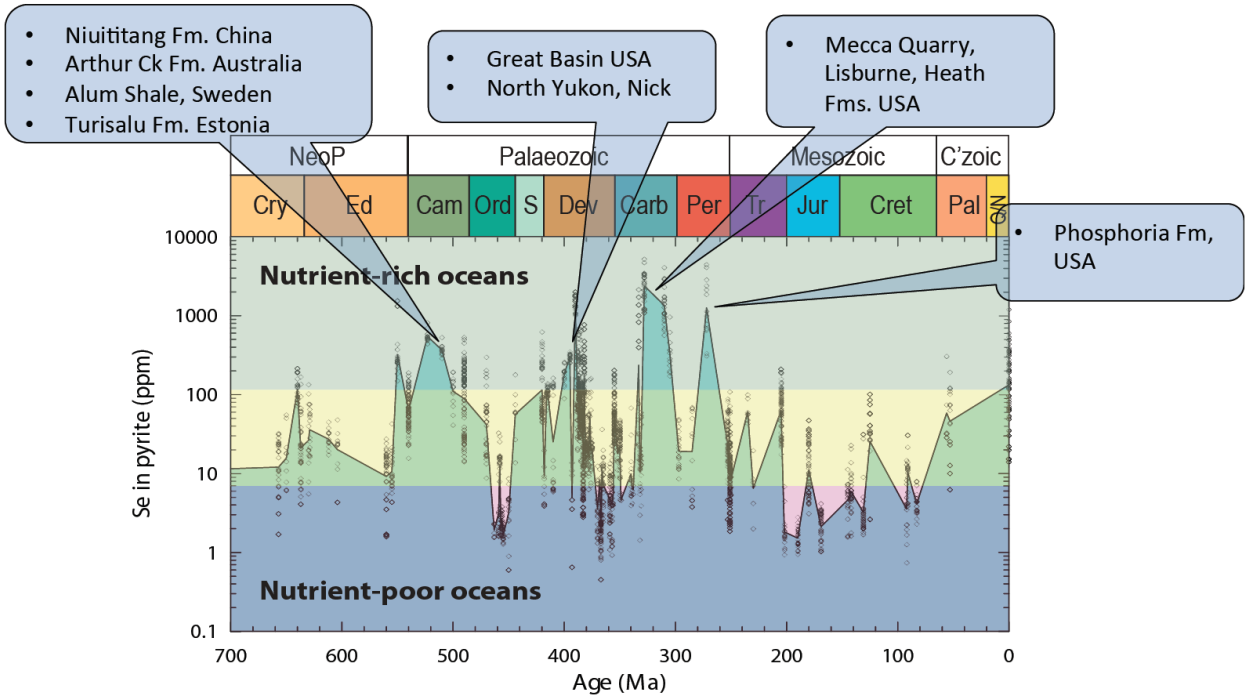

Figure 8.3. Mean Se content of pyrite (proxy for atmospheric O_2) from 700 Ma to present, with major black shale enrichments marked (after Large et al., 2015)

8.2.5. Proterozoic geodynamics, oxygenation and enrichment mechanisms

While the potential causational mechanisms discussed for Phanerozoic shale enrichments are constrained by a greater understanding of the geochemical evolution of Earth's surface and oceans, our understanding of the Precambrian is comparatively inhibited. This section reviews and discusses our state of knowledge of this time period, and whether the processes proposed as drivers to Phanerozoic HMBS hold true in the Pre-Cambrian. One of the key differences in black shale enrichment during these two time periods is the nature of the enrichment itself. Mesozoic enrichments, and onwards, tend to be thin horizons of very high grades, while the Pre-Cambrian HMBS examples tend to be characterized by thick, but low grade, sequences (i.e., Talvivaara). The Paleozoic Alum, Turisalu, and Chinese shales appear to be a transition between the two. This feature suggests that the nature of black shale enrichment may have changed through time. Possible explanation and processes are discussed and a differing model for Pre-Cambrian HMBS is proposed.

The second oxygenation event (G.O.E. 2) before the Phanerozoic helped to establish a, comparatively, more stable oxygenated atmosphere, biosphere, and ocean system. It is broadly accepted that at this stage the majority of the world's oceans were well ventilated and atmospheric oxygen was on the order of present day levels (Berner, 2009; Glasspool and Scott, 2010). However, the conditions in the Pre-Cambrian were drastically different. The Proterozoic period was buffered by significant oxidation events and 'Snowball Earth' style glaciations. Recently, there has been growing support that the Great Oxidation Event was a geologically short and punctuated interval, with latest, high resolution sampling (Luo et al, 2016) suggesting that dramatic oxygen increase occurred on the time scale of 1 to 10 million years at ~ 2.33 Ga. This supports previous proposals by workers who suggest that transition between a methane dominated atmosphere and a more oxygenated atmosphere was short and dramatic. Bekker et al. (2012) proposed that oxygen may have even reached values almost close to that of the Phanerozoic. This idea has been utilized by others that argue for a rapid rise of oxygen in the wake of GOE (e.g. Bekker and Holland, 2012; Harada et al., 2015; Luo et al., 2016).

Sediment metal enrichments in the Pre-Cambrian are broadly constrained to three time periods. Two of which correspond to periods of global glaciation and oxygenation. The other is during the Meso-Proterozoic where significant Zn-Pb enrichments are found in the McArthur Basin, Australia. Here, a number of world-class economic deposits are found. Their formation history has been studied in depth (e.g. Large et al., 2000) and their metal enrichments are related to SEDEX style mineralization. While the nature of the seawater and atmosphere played a role in facilitating the conditions for metal enrichment they are not the focus of this discussion.

Black shale enrichments are proposed to be a function of the complex interplay between tectonic, biological and atmospheric factors introducing nutrient elements into the ocean. This model may be readily applicable to the Phanerozoic where diverse life had been established and supercontinent cycles, along with periods of volcanic activity, are likely the key drivers to weathering and nutrient input to basins. However, the widespread deposition of the black shales and sedimentary metal enrichments during Archean to Paleoproterozoic time may not be as straightforward. Continental landmass was significantly less during this period and early supercontinents may have been comparatively smaller

than during the Phanerozoic. This begs the question as to whether there may be a different geodynamic and tectonic drivers facilitating metal input into basins. In this section, the notion that the Pre-Cambrian and Phanerozoic exhibit different states of the Earth system, in that "typical" geological processes may manifest and exert difference influences when boundary conditions are significantly different. The Archean and Proterozoic periods had limited biological activity compared to the Phanerozoic. The composition of the atmosphere was dominated methane in the Archean and low oxygen, high carbon (methane and CO_2) during the Proterozoic (Claire et al., 2006). This means that climate, its sensitivity and response to perturbations, may manifest in drastically different ways compared to the Phanerozoic. Namely, the late-Archean and Proterozoic were notably dominated by periods of global glaciation and while supercontinent formation is believed to have occurred (i.e. 2.7 Ga Kenorland and Nuna~1.9 Ga; Rogers and Santosh, 2002) it is likely that these large-scale glaciations, coupled with changes in the nature and composition of the atmosphere was also a likely driver for metal enrichments and bio-productivity blooms.

A potential series of events to account for organic carbon build up and metal enrichment in the rock record is outlined below. Here, it is proposed that increased bio-productivity, and metal transfer to the sediments, is likely a natural result of the manifestation of various geochemical and geodynamics changes that occurred during the Archean-Paleoproterozoic transition:

1) The pulses or 'whiffs' of oxygen (~3.0 Ga to 2.5 Ga) correspond to periods of initial (super-) continent formation that promote zones of upwelling and the concentration of detritus, stimulating photosynthetic biological activity, and forming oxygen oases along the continental margins (e.g. Caldeira & Kasting, 1992).

2) Eventually, O_2 in the atmosphere builds up and reaches a critical tipping point in the methane-rich Archean atmosphere which triggers a climatic response in the form of methane collapse, leading to global cooling and glaciation (i.e. Huronian glacial episode, ~2.46 Ga). During the colder and dryer conditions of glaciation, UV photolysis of water leads to the formation of hydrogen peroxide (Liang et

al., 2006) and draws down the O_2 levels in the atmosphere. Since there is no Ozone layer established at this time, the UV photolysis process may be very efficient on a large scale.

3) Hydrogen peroxide, which has the same freezing temperature as water, becomes preserved within the ice.

4) As O_2 levels being to drop and volcanic outgassing continues, photosynthesis is inhibited due to ice coverage, CO_2 and methane levels increase, the climate becomes warmer and the glaciers begin to melt. Hydrogen peroxide is released leading to another pulse of O_2, along with a short period (a few to 10 m.y.) of sustained bio-productivity as a result of outwash of glacial detritus and localized areas of O_2. Any O_2 not first bound by ferrous iron, manganese of other reduced chemical in oceanic surface waters (Kasting, 1987; Kasting and Ono, 2006) would remain dissolved, leading to net increase in O_2. Again, this leads to turn over and glaciation, but on a larger scale due to higher oxygen levels that perturb the current atmospheric and climate state. Photolysis, sequestration, and then release of hydrogen peroxide occur again. This results in an incremented increase in atmospheric O_2, nutrient input and biomass blooms corresponding to the end of each glacial cycle.

5) The change in atmospheric composition culminates in the first sustained global glacial episode- the Makganyene glaciation (~ 2.3Ga) following a rise of oxygen to above $x10^{-5}$ PAL, thereby inhibiting the photochemical fractionation of ^{33}S (Kopp et al., 2005; Luo et al., 2016). This, again, sequesters hydrogen peroxide but on a more profound scale due to the global nature of this glacial episode (a "Snowball"). Laing et al. (2006) modeled the potential hydrogen peroxide build up during a millions of year global glaciation, where the ozone layer had not been established and UV penetration was high. Their results suggested that there was a potential to generate and sequester x0.1 to x1 atmosphere equivalent H_2O_2 during a 10s m.y. sustained 'Snowball- style' glaciation. During de-glaciation the hydrogen peroxide is released in large quantities, stimulating a period of bio-productivity in which the feedbacks, already eluded to in the Phanerozoic examples, begin to become established. Increased

productivity increases atmospheric oxygen levels, potentially reaching values to close to that of the Phanerozoic for a short time (i.e. Bekker and Holland, 2012). Critically, it may have been that in this interval levels equivalent to 1% of the present atmospheric level (PAL) were reached, allowing aerobic respiration to become more energetic than anaerobic fermentation (Goldblatt et al., 2006), leading to increased O_2 production. Large changes in the balance of CO_2 and methane coupled with increasing productivity, increasing oxygen and carbon sequestration likely facilitated the Lomagundi- Jatlui carbon isotope excursion- the largest recorded in the rock record (Melezhik et al., 2013, Martin et al., 2013). It is towards the end of this time that deposition of metal-rich black shales occur (e.g. Talvivaara) where atmospheric oxygen, bio-productivity, oxidative weathering were all at their maximum and strong redox stratification of the ocean existed.

A compilation of the majority of biochemical cycles during this time period exhibit changes in the build up and aftermath of each glacial period (Fig 8.5.). For example there is a dramatic narrowing of the range of mass independent fractionation of sulfur, likely owing to the decreasing efficiency of UV penetration to allow for the photochemical reactions that produce these fractionations. Sulfate levels gradually begin to rise during the Paleoproterozoic and the ^{34}S values of sulfide and sulfate begin to display larger fractionations between the two species. This suggests that the seawater sulfate reservoir expanded in the wake of the G.O.E and glacial episodes and sulfur reducing bacteria had an open system with respect to sulfate, leading to ever increasing fractionation (Scott et al., 2014). Carbon isotopes begin to fluctuate in response to overturn in the carbon budget of the atmosphere and proliferation of organic biomass. Nitrogen isotope record begins to show increased fractionation throughout the Paleoproterozoic while the phosphorous also increases in the wake of the GOE (Bekker and Holland, 2012). These factors likely relate to increased nutrient supply and trophic zone productivity. Supporting this proposal is the content of several bio-essential elements in pyrite that also appear to vary through this interval, before all decreasing into the middle-Proterozoic.

Furthermore this may explain some of the factors that led to the apparent geochemical and biological status that is the 1.8 to 0.8 Ga “Boring Billion” period. The fluctuations in atmospheric, biological, and

geochemical cycles, and their feedbacks were likely not sustainable long term and led to a period of apparent geochemical stasis. When biological uptake eventually exceeded supply (i.e. ~ 1.9 Ga, in the aftermath of the 'Shunga event') bio-productivity decreased and oxygen levels began to drop, but did not return to pre-G.O.E. values. Since an oxygenated atmosphere had been established by this point, simple changes in O_2/CO_2 in the atmosphere were not likely dramatic enough to allow for large scale glaciation, and plate tectonic process remained muted, resulting in limited weathering and nutrient input in order to stimulate bio-productivity or oxygen production.

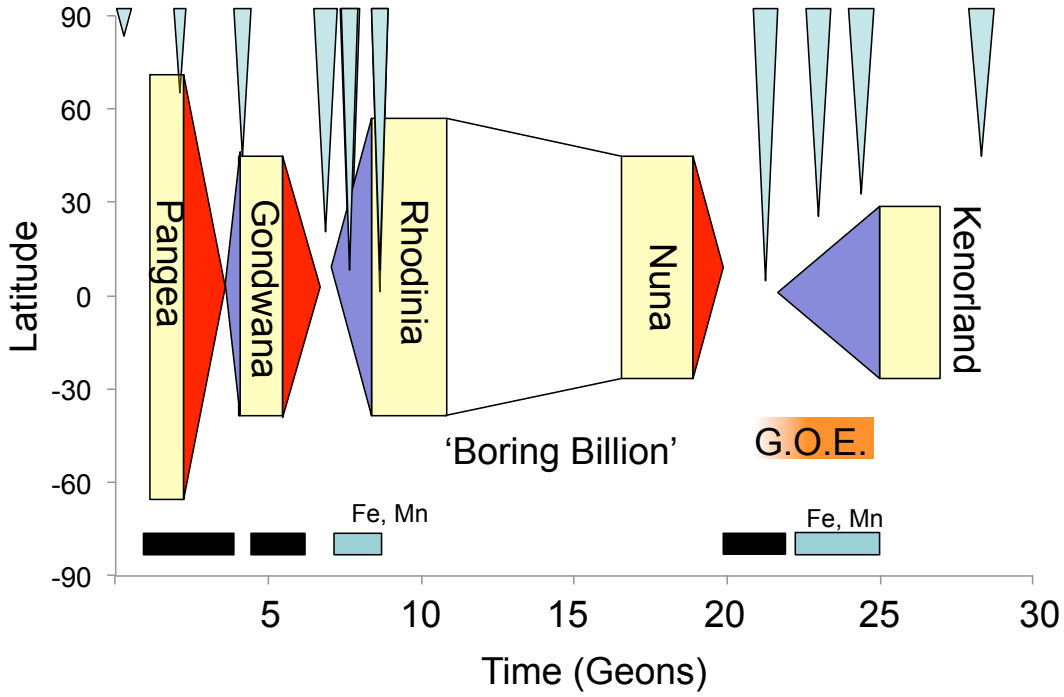

Figure 8.4. Schematic time-space plot of supercontinents and major glacial episodes. Size of supercontinents on y-axis relates to landmass area (converted from km^2 to degrees in order to show paleo-latitude extent), icicles hanging down denote equator-ward extent of glaciations (based on data from Evans et al., 2003 and Raub, unpublished). Periods of orogenesis are red and periods of continental dispersal are blue. Timings of major black shale and Fe, Mn deposits are also marked.

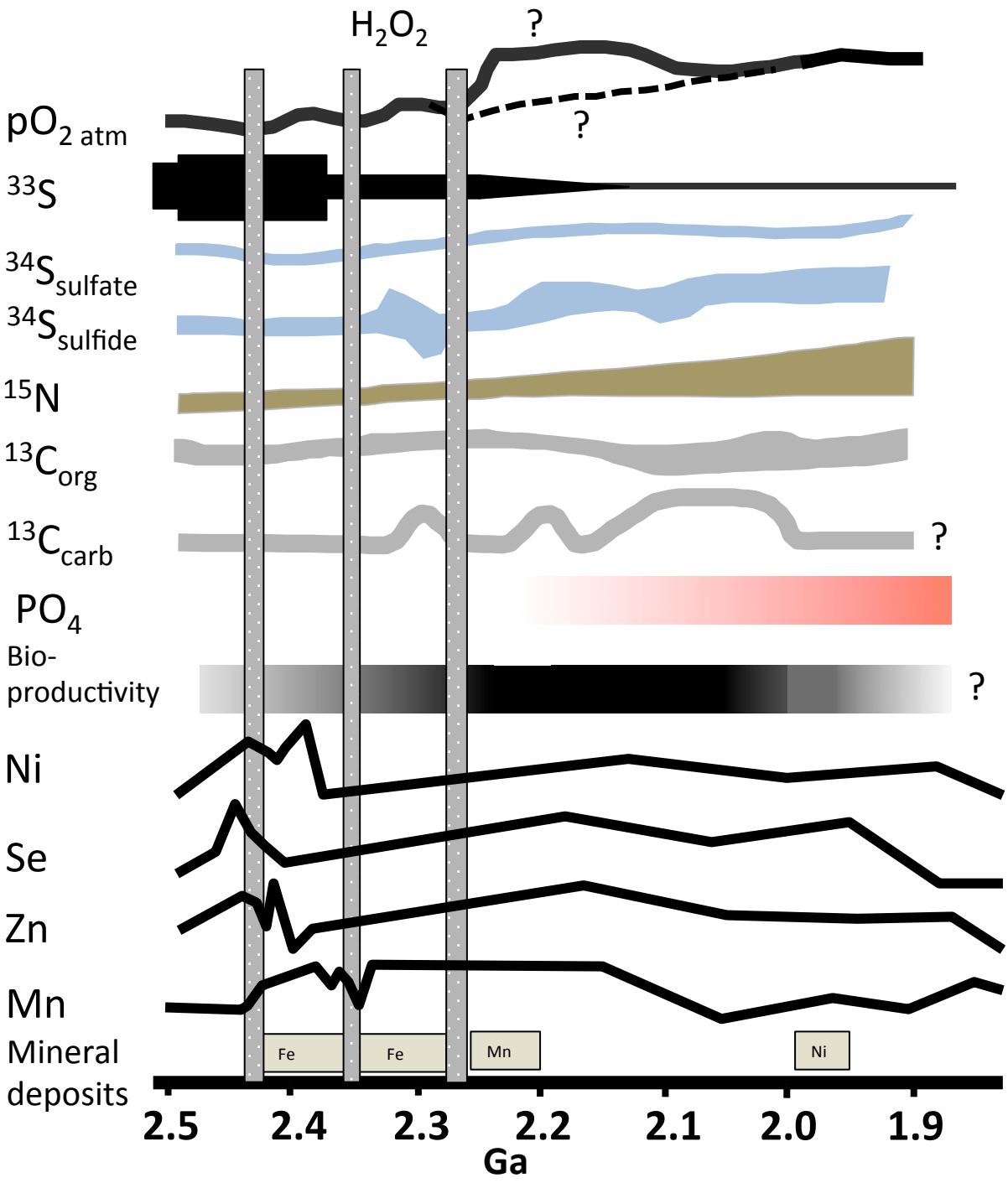

Figure 8.5. Schematic summary of various biogeochemical profiles across the Archean/ Paleproterozoic boundary (after Melezhik et al., 2013; Laakso and Schrag, 2014; Harada et al., 2015). Dashed line in the atmospheric profile portrays the traditional, gradual increase model (e.g. Berner, 2006) whereas the solid line portrays an 'overshoot' style event (Bekker and Holland, 2012). Nickel, Se, Zn and Mn profiles are from sedimentary pyrite (Large et al., in prep.).

8.2.6. Conclusion

This chapter presents an integrated mechanism to explain the relationship between black shale metal enrichments, tectonic processes and oxygenation. The argument presented here suggests that a combination of increased nutrient supply, an increase in bio-productivity, and strong redox stratification between increasing oxygen levels in the atmosphere, and development of low-oxygen depositional sites are the critical factors in facilitating black shale enrichment. Nutrient delivery can be enhanced during periods of continental uplift, collision or widespread glaciation, helping to introduce metals into the ocean and stimulate the oceanic biomass. As bio-productivity increases so does photosynthesis, culminating in down draw of CO_2 and increase in O_2. This leads to enhanced weathering of the continents and the introduction of more nutrient elements. A consequence of the sustained rise in productivity is continuous sinking of voluminous amounts of organic matter, over 90 % of which re-oxidizes, generating anoxic to euxinic bottom waters (Canfield, 1998). Thus conditions are created to favor the deposition of metalliferous black shales. The cycle begins to break when uptake of nutrients exceeds supply leading to a contraction of biomass as organic matter, carrying trace elements, begins to sink to the seafloor and degrade.

These cycles and interplays of punctuated atmospheric oxygen increase and tectonic processes may control the secular distribution of HMBS during the Phanerozoic: (1) Early to Late Cambrian (525-500 Ma; East African-Antarctic orogeny); (2) Middle Devonian (400-380 Ma; Appalachian-Caledonian orogeny); (3) middle to late Carboniferous (330-305 Ma; Hercynian- Alleghenian orogeny); (4) Middle Permian (~270 Ma, central Asian orogeny).

The mechanism outlined above proposes that continental collision and oxidative weathering are the critical factors that introduce trace elements into the ocean basins. However, the basin architecture during these events will also likely be influenced by the tectonic regime, meaning that it may become semi-restricted, promoting localized upwelling zones, helping to precondition the depositional setting for the development of low-oxygen conditions and the preservation of metals. Volcanic activity

supplying CO_2 to the atmosphere and increased nutrients to the oceans (Larson and Erba, 1999; Meyer and Kump, 2008) may also play a role in these processes.

Continental collisional events provide an apt mechanism for increased metal and nutrient supply to basins during Phanerozoic times where large landmasses had been established and climatic perturbations were not as dramatic. However, during the Pre-Cambrian, in particular the Paleoproterozoic, it is likely that other geodynamic factors could have played a role in facilitating the input mechanism for detrital nutrient trace elements. Since the nature of the Proterozoic atmosphere, oceans and climate were significantly different in may be argued that a combination of widespread glaciation, tectonic processes and overturn of many biogeochemical cycles with an anoxic to euxinic ocean likely culminated in large black shale deposition and enrichments.

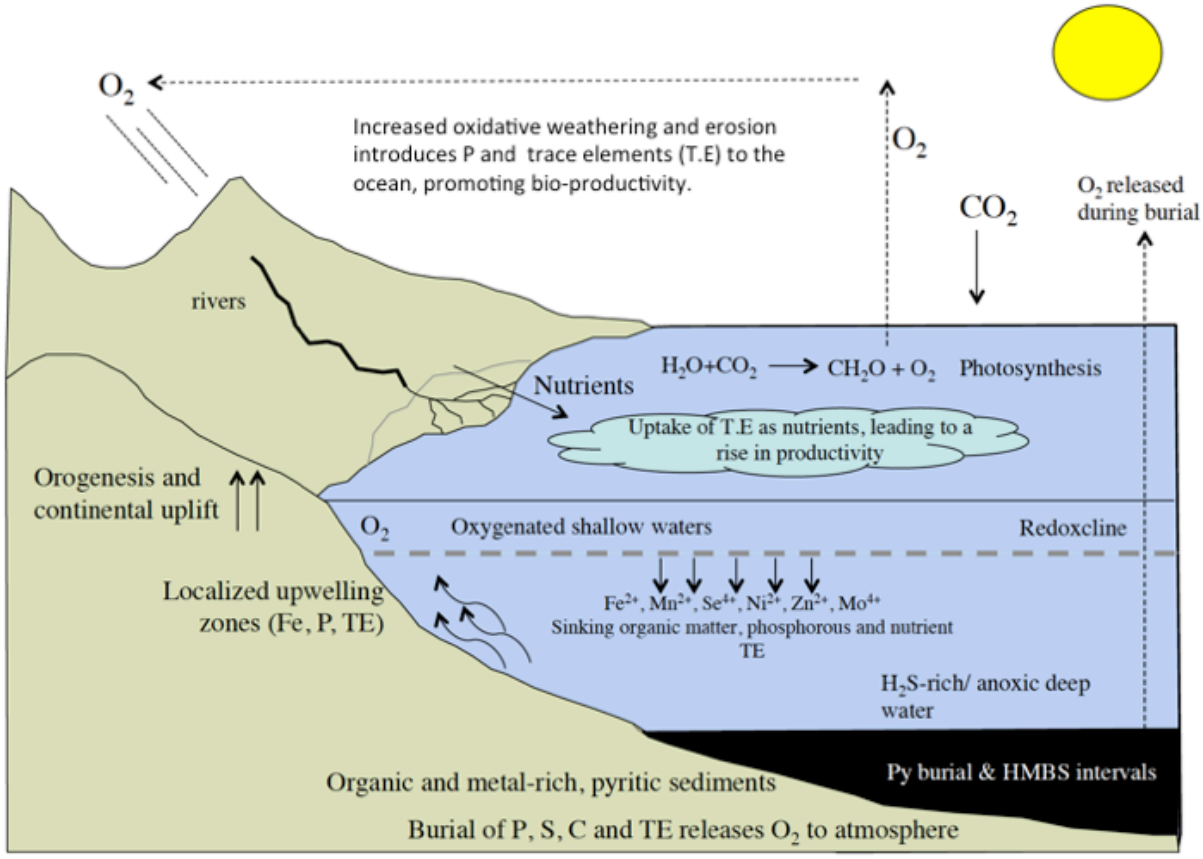

Figure 8.6. Schematic summary of nutrient input, atmospheric regulation, and feedbacks associated with HMBS formation.

The deposition of HMBS likely represents the short-term peak of each of these processes as well as potentially signifying the tipping point towards the re-establishment of 'normal' black shale deposition. This transition between the effects, and efficiencies, of these processes may also explain the changing nature of HMBS. The mid to Late Phanerozoic exhibit, relatively, narrow and concentrated enrichment intervals (m-scale), while the Paleoproterozoic HMBS (e.g. Talvivaara), deposited under a strongly redox stratified oceans and dramatic oxygenation, comprise a larger volume of black shale (10s- 100s m). The Cambrian and Ordovician examples that are both high grade and high tonnage may represent a transition between these two modes of HMBS enrichments, and the Earth's climatic state.

8.3. References

Baird, G. C., and Brett, C. E., 1986. Erosion on an anaerobic seafloor: significance of reworked pyrite deposits from the Devonian of New York State: Palaeogeography, Palaeoclimatology, Palaeoecology, 57, p. 157-193.

Baturin, G.N., 2011. Geochemistry of sapropel in the Black Sea. Geochemistry International, 49, p. 531–535.

Bekker, A., and Eriksson, K.A., 2003. A Paleoproterozoic drowned carbonate platform on the southeastern margin of the Wyoming Craton: a record of the Kenorland breakup. Precambrian Research, 120, p. 327-364.

Bekker, A., and Holland, H.D., 2012. Oxygen overshoot and recovery during the early Paleoproterozoic. Earth and Planetary Science Letters, 317– 318, p. 295–304.

Bekker, A., Karhu, J.A., Eriksson, K.A., and Kaufman, A.J., 2003. Chemostratigraphy of Paleoproterozoic carbonate successions of the Wyoming Craton: tectonic forcing of biogeochemical change? Precambrian Research, 120, p. 279-325.

Berner, R.A., 2006. GEOCARBSULF: a combined model for Phanerozoic atmospheric O 2 and CO 2. Geochimica et Cosmochimica Acta, 70, p. 5653-5664.

Berner, R.A., 2009. Phanerozoic atmospheric oxygen: New results using the geocarbsulf model. American Journal of Science, 309, p. 603–606.

Burke, W.H., Denison, R.E., Hetherington, E.A., Koepnick, R.B., Nelson, H.F. and Otto, J.B., 1982. Variation of seawater 87Sr/86Sr throughout Phanerozoic time. Geology, 10, p. 516-519.

Caldeira, K., and Kasting, J.F., 1992. Susceptibility of the Early Earth to Irreversible Glaciation Cause by Carbon Dioxied Clouds. Nature 359, p. 226-228.

Canfield, D.E., 1998. A new model for Proterozoic ocean chemistry. Nature, 396, p. 450–453.

Cawood, P.A., Hawkesworth, C.J. 2014. Temporal relations between mineral deposits and global tectonic cycles. Geological Society Special Publication, 393, p. 9-21.

Cawood, P.A. 2005. Terra Australis Orogen: Rodinia breakup and development of the Pacific and Iapetus margins of Gondwana during the Neoproterozoic and Paleozoic. Earth-Science Reviews, 69, p. 249-279.

Claire, M.W., Catling, D.C., Zahnle, K.J., 2006. Biogeochemical modelling of the rise in atmospheric oxygen. Geobiology, 4, p. 239-269.

Condie, K.C., 2015. Earth as an evolving planetary system. Academic Press.

Condie, K.C., Des Marais, D.J., Abbott, D. 2001. Precambrian superplumes and supercontinents: a record in black shales, carbon isotopes, and paleoclimates? Precambrian Research, 106, 239-260.

Coveney, R.M., and Glascock, M.D., 1989. A review of the origins of metal-rich Pennsylvanian black shales, central U.S.A., with an inferred role for basinal brines. Applied Geochemistry, 4, p. 347–367.

Coveney, R.M., Leventhal, J.S., Glascock, M.D., and Hatch, J.R., 1987. Origins of metals and organic matter in the Mecca Quarry Shale member and stratigraphically equivalent beds across the Midwest. Economic Geology, 82, p. 915–933.

Evans D.A.D., 2003. True polar wander and supercontinents. Tectonophysics, 362, p.303-320

Goldblatt, C., Lenton, T., Watson, 4., 2006. Bistability of atmospheric oxygen and the Great Oxidation. Nature, 443, p. 683- 686.

Fleurance, S., Cuney, M., Malartre, F., and Reyx, J., 2013. Origin of the extreme polymetallic enrichment (Cd, Cr, Mo, Ni, U, V, Zn) of the Late Cretaceous– early Tertiary Belqa Group, central Jordan. Palaeogeography, Palaeoclimatology, Palaeoecology, 369, p. 201–219.

Glasspool, I.J., and Scott A., 2010. Phanerozoic atmospheric oxygen concentrations reconstructed from sedimentary charcoal. Nature Geoscience, 3, p. 627–630.

Gregory, D., Meffre, S., and Large, R., 2014. Comparison of metal enrichment in pyrite framboids from a metal-enriched and metal-poor estuary: American Mineralogist, 99, p. 633-644.

Harada, M, Tajika, E., Sekine, Y., 2015. Transition to an oxygen-rich atmosphere with an extensive overshoot triggered by a Paleoproterozoic Snowball. Earth and Planetary Science Letters 419, p. 178–186.

Huerta-Diaz, M.A. & Morse, J.W., 1990. A Quantitative Method for Determination of Trace Metal Concentrations in Sedimentary Pyrite. Marine Chemistry, 29, p. 119-144.

Huerta-Diaz, M. A., and Morse, J. W., 1992, Pyritization of trace metals in anoxic marine sediments: Geochimica et Cosmochimica Acta, v. 56, no. 7, p. 2681-2702.

Huyck, H.L.O., 1989. When is a metalliferous black shale not a black shale?: U.S. Geological Survey Circular 1058, p. 42–56.

Jenkyns, H. C., 2010. Geochemistry of ocean anoxic events. Geochemistry Geophysics Geosystems, v. 11, 30 p.

Jiang, S.Y., Yang, J.H., Ling, H.F., Chen, Y.Q., Feng, H.Z., Zhao, K.D. and Ni, P., 2007. Extreme enrichment of polymetallic Ni–Mo–PGE–Au in Lower Cambrian black shales of South China: an Os isotope and PGE geochemical investigation. Palaeogeography, Palaeoclimatology, Palaeoecology, 254, p. 217-228.

Kasting, J.F., Ono, S. 2006. Palaeoclimates: the first two billion years. Philosophical Transactions of the Royal Society of London B: Biological Sciences- B; Biological Sciences, 361, p. 917- 929.

Kopp, R. E., Kirschvink, J. L., Hilburn, I. A., Nash, C.Z., 2005. The Paleoproterozoic Snowball Earth: A climate disaster triggered by the evolution of oxygenic photosynthesis. Proceedings of the National Academy of Sciences, 102, p. 11131-11136.

Kirschvink, J.L., Gaidos, E.J., Bertani, L.E., Beukes, N.J., Gutzmer, J., Maepa, L.N., and Steinberger, R.E., 2000, Paleoproterozoic Snowball Earth: Extreme climatic and geochemical global change and its biological consequences:, 97, p. 1400-1405.

Kirschvink, J.L., Kopp, R.E., 2008. Palaeoproterozoic ice houses and the evolution of oxygen-mediating enzymes: the case for a late origin of photosystem II. Philosophical Transactions of the Royal Society of London B- Biological sciences, 363, p. 2755- 2765.

Laakso, T.A. and Schrag, D.P., 2014. Regulation of atmospheric oxygen during the Proterozoic. Earth and Planetary Science Letters, 388, p. 81-91.

Large, R.R., Bull, S.W., and McGoldrick, P.J., 2000. Lithogeochemical halos and geochemical vectors to stratiform sediment hosted Zn-Pb-Ag deposits. Part 2: HYC deposit, Northern Territory. Journal of Geochemical Exploration, 64, p. 105–126.

Large, R.R., Halpin, J.A., Danyushevsky, L.V., Maslennikov, V.V., Bull, S.W., Long, J.A., Gregory, D.D., Lounejeva, E., Lyons, T.W., Sack, P.J. and McGoldrick, P.J., 2014. Trace element content of sedimentary pyrite as a new proxy for deep-time ocean–atmosphere evolution. Earth and Planetary Science Letters, 389, p. 209-220.

Large, R.R., Halpin, J.A., Lounejeva, E., Danyushevsky, L.V., Maslennikov, V.V., Gregory, D., Sack, P.J., Haines, P.W., Long, J.A., Makoundi, C. and Stepanov, A.S., 2015. Cycles of nutrient trace elements in the Phanerozoic ocean. Gondwana Research, 28, p. 1282-1293.

Larson, R.L. and Erba, E, 1999. Onset of the mid-Cretaceous greenhouse in the Barremian- Aptian: Igneous events and the biological, sedimentary, and geochemical responses. Paleoceanography, 14.

Lehmann, B., Frei, R., Xu, L., and Mao, J., 2016. Early Cambrian black shale hosted Mo-Ni and V mineralisation on the rifted margin of the Yangtze Platform China: Reconnaissance chromium isotope data and a refined metallogenic model. Economic Geology, 111, p. 89–104.

Leventhal, J.S., 1991. Comparison of organic geochemistry and metal enrichment in two black shales: Cambrian Alum Shale of Sweden and Devonian Chattanooga Shale of United States. Mineralium Deposita, 26, p. 104-112.

Lewis, S.E., Henderson, R.A., Dickens, G.R., Shields, G.A., and Coxhell, S., 2010. The geochemistry of primary and weathered oil shale and coquina across the Julia Creek vanadium deposit (Queensland, Australia): Mineralium Deposita, 45, p. 599–620.

Liang, M., Hartman, H., Kopp, R. E., Kirschvink, J. L., and Yung, Y.L., 2006. Production of hydrogen peroxide in the atmosphere of a Snowball Earth and the origin of oxygenic photosynthesis. Proceedings of the National Academy of Sciences, 103, p. 18896-18899.

Luo, G., Shuhei, O, Beukes, N.J., Wang, D.T., Xie, S., and Summons, R.E., 2016. Rapid oxygenation of Earth's atmosphere 2.33 billion years ago. Science Advances, 2, 1600134.

Lyons, T. W., Anbar, A. D., Severmann, S., Scott, C., and Gill, B. C., 2009, Tracking euxinia in the ancient ocean: a multiproxy perspective and Proterozoic case study: Annual Review of Earth and Planetary Sciences, v. 37, p. 507-534.

Mao, J., Lehmann, B., Du, A., Zhang, G., Ma, D., Wang, Y., Zeng, M., and Kerrich, R., 2002, Re-Os dating of polymetallic Ni-Mo-PGE-Au mineralization in Lower Cambrian black shales of South China and its geologic significance: Economic Geology, v. 97, no. 5, p. 1051-1061.

Martin, A.P., Condon, D.J., Prave, A.R., Melezhik, V.A., Lepland, A. and Fallick, A.E., 2013. Dating the termination of the Palaeoproterozoic Lomagundi-Jatuli carbon isotopic event in the North Transfennoscandian Greenstone Belt. Precambrian Research, 224, p.160-168.

McLennan, S.M., 2001. Relationships between the trace element composition of sedimentary rocks and upper continental crust. Geochemistry Geophysics Geosystems (paper # 2000GC000109).

Melezhik, V.A., Filippov, M.M. and Romashkin, A.E., 2004. A giant Palaeoproterozoic deposit of shungite in NW Russia: genesis and practical applications. Ore geology reviews, 24, p.135-154.

Melezich, V. A., Prave, A., Fallick, A.E., Kump, L., Struass, H., Lepland, A., Hanski, E., (Eds), 2013. Reading the Archive of Earth's oxygenation. Volume 1.: The Paleoproterozoic of Fennoscandia as Context for the Fennoscandian Arctic Russia Drilling Early Earth Project. Frontiers in Earth Sciences. Springer, Hiedelberg.

Piper, D. Z., and Dean, W. E., 2002, Trace-element deposition in the Cariaco Basin, Venezuela Shelf, under sulfate-reducing conditions: A history of the local hydrography and global climate, 20 ka to the present: US Geological Survey, 2330-7102.

Rogers, J. J., Santosh, M., 2002. Configuration of Columbia, a Mesoproterozoic supercontinent. Gondwana Research, 5, p. 5–22.

Rollinson, H.R., 1993. Using geochemical data: evaluation, presentation, interpretation, Longman Group UK.

Scott, C., Wing, B., Bekker, A., Planavsky, N.J., Medvedev, P., Bates, S.M., Yun, M., and Lyons, T.W., 2014. Pyrite multiple-sulfur isotope evidence for rapid expansion and contraction of the early Paleoproterozoic seawater sulfate reservoir. Earth and Planetary Science Letters, 389, p. 94–104.

Scott, C., Kelley, K.D., Slack, J.F., 2014. The geobiology of sediment-hsted ore deposits. Society of Economic Geologists Special Publication, 18, p. 17-35.

Slack, J.F., Selby, D., and Dumoulin, J.A., 2015. Hydrothermal, biogenic, and seawater components in metalliferous black shales of the Brooks Range, northern Alaska: Syn-sedimentary metal enrichment in a carbonate ramp setting. Economic Geology, 110, p. 653–675.

Steiner, M., Wallis, E., Erdtmann, B.D., Zhao, Y. and Yang, R., 2001. Submarine-hydrothermal exhalative ore layers in black shales from South China and associated fossils—insights into a Lower Cambrian facies and bio-evolution. Palaeogeography, Palaeoclimatology, Palaeoecology, 169(, p. 165-191.

Trabucho Alexandre, J., Tuenter, E., Henstra, G. A., van der Zwan, K. J., van de Wal, R. S. W., Dijkstra H. A., and de Boer, P. L., 2010. The mid-Cretaceous North Atlantic nutrient trap: Black shales and OAEs, Paleoceanography, 25, PA4201.

Tribovillard, N., Algeo, T. J., Lyons, T., and Riboulleau, A., 2006, Trace metals as paleoredox and paleoproductivity proxies: An update: Chemical Geology, v. 232, no. 1, p. 12-32.

Wedepohl, K.H. 1995. The composition of the continental crust. Geochemica Cosmochemica Acta, 59, p.1217- 1232.

Xu, L.G., Lehmann, B., and Mao, J.W., 2013. Seawater contribution to polymetallic Ni-Mo-PGE-Au mineralization in Early Cambrian black shales of South China. Evidence from Mo isotope, PGE, trace element, and REE geochemistry. Ore Geology Reviews, 52, p. 66–84.

Chapter 9

Conclusions and future work

9.1. Conclusions

The work presented in this thesis has aimed to address some of the geochemical complexities associated with black shale metal enrichment and the role of sulfides in influencing and archiving such processes. Also presented is a new model that aims to address the secular nature of black shale metal enrichment through time. This model proposes four critical factors in attaining large metal endowment: 1) A period of dramatically increased nutrient supply. 2) Increased bio-productivity and pulses in atmospheric O_2. 3) Sustained positive feedbacks between detrital and input biological productivity. 4) The generation of strong redox stratification in the basin in order to facilitate maximum metal accumulation and preservation. Chapters 5, 6, 7 and 8 provide an original contribution in addressing aspects of sulfide chemistry and metal enrichments in black shales in the context of primary enrichments, as a function of geodynamic processes, and in terms of mechanisms to mobilize and concentrate metals upon alteration of original metal-rich sequence.

Chapter 5 presents data that shows a Cambro-Ordovician sequence in NW Estonia captures the largest global carbon isotope excursion of the Phanerozoic and has never before been documented in this part of Baltica. The high-resolution dataset captures the prelude and aftermath of this event where a change in tectonic forcings, led to enhanced phosphogenesis and bio-productivity, and may have facilitated the isotope event. In the aftermath of this the shallow shelf of Baltica was likely euxinic to anoxic, helping to facilitate metal enrichment. The powerful use of pyrite chemistry along with other whole-rock techniques has allowed for a greater understanding as to the nuances of this transition that may have otherwise been overlooked.

Chapter 6 discusses the complexity of the Talvivaara deposit and presents a summary of pyrite paragenesis and geochemistry, suggesting that the original depositional environment was extremely metal rich, and likely was a product of enhanced oxidative weathering and euxinia in the wake of the G.O.E. This model differs from those previously published that favor a major hydrothermal component to the metal enrichment. Furthermore, the preservation of early, diagenetic pyrite means that some of its trace element signature can be analyzed to help understand the nature of the depositional environment. This has allowed for the study of the effects of metamorphism on the original metal-rich sedimentary package, and suggests that the breakdown of early metal-rich pyrite, and organic matter, released trace elements leading to formation of the current ore assemblage.

Chapter 7 builds on the concepts proposed in Chapter 6 and presents an experimental study coupled with real-word evidence that pyrite may convert to pyrrhotite at lower temperatures than previously considered. Here, a concept is presented that suggests the break down of organic matter in black shales during late diagenesis or catagenesis may be able to provide sufficient reduction potential in order to start the conversion. Here, it is proposed that the conversion likely starts via solid-state diffusion where sulfur begins to desorb at the boundary with the organic material in the rock, resulting in a pyrrhotite rim to the pyrite. Since the conversion is likely rate-limited by the diffusion of iron and sulfur in the mineral then the influence of additional trace elements in the Fe and S sites in the crystal lattice may also effect the efficiency of this reaction. Furthermore, the concept that heat generation during the reduction to pyrrhotite may help to further the progress of the reaction at varying scales is an idea that has not been fully assimilated into previous models for orogenic deposits.

Chapter 8 presents a compilation of data from various metalliferous black shales through geological time and presents a potential mechanism for their enrichment. The secular distribution of metal-rich black shales in the Phanerozoic may represent periods of increase atmospheric oxygenation, facilitated by increased bio-productivity as a function of trace metal input during collisional episodes. The

collisional episodes may alter the basin circulation patterns leading to localized upwelling zones and help to precondition the basin for black shale formation. Increased bio-productivity as a function of upwelling and detrital input leads to an increase in atmospheric oxygen and the weathering of the continents. This establishes a cycle of increasing biomass and atmospheric oxygen until uptake exceeds supply and the cycle begins to break. Proterozoic metal enrichments are suggested to follow a similar process, however the initial increase in oxygen and supply of nutrients is likely related to widespread glacial activity- something that is lacking in Phanerozoic record.

9.2. Future work and questions arising from this study

1) This study has displayed evidence that the chemistry of sedimentary pyrite can be an effective tool to aid in the understanding of primary enrichment mechanisms during black shale deposition. However there are still aspects that require additional work- in particular, can we exactly quantify and model trace metal uptake by pyrite as a function of the depositional environment? This is something that can be addressed using samples from IODP cores of recent sediments. For example, the recent IODP Exp. 347, on the Baltic Sea, recovered fresh pyritic muds along with corresponding pore water chemistry. By building an integrated model that looks at pore water chemistry, biology and sediment chemistry through the profile may help to quantify its affects on the coeval pyrite formation.

2) How common is the conversion of pyrite to pyrrhotite at low temperatures? Additional material from black shales in the prehnite to pumpellyite facies range may help to address this question. Rocks from the Otago Schist can be revisited in addition to other classic Barrovian sequences. In addition, a detailed study of sulfide minerals in oil shales may also help to constrain the dynamics of the transition and whether the application of pyrite and pyrrhotite chemistry on surface rocks can be another useful tool in identifying prospective hydrocarbon sources at depth. In addition, further experimental work could be

undertaken where pyrite is heated in various atmospheres, like in previous studies but then analyzed by LA-ICP-MS mapping. This is a technique not available to researchers when conducting the original experiments. In addition, this may help to addresses the influence of other mineral phases in black shales and the effect that they may have in buffering the conversion at lower temperatures and the distribution of trace elements. From this, additional modeling of heat flow and the propagation of redox, pH and Eh fronts through a rock mass at various scales, and at low temperatures, may help to develop this concept.

3) What is the driver of the end Cambrian SPICE event? Many localities, and now Pakri, Estonia, archive this event, and exhibit evidence for dramatic variation in relative seawater accompanying the carbon isotope excursion. Traditional tectonic processes cannot easily account for both atmospheric carbon fluctuations and rapid sea-level rise in such a short geological period (a few m.y). Do we need to appeal to non-uniformitarian geological processes?

4) What is the exact fate of many trace elements in black shales and can we fully model and quantify their behavior? This is a question can be addressed via a series of experimental growth studies of diagenetic pyrite. For example, creating a controlled environment featuring a supply of organic matter of known composition and simulating a variety of low-oxygen conditions (i.e. anoxic, euxinic and dysoxic) along with 'seawater' with a particular concentration of trace elements. This way, one may be able to accurately measure and quantify the trace metal budget between seawater, organics and the sulfide minerals forming. In addition it may also add to our understanding of pyrite growth mechanisms i.e via a precursor mono-sulfide? Or as growth surfaces associated with degrading organic matter? And at what stage in this process do trace metals become concentrated in pyrite? Combining such an approach with recent sediment cores, such as IODP 347, mentioned above, could lead to the ability to accurately model reaction kinetics of certain trace elements with pyrite as a function varying redox state, based on both experimental and real-world data.

5) Are there additional tools that can be added in order to support the dataset compiled here? The multi-proxy approach adopted here has shown that pyrite, whole-rock geochemistry and isotope geochemistry can be effectively used in unison to fully interrogate ancient black shales and their depositional environment. Each of these approaches help to speak to various aspects of the depositional environment, pyrite can allow us to understand the range and variability within a sample, whilst also showing nuances that may not be discernable in whole-rock values. Whole-rock geochemistry allows us to speak to the overall enrichments in the rock while carbon and sulfur isotopes can inform us about the biological activity within the basin and the state of the ocean/atmosphere/climate cycle. An additional, and powerful, technique to add to this arsenal lies in the biochemistry of organic matter and biomarkers that could add a new, exciting dimension to this work. Furthermore, Fe-speciation studies and Mo isotopes on the Estonian samples could add another dimension to this work in further constraining the development of euxinia, along with producing one of the most comprehensive multi-proxy, high resolution datasets.

6) Further work in understanding the Talvivaara deposit. The new, detailed sulfide paragenesis presented here, especially the using the in-situ $\delta^{34}S$ approach, is a powerful tool to address such metamorphogenic, or altered, deposits. ^{33}S data for the earliest pyrite generate has been conducted but this can be augmented with ^{36}S in order to fully understand the dynamics of the system. Furthermore, the application of ^{33}S and ^{36}S throughout the sulfide paragenesis can aid in our understanding of ^{33}S dynamics during closed-system, high-grade metamorphism. This may have further implications for our understanding of the MIF signature in ancient, deformed settings.